Straightforward functionalization of mesoporous silica nanoparticles for therapeutic applications

kumulative

Dissertation

zur Erlangung des akademischen Grades Dr. rer. nat.

der Fakultät für Naturwissenschaften der Universität Ulm

vorgelegt von

Roman Schmid

geboren in Isny im Allgäu

Ulm, 2023

Amtierender Dekan:	Prof. Dr. Kay-E. Gottschalk
Erstgutachter:	Prof. Dr. Mika Lindén
Zweitgutachter:	Prof. Dr. Holger Barth
Tag der Promotionsprüfung:	24.04.2024

Universität Ulm

Institut für Anorganische Chemie II

Abstract

In the last decades nanomaterial-based drug delivery has become a major field in biomedical and chemical research due to its high potential to overcome challenges commonly associated with novel therapeutic drugs, such as low bioavailability, premature degradation or limited targetability. Amongst the many nanomaterials discussed within this research area, mesoporous silica nanoparticles (MSN) have evolved as one of the most pursued material classes. Unique properties, like their large specific surface area, high porosity, tunability of surface charge and functional motifs as well as overall good biocompatibility, make them highly promising candidates for drug delivery applications. However, despite many research efforts, only few silica-based materials have made their way into clinical trials so far. Reasons for this are versatile and include administration-specific hurdles challenging the applicability of these materials, as well as laborious and complex synthesis and testing procedures. Thus, in this thesis focus was laid on the synthesis and functionalization of MSN to overcome challenges often confronted upon oral or intravenous administration. In addition, novel formulation and testing concepts as well as insights into peptide-based drug loading mechanisms are presented to save research resources in future studies.

In the first part of this work design-criteria for effective oral administration of nanoparticles were identified. Elongated MSN were synthesized and further functionalized with either polyethylene glycol (PEG) or hyaluronic acid (HA) to exhibit increased retention and residence time in the gastrointestinal tract dependent on the health status of the intestinal tissue *in vivo*, which is a pre-requisite for functional drug delivery. While PEGylated particles were abundant in healthy tissue, HA functionalized particles clearly experienced accumulation in inflamed tissue, which is beneficial for the treatment of inflammatory diseases, like inflammatory bowel disease. These findings were connected to different behavior on mucus-secreting cell cultures *in vitro* depending on the functional motif of the MSN, indicating the usefulness of such *in vitro* methods to predict the outcome of *in vivo* studies. Moreover, PEG particles were shown to be taken up into systemic circulation and into the organs to some extent, potentially enabling not only locally restricted but systemic drug delivery as well.

Furthermore, a cell-based *in vitro* screening method was proposed to identify most promising MSN types regarding their targetability towards tumor cells against their clearance by macrophages. For this purpose, the uptake of differently charged and functionalized particles into PC-3 cells or THP-1 cells was investigated via laser scanning confocal microscopy and flow cytometry. While no clear trend was observed for the uptake into cancer cells, the internalization into the macrophage model cells was strongly dependent on the extent of serum protein adsorption onto the particles. By introducing a cell type specific uptake ratio, PEGylated MSN were identified as

the most promising particle type with high uptake into cancer cells, but at the same time low internalization into macrophages, a finding which was connected to former literature studies. Overall, this simple screening method proposed within this thesis may both reduce future research effort necessary and help paving the way of MSN into the clinics.

In the second part of this thesis, straight forward formulation and screening methods were proposed. In general, rapid adsorption of serum proteins followed by fast blood clearance of MSN remain the most challenging barriers for their intravenous administration, and PEG is the most studied polymer for overcoming these hurdles. However, PEGylation methods mostly used in literature are complex and the synthesis parameters and the high PEGylation degrees can negatively influence drug loading efficiency. Thus, in this work, adsorption of PEG onto silica nanoparticles and subsequent drug loading in different solvents were thoroughly studied and identified as promising concept for effective and straightforward formulation strategies for future clinical use. By in-depth examination of adsorption isotherms for varying PEG sizes, solvents and silica nanoparticle types, detailed insights into solvent-dependent conformational states and the localization of PEG on the particles were obtained. While PEG exhibited an upright-orientated dense brush conformation in water, a rather flat conformation was observed when adsorption took place in dichloromethane. This finding was reflected by differences in serum protein adsorption investigated via gel electrophoresis. Moreover, the PEG was found to be mainly located within the pore systems which has important implications on drug loading efforts. By changing the solvent type upon drug loading/before PEG adsorption high drug loading and PEGylation degrees were obtained which may enable prolonged circulation times of these highly loaded drug carriers.

Finally, adsorption studies of a novel peptide-based drug onto silica nanoparticles with different pore structures and sizes were presented. JM#21 was used as a novel drug to gain insights into adsorption mechanisms and dependencies on particle properties such as porosity, hydrophobicity or charge. By tuning the peptide charge state via pH variation, adsorption was shown to be mainly driven by electrostatic attraction between the silica support and the peptide as well as intermolecular repulsion and charge dependent peptide structure. The adsorption isotherms and maximum loading degrees were proven to be strongly dependent on the pore size and its limitation on the adsorption geometry. These results were supported by computational peptide modelling studies. Moreover, under electrostatically unfavorable conditions, high loading levels could be obtained by increasing the particle’s hydrophobicity. The peptide-loaded particles were tested in a functional, cell-based *in vitro* assay proving that the labile peptide was successfully protected by the carrier and that it was released in a fully functional form. This work provides valuable knowledge about the optimization of adsorption parameters to enable efficient peptide-based drug

loading into MSN and underlines the potential of MSN as innovative and promising drug delivery platform.

Zusammenfassung

In den letzten Jahrzehnten hat sich der Transport von Medikamentenwirkstoffen mithilfe von Nanomaterialien zu einem wichtigen Bereich in der biomedizinischen und chemischen Forschung entwickelt. Dieser bietet ein großes Potenzial zur Überwindung von Problemen, welche häufig mit neuartigen therapeutischen Arzneimitteln assoziiert sind, wie beispielsweise geringe Bioverfügbarkeit, vorzeitiger Wirkstoffabbau oder begrenzte Zielgerichtetheit. Unter den vielen Nanomaterialien, welche derzeit erforscht werden, haben sich mesoporöse Silikananopartikel (MSN) zu einer der am meisten untersuchten Materialklassen entwickelt. Einzigartige Eigenschaften wie ihre große spezifische Oberfläche, ihre hohe Porosität, die Variabilität ihrer Oberflächenladung sowie ihre Modifizierbarkeit mit funktionalen Molekülen, wie auch ihre gute Biokompatibilität machen sie zu vielversprechenden Kandidaten für den Transport von Medikamentenwirkstoffen. Trotz zahlreicher Forschungsanstrengungen haben jedoch bisher nur wenige Materialien auf Silikabasis den Weg in klinische Studien gefunden. Dies mag an den vielseitigen und verabreichungsspezifischen Hürden liegen, die die Anwendbarkeit dieser Materialien erschweren, sowie an den aufwändigen und komplexen Synthese- und Testverfahren. Daher wurde in dieser Arbeit der Schwerpunkt auf die Synthese und Funktionalisierung von MSN gelegt, um jene Herausforderungen zu überwinden, welche bei der oralen oder intravenösen Verabreichung häufig auftreten. Darüber hinaus werden neue Formulierungs- und Testkonzepte sowie Einblicke in peptidbasierte Wirkstoffbeladungsmechanismen vorgestellt, um in zukünftigen Studien Forschungsressourcen zu sparen.

Im ersten Teil dieser Arbeit wurden Design-Kriterien für eine wirksame orale Verabreichung von Nanopartikeln ermittelt. Hierfür wurden längliche MSN synthetisiert und entweder mit Polyethylenglykol (PEG) oder Hyaluronsäure (HA) funktionalisiert, um eine erhöhte Retention und Verweildauer im Gastrointestinaltrakt in Abhängigkeit vom Gesundheitszustand des Darmgewebes *in vivo* zu erreichen, was eine Voraussetzung für eine effektive Medikamentenverabreichung ist. Während PEGylierte Partikel in gesundem Gewebe reichlich vorhanden waren, reicherten sich HA-funktionalisierte Partikel eindeutig in entzündetem Gewebe an, was für die Behandlung von entzündlichen Erkrankungen, wie beispielsweise „Inflammatory Bowel Disease“, von Vorteil ist. Diese Ergebnisse wurden in Zusammenhang mit dem unterschiedlichen Verhalten auf Mucus-produzierende Zellkulturen *in vitro* in Abhängigkeit von der Oberflächenfunktionalisierung der Partikel gebracht, was auf die Nützlichkeit solcher *in vitro*-Methoden zur Vorhersage der Ergebnisse von *in vivo*-Studien hinweist. Darüber hinaus konnte gezeigt werden, dass PEG-Partikel in gewissem Umfang in den Blutkreislauf und in die Organe aufgenommen werden, was möglicherweise nicht nur eine lokal begrenzte, sondern auch eine

systemische Verabreichung von Medikamenten ermöglicht.

Darüber hinaus wurde eine zellbasierte *in vitro*-Screening-Methode untersucht, um die vielversprechendsten MSN-Typen hinsichtlich ihrer zielgerichteten Aufnahme in Tumorzellen gegenüber ihrer Aufnahme in Makrophagen zu identifizieren. Zu diesem Zweck wurde die Internalisierung von unterschiedlich geladenen und funktionalisierten Partikeln in PC-3-Zellen oder THP-1-Zellen mittels konfokaler Laser-Scanning-Mikroskopie und Durchflusszytometrie untersucht. Während für die Aufnahme in Krebszellen kein eindeutiger Trend beobachtet werden konnte, war die Internalisierung in die Makrophagen-Modellzellen stark abhängig vom Ausmaß der Serumproteinadsorption auf den Partikeln. Durch die Einführung eines zelltypspezifischen Aufnahmeverhältnisses wurden PEGylierte MSN als der vielversprechendste Partikeltyp identifiziert, der eine hohe Aufnahme in Krebszellen, aber gleichzeitig eine geringe Internalisierung in Makrophagen aufwies, ein Ergebnis, welches durch bestehende Literaturstudien bestätigt wird. Die in dieser Arbeit vorgeschlagene einfache Screening-Methode könnte perspektivisch sowohl zukünftigen Forschungsaufwand verringern als auch den Weg von MSN in den klinischen Einsatz ebnen.

Im zweiten Teil dieser Arbeit werden einfache Formulierungs- und Screening-Methoden präsentiert. Die schnelle Adsorption von Serumproteinen, gefolgt von der schnellen Ausscheidung von MSN aus der Blutzirkulation, stellt nach wie vor die größte Herausforderung bei deren intravenösen Verabreichung dar, wobei PEG das am häufigsten untersuchte Polymer zur Lösung dieses Problems darstellt. Die meisten der in der Literatur vorgeschlagenen Methoden zur PEG-Funktionalisierung sind jedoch komplex, und die verwendeten Syntheseparameter sowie die angestrebten hohen PEGylierungsgrade können die Effizienz der späteren Medikamentenbeladung negativ beeinflussen. Daher wurde die Adsorption von PEG auf Silikananopartikel und die anschließende Beladung mit Wirkstoffen in verschiedenen Lösungsmitteln untersucht und als vielversprechendes Konzept für wirksame und unkomplizierte Formulierungsstrategien für den künftigen klinischen Einsatz identifiziert. Durch die detaillierte Untersuchung der Adsorptionsisothermen von PEG mit unterschiedlichem Molekulargewicht in verschiedenen Lösungsmitteln und auf verschiedenen Partikelarten, konnten detaillierte Einblicke in lösungsmittelabhängige Konformationszustände und die Lokalisierung des Polymers auf den Partikeln gewonnen werden. Während PEG in Wasser eine aufrecht orientierte dichte „brush“-Konformation aufwies, wurde bei der Adsorption in Dichlormethan eine eher flache Adsorptionsgeometire beobachtet. Dieser Befund spiegelte sich in deutlichen Unterschieden bei der Adsorption von Serumproteinen wider, welche mittels Gelelektrophorese untersucht wurde. Außerdem wurde festgestellt, dass sich das PEG hauptsächlich innerhalb der des Porensystems befindet, was wichtige Auswirkungen auf die Beladung mit Wirkstoffen hat. Durch Änderung des

Lösungsmitteltyps nach der Medikamentenbeladung beziehungsweise vor der PEG-Adsorption wurden eine hohe Beladung und gleichzeitig ein hoher PEGylierungsgrad erreicht, was eine effiziente Medikamentenbeladung und gleichzeitig eine längere Zirkulationsdauer im Blut ermöglichen könnte.

Darüber hinaus wurden Adsorptionsstudien eines neuartigen peptidbasierten Wirkstoffs auf Silikananopartikeln mit unterschiedlichen Porenstrukturen und -größen durchgeführt. JM#21 wurde als Modellwirkstoff verwendet, um Einblicke in die Adsorptionsmechanismen und deren Abhängigkeit von Partikeleigenschaften wie Porosität, Hydrophobizität und Ladung zu gewinnen. Es wurde gezeigt, dass die Peptidadsorption hauptsächlich durch elektrostatische Anziehung zwischen Silikaoberfläche und dem Peptid sowie durch intermolekulare Abstoßung und die ladungsabhängige Peptidstruktur gesteuert wird. Dabei hingen die Formen der Adsorptionsisothermen und die maximalen Beladungsgrade entscheidend von der Porengröße und deren begrenzenden Einfluss auf die Adsorptionsgeometrie ab. Diese Ergebnisse wurden durch computergestützte Peptidmodellierungsstudien unterstützt. Zudem konnten unter elektrostatisch ungünstigen Bedingungen hohe Beladungsgrade durch die Einführung hydrophober Oberflächenfunktionen erzielt werden. Die Peptid-beladenen Partikel wurden in einem funktionellen, zellbasierten *in vitro*-Assay getestet. Hierbei stellte sich heraus, dass das labile Peptid erfolgreich durch dessen Beladung in die Partikel vor vorzeitigem Abbau geschützt, und in voll funktionsfähiger Form freigesetzt wurde. Diese Arbeit liefert wertvolle Erkenntnisse für die Optimierung von Adsorptionsparametern, um eine effiziente Beladung von MSN mit peptidbasierten Wirkstoffen zu ermöglichen und demonstriert das Potenzial von MSN als innovative und vielversprechende Trägerplattform für den Transport von Medikamentenwirkstoffen.

Table of contents

Abstract I

Zusammenfassung IV

Table of contents VII

List of publications IX

Table of figures X

Table of figures X

Abbreviations XIII

I Introduction 1

1. Nanoparticles for therapeutic applications 1

1.1. Oral administration of nanoparticles 3

1.1.1. Factors influencing particle retention in healthy intestinal tissue 4

1.1.2. Targeting the inflamed intestinal tissue 10

1.2. Intravenous administration of nanomaterials 11

1.2.1. Particle parameters influencing cellular uptake and biodistribution 11

1.2.2. Protein adsorption onto nanoparticles 16

1.3. The “nano problem“: area of conflict for therapeutic formulations 26

2. Mesoporous silica nanoparticles for biological applications 28

2.1. Synthesis of mesoporous silica nanoparticles 29

2.2. Functionalization of silica nanoparticles via covalent coupling 31

2.3. Functionalization of MSN with active biocomponents 36

2.4. PEG adsorption onto MSN: The solution to the nano problem? 39

II Motivation and aims of the thesis 42

III Results and discussion 47

1. Testing of MSN in biological settings 47

2. Drug loading and formulation of MSN 53
IV Conclusion and outlook 59
V References 63
VI Publications 93
1. Declaration of authorship 93
1.1. Publication I 93
1.2. Publication II 93
1.3. Publication III 93
1.4. Publication IV 94
2. Publication I 95
3. Publication II 113
4. Publication III 126
5. Publication IV 141
VII Supporting information to the publications 154
1. Publication I 154
2. Publication II 166
3. Publication III 173
4. Publication IV 183
VIII List of publications and Curriculum Vitae 196
1. List of publications during PhD research 196
2. Curriculum Vitae 198
IX Note of thanks 199
X Eidesstattliche Erklärung 200

List of publications

This cumulative thesis is based on the following publications, which were submitted to peer-reviewed journals:

Straightforward adsorption-based formulation of mesoporous silica nanoparticles for drug delivery applications.

Schmid R*, Neffgen N*, Lindén M., J Colloid Interface Sci. 2023, 640, 961-974. https://doi.org/10.1016/j.jcis.2023.03.012. (*equal contribution)

Published by Elsevier, Copyright © 2023. This is an open access article under the CC BY NC 4.0 license (https://creativecommons.org/licenses/by-nc/4.0/).

Towards a simple in vitro surface chemistry pre-screening method for nanoparticles to be used for drug delivery to solid tumours.

Schmid R, Kaiser J, Willbold R, Walther N, Wittig R, Lindén M. Biomater Sci. 2023,11, 6287-6298. https://doi.org/10.1039/D3BM00966A.

Published by Royal Society of Chemistry, Copyright © 2023. This is an open access article under the CC BY-NC 3.0 license (https://creativecommons.org/licenses/by-nc/3.0/).

Surface functionalization affects the retention and bio-distribution of orally administered mesoporous silica nanoparticles in a colitis mouse model.

Schmid R, Volcic M, Fischer S, Qu Z, Barth H, Popat A, Kirchhoff F, Lindén M. Sci Rep 13, 20175 (2023). https://doi.org/10.1038/s41598-023-47445-6.

Published by Springer Nature, Copyright © 2023. This is an open access article under the CC BY 4.0 license (https://creativecommons.org/licenses/by/4.0/).

Confinement and polarity effects on the peptide packing density on mesoporous silica nanoparticles.

Beitzinger B*, Schmid R*, Jung C, Tiwary K, Hermann P, Jacob T, Lindén M. Langmuir 2024, 40, 8, 4294–4305. https://doi.org/10.1021/acs.langmuir.3c03513. (*equal contribution)

Copyright © 2024 The Authors. Published by American Chemical Society. This is an open access article under the CC BY 4.0 license (https://creativecommons.org/licenses/by/4.0/).

Table of figures

Figure 1. Schematic overview of different types of nanomaterials. (reprinted from: Abuzer Alp Yetisgin, Sibel Cetinel, Merve Zuvin, Ali Kosar, Ozlem Kutlu, “Therapeutic Nanoparticles and Their Targeted Delivery Applications”, Molecules, Volume 25, page 3, ©2020, https://doi.org/10.3390/molecules25092193, CC BY 4.0 https://creativecommons.org/licenses/by/4.0/)[2] 2

Figure 2. Schematic representation of the size exclusion effect of mucus on the diffusion and transport of particles. Moreover, the permeability of particles can be influenced by tuning the particles’ surface properties, rendering them mucus-adhesive and non-adhesive/mucus-permeable. (reprinted from: José das Neves, Mansoor Amiji, Bruno Sarmento “Mucoadhesive nanosystems for vaginal microbicide development: friend or foe?”, Wiley Interdisciplinary Reviews: Nanomedicine and Nanobiotechnology, Volume 3, page 392, ©2011, https://doi.org/10.1002/wnan.144 with friendly permission by John Wiley and Sons)[59] 6

Figure 3. Schematic illustration of the influence of particle properties on their fate upon contact with mucosal surfaces. Mucoadhesive/non-penetrative particles get entrapped within the mucus, or are not able to penetrate into the mucus layer in the first place. As mucus gets constantly renewed, steady turn over rates causing the particles to stay localized within the lumen and eventually to be transported-off site along with shedded mucus and luminal contents in the range of minutes (min) to hours (hrs). On the other hand, mucus-penetrating particles are able to diffuse through the mucus layer towards the epithelia, causing an increased exposure of cells to the drug transporter and its cargo. The particles are protected against clearance and exhibit a longer retention as their non-penetrative analoques on the healthy mucosa. (reprinted from: Samuel K. Lai, Ying-Ying Wang, Justin Hanes “Mucus-penetrating nanoparticles for drug and gene delivery to mucosal tissues”, Advanced Drug Delivery Reviews, Volume 61, page 164, ©2009, https://doi.org/10.1016/j.addr.2008.11.002 with friendly permission by Elsevier)[25] 7

Figure 4. Trajectories (duration of 3 s) on mucus of excised mouse colorectal tissue and spatial distribution on mucus-adhesive (MAP, red) and mucus-penetrative (MPP, green) particles in colorectums of mice. MPP are able to penetrate through the mucus layer resulting in an uniform translocation across the tissue surface, while non-penetrating MAP are aggregated and localized preferentially in the center of the lumen. (reprinted from: Katharina Maisel, Laura Ensign, Mihika Reddy, Richard Cone, Justin Hanes, “Effect of surface chemistry on nanoparticle interaction with gastrointestinal mucus and distribution in the gastrointestinal tract following oral and rectal

administration in the mouse", Journal of Controlled Release, Volume 197, page 52, ©2015, https://doi.org/10.1016/j.jconrel.2014.10.026 with friendly permission by Elsevier)[40] 9
Figure 5. Schematic drawing of the principle of passive tumor tissue targeting. While normal tissue is well drained via the lymphatic system, tumor tissue vasculature exhibits pronounced leakiness enabling increased nanoparticle uptake into the tissue. (reproduced with permission by Springer Nature from: Zahid Hussain, Shahzeb Khan, Muhammad Imran, Muhammad Sohail, Syed Wadood Ali Shah, Marcel de Matas, "PEGylation: a promising strategy to overcome challenges to cancer-targeted nanomedicines: a review of challenges to clinical transition and promising resolution", Drug Delivery and Translational Research, Volume 9, page 726, ©2019, https://doi.org/10.1007/s13346-019-00631-4)[126] 14
Figure 6. Schematic overview of PC formation on nanoparticles. A) The dynamic nature of the corona is governed by high and low affinity proteins causing a continuous protein exchange and the formation of a hard and soft corona. B) The extent and identity of protein adsorption depends on the physico-chemical properties of the particles. (Used with friendly permission of Royal Society of Chemistry from: Cindy Gunawan, May Lim, Christopher P. Marquis, Rose Amal, "Nanoparticle–protein corona complexes govern the biological fates and functions of nanoparticles", Journal of Materials Chemistry B, Volume 2, page 2062 ©2014, https://doi.org/10.1039/C3TB21526A)[147] 19
Figure 7. The chain conformation of surface-bound PEG depends on the grafting density and PEG molecular weight. (modified (cropped from original figure) from Mengyi Li, Shuai Jiang, Johanna Simon, David Paßlick, Marie-Luise Frey, Manfred Wagner, Volker Mailänder, Daniel Crespy, Katharina Landfester "Brush Conformation of Polyethylene Glycol Determines the Stealth Effect of Nanocarriers in the Low Protein Adsorption Regime", Nano Letters, Volume 21, page 1592, ©2021, https://doi.org/10.1021/acs.nanolett.0c03756, CC BY 4.0 https://creativecommons.org/licenses/by/4.0/)[213] 22
Figure 8. Schematic drawing of the conformation classification of surface-bound PEG. S is the spatial distance between two neighbored chains, R_f is the Flory radius, which depends on the number of ethylene glycol units, the monomer length and the solvent. With increasing packing density, the chain distance decreases causing the polymer coils to adapt an upright orientation, eventually resulting in a dense brush regime. (Used with friendly permission of Royal Society of Chemistry from Xiaoli Liu, Lin Yuan, Dan Li, Zengchao Tang, Yanwei Wang, Gaojian Chen, Hong Chen, John L. Brash, "Blood compatible materials: state of the art", Journal of Materials Chemistry B, Volume 2, page 5722 ©2012, https://doi.org/10.1039/C4TB00881B)[198] 24
Figure 9. Hydrolysis and condensation reactions of a silica precursor during the sol-gel process (R = alkyl, H) according to Brinker et al.[253] 29

Figure 10. Co-condensation approach to obtain functionalized MSN. A functional silane (R = organic residue) is introduced along with the main precursor (TEOS in this case). The functional group is evenly distributed across the porous silica. (reprinted from Frank Hoffmann, Maximilian Cornelius, Jürgen Morell, Michael Fröba “Silica-Based Mesoporous Organic–Inorganic Hybrid Materials”, Angewandte Chemie - International Edition, Volume 45, page 3220 ©2006, https://doi.org/10.1002/anie.200503075 with friendly permission by John Wiley and Sons)[271] ... 32
Figure 11. Schematic drawing of EDC/NHS coupling chemistry. Upon pre-activation of the carboxylic acid with the carbodiimide EDC, the conjugate can be reacted with sulfo-NHS forming a stable intermediate for further coupling with a primary amine forming an amide bond. 34
Figure 12. Schematic overview of functionalization of MSN with different biocomponents such as antibodies, imaging agents or therapeutic drugs. In this example, PEI was used as anchoring groups and covalent functionalization was achieved via amide coupling chemistry. (Used with friendly permission of Royal Society of Chemistry from Jessica M. Rosenholm, Cecilia Sahlgren, Mika Lindén, “Towards multifunctional, targeted drug delivery systems using mesoporous silicananoparticles – opportunities & challenges”, Nanoscale, Volume 2, page 1874 ©2009, https://doi.org/10.1039/C0NR00156B)[119] 36
Figure 13. Schematic drawing of functionalization of rod-shaped MSN with PEG or HA for targeting healthy or inflamed intestinal tissue. 43
Figure 14. Schematic drawing of a straight-forward formulation process of PEGylated, drug-loaded MSN based on adsorption in solvents with orthogonal polarity. 45

Abbreviations

APTES	(3-aminopropyl) triethoxysilane
µm	micrometer
AR	aspect ratio
BET	Brunauer-Emmett-Teller
BSA	bovine serum albumin
BSA	bovine serum albumin
cm	centimeter
cmc	critical micelle concentration
CTAB	cetyltrimethylammonium bromide
CXCL12	C-X-C motif chemokine 12
CXCR4	C-X-C chemokine receptor type 4
Da	Dalton
DCC	N',N'-dicyclohexyl carbodiimide
DLS	dynamic light scattering
DMON	MSN with dendritically arranged pores and organic moieties
DMON_c	MSN with dendritically arranged pores and organic moieties, calcined
DMSN	MSN with dendritically arranged pores
EDC	3-(3-dimethylaminopropyl)carbodiimide
EMA	European Medicines Agency
EPIX4	endogenous CXCR4 antagonist
FCS	fetal calf serum
FDA	Food and Drug Administration
g	gramm
GIT	gastro-intestinal tract
HA	hyaluronic acid
i.v.	intravenous
JM#21	model peptide
kDa	Kilodalton
kg	kilogramm

KPI	key performance indicator
m	meter
MAP	mucus-adhesive particle
MDa	Megadalton
ml	milliliter
MPP	mucus-penetrating particle
MPS	mononuclear phagocyte system
mRNA	messenger ribonucleic acid
MSN	mesoporous silica nanoparticles
MSNc	calcined mesoporous silica nanoparticles
MSN-COOH	carboxy functionalized MSN
MSN-HA	hyaluronic acid functionalized MSN
MSNhex	MSN with hexagonally arranged pores
MSN-NH2	amino functionalized MSN
MSN-PEG	PEG functionalized MSN
MSNrod	elongated, rod-like MSN
MTX	mitoxantrone
Mw	Molecular weight
NHS	N-hydroxysuccinimide
NLDFT	non-local density functional theory
nm	nanometer
NMR	nuclear magnetic resonance
NSN	non-porous silica nanoparticles
NSNc	calcined non-porous silica nanoparticles
Papp coefficient	apparent permeability coefficient
PC	protein corona
PEG	poly(ethylene glycol)
PEG2k	PEG with a molecular wight of 2000 Da
PEG5k	PEG with a molecular wight of 5000 Da
PEI	poly(ethyleneimine)
pI	point of isoelectric charge
PLGA	poly(lactic-co-glycolic acid)
PMA	phorbol 12-myristate 13-acetate

PMO	periodic mesoporous organosilicas
PS	polystyrene
RES	reticuloendothelial system
SAXS	small-angle x-ray scattering
TEER	trans-epithelial electrical resistance
TEOS	tetraethyl orthosilicate
TJ	tight junctions
TMOS	tetramethyl orthosilicate
V	volume

I Introduction

1. Nanoparticles for therapeutic applications

In 2020, the world was hit by the COVID-19 pandemic leading to enormous research efforts for the fast development of vaccines against the SARS-CoV-2 virus. By January 2021 two mRNA-based vaccines, BNT162b2 by Pfizer/BioNTech and mRNA-1273 by Moderna, were approved by the European Medicines Agency (EMA). This immense success would have not been possible without the protection and intracellular delivery of the fragile mRNA compound via a drug delivery platform, in this case PEGylated lipid nanoparticles. This underlines the high potential of nanoparticles for drug delivery and therapeutic applications in general.[1] The term “nanoparticles” refers to particulate structures in the sub-micrometer range which can consist of a brought variety of materials, e.g. polymers, metals and metal oxides, liposomes, carbon (see Figure 1). In recent years, nanoparticles have been suggested for use in medical applications, such as imaging, tissue engineering, diagnostics, thermal therapy, or drug delivery. In the field of drug delivery, these materials promise advantages over conventional approaches, like site-targetability, higher efficiencies, improved biodistribution, and the reduction of negative drug-related side-effects.[2] However, the physicochemical and biological properties of nanoparticles can be diverse, and much effort and consideration must be put into the design of a functional drug carrier depending on the specific application. The administration ways of drug carriers are versatile and can include the intra peritoneal, transdermal, buccal, inhalative, intravenous or the oral route, whereas each route comes with specific requirements to the delivery platform. Thus, in the following chapters, the focus will be primarily on the requirements of oral and intravenous applications of nanomaterials in general as well as the physicochemical properties required for overcoming these barriers.

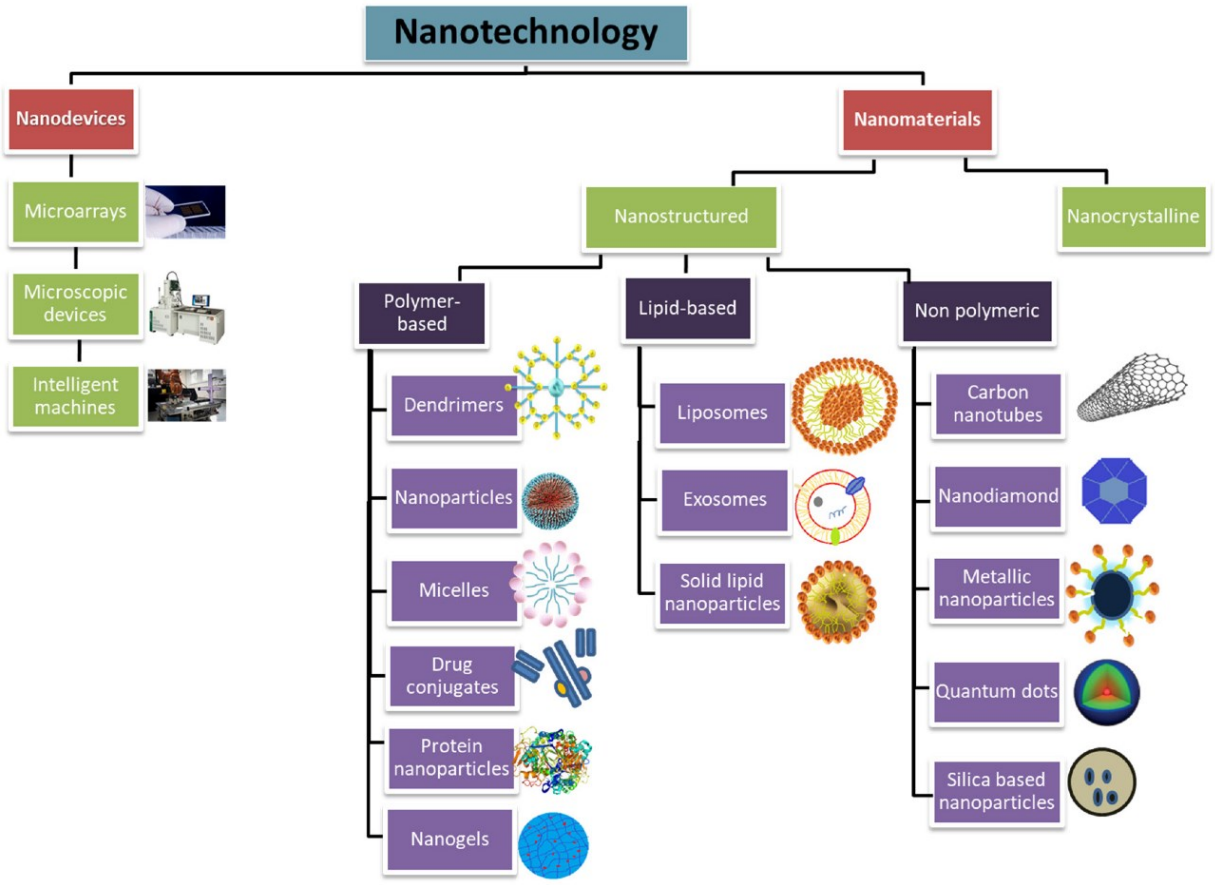

Figure 1. Schematic overview of different types of nanomaterials. (reprinted from: Abuzer Alp Yetisgin, Sibel Cetinel, Merve Zuvin, Ali Kosar, Ozlem Kutlu, "Therapeutic Nanoparticles and Their Targeted Delivery Applications", Molecules, Volume 25, page 3, ©2020, https://doi.org/10.3390/molecules25092193, CC BY 4.0 https://creativecommons.org/licenses/by/4.0/)[2]

1.1. Oral administration of nanoparticles

The oral administration of therapeutic drugs offers numerous advantages over other routes of administration. These include, for example, low formulation costs, the reduction of infection risks and higher patient compliance due to simple and painless handling,[3] which is why this form of administration is particularly interesting for long-term therapies. However, drugs administered in their free form often have a low general bioavailability and no control over drug delivery rates. This is due to strong fluctuations in pH and the presence of enzymes in the gastrointestinal tract (GIT), which can lead to premature degradation of active ingredients. This may especially be the case for peptide-based therapeutics.[4] In addition, the active ingredient must be able to be absorbed efficiently in the intestine, which is often inhibited, especially for water-insoluble substances or macromolecules.[4-7] To overcome these obstacles, nanoparticles, *i.e.* particles with sizes below 1 µm, have received increasing attention as drug delivery platforms in recent years. Typical materials for this purpose are metals and metal oxides, polymers, proteins, lipids, or polysaccharides. An increase in drug absorption and bioavailability can be achieved, for example, by modulation of tight junctions (TJ) of the intestinal epithelium. TJ consist of the transmembrane proteins occludin, claudin and junction adhesion molecules and are located at the points of contact between adjacent epithelial cells. TJ proteins are responsible for the diffusion of small moieties and are therefore important for the regulation of water and ion balance between apical and basal epithelial sides. In addition, they play an important role in the trans-epithelial transport of biologically active substances, such as cytokines.[8] By modulation of the transmembrane proteins, opening of TJ can be achieved enabling increased trans-epithelial transport of small molecules and potentially even macromolecules, making them a promising target for increasing systemic resorption of drugs.[3] Stimuli for modulation and increase of permeability of TJ are diverse and can include bacteria or cytokines such as tumor necrosis factor (TNF)-α and interferon (IFN)-γ, leading to a “leaky” epithelium. This condition plays an important role in inflammatory diseases of the GIT, which is accompanied by infiltration of bacteria and diarrhea.[9-13] Thus, TJ modulation should be handled with care and in a controlled way, and reversible strategies for enabling this delivery route have been suggested. Permeability and opening of TJ can be quantified via measuring the trans-epithelial resistance (TEER) between the apical and basal side of a model epithelium or by determining the apparent permeability coefficients (Papp) of, for example, fluorescent markers. Polycations such as chitosan[14,15] and its more soluble derivative N-trimethyl chitosan,[16,17] poly(amidoamine)[18,19] or poly(lysine)[20] are reported to increase the permeability of the epithelium. Moreover, different types of nanoparticles were proven to decrease TEER and to enable

permeation of drugs. Loo *et al.*[21] examined the influence of various cationic polymer-DNA nanoparticles on changes in TEER values which was inversely proportional with the particle's positive zeta potential. However, anionic nanoparticles have also been shown to exhibit similar effects on the epithelium.[22,23] In addition, decrease of TEER, *i.e.* increase of permeability, upon incubation with silica nanoparticles was found to be dependent on particle concentration.[23] A recent study by Lamson *et al.*[24] showed that the permeation-enhancing effect of different nanoparticle types is a function of material, size, and charge. Silica nanoparticles had the most negative charge among the tested materials and exercised the strongest effect, where particles smaller than 100 nm lead to strongest decrease in TEER. In the same study, *in vitro* permeation experiments were linked to increased oral bioavailability of insulin and exenatide *in vivo*, when the drug was subsequently administered after silica nanoparticles. This is further pronouncing the validness of such *in vitro* studies and the high potential of such nanoparticle-based co-formulations for oral drug delivery. Moreover, all TJ modulations were fully reversible, and the particles had no damaging effects on the epithelial tissue.

1.1.1. Factors influencing particle retention in healthy intestinal tissue

Not only systemic absorption and distribution of drugs can be achieved with the help of nanoparticles, but also their release within the GIT to enable localized therapy of various diseases, such as cancerous tumors or inflammatory bowel disease (IBD). Thus, ensuring prolonged residence times of the particles, and with that increased concentrations of the released drug, at the therapeutic target site is a major challenge for oral drug delivery platforms. The intestinal epithelium is covered with a protective mucus layer, consisting of glycoproteins. These so-called mucins have a molecular mass of 0.5-40 MDa and possess a negative charge due to terminal sialic acid and sulfonic acid residues.[25] Due to hydrophobic, electrostatic interactions as well as hydrogen bonds, the mucins form a cross-linked, hydrogel-like layer, serving as an important protective barrier in healthy tissues against the infiltration of pathogens, such as bacteria, viruses and particles, as well as toxins and acidic pH values.[26] The mucus layer in the stomach and colon consists of a firmly adherent and a loosely adherent layer, whereas in the small intestine there is only a thin lining present. The mucus has a mesh size of 10-500 nm and its thickness varies depending on localization along the GIT as well as on species. In the colon, mucus in human is reported to be 100-200 µm thick, while in rats, thickness is much higher with about 830 µm.[25,27] The mucus is continuously regenerated by goblet cells of the epithelium and therefore undergoes constant renewal, shearing and shedding. This way, around 1 kg of mucus is produced in an adult human every day.[28,29] To overcome this barrier for drug transporters, the most common strategies

are the synthesis of either mucus-adhesive or mucus-penetrating nanoparticles (see Figure 2). Both approaches aim to increase the retention of the particles along the intestinal wall, and thus the prolongation of the time window for effective drug release. Mucus-adhesive nanoparticles are characterized by strong interactions with mucins, which are intended to achieve strong adhesion to the mucosa. In contrast, weak non-adhesive interactions are desired to achieve penetration of the nanoparticles through the mucus layer towards the intestinal epithelium. By choosing particle size, shape, charge and functionalization of the particles, their penetrability through the mucus layer may be controlled.

Due to the restricting nature of the mucus mesh size, particle transport and entrapment are dependent on particle size. Particles with sizes over 200 nm are reported to be diffusion limited in different types of mucus in general.[30-33] However, *ex vivo* studies on colonic tissues of mice demonstrated that even mucus-penetrating polystyrene (PS) nanoparticles with a size of 200 nm and functionalized with polyethylene glycol (PEG) were entrapped in mucus while 100 nm particles were not, indicating that the average mesh size of mouse colonic mucus might be even smaller, and that particle sizes below 200 nm are favorable if diffusion through mucus is aimed for.[34]

The high charge density of mucus caused by their anionic side chain groups is another important parameter potentially influencing particle interaction. Cationic silica nanoparticles are prone to be immobilized by strong electrostatic interactions resulting in mucus-adhesiveness, *i.e.* low penetrability, whereas anionic silica particles are readily transported through mucus.[35]

By introducing functional groups, the passive interaction of nanoparticles with mucus can be modified. One example of such a passive biocomponent would be PEG, which is a common mean for rendering different types of particles mucus-penetrative.[31,35-42] In particular, Lai *et al*.[37] reported that the diffusion coefficient of PEGylated PS particles as large as 500 nm was only 4-fold lower in cervicovaginal mucus as compared to water, whereas the diffusion of their non-PEGylated counterparts was decreased by a factor of 40000. The influence of PEG on diffusivity was also confirmed by *ex vivo* diffusion studies on colonic tissue, which demonstrated that PEGylation of PS nanoparticles increased their mucosal transport.[34] The influence of the PEG-functionality on mucus-permeability is depending on molecular weight and packing density of the polymer. For instance, Xu *et al*.[38] functionalized poly (lactic-co-glycolic acid) (PLGA) nanoparticles with PEG_{5k} at different surface densities and tested their transport on mucus tissue *ex vivo*. Inhibition of mucin binding, increase of mucus-penetration and coverage on mucosal tissues were facilitated by PEG contents of 5 wt% or higher corresponding to 10 polymer chains per 100 nm² (*i.e.* dense brush conformation). Wang *et al*.[43] found that PS particles PEGylated with PEG_{2k} or PEG_{5k} were readily diffusing through mucus, but particles with PEG_{10k} did not so, despite having similar grafting densities. Moreover, they demonstrated that the reduction of coating densities of PEG_{2k} decreased

diffusion rates to a level similar to high density PEG_{10k}-particles.

In contrast, mucus-adhesiveness can be achieved by functionalization with polymers offering strong interactions with mucus via covalent linkage, hydrogen bonds, electrostatic or hydrophobic, as well as van der Waals interactions. [44] For instance, thiolated polymers are reported to form disulfide bonds with the cysteine containing mucins leading to mucus-adhesive properties when introduced to nanoparticles.[45-47] The most common polymer which is used for this purpose is, however, chitosan. Chitosan is a chitin-derivative obtained by de-acetylation under basic conditions and its mucus-adhesive properties were demonstrated in numerous studies.[48-51] Due to its iso-electric point (IEP = 6.3), the mucus-adhesive properties of the polymer are the results of various interactive forces, and the extent of their contribution are dependent on pH. At acidic pH values, electrostatic forces between protonated amino groups and negatively charged mucins are the main contributor to the attraction. At these conditions, acetylation degree and electrostatic ion screening strongly influences mucin binding strength. However, as the protonation degree decreases with increasing pH, the polymer solubility and the power of electrostatic attraction decrease, and hydrogen bonding as well as hydrophobic interaction remain as attractive forces at neutral pH.[52,53] Additionally, chitosan coatings were also utilized to achieve pH-responsive drug carriers.[54-58]

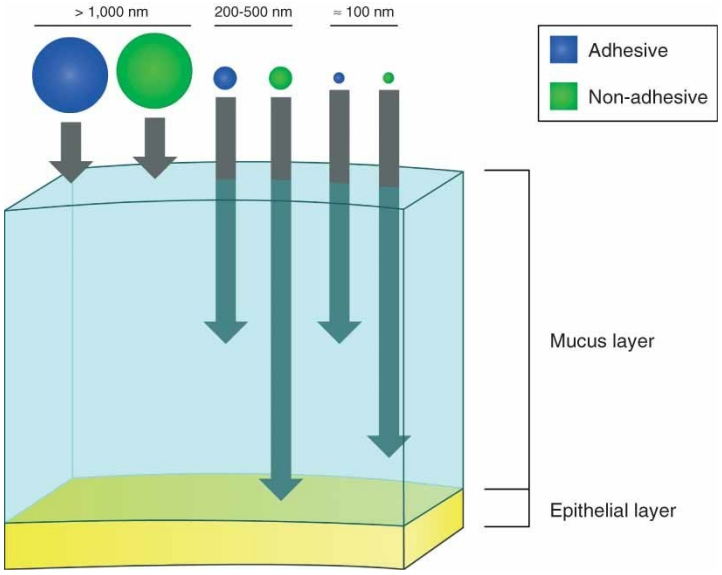

Figure 2. Schematic representation of the size exclusion effect of mucus on the diffusion and transport of particles. Moreover, the permeability of particles can be influenced by tuning the particles' surface properties, rendering them mucus-adhesive and non-adhesive/mucus-permeable. (reprinted from: José das Neves, Mansoor Amiji, Bruno Sarmento "Mucoadhesive nanosystems for vaginal microbicide development: friend or foe?", Wiley Interdisciplinary Reviews: Nanomedicine and Nanobiotechnology, Volume 3, page 392, ©2011, https://doi.org/10.1002/wnan.144 with friendly permission by John Wiley and Sons)[59]

Counterintuitively, mucus-adhesiveness can even be disadvantageous if a long therapeutic window and a spatially uniform particle distribution across the epithelium is desired. Due to their inability to diffuse into the mucus layer, the particles may remain in the outer mucus layer and/or within the central lumen and therefore rapidly transported off-site along with the rest of the intestinal contents (see Figure 3).[25,60] This can be attributed to high colonic mucus turnover rates reported to be approximately 1-2 h in mice and 1-4.5 h in rats, respectively.[61,62]

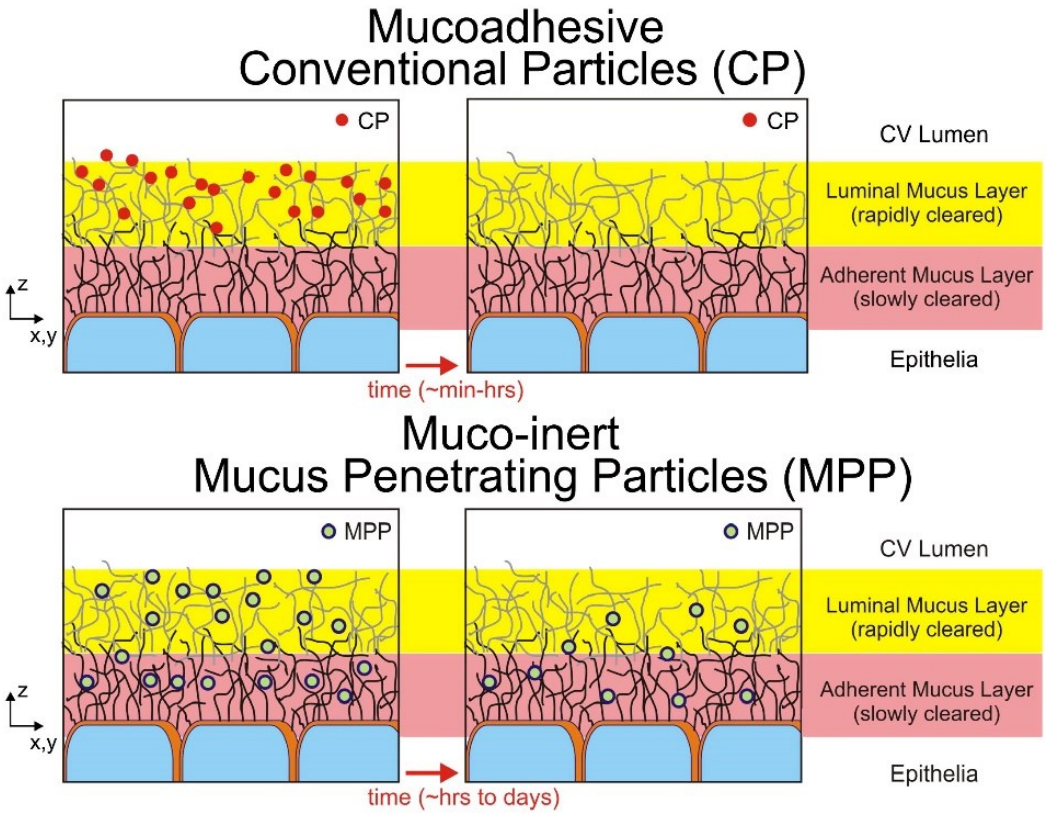

Figure 3. Schematic illustration of the influence of particle properties on their fate upon contact with mucosal surfaces. Mucoadhesive/non-penetrative particles get entrapped within the mucus, or are not able to penetrate into the mucus layer in the first place. As mucus gets constantly renewed, steady turn over rates causing the particles to stay localized within the lumen and eventually to be transported-off site along with shedded mucus and luminal contents in the range of minutes (min) to hours (hrs). On the other hand, mucus-penetrating particles are able to diffuse through the mucus layer towards the epithelia, causing an increased exposure of cells to the drug transporter and its cargo. The particles are protected against clearance and exhibit a longer retention as their non-penetrative analoques on the healthy mucosa. (reprinted from: Samuel K. Lai, Ying-Ying Wang, Justin Hanes “Mucus-penetrating nanoparticles for drug and gene delivery to mucosal tissues”, Advanced Drug Delivery Reviews, Volume 61, page 164, ©2009, https://doi.org/10.1016/j.addr.2008.11.002 with friendly permission by Elsevier)[25]

For example, Maisel *et al*.[40] studied the distribution of mucus-adhesive (MAP) and mucus-penetrating (MPP) PS particles in the GIT of mice. After oral gavage of the 200 nm particles, MPP were found to readily penetrate the villi and to be evenly distributed over the epithelium of the small intestine, whereas MAP were localized as aggregates in the lumen. Interestingly, this was not only the case in fasted mice, but also in animals in the fed-state indicating that MPP are able to leave the digesta and to penetrate towards the epithelium. However, differences between MAP and MPP were diminished when the oral gavage was conducted with a high volume of fluid indicating alterations of diffusion-control at high water contents. In the colorectum, MPP uniformly coated the epithelial surface when administered via enema, while MAP again were trapped in the mucus layer (see Figure 4). The influence of particle size on the tissue coverage of MPP was also investigated, and MPP larger than 200 nm were found to be less well distributed. Similar findings with different particle types and mucosal tissues were recently reported.[38,63-66]

Another strategy to naturally increase the retention of nanoparticles within the GIT is the modification of particle shape. Two comprehensive studies by Li *et al*.[67] and Zhao *et al*.[68] reported the biodistribution of all-silica MSN in the GIT of mice upon oral administration and the of influence their aspect ratio (AR, length/width ratio). In general, elongated particles with an AR of 4 or 5 were shown to reside longer in the GIT than their spherical counterparts and were excreted mainly via feces as long as 7 days after gavage. Furthermore, systemic absorption of elongated particles into the organs was observed as well, but not in such an extent as for spherical MSN, and their absorption kinetics seemed to be slower.

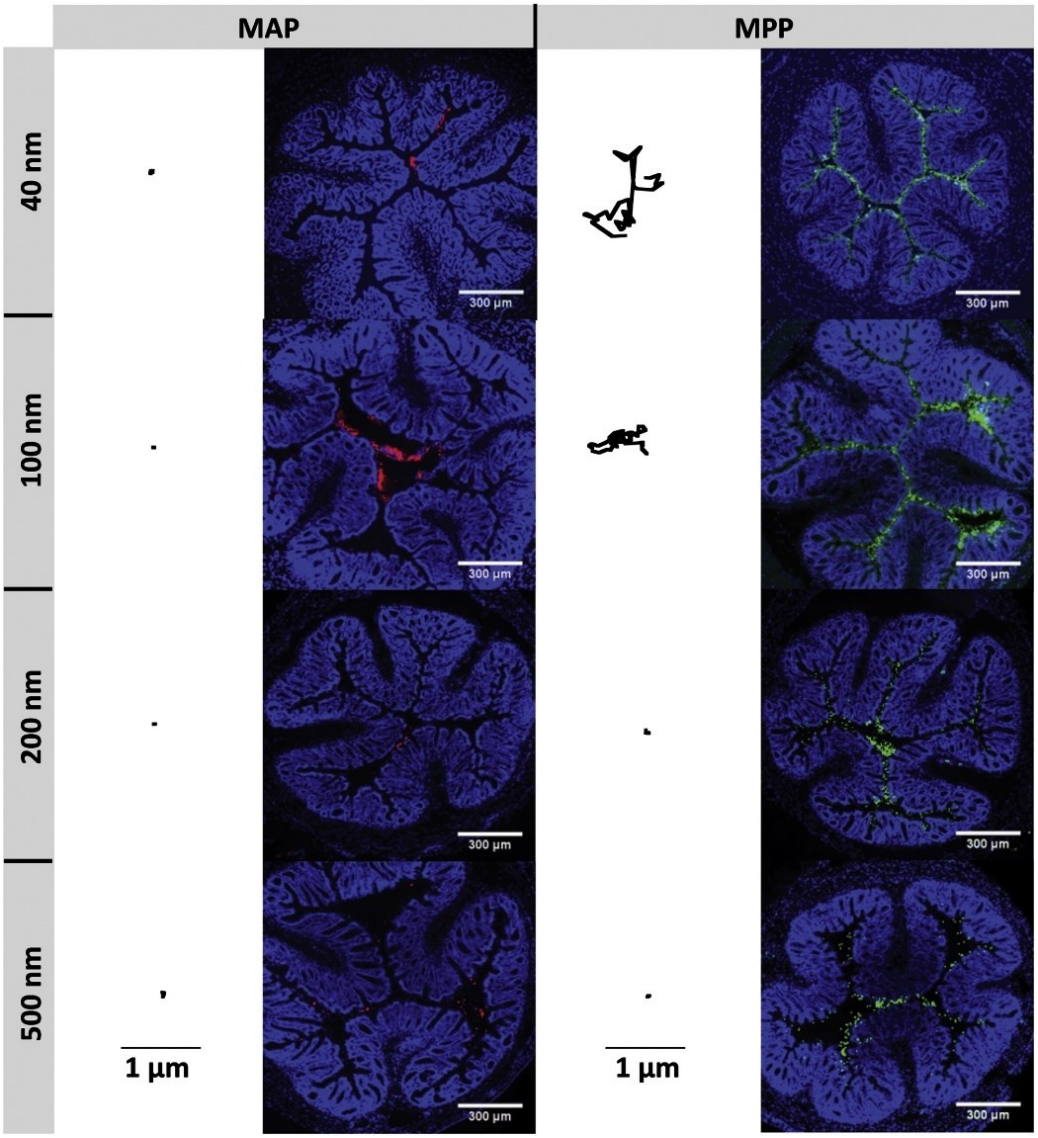

Figure 4. Trajectories (duration of 3 s) on mucus of excised mouse colorectal tissue and spatial distribution on mucus-adhesive (MAP, red) and mucus-penetrative (MPP, green) particles in colorectums of mice. MPP are able to penetrate through the mucus layer resulting in an uniform translocation across the tissue surface, while non-penetrating MAP are aggregated and localized preferentially in the center of the lumen. (reprinted from: Katharina Maisel, Laura Ensign, Mihika Reddy, Richard Cone, Justin Hanes, “Effect of surface chemistry on nanoparticle interaction with gastrointestinal mucus and distribution in the gastrointestinal tract following oral and rectal administration in the mouse”, Journal of Controlled Release, Volume 197, page 52, ©2015, https://doi.org/10.1016/j.jconrel.2014.10.026 with friendly permission by Elsevier)[40]

1.1.2. Targeting the inflamed intestinal tissue

In contrast to healthy intestinal tissue, the mucosa and thus the mucus barrier can be damaged in some diseases. One example for this would be IBD, of which the most common forms are ulcerative colitis and Crohn's disease. IBD is a globally occurring disease with a rapidly increasing prevalence, especially in countries with western lifestyles. In 2017, 6.8 million cases were registered worldwide.[69] The exact causes of the disease are not fully understood yet, but possible factors include industrialization, dietary habits, as well as genetic predisposition.[70,71] During the course of the disease, the protective mucus layer gets destroyed, resulting in infiltration of pathogens into the intestinal tissue, and erosion and leakage of the intestinal epithelium. As a result, inflammation and ulceration of the intestinal wall occur leading to the typical symptoms like bloody diarrhea, abdominal pain, weight loss and fever. While Crohn's disease can affect the entire GIT, ulcerative colitis is mainly limited to the colon and anus.[72] With the intention of effective therapy of inflamed intestinal tissue, nanoparticles accumulating under these conditions are aimed for, potentially prolonging the local release of drugs at the site of disease. For example, PEGylated PS or poly(lactic-co-glycolic acid) (PLGA) particles were found to penetrate deeper into inflamed intestinal tissue than their non-PEGylated counterparts.[40,64] Modification of particle charge has also been suggested for potential accumulation, as cationic proteins such as transferrin or eosinophil are abundant in inflamed GIT tissues, and negative particle charge may increase adherence to inflamed mucosa.[73,74] Targeting of specific cell receptors, such as CD44,[75-77] which are overexpressed in inflamed tissue may also be a valid strategy using active biocomponents. Several studies reported increased interaction of the anionic polymer hyaluronic acid (HA) with cells overexpressing CD44.[78-82] Combined treatment of rats exhibiting colonic inflammation with free HA and mesalamine accelerated wound healing, a result which was ascribed to the adherence of HA to the ulcerated tissue *in vivo*.[83] Xiao *et al*.[84] synthesized drug-loaded, multistage PLGA-HA nanoparticles embedded in a hydrogel, which were orally administered to mice with induced colitis, leading to an alleviating effect on inflammation. Targeting of inflamed tissue with complex, hierarchical vehicles including HA was also demonstrated by Li *et al*.[85] Furthermore, HA-based nanogels were reported to be mucus-adhesive on mucus-producing cell co-cultures,[86] which may even have an alleviating effect on GIT accumulation, especially if there are regions with an intact mucosa left, as discussed earlier.

1.2. Intravenous administration of nanomaterials

Besides the oral route, intravenous injection of drugs is one of the most common administration techniques, as it comes with several advantages. High concentration levels of the applicated therapeutics can be reached quasi instantly and a brought system distribution over the body can be achieved. However, this comes at cost of target-selectivity potentially increasing systemic side-effects of the treatment, as it is for example often the case in cancer therapy. Additionally, interaction of the therapeutic compounds, for example peptide-based drugs, with serum proteins or enzymes may lead to pre-mature degradation and fast declining drug levels. Hence, in the last decades, development of drug delivery platform shifted into scientific focus, with the strive to overcome the limitations of intravenous administration of drugs.[87] In the following chapters, strategies to increase selective cell internalization of such platforms as well as means to overcome the major drawback of these platforms, such as unspecific adsorption of serum proteins followed by short blood circulation times and fast system clearance, will be discussed.

1.2.1. Particle parameters influencing cellular uptake and biodistribution

One intention for the use of drug delivery platforms is the reduction of systemic side effects due to uncontrolled release and distribution of the therapeutic by selectively address the site of disease, for example the tumor tissue or the cancerous cells themselves. Passive control of selective particle uptake into cells as well as of its kinetics and their biodistribution can be achieved via modification of size, charge, and functionalization of the drug transporter.

Size-dependency of uptake of different types of particles into various cell lines is reported in literature.[88-96] In general, particle internalization is favored for particles with diameters in the range of 100 nm or smaller. In particular, dos Santos *et al*.[97] investigated the uptake of PS nano- and microparticles into cancerous epithelial cells (HeLa, A549), astrocytes (1321N1), endothelial cells (HCMEC D3), and murine macrophages (RAW 264.7). The particles had diameters in the range of 40 nm to 2 µm. Overall, the highest uptake for all materials was observed into macrophages, while the uptake was lowest into epithelial cells, whereas small particles were taken up at a higher extent and rate in general for all cell lines investigated. However, the ratio of internalization into macrophages over the other cell lines decreased as the diameter increased indicating loss of selectivity towards macrophages at increasing particle size. He *et al*.[98] reported the uptake and biodistribution of PS-based nanoparticles with sizes of 150-500 nm. Large particles were internalized into macrophages to a higher extent, but the exact opposite was the case for two

cancer cell lines (L-02 cells and SMMC-7721 cells). Biodistribution experiments *in vivo* revealed that tumor accumulation of 150 nm particles was highest, whereas 500 nm particles were mainly found in liver and spleen. This was ascribed to an enhanced blood circulation time of the smaller particles. Particle size has also been shown to influence blood circulation time and biodistribution *in vivo*. In general, sizes over 150-200 nm are accumulating preferably in the spleen and liver, whereas particles as small as 5 nm or below undergo rapid renal clearance. Particles in the micrometer range (> 2 µm) are additionally entrapped in the capillaries of the lungs, giving a rational window for desired particle sizes for increased blood circulation times.[87]

Another factor which may influence cellular uptake and blood circulation time is particle shape.[91,92,99,100] Champion *et al*.[101] demonstrated that macrophage phagocytosis of spherical and elongated PS particles depends on their geometry as well as on their orientation. The complexity of the actin structure which has to be formed for phagocytosis was affected by the particle orientation. For spherical particles phagocytosis was completed, even when the particle size was similar to the cell dimensions. However, for elongated particles, this was only the case when their major axis was orientated orthogonal towards the cell surface. On the other hand, a parallel orientation led to a simple spreading of the actin structure on the particle surface and no complete internalization occurred. In connection to this, an increase of the aspect ratio of silica nanoparticles is reported to lead to pronounced accumulation in the lung and spleen.[100,102] Particle shape can also affect the dynamic behavior under fluid flow conditions changing the particle's margination and potentially increasing the interaction with blood vessel walls.[103]

Selectivity of cellular internalization and biodistribution can also be influenced by particle charge. Due to electrostatic interactions with the cell membrane,[104,105] cationic particles are readily internalized non-specifically into cells in general,[106,107] and more specific, into various cancer cell lines.[98,108-113] For example, internalization of cationic liposomes into angiogenic endothelial cells was observed to be higher than for anionic and neutral liposomes which may be utilized for passive targeting of angiogenic blood vessels in tumors.[114] He *et al*.[98] reported a higher tumor accumulation in an *in vivo* mouse model of polymeric nanoparticles with increasing cationic charge, while increasing the absolute surface charge of anionic particles had the opposite effect. Lunov *et al*.[115] studied the cellular uptake of positively and negatively charged PS nanoparticles with a zeta potential of + 56 mV and -46 mV, respectively (measured in 1 mM KCl, pH 7). Particle internalization into cells was investigated for human macrophages, and for monocytic THP-1 cells which were differentiated via treatment with phorbol-12-myristate-13-acetate (PMA) into a macrophage-like phenotype. In general, monocytes derive from the bone marrow and differentiate into macrophages upon emigration into tissues. PMA-differentiated THP-1 cells may be used as (simplified) macrophage model.[116,117] Interestingly, Lunov *et al*.[115] demonstrated that the extent of

particle uptake into macrophages is comparable to that into PMA-differentiated THP-1 cells (but not for non-differentiated THP-1), although the mechanism of uptake was different. Overall, the anionic particles were internalized to a higher extent into these cell lines than their cationic counterparts. These results were reflected in their tissue distribution in an *in ovo* tumor xenograft model, where the cationic particles were taken up by macrophages but also by tumor cells, while the anionic particles were found mainly associated to macrophages in the liver and to a small extent to macrophages residing in the tumor, but not in tumor cells. Importantly, these findings were connected to an overall higher serum protein adsorption onto the anionic PS particles in this case, leading to an increased liver uptake. In contrast, Souris *et al*.[118] reported accelerated blood clearance of cationic mesoporous silica nanoparticles (MSN) via the liver compared to anionic particles, and the authors postulated that the reason for this was due to higher surface charge mediated serum protein adsorption. These different findings pronounce the complex interplay between particle characteristics and their biological environment which determines the particle's fate within the body.

Besides the physicochemical properties of the basic drug carrier, functionalization of its external surface with chemical motifs can influence the interaction with cells and the biodistribution upon intravenous injections, which can be utilized to target specific cell types or tissues.[119] For this purpose, the introduction of targeting ligands, such as folic acid,[108,120,121] antibodies,[122] growth factors[123] or other motifs[88,124] has been proposed. However, one of the most common approaches to achieve particle accumulation in tumor tissues is by utilizing the enhanced permeability and retention effect (EPR) by increasing the transporter's blood circulation time. The EPR effect is based on the pronounced angiogenic nature of tumor tissue and the increased permeability of the blood vessels within, which is necessary to cover the high demand for nutrients and oxygen of such tissues.[125] (see Figure 5).

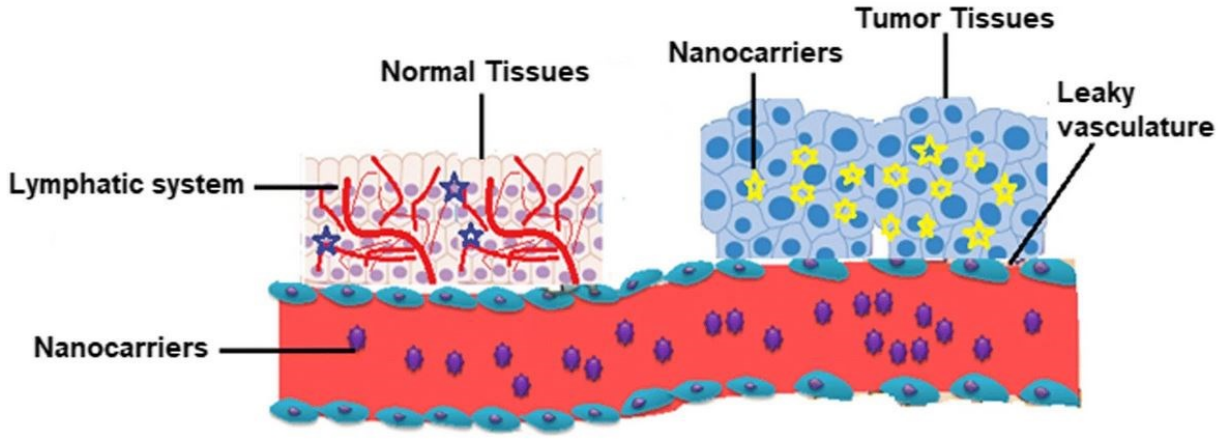

Figure 5. Schematic drawing of the principle of passive tumor tissue targeting. While normal tissue is well drained via the lymphatic system, tumor tissue vasculature exhibits pronounced leakiness enabling increased nanoparticle uptake into the tissue. (reproduced with permission by Springer Nature from: Zahid Hussain, Shahzeb Khan, Muhammad Imran, Muhammad Sohail, Syed Wadood Ali Shah, Marcel de Matas, "PEGylation: a promising strategy to overcome challenges to cancer-targeted nanomedicines: a review of challenges to clinical transition and promising resolution", Drug Delivery and Translational Research, Volume 9, page 726, ©2019, https://doi.org/10.1007/s13346-019-00631-4)[126]

Typically, non-optimized nanoparticles are cleared from the blood stream within minutes.[127] Enhancing blood circulation times of particles is strived for by using stealth functionalities with the aim for effective serum protein adsorption inhibition (as discussed in detail in chapter 1.2.2), and thus to protect the particles against fast clearance by the organism's mononuclear phagocyte system (MPS), also known as the reticuloendothelial system (RES), which is rich in monocytes and macrophages. Such prolongation of circulation times could be achieved, for example, with HA.[79,128] However, the most prominent example of such a motif is PEG, which has also been utilized for this purpose as co-functionality together with HA to additionally enable active targeting of CD44 receptors of cancer cells.[128] The "PEG-effect" is mainly ascribed to diminished opsonization and reduced phagocytosis.[126,129] PEGylation of nanoparticles was repeatedly shown to reduce internalization by macrophages and/or monocytes.[130-132] Kramer *et al*.[133] demonstrated the possibility of passive accumulation of cationic silica nanoparticles in prostate cancer tumors (LNCaP and PC-3) *in vivo* via the EPR effect. By PEGylation, the particles' blood circulation time was substantially prolonged, while non-PEGylated particles were cleared from the blood stream to the liver within one hour. The longer circulation times of PEG-MSN resulted in a continuous increase of particle concentration within the tumor tissue, but also in the spleen due to repeated passage through this organ. Particle accumulation was found to be more pronounced in the LNCaP tumor as compared to the PC-3 tumor, which was related to the higher degree of

vascularization of the former tissue. Successful tumor treatment via doxorubicin-loaded MSN functionalized with a polyethyleneimine (PEI)-PEG copolymer was demonstrated by Meng *et al.*[134] The polymer functionality led to particle accumulation in the tumor via the EPR effect, resulting in tumor shrinking and reduction of severe systemic side effects compared to the free drug. In another study, Perrault *et al.*[135] reported that the increase of molecular weight of the PEG grafted onto particles was proportional to circulation half-life, and a change from PEG_{2k} to PEG_{5k} resulted in a half-life prolongation by a factor of 14. Similar correlation of circulation times on PEG molecular weight was previously reported.[136,137] Blood circulation time is also dependent on PEG grafting density, and very high densities (dense brush conformation) were shown to reduce particle uptake into THP-1 cells resulting in lower clearance rates from the blood.[132] Zhang *et al.*[138] studied the biodistribution of PEGylated 50 nm gold nanoparticles as well as of PEGylated gold aggregates. The PEGylated particles exhibited a long blood circulation time and a decreased liver accumulation as compared to the aggregates, but at the same time an increased content in the spleen after 24 h was detected. Interestingly, this study investigated time scales much longer than usually reported in literature with a period of 6 months after injection of a single dose. Even after half a year, particles were abundant in the liver (~30 %ID/g), kidneys (~4 %ID/g) and spleen (~12 %ID/g), raising the questions about the biodegradability, *i.e.* the possibility of dissolution and clearance, of such particle materials. In the same study, particle internalization into Raw 264.7 macrophages was also examined, and no differences between the samples were found, pronouncing the necessity for more developed *in vitro* screening methods for the prediction of *in vivo* behavior. Further examples of circulation time enhancement of drug carriers via PEGylation can be found in literature.[88,139-142]

Besides prolongation of blood circulation time and diminishment of accumulation in organs rich in macrophages, PEGylation can affect cell uptake into the target cells.[136,143,144] For example, PEGylation of cationic gold nanoparticles resulted in decreased internalization into PC-3 cancer cells.[91] Choi *et al.*[145] reported that uptake rates of HA-based nanoparticles into cancer cells was inversely dependent on the PEGylation degree, but at the same time the liver uptake was reduced and their circulation time in the blood was increased, finally resulting in increased tumor accumulation of the PEGylated particles. Thus, this remains as a classic optimization problem: on the one hand, PEGylation is needed for evading the clearance by macrophages and accumulation in organs of the defense system, on the other hand PEGylation should not interfere with uptake by target cells/tissues. Examination of such complex interplays is challenging and often requires broad sample/parameter matrices. However, considering time and labor as well as ethics, execution of such screenings via *in vivo* experiments appears to be not reasonable. Therefore, *in*

vitro screening systems should be used predominantly to narrow the sample matrix for further *in vivo* experiments down to the most promising candidates.

1.2.2. Protein adsorption onto nanoparticles

Upon intravenous injection, drug carriers in general, and nanoparticles in particular, are prone to fast adsorption of blood constituents, like serum proteins leading to a formation of a protein corona (PC), within seconds to minutes.[146] The PC is determining the biological identity of the particles, and its extent and configuration play a major role in the interaction thereof with cells as well as in their overall fate in the organism, *i.e.* their biodistribution[104,127,147] For instance, Lesniak *et al.*[148] studied the interplay of silica nanoparticles with various cancer cell lines in the presence and absence of serum containing medium. Under serum-free conditions stronger adhesion to the cell membrane and higher uptake ratios were observed and their intra-cellular localization differed compared to their protein coated counterparts. Adsorption control over specific proteins can also be of advantage and may be utilized to target specific organs, including liver, blood-brain-barrier, lung, spleen and kidneys.[149,150] In addition, protein adsorption can influence the dissolution behavior of nanomaterials, which may have important implications on their biodegradability (as discussed earlier) or drug release kinetics, especially when the release is particle dissolution-driven. For instance, PC formation on the external surface of MSN decreased their dissolution rates.[151,152] Another example, how PC can influence the biological fate of nanoparticles, was reported by Beck *et al*.[153] MSN were functionalized with the targeting ligand anti-B220 to specifically address B220 antibody-positive leukemia stem cells. The extent of protein adsorption influenced the particle internalization not in an inversed proportional fashion as expected, but rather an optimal degree of protein adsorption was identified, promoting higher cellular uptake. This may be ascribed to supporting effects by PC constituents on the ligand's orientation and accessibility. On the other hand, loss of targeting capabilities upon serum protein adsorption on the surface of nanoparticles was previously reported by Salvati *et al*.[154]

However, adsorption of plasma protein also influences the blood circulation time of the drug carrier, which is an important parameter for effective drug delivery capability. In general, nanoparticles are identified and eliminated by cells of the MPS/RES upon intravenous injection.[155] This often leads to an accumulation of particles in defense organs rich in phagocytotic cells, such as the liver or spleen, undermining their therapeutic effectivity. The internalization of nanoparticles by cells of the immune system can be ascribed to PC formation and the role of specific proteins is subject to ongoing research activities. Serum proteins are classified as opsonins and dysopsonins based on their promoting or inhibiting effect on uptake into immune cells. Opsonins, such as

complement pathway proteins, immunoglobulins, fibrinogen and apolipoproteins are reported to promote phagocytosis by macrophages.[147,156] In a comprehensive study, Tenzer *et al*.[157] analyzed the PC on silica nanoparticles and identified 125 individual proteins, among which, serum albumin (69 kDa) and apolipoprotein A-I (31 kDa) were the most abundant in the PC constituting about 12 % and 10 % of total protein content, respectively. Albumin is often classified as dysopsonin, opposing the effects of opsonins and reducing hepatic clearance from the blood.[158,159] On the other hand, nanoparticles coated with albumin have been reported to be recognized by immune cells of the MPS inducing particle uptake.[160] In particular, Fleischer *et al*.[161] studied the adsorption of bovine serum albumin (BSA) on anionic and cationic PS particles. Upon binding to cationic particles, denaturation of BSA took place, which re-directed the internalization mechanism to scavenger receptors, while the protein's native structure upon adsorption onto negative particles was retained, resulting in cell-particle interactions governed via albumin receptors. Mortimer *et al*.[162] demonstrated the unfolding of albumin upon adsorption onto silica nanoparticles resulting in a denatured state similar to what can be observed after heat-induced denaturation, which resulted in increased uptake into differentiated THP-1 cells via a scavenger receptor-mediated pathway. These findings indicate that the fate of particles not only depends on the identity and number of adsorbed proteins, but also on their structural changes upon adsorption. In connection to this, denaturation of free albumin is known to induce clearance of the protein from the bloodstream by macrophages via scavenger receptors.[163] Overall, the exact role of albumin adsorption on the particle's biological fate is controversial and may depend on several parameters such as protein structure, material type, particle size and charge, as well as hydrophobicity. In general, overall minimization of unspecific protein adsorption to prolong blood circulation times is still considered as a major goal of drug delivery research.[87] Thus, in the following, parameters influencing serum protein adsorption and strategies for minimization of such will be discussed in detail.

The processes behind PC formation onto nanoparticles are complex and still not fully understood, which is why protein adsorption is still subject of intensive research. In general, the adsorption kinetics of proteins upon contact with nanoparticles are fast, and PC formation happens quasi instantaneously.[164] However, the specific corona composition is dynamic, and the abundance and concentration of a particular protein within the PC may change over time. This dependence of PC composition on protein adsorption kinetics is known as the Vrooman effect.[165] Upon contact with biologic media, highly abundant proteins with low surface affinity are forming a pre-liminary PC. Over time, these proteins are replaced by such with higher affinity, resulting in the formation of a tightly bound protein hull. Further adsorption onto this "hard corona" takes place via protein-protein interactions forming a weakly bound "soft corona", which is much more dynamic in nature (see

Figure 6A).[147,166,167] Both layers combined have a thickness of approximately 7-9 nm.[168]
Hydrophobic interactions are one of the main drivers for protein adsorption onto nanoparticles.[169] Hydrogen bonds, entropy effects through the release of hydration water as well as the enthalpic contribution of the necessary conformational change also influence the adsorptive strength, and in general, PC formed onto hydrophobic nanomaterials are more stable than on hydrophilic materials.[156,170] However, dependent on material type and solvent composition, electrostatic contributions and ion screening effects can also play an important role.[171,172]
Other particle related parameters influencing PC formation are versatile (see Figure 6B). For instance, the influence of particle size and curvature on the abundance and composition of PC has also been studied.[131,157,173-175] Clemments *et al.*[176] reported that silica nanoparticles with small diameters adsorbed the highest amounts of proteins due to their large specific surface area, and small molecular weight proteins were enriched on these particles. PC formation and thus their biological fate can also be affected by the surface charge of the particles.[107] In general, high surface charge densities promote protein adsorption.[173] For example, Gessner *et al*.[177] synthesized PC particles with varying anionic surface charge densities, but with constant diameters and comparable surface hydrophobicity. Upon incubation with human plasma, the total number of adsorbed proteins positively correlated with increasing charge densities, but the PC composition was not affected. In contrast, qualitative and quantitative PC composition was reported to vary depending on the charge density of cationic liposomes.[178] However, in this study the lipid composition of the liposomes was different, emphasizing the importance of material chemistry on the adsorption of specific proteins. As proteins have a defined point of isoelectric charge (pI), which is determined by the amino acid sequence, the surface charge sign additionally influences PC composition.[173,179] However, the qualitative abundance of a specific protein with a defined pI can also be independent from whether if the particles are anionic or cationic, but the adsorbed amount, as well as the binding strength may change, indicating that proteins can adsorb with different domains accompanied with conformational changes on the surface.[180]

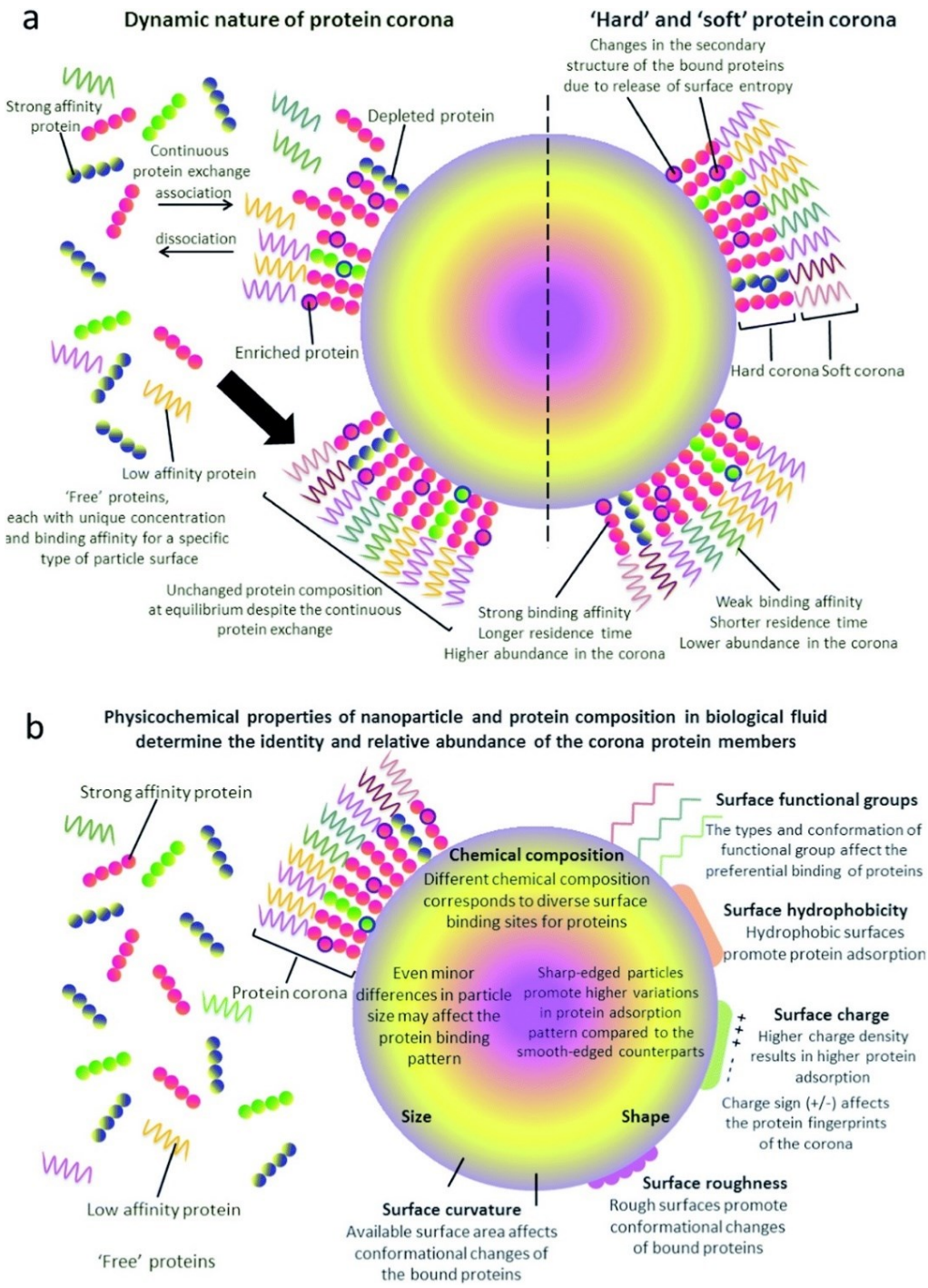

Figure 6. Schematic overview of PC formation on nanoparticles. A) The dynamic nature of the corona is governed by high and low affinity proteins causing a continuous protein exchange and the formation of a hard and soft corona. B) The extent and identity of protein adsorption depends on the physico-chemical properties of the particles. (Used with friendly permission of Royal Society of Chemistry from: Cindy Gunawan, May Lim, Christopher P. Marquis, Rose Amal, "Nanoparticle–protein corona complexes govern the biological fates and functions of nanoparticles", Journal of Materials Chemistry B, Volume 2, page 2062 ©2014, https://doi.org/10.1039/C3TB21526A)[147]

As discussed earlier, opsonization directly affects the biodistribution and blood clearance of drug carriers. Hence, minimization and control of unspecific protein adsorption is one of the main pillars of the design of drug delivery platforms, and several strategies have been proposed using different kinds of surface functionalities including passive biocomponents. For example, the fact that charge density promotes protein adsorption as discussed above can be utilized to diminish protein adsorption on zwitterionic materials. These coatings are typically comprised of cationic and anionic groups resulting in a pI of the material near neutral, physiological pH values. Additionally, such materials are typically highly hydrated due to their hydrophilic nature and high ionic solvation, which lowers the protein/hydration water surface energy and potential energy gain through protein adsorption.[181-184] Such zwitterionic surfaces can be achieved by introducing peptides,[185] succinylated PEI,[186] polymers based on monomers such as sulfobetaine,[187-189] carboxybetaine,[190-192] or phosphorylcholine[193,194] or other motifs.[181,195] For example, Ashraf *et al*.[196] presented a straightforward synthesis route for zwitterionic CdSe/CdS/ZnS by attachment of a small ligand via thiol coupling chemistry to modify protein adsorption. Debayle *et al*.[197] functionalized quantum dots with poly sulfobetaine to completely suppress adsorption of BSA.

In addition, steric repulsion and hinderance has been reported as a mean to reduce protein-surface interactions. This can be achieved via functionalization with large polymer chains, which compression by an approaching protein is energetically unfavorable. This is especially the case when the polymer is hydrophilic, which results in large hydration degrees due to hydrogen bonding creating an energy barrier for protein adsorption.[182,184,198,199] Examples of such polymers are polyvinylpyrrolidone,[200] poly(hydroxyethyl methacrylate),[201] poly(dimethyl aminoethyl methacrylate)[202] and dextran.[203,204]

However, the most prominent polymeric functionalization used for protein adsorption inhibition onto nanomaterials is without doubt PEG. PEG is a non-ionic polymer consisting of ethylene glycol subunits, of which each can bind three water molecules.[1,205] Several PEG-protein conjugates for therapeutic uses were already approved by the Food and Drug Administration (FDA) and PEG in general has been considered nonimmunogenic and safe.[206,207] The attenuating effect of PEG on non-specific protein adsorption is based on its high hydrophilicity and water-binding capacity rendering the particle surface “water-like” and minimizing the interfacial free energy. The hydration capacity of PEG ins dependent on the chain length and compression of the PEG layer through an approaching protein comes with energetically unfavorable PEG reorganization and loss of hydration water.[155,208] Moreover, the extent of adsorption inhibition is dependent on several parameters, like molecular weight and grafting density.[209] The interplay of chain length and distance between the anchor points determine the polymer conformation on the particle surface and will be discussed in detail later. In general, increasing the grafting density at a constant

molecular weight or vice versa comes with more stretched polymer chains forming a so-called brush conformation, while coiled structures are depicted as a mushroom conformation (see Figure 7). Simulation studies by Lee *et al.*[210] revealed that the ability of human serum albumin (HSA) to diffuse through a PEG layer towards a surface and subsequent adsorption depends on the transition from a mushroom to a brush regime. The mushroom conformation did not sufficiently inhibit protein binding to the surface, but the dense brush conformation did, and the final distance between HSA and surface was proportional on the polymer's molecular weight, *i.e.* the PEG layer thickness. As dense brush conformations can be achieved by high PEG grafting densities, a high PEGylation degree is a major design criterion for drug transporters and is considered crucial for effective inhibition of non-specific protein adsorption. The diminishing effect of packing density on protein adsorption has been investigated in several studies.[131,211-216] Furthermore, the low extent of protein adsorption which can be achieved by a dense brush PEG layer was directly linked to lower uptake ratios by cells of the immune system.[131,212,213,217] These findings nicely mirror the stealth effect such particle modifications exhibit, and which has been demonstrated in various *in vivo* distribution studies as previously discussed in chapter 1.2.1. For example, Perry *et al.*[218] synthesized hydrogel nanoparticles functionalized with PEG_{5k} with high (0.083 chains/nm²) or low (0.028 chains/nm²) chain densities. The protein mass adsorbed onto the densely coated particles was decreased to about 24 % and 30 % of the mass on non-PEGylated and low-PEGylated particles, respectively. Interestingly, both PEG densities seemed to decrease macrophage uptake and increase blood circulation time on a short-term scale (2 h) in a similar manner. However, the particles with a high grafting density showed a higher abundance in the blood at longer time scales (24 h). Moreover, these particles were found to be less accumulated in the liver, but to a slightly higher extent in the spleen, compared to the low PEG density particles, which is in line with the results reported by Kramer *et al.*[133] as discussed above.

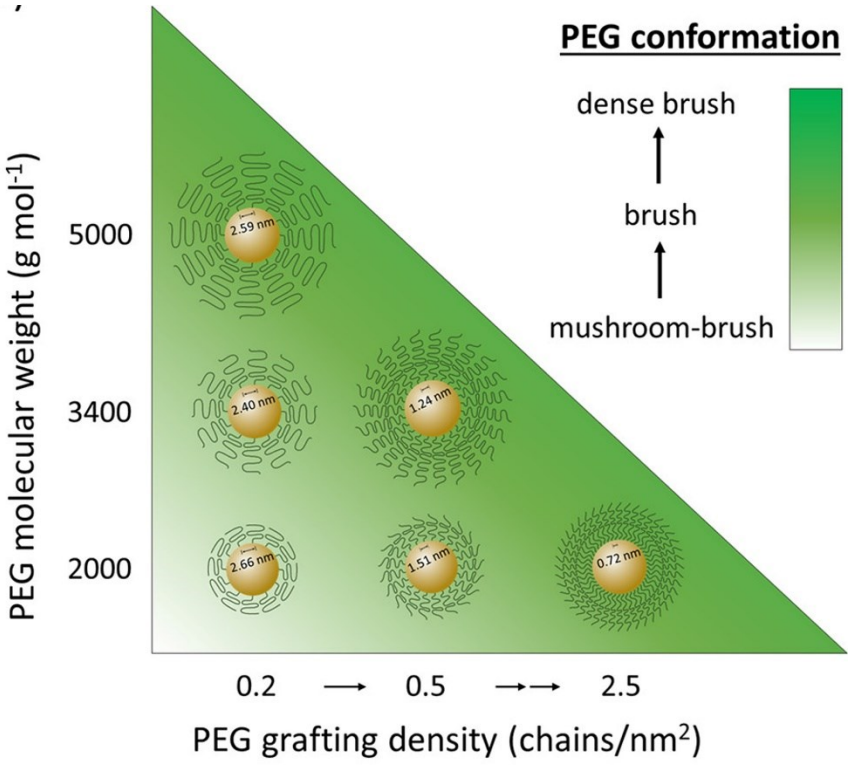

Figure 7. The chain conformation of surface-bound PEG depends on the grafting density and PEG molecular weight. (modified (cropped from original figure) from Mengyi Li, Shuai Jiang, Johanna Simon, David Paßlick, Marie-Luise Frey, Manfred Wagner, Volker Mailänder, Daniel Crespy, Katharina Landfester "Brush Conformation of Polyethylene Glycol Determines the Stealth Effect of Nanocarriers in the Low Protein Adsorption Regime", Nano Letters, Volume 21, page 1592, ©2021, https://doi.org/10.1021/acs.nanolett.0c03756, CC BY 4.0 https://creativecommons.org/licenses/by/4.0/)[213]

As previously mentioned, protein adsorption inhibition by PEG strongly depends on chain density and chain length/molecular weight, which determines the conformation of the polymer on the particle surface. According to the theory of de Gennes,[219] the dimension (Flory radius, R_f) of the polymer coil can be estimated by the molecular weight, *i.e.* the number of ethylene glycol units (N), and the monomer length (l):

$$R_f = lN^{\nu}$$

The coil formation is also dependent on the solvent used, which is represented by the Flory exponent (v). Good solvents such as water induce an expanded coil state (v = 0.6).[219] For example, in the case of PEG_{5k} (N = 113; l = 0.278 nm)[220] a Flory radius of 4.7 nm can be calculated and for PEG_{2k} 2.7 nm (N = 44) can be obtained.

By assuming a circular adsorption area (A), the intermolecular distance between the polymer chains (S) is given by:

$$S = 2\sqrt{\frac{A}{\pi}}$$

Considering the polymer packing density, a measure for the superficial PEG conformation can be constituted with $\frac{S}{2R_f}$. For values ≥ 1, the PEG exhibits a mushroom conformation, where the chains adopt a coil-like conformation according to its free form. A dilute or dense brush conformation is assumed for ratios < 1 and ≤ 0.5, respectively, leading to chains exhibiting a more extended/stretched conformation (see Figure 8).[209,221] The thickness (L) of a formed PEG layer can be calculated considering the monomer length (l), the number of monomer units (N) and the spatial distance between two PEG chains (S):[218]

$$L = \frac{Nl^{5/3}}{S^{2/3}}$$

In the case of PEG_{5k}, this would give a theoretical layer thickness of 4.7 nm and a packing density of 0.057 chains/nm², if the polymer is present as a dense brush layer ($\frac{S}{2R_f}$ = 0.5). Moghimi ***et al.***[222] reported a layer thickness of 10 nm of a polyoxyethylene-polyoxypropylene block co-polymer with a molecular weight of 10 kDa to be necessary for effective attenuation of hydrophobic interactions between proteins and the particle surface. Walkey ***et al.***[131] studied the extent of serum protein adsorption onto gold nanoparticles PEGylated with PEK_{5k} at different grafting densities and particle sizes. The chain densities ranged from 0 chains/nm² up to 1.2 chains/nm², corresponding to a theoretical layer thickness of 13 nm and a $\frac{S}{2R_f}$ value of 0.11, ***i.e.*** an extreme dense brush regime. For all particle sizes, the amount of adsorbed protein decreased in a non-linear fashion with increasing chain density. In the case of 90 nm particles a chain density of 0.25 chains/nm² ($\frac{S}{2R_f}$ = 0.24) reduced the protein adsorption to around 50 % of the non-PEGylated particles, and virtually no adsorption was observed at 0.8 PEG/nm² ($\frac{S}{2R_f}$ = 0.13). Interestingly the protein adsorption levels increased as the particle diameter decreased. For 15 nm particles, an even higher chain density of 1.2 chains/nm² was needed to reduce the protein adsorption to a level of 6 %. This finding was ascribed to an increasing surface curvature resulting in a reduced steric repulsion between neighbored PEG chains. This means that the polymer molecules would adapt a rather flat conformation lowering the barrier against protein adsorption, and higher densities (lower $\frac{S}{2R_f}$ values) are needed to effectively shield the surface against adsorption. However, the extent of protein adsorption onto the non-PEGylated particles was also depending on the

diameter, where smaller particles adsorbed more protein, indicating an attenuating effect of surface curvature on its own, which is in line with the study by Clemments *et al*.[176] as discussed above. Moreover, in the work by Walkey *et al*.[131] the influence of grafting density on the uptake into murine J774A.1 macrophages was also investigated. While non-functionalized particles were readily internalized into cells, the uptake of PEGylated particles was a function of grafting density and up to a chain density of 0.5 chains/nm² the cellular uptake was drastically reduced. Further increase in grafting densities did not affect the interaction with cells indicating that complete prevention of protein adsorption is not necessary to diminish macrophage uptake.

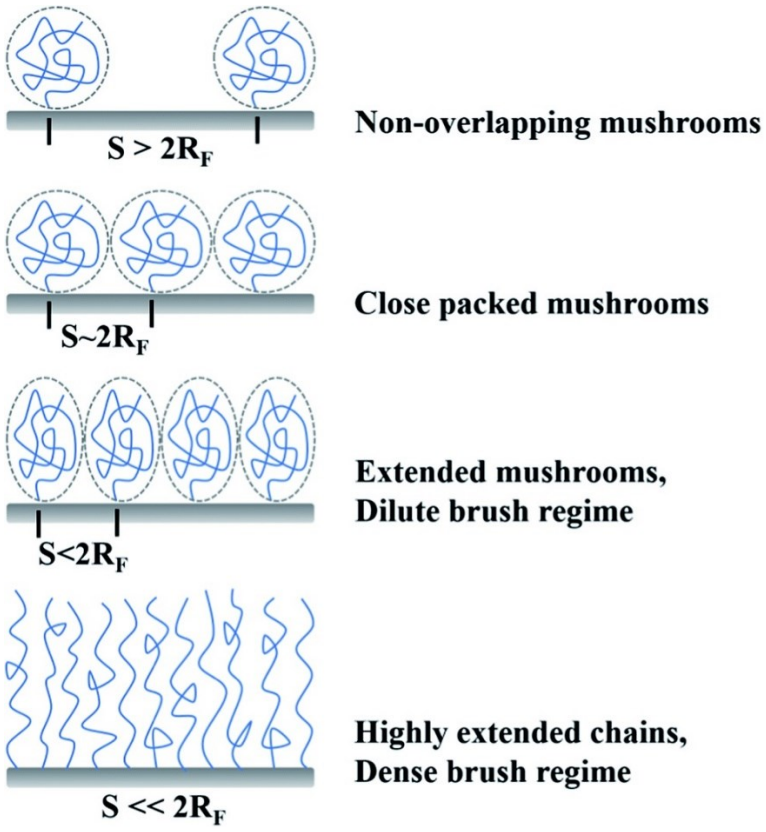

Figure 8. Schematic drawing of the conformation classification of surface-bound PEG. S is the spatial distance between two neighbored chains, R_f is the Flory radius, which depends on the number of ethylene glycol units, the monomer length and the solvent. With increasing packing density, the chain distance decreases causing the polymer coils to adapt an upright orientation, eventually resulting in a dense brush regime. (Used with friendly permission of Royal Society of Chemistry from Xiaoli Liu, Lin Yuan, Dan Li, Zengchao Tang, Yanwei Wang, Gaojian Chen, Hong Chen, John L. Brash, “Blood compatible materials: state of the art”, Journal of Materials Chemistry B, Volume 2, page 5722 ©2012, https://doi.org/10.1039/C4TB00881B)[198]

As mentioned, the conformation and dimension of a PEG molecule in solution are solvent-depend. Selli *et al*.[223] simulated the conformation of a small molecular weight PEG (516 Da) upon grafting to a TiO2 surface in water and dichloromethane. In DCM the polymer was arranged in a more coiled conformation and closer to the surface as compared to water at low densities. Due to lower PEG/solvent and solvent/TiO2 interactions in DCM, the PEG chains were bound to the surface via several oxygen atoms per chain, while in water the PEG/solvent interaction is stronger leading to a complete immersion of the PEG chain into the solvent.

All these findings elucidate the complex interplay of factors like PEG molecular weight, grafting density or solvent/polymer and solvent/support interactions, which has important implications on the PEGylation of drug transporters and the effectiveness of such on the inhibition of serum protein adsorption and the biological fate of the nanomaterials.

1.3. The “nano problem“: area of conflict for therapeutic formulations

Besides the basic design criteria for drug carriers and their functionalization with passive biocomponents for passing the limitations of various administration routes, the introduction of active biocomponents to fulfill the actual therapeutic aim is the third major challenge on the road to an optimized drug delivery platform. This may be accomplished via covalent linkage or via adsorption of the active compound. Numerous studies on such approaches were previously reported for many different nanomaterial classes including the loading of small molecular drugs,[224,225] chemotherapeutics,[226-229] siRNA,[230] or peptide-based therapeutics,[231-234] and many more examples can be found in literature. Drug loading is of course dependent on many parameters such as material type, adsorptive interactions between the drug and the support or adsorption conditions, which may lead to variations in achievable loading degrees. For example, for the hydrophobic anti-cancer drug docetaxel a loading degree into liposomal carriers of ~0.1 wt% was reported,[235] while into MSN, ~8 wt% could be achieved.[236] Moreover, peptide drug loading levels in MSN can be even higher exceeding 25 wt%.[233,234] However, many drug loading studies only consider the possibility of high loadings into/onto the basic particles, but not into the particle in its final form intended for a specific administration route *in vivo*, *i.e.* particles functionalized with other passive biocomponents. Rather low drug loading levels and/or low loading efficiencies for such materials are reported in the range of < 5-10 wt% and 40-60 %, respectively.[237-242] As the knowledge about biological challenges for drug delivery grows, also the design of the carrier platform becomes more complex, and various synthesis steps beginning from the basic material have to be carried out to yield the final product. However, such processing may interfere with pre-loaded drugs, or if the active biocomponent would be post-loaded onto the final particles, adsorption might be obstructed by the already grafted motifs. [209] In addition, extensive post-modification of PEGylated particles may interfere with their desired stealth properties.[127] In general, the introduction of this stealth polymer has been reported to influence drug encapsulation efficiencies into different types of nanoparticles.[143,229,243-245] For example, the encapsulation efficiency of paclitaxel into PEG-polycaprolactone core-shell nanoparticles was shown to be dependent on the composition of the basic co-polymer.[143] A strong decrease of glucose encapsulation into liposomes upon increasing their PEGylation degree was reported by Nicholas *et al*.[244] Here, a functionalization degree of 2.5 mol% of PEG_{5k} resulted in an obstructed drug loading down to a level of 40 % of the native liposomes, while a similar effect in the case of PEG_{2k} was only observed at 3.75 to 5 mol%. Moreover, the release of glucose was pronounced

by increased PEG content, and the results were connected to higher numbers of bilayer defects and mass-dependent changes in PEG conformation. Furthermore, passive biocomponents can also affect drug release behavior.[143,245-249] Kanamaru *et al.*[246] studied PEGylated polymeric particles loaded with two fluorophores as model drugs. The *in vivo* release of the hydrophilic drug was pronounced due to its localization close to the hydrated PEG-shell, whereas the hydrophobic drug was associated within the hydrophobic particle core, and the hydrated PEG layer functioned as a release barrier. These examples from literature illustrate how an extensive design of drug carriers could even oppose their actual purpose, namely the loading and delivery of drugs. This gives rise to the “nano problem”: complex and highly functional materials can be synthesized, eventually including many process steps, which may come along with low product yields and problems with scalability of production processes, limiting their economic profitability, and thus, their transferability into actual pharmaceutical products. At the same time drug loading and release behavior may be altered in an unfavorable fashion, which, in turn, would lead to very high particle concentrations required to achieve a therapeutic effect, potentially accompanied by toxic side-effects. [250] Thus, more facile and efficient formulation concepts are needed in order to pave the way of such innovative materials into the clinic.

2. Mesoporous silica nanoparticles for biological applications

In the last 20+ years a lot of effort has been spent on the synthesis and application of porous silica materials. High specific surface areas, tunable pore sizes and volumes, as well as versatile options for chemical modification make these materials highly interesting in many fields such as catalysis, de-contamination, carbon capturing and chemical engineering. Moreover, special interest has been brought to mesoporous silica nanoparticles (MSN) for drug delivery applications. For therapeutic use, the particles typically have pore diameters in the range of 2-20 nm and particle sizes below 400 nm. Compared to other material types, silica offers a variety of benefits. The surface charge and hydrophobicity can be chosen at will and further active and passive biocomponents can be introduced either via covalent linkage or adsorption. Control of dissolution rates in physiological media can be achieved by varying condensation degrees or surface modifications, which may be useful for dissolution-driven drug release kinetics. Additionally, dissolvability of MSN and low overall cytotoxicity over a wide concentration range, account for their biocompatibility. In particular, silica in general is considered as “Generally Recognized as Safe” (GRAS) for the use in cosmetics and as a food additive by the FDA (US Food and Drug Administration).[251] However, careful evaluation and design of the particle’s physicochemical properties depending on the intended therapeutic application and administration route is needed, and the different aspects of drug carrier design emerging from the criteria discussed in the previous chapters can readily be fulfilled by MSN. Thus, in the following chapters, light will be shed on the general synthesis of silica nanoparticles and different functionalization techniques of this promising material type.

2.1. Synthesis of mesoporous silica nanoparticles

Synthesis of silica nanoparticles with controlled sizes can be achieved via a bottom-up approach using sol-gel chemistry, which was first reported by Stöber *et al*.[252] The process is based on hydrolysis and condensation reactions of an alkoxy silicate precursor, typically tetramethyl orthosilicate (TMOS) or tetraethyl orthosilicate (TEOS), in an alcohol/water mixture under acidic or basic catalyzed conditions. The formation of particles is a multi-step process, which starts with hydrolysis of the alkoxy monomer accompanied by the release of the respective alcohol. Subsequent reaction between two monomers can occur vial alcohol condensation or water condensation reactions (see Figure 9).[253]

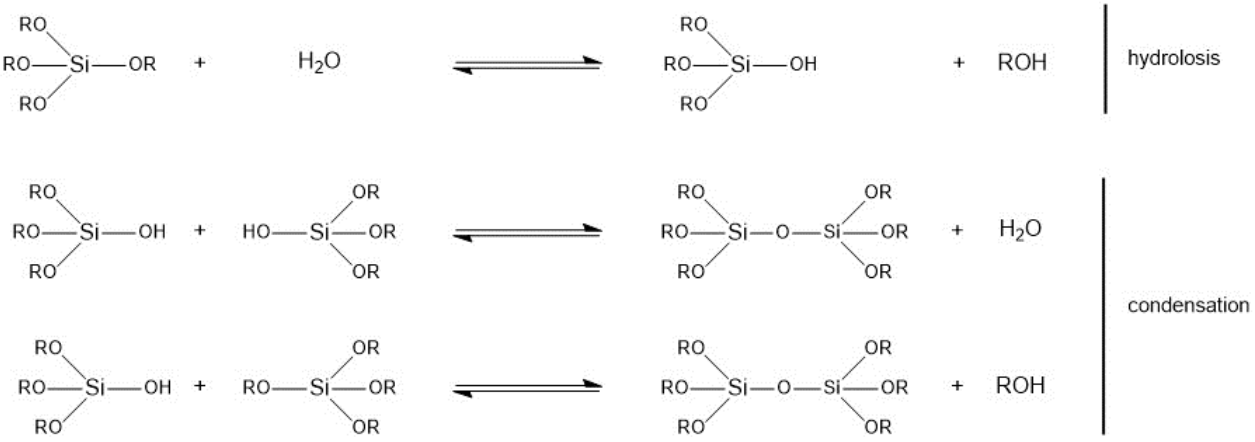

Figure 9. Hydrolysis and condensation reactions of a silica precursor during the sol-gel process (R = alkyl, H) according to Brinker *et al*.[253]

These dimers can further react through polycondensation to trimers, and subsequently to oligomers, resulting in the formation of numerous nuclei. Control over electrostatic attraction and repulsion between the silica species can be influenced by pH and salt concentration and determines whether a gel or a particulate sol is obtained. Under basic, low salt conditions, a stable sol is obtained, and particle formation continues via nucleation and growth. The process thereof can be explained by two different models. According to the modell of LaMer,[254] the concentration of hydrolyzed species increases until supersaturation is reached. Upon exceeding a critical concentration, fast condensation and formation of nuclei occurs, resulting in a decreasing monomer concentration below a level where no further nucleation occurs. In the following, hydrolyzed species, react with the already formed nuclei. Further particle growth proceeds via monomer addition to the existent nuclei, while the total number of nuclei remains constant as the synthesis progresses, and a saturation concentration is reached.[253,255] In contrast, the aggregative

growth model postulates that, as oligomer formation proceeds, primary particles are formed, and further particle growth happens by addition/aggregation of primary particles.[256,257] Nevertheless, the final particle size can be precisely adjusted by controlling reaction parameters, such as temperature, solvent mixture and concentrations of precursor and base, resulting in variation of hydrolysis and condensation kinetics of the monomers.[258]

Moreover, the final particle shape can also be modulated. By changing the concentrations of CTAB, ammonia and TEOS, Huang *et al*.[99] were able to precisely control the aspect ratio of the MSN, yielding rod-like particles. Beck[259] further modified this synthesis by adding ethylene glycol, yielding spherical particles, but with the same pore structure. However, other shapes can be obtained as well, such as platelets[260] or doughnut-like structures.[261]

Porous particles can be synthesized by using surfactants as endotemplates.[262] Typically used surfactants, such as cetyltrimethylammonium bromide (CTAB), are comprised of a hydrophilic quaternary ammonium head group and a hydrophobic alkyl chain, which leads to self-organization as micelles when the critical micelle concentration (cmc) is reached. For example, the cmc of CTAB in water is 0.9 mM. However, in a solvent mixture of ethanol/water, as it is often used for the synthesis of MSN, the cmc of CTAB increases to values exceeding those usually present in the reaction mixture, e.g. 22 mM for 50 v/v% ethanol.[263] Nevertheless, the surfactant forms a mesophase via a cooperative mechanism by association of hydrolyzed and partially condensed silica species due to electrostatic attraction with the surfactant, and subsequent incorporation of the surfactant into the silica network as silica condensation proceeds.[264] The particle's final pore diameter can be tuned by variations of the surfactant's alkyl chain length and counter-ion, or by using co-surfactants and hydrophobic swelling agents, such as N,N-dimethylhexadecylamine or toluene.[265-268] Finally, the surfactant can be removed after particle formation either via extraction in solution or calcination. The former is based on attenuating the electrostatic attraction between surfactant and silica support via protonation or ion exchange, which can be done with for example acidified ethanol or an ethanolic solution of ammonium nitrate. In contrast, calcination results in complete removal of all organic components, as well as further condensation of the silica network, which in turn may influence dissolution kinetics of the material.[269] However, surfactant removal via extraction in solution preserves the organic moieties, which were introduced via co-condensation in the sol-gel process. This is crucial if MSN pre-functionalized with small groups are aimed for, as it will be discussed in the next chapter.

2.2. Functionalization of silica nanoparticles via covalent coupling

In general, functionalization of silica nanoparticles with passive biocomponents, such as charged groups or polymers, can be achieved by two approaches: co-condensation or post-grafting. The co-condensation approach is based on the introduction of a functional silane (typically organo(trialkoxy) silanes) during the particle synthesis, where a mixture of the main silica precursor and the silane is added. Hydrolysis and condensation reactions take place as described above, but the functional silane gets homogenously distributed across the silica network and reaches towards the final porous space (see Figure 10), and may happen to be inaccessible if the groups are incorporated within the network.[270] Due to the fact that the silane exhibits at least one alkoxy group less than the main precursor, lower condensation degrees and mesoscopic order occur, and the extent thereof is depending on the silane concentration, binding stoichiometry, and the steric dimension of the functional group.[271] In order to preserve the introduced groups, template extraction may not be done via calcination, but via extraction in solution. While this co-condensation results in MSN with functional groups equally distributed on the external and the internal surface, it also comes with drawbacks, such as labor-intensive material processing and limitations regarding the size and nature of the functional groups and the potential decrease of pore volume and diameter. As these groups are incorporated across the whole silica network, typically used silanes should have rather low molecular weights. However, a wide range of functional groups can be used, including amino or carboxy groups as simple means for particle charge modification, or isocyanates, thiols, sulfonates, and epoxy or vinyl groups, which may act as coupling reactants for further post-functionalization.[272-275] Some of these groups can be easily transformed post-synthesis to other functionalities yielding bi-functional nanoparticles, for example via reaction of co-condensed amino groups with succinic anhydride.[153,276] Additionally, surface hydrophobicity can be tuned by the introduction of small hydrophobic moieties.[277] On another note, if multivalent organo-silanes are used, periodic mesoporous organosilicas (PMO) can be obtained.[278]

Moreover, spatial control of the group's localization can be achieved. Kecht *et al*.[279] demonstrated the synthesis of MSN exhibiting a core-shell functionality via a delayed co-condensation approach, where the addition of different silanes during the synthesis took place sequentially. In a first step, TEOS was used to form preliminary particles, upon which a mixture of TEOS and (3-aminopropyl) triethoxysilane (APTES) was added. The synthesis yielded particles with an all-silica core, on which silanol groups were present within the pores, and amino groups were solely found on the particle's external surface. Such core-shell functionalities may be of advantage for the

development of drug adsorption and functionalization strategies. The introduction of larger moieties like PEG via delayed co-condensation was also previously reported in literature.[280,281]

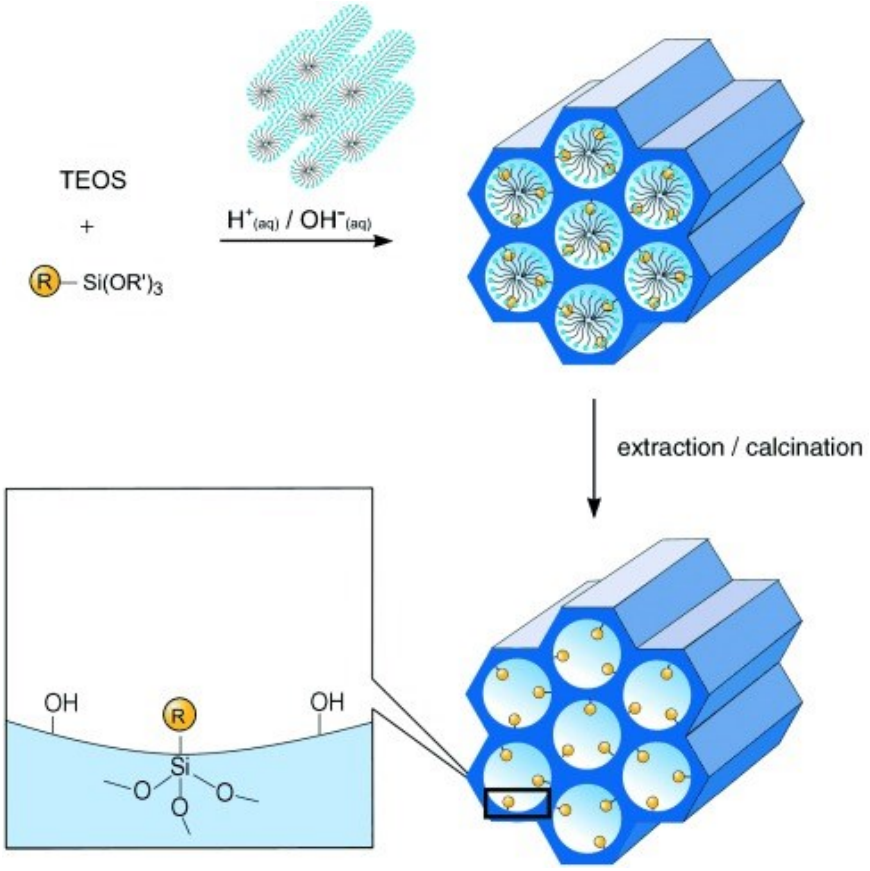

Figure 10. Co-condensation approach to obtain functionalized MSN. A functional silane (R = organic residue) is introduced along with the main precursor (TEOS in this case). The functional group is evenly distributed across the porous silica. (reprinted from Frank Hoffmann, Maximilian Cornelius, Jürgen Morell, Michael Fröba “Silica-Based Mesoporous Organic–Inorganic Hybrid Materials”, Angewandte Chemie - International Edition, Volume 45, page 3220 ©2006, https://doi.org/10.1002/anie.200503075 with friendly permission by John Wiley and Sons)[271]

As already mentioned, the introduction of functional groups via co-condensation may be not suitable for different reasons. Thus, functionalization of MSN can also be achieved via post-grafting techniques, which can be of interest when the all-silica particles should be modified without alteration of the silica network itself. Reactants which can be used for this purpose include disilazanes, allyl silanes, aryl silanes, trichlorosilane or silyl-imidazoles.[282] However, the most common post-grafting strategy is, similar to the co-condensation approach, the use of relatively simple trialkoxy silanes. These silanes are commercially available offering a variety of functional groups. Since alkoxy groups are sensitive to hydrolysis, silane coupling is mostly executed under

water-free conditions at high temperatures, to counter pre-mature silane condensation. For instance, amino-functionalized MSN can be synthesized via post-grafting of APTES in toluene at high reaction temperatures. [283] However, also silane grafting in aqueous media has been reported.[284]

In addition to small silane moieties, also larger molecules can be grafted onto the silica surface, for example PEG silanes.[285] However, as the post-grafting proceeds, further attachment of polymer chains can be sterically hindered by already grafted polymer chains, especially if the polymers have high molecular weights. In addition, intermolecular condensation reactions can occur. For example, Issa *et al*.[286] reported high grafting densities of 1.02 chains/nm² for a PEG_{5k}-silane. This was explained by intermolecular condensation between the alkoxy silane groups and the terminal hydroxy groups of the polymer, and the extent of the condensation reaction was proportional to the molecular weight.

Moreover, depending on size and coupling kinetics of the silane, the diffusion depth into the pores may be limited, which can result in pre-dominant reaction at the pore entrances, and eventually pore blocking (as discussed later). Although, diffusion limitation does not account in such an extent for small-sized silanes, like APTES, heterogeneous distribution of functional groups after post-grafting has been reported. Millot *et al*.[287] investigated the grafting of APTES on silica surfaces under reaction conditions often applied in literature via solid-state ^{29}Si-NMR. Intriguingly, only a fraction of the siloxane bridges was formed between the silane and the support, but the vast majority was attributed to homo-condensation between APTES moieties, which were only connected to the surface via few anchoring points (only ~ 5 % of total siloxane bridges). Thus, silane post-grafting comes with limitations on its own, and the choice of the functionalization strategy should be evaluated according to the feasibility of the synthesis and the required characteristics of the final material.

If the silica surface has been already functionalized either by silane-based co-condensation or post-grafting techniques, passive biocomponents, such as antibodies, targeting ligands, fluorophores or polymers can be introduced via different coupling chemistries. These methods include, for example, epoxy-amine coupling, epoxy-alcohol coupling, di-sulfide bridging, carboxy-thiol coupling, maleimide-thiol coupling, click-chemistry, isocyanate-alcohol coupling, isothiocyanate-amine coupling or biotin-avidin coupling.[286-296] A very common approach is the amide formation of surface-bound amino groups with a conjugate exhibiting a carboxy group or *vice versa*. For this purpose, the carboxy group is pre-activated, and further equipped with a good leaving group. Besides others, pre-activation of carboxylic acids can be achieved using carbodiimides, like 1-ethyl-3-(3-dimethylaminopropyl) carbodiimide (EDC) or N',N'-dicyclohexyl

carbodiimide (DCC), yielding an O-acylisourea compound, which is sensitive to hydrolysis. To increase the coupling efficiencies, this intermediate can be further reacted with N-hydroxysuccinimide (NHS) or N-hydroxysulfosuccinimide (see Figure 11). The reaction gives a hydrolytic stable NHS ester, representing a good leaving group for the coupling with primary amines via nucleophilic substitution resulting in amide formation.[297-299] The efficiency of this coupling strategy is dependent on pH, and good yields can be achieved in amine- or carboxy-free buffers at neutral pH values. With this coupling method, large moieties can be bound to silica nanoparticles. For instance, Kunc *et al*.[300] demonstrated the conjugation of antibodies via steric demanding crosslinkers based on carboxylated dextran to amino-functionalized silica nanoparticles via EDC/NHS coupling chemistry.

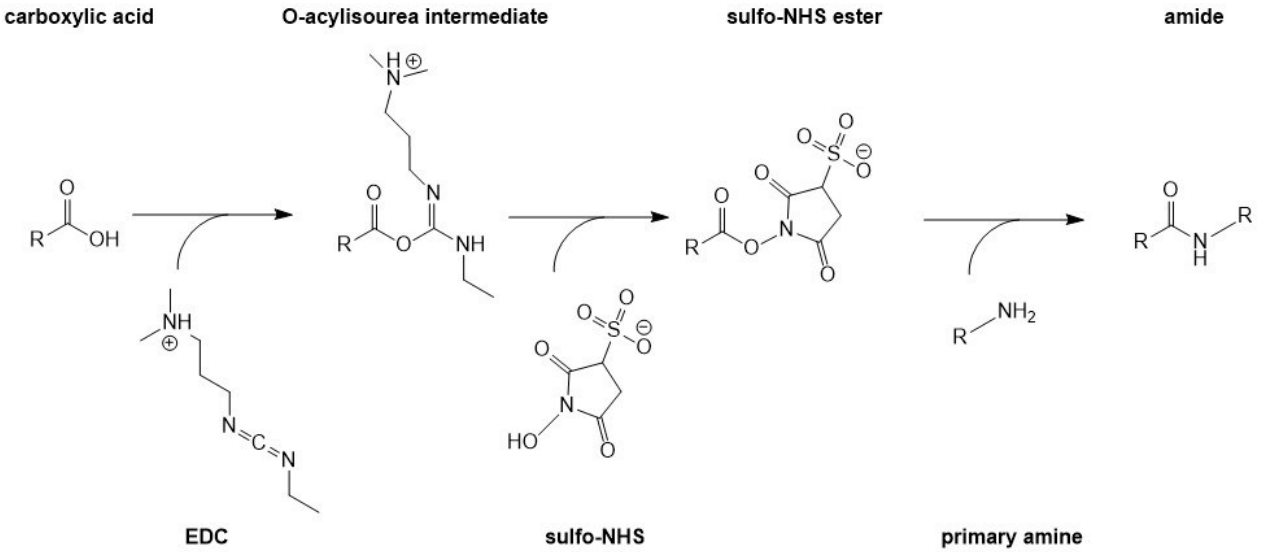

Figure 11. Schematic drawing of EDC/NHS coupling chemistry. Upon pre-activation of the carboxylic acid with the carbodiimide EDC, the conjugate can be reacted with sulfo-NHS forming a stable intermediate for further coupling with a primary amine forming an amide bond.

In a comprehensive study, von Baeckmann *et al*.[301] compared different MSN functionalization strategies using the example of PEGylation and the influence of the linking chemistry on the final physicochemical particle properties as well as on serum protein adsorption. The investigated PEGylation strategies included amine-NHS, thiol-carboxylate, thiol-maleimide, amine-epoxy or amine-isocyanate coupling, as well as silane grafting. Silane or thiol-maleimide chemistry enabled the highest PEGylation degrees exceeding 20 wt% (for PEG_{20k}-silane even over 25 wt%), and in the case of thiol-maleimide 20 wt%, irrespective of the PEG molecular weight, whereas amine-NHS and amine-epoxy coupling were less sufficient. In the case of high molecular weight PEG-silane, no T-species were detected by solid-state NMR studies raising the question, if the

purchased polymer was present as actual silane, and thus if the PEG was covalently attached or adsorbed. However, all PEG-MSN exhibited a decreasing specific surface area dependent on the amount of polymer, but irrespective of the coupling chemistry. The surface areas and pore volumes of PEG-MSN produced by amine-NHS coupling were extraordinarily low, indicating that the polymer was preferentially localized within the pores and/or that strong particle dissolution accompanied with pre-mature hydrolysis of PEG-NHS esters during the reaction in PBS caused the ineffectiveness of amine-NHS coupling. Finally, serum protein adsorption was shown to be diminished at high PEG masses, but no general trend for intermediate and low PEG amounts was identified. Interestingly, despite variances of data, PEG-MSN synthesized via amine-NHS coupling seemed to be fairly efficient in protein adsorption inhibition, *i.e.* low protein adsorption at low PEG masses. This could mean, that the decrease of surface area and pore volume was indeed due to silica dissolution and a collapsing pore system, and that the low surface area available for PEG coupling was the reason for low PEG masses bound. In turn the PEG would have been densely packed resulting in the low protein adsorption levels at these PEG amounts.

2.3. Functionalization of MSN with active biocomponents

Similar to other nanomaterials (see chapter 1.3), MSN can be equipped with a variety of active biocomponents fulfilling versatile functions.[119] Such functional moieties can include antibodies,[122,153,302-305] imaging agents,[306-311] or targeting ligands.[312-316] In most cases, these biocomponents are covalently attached to the particles (see Figure 12).

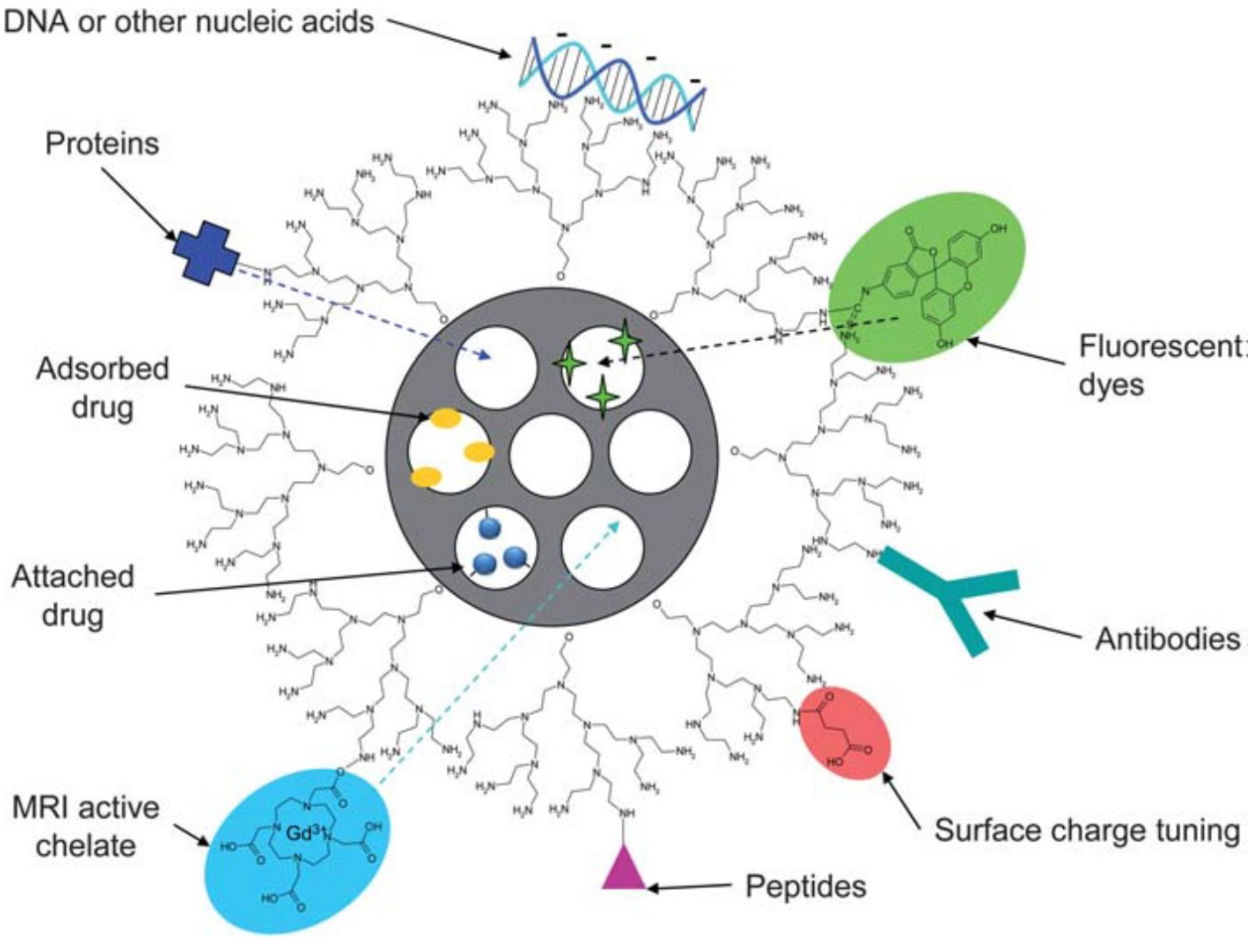

Figure 12. Schematic overview of functionalization of MSN with different biocomponents such as antibodies, imaging agents or therapeutic drugs. In this example, PEI was used as anchoring groups and covalent functionalization was achieved via amide coupling chemistry. (Used with friendly permission of Royal Society of Chemistry from Jessica M. Rosenholm, Cecilia Sahlgren, Mika Lindén, "Towards multifunctional, targeted drug delivery systems using mesoporous silicananoparticles – opportunities & challenges", Nanoscale, Volume 2, page 1874 ©2009, https://doi.org/10.1039/C0NR00156B)[119]

Moreover, MSN can be loaded with therapeutic drugs, which may be achieved via covalent linkage or adsorption-based methods. Covalent drug linkage may be preferred for therapeutics which only show low adsorptive affinity to silica, and it may also come with additional advantages like slow

release kinetics, increased therapeutic efficiency, optimized biodistribution and low systemic toxicity.[251] For instance, Rosenholm *et al*.[317] attached methotrexate (MTX) using a PEI linker to the external surface of MSN. In this case, MTX served as both, chemotherapeutic agent and targeting ligand, resulting in an increased apoptosis of cancer cells compared to a healthy cell line upon treatment with the particles, while MTX in its free form affected both cell lines in a similar extent. Moreover, drug release was shown to happen mainly in the acidic environment of the endosomes of the cancer cells, where the MTX was slowly cleaved from the MSN via proteolysis, avoiding pre-mature, extracellular drug release. Such triggered release of covalently bound drugs can also be achieved, for example, via reduction of di-sulfide bonds by cell-produced antioxidants,[318] or enzymatic cleavage,[319] allowing control over site of release and release kinetics. However, when using such a drug loading approach, it must be ensured that the key physicochemical parameters of the MSN (+ linked drug), like surface charge or colloidal stability, are not altered in a critical, dysfunctional manner, and that the drug itself maintains its active structure upon cleavage.[251] In addition, the release kinetics have to match the requirements of the therapeutic approach. Thus, adsorption-based drug loading remains as the standard approach for drug delivery formulations. Adsorption onto/into MSN has been reported for a variety of therapeutics, especially chemotherapeutics, such as doxorubicin, paclitaxel, daunorubicin, and others.[250] In the recent years, however, peptide-based drugs have gained increasing attention for drug delivery concepts. Due to their often observed pre-mature degradation (e.g. by proteolysis) upon contact with biological fluids within the range of minutes to hours,[320-323] this drug class is predestined to be administered via drug delivery platforms. Adsorption and delivery of peptide drugs has been demonstrated for several therapeutic classes, like anti-diabetic,[24,58,324-326] anti-microbial,[232,234,327-329] or anti-viral[330] peptides. In general, peptide adsorption onto silica may be mainly governed by van der Waals forces, hydrogen bonds or ionic forces.[331] As the sequential combination of amino acids is quasi-indefinite, the physicochemical properties (dimension, charge, hydrophobicity etc.) of peptide-based drugs are broad. Thus, tunability of carrier properties accordingly is essential for efficient and effective drug loading - a pre-requisite which MSN do fulfill. Several studies have focused on electrostatics as the main driving force for peptide adsorption.[232-333] Puddu *et al*.[334] studied the adsorption of three model peptides (cationic, neutral and anionic) onto non-porous silica particles at pH 7 and pH 3, *i.e.* pH values where the silica surface would be of negative or neutral charge. As expected, the cationic peptide exhibited the strongest binding. However, adsorption of neutral and anionic peptides was not zero, indicating entropic effects trough dehydration and the involvement of non-electrostatic forces (van der Waals forces and/or hydrogen bonding) between the silica surface and peptide molecules, as well as between the peptide molecules themselves. These contributions were also validated for the

cationic molecules via adsorption thereof onto neutral silica surfaces at low pH. However, not much is known about the influence of particle shape, pore size and volume on peptide adsorption. Braun *et al*.[233] studied the adsorption of the cationic anti-microbial peptide calcitonin on all-silica MSN with uniform pore diameters of 3 nm or with a bimodal pore size distribution of 8 nm and 27 nm. For the small-pore particles, an initially steep, two-step adsorption isotherm with an intermediate plateau was recorded. In contrast, peptide adsorption onto large-pore particles proceeded in a linear manner in the medium concentration range, without reaching a defined plateau. In both cases, the maximum loading degree was about 25 wt%. SDS-PAGE of peptide solutions in PBS revealed formation of dimers, trimers and tetramers at increasing calcitonin concentrations, which was connected to the different isotherm forms. At low calcitonin concentrations, the dimer size fitted well to the small pore sizes enabling multi-valent peptide-silica interactions in the confined pore space resulting in strong attraction. In contrast, for large pore diameters, enhanced adsorption took place only at higher concentrations, *i.e.* for larger aggregates. This study demonstrated the influence, pore size exhibits on peptide adsorption. However, more information about peptide adsorption behavior on a brought range of different particle characteristics, such as functional groups, pore size and geometry, and hydrophobicity, but also about the influence of peptide properties, like pH dependent charge, conformation and size are needed in order to develop general concepts for the design of efficient peptide loading strategies.

2.4. PEG adsorption onto MSN: The solution to the nano problem?

As already discussed in chapter 1.3, PEGylation of nanomaterials can result in pore blocking and potential alteration of drug loading and release behavior. Specifically in the case of MSN, covalent linkage of PEG either via co-condensation or post-grafting techniques was reported to decrease the pore volume and the specific surface area of the final particles. Cauda *et al*.[280] reported the synthesis of PEGylated core-shell MSN via a delayed co-condensation approach. A PEG silane was added to the particle synthesis 30 min into the reaction, yielding a PEG shell with different molecular weights (PEG_{550}, PEG_{5k}, and mixed PEG_{550}-PEG_{5k}). The PEG shell reduced the dissolution rate of the particles in simulated body fluid (SBF), which was the main subject of the study, but also decreased their specific surface area and pore volume as compared to the native all-silica particles. Zhu *et al*.[335] demonstrated the potential of hollow MSN as drug delivery vehicles, which were PEGylated via a post-grafting technique. The PEGylated particles had a decreased doxorubicin loading efficiency compared to the basic MSN (69.6 % vs. 83.4 %). This drawback, however, was compensated in this case by a higher uptake of PEG-MSN into cancer cells and subsequently lower levels of cell viability. Low doxorubicin loading degrees were also reported after PEGylation of HA functionalized MSN (~ 3 wt%) and the drug release was rather fast reaching a cumulative release of 70 % after 2 h.[336] Another example for the alteration of drug load by PEGylation was shown by Wani *et al*.,[229] who grafted PEG-silane to rod-like MSN and consecutively adsorbed the chemotherapeutic MTX onto particles in PBS mediated by electrostatic attraction. Compared to the non-PEGylated particles, the MTX load decreased with increasing PEG amount from ~ 30 wt% to ~ 18 wt% at high drug loading concentrations, and from ~ 19 wt% to ~ 2 wt% at low loading concentrations, respectively. At the same time, release kinetics of MTX were promoted for the PEG-MSN. Decreasing drug loadings with increasing functionality of the carrier due to reduction of pore volume and surface area was also observed for non-PEGylated MSN.[337] These examples demonstrate again the potential interference of functionalization approaches in general, and of PEGylation strategies in particular, with drug loading procedures. The potential competition of the polymer with drug molecules over adsorption/binding sites pronounces the need for more efficient, but still straight-forward, formulation and functionalization strategies. Such an approach could include sequential drug loading and functionalization, where a drug would be loaded into the MSN first. Subsequently, PEGylation would be carried out in a solvent, where the drug would not be soluble to prevent pre-mature drug release. Due to the amphiphilic nature of ethylene glycol subunits, PEG is soluble in water and a brought spectrum of organic solvents,[338] providing flexibility in the choice of solvent.

However, as the effectiveness of coupling chemistries depend on factors like solvent polarity, temperature, or reactants, harmful interactions of such parameters with the loaded drug can not be excluded. Thus, PEGylation would have to be carried out not covalently, but through adsorption.

Adsorption of PEG onto silica surfaces has been investigated in several studies. Diffusion of PEG_{6k} into the micropores of a hydrophobic zeolite material with pore diameters of 1.58 nm was reported in literature.[339] PEG adsorption from aqueous solution onto silica nanoparticles with a size of 10 nm was investigated by Liu *et al*.[340] The PEG mass adsorbed onto the particles was linearly dependent on the initial PEG concentration until a plateau was reached. Transforming these results into a classic isotherm (adsorbed mass vs. equilibrium concentration), this would result in very steep isotherms indicating strong adsorptive forces between the polymer and the surface. Wisniewska *et al*.[341] studied the influence of pH, temperature and molecular weight on PEG adsorption onto silica nanoparticles. Overall, the adsorbed amounts were constant over a wide pH range (pH 3-9), elucidating the dominant role of hydrogen bridges for the adsorptive interaction over the role of electrostatic contributions. Hydrogen bridges can be formed between both, protonated as well as deprotonated surface silanol groups, and the oxygen atoms of the polymer. Rising temperatures from 15 °C to 35 °C exhibited a promoting effect on the total adsorbed mass. This was explained by a denser packing of the chains and a more stretched/upright conformation at higher temperatures, which was supported by higher adsorption masses for high molecular weight PEG compared to low molecular weight PEG at a given equilibrium concentration and temperature. Furthermore, the influence of molecular weight on PEG adsorption in water onto microporous silica with pore sizes of 300 nm was studied by Trens *et al*.[342] Again, adsorption isotherms were shown to be steep, and adsorption equilibrium was reached within 1 h. The adsorption isotherm plateaus increased with increasing molecular weight (0.4 kDa to 5 kDa) up to 0.53 mg m^{-2} for PEG_{5k}. Moreover, microcalorimetry measurements showed, that at low PEG concentrations, *i.e*. no full coverage of the surface, the differential enthalpy of displacement of surface bound water by the polymer (measured as kJ / mol monomer) was independent of the polymer size indicating a flat initial adsorption geometry. However, as PEG concentrations were raised, the differential enthalpy of displacement per segment decreased, despite the increasing PEG amounts adsorbed. This means, that the polymer chains developed a more upright orientated conformation as PEG concentrations rose, and that further chain adsorption mainly took place by replacement of pre-adsorbed polymer segments. Moreover, the integral enthalpy of displacement per segment measured from zero coverage to the adsorption maximum decreased with increasing molecular weight indicating that larger polymer chains can form longer tails towards the solvent.

Overall, adsorptive interaction of PEG with silica is strong, which raises the question if pre-loaded

drugs can withstand PEG adsorption or if it will be displaced in the process. However, further work is needed as literature about the influence of adsorption solvent on the PEG conformation and the resulting effect on protein adsorption inhibition is scarce.

To conclude, covalent attachment of passive biocomponents, comes with a variety of limitations. Many proposed drug carrier systems are of a complex design to tackle several therapeutic challenges at once, for example protein adsorption inhibition, triggered drug release, or targeting strategies. Multi-stage synthesis approaches for such materials are rather complex and labor-intensive. However, also more simple methods for covalent attachment of moieties may include experimental conditions, such as high temperatures, reactive coupling agents or solvent, which may not be compatible with pre-loaded drugs. Drug loading post-functionalization can be impaired by grafted polymers, for example due to pore blocking. Hence, in this work a functionalization concept is proposed based on sequential adsorption of the active and passive biocomponent, in this case a model drug and PEG.

II Motivation and aims of the thesis

MSN are highly promising materials for drug delivery applications potentially enabling high concentrations of active compounds selectively at the site of disease and protection of labile drugs. Despite of many years of research this material class barely has made its transition into the clinics,[2] and only a few silica-based nanomaterials were investigated in clinical trials for imaging or drug delivery applications.[343] For example, silica particles were shown to improve the bioavailability of fenofibrate by 54 % (loaded via wet impregnation) upon oral administration to humans.[344] Silica nanoparticles with sizes of 6-10 nm (Cornell dots) were successfully intravenously administered for the use as imaging agents, and no severe side-effects were observed.[345] [346] These examples demonstrate that the high promises made by researchers over the years are in no way empty words. However, the reasons for the low clinical translation of MSN are various and may include the lack of straight-forward and efficient loading and formulation strategies as well as the need for screening methods to predict the site-specificity of particle accumulation and distribution – challenges, which have to be addressed in order to pave the way of MSN into the clinics.

Controlling the biodistribution of drug carriers via functionalization with passive components, like polymers, presents a common and promising approach, due to well-studied synthesis routes and influences on the physicochemical parameters of the carrier. To this date, a lot of research effort has been made for the development of drug delivery platforms for oral administration. This research field includes many types of nanomaterials and functionalities, and numerous studies focused on the *in vitro* and *in vivo* behavior of these materials and the influence of particle parameters like size, shape, charge or surface functionalization on mucus-interaction and intestinal particle distribution and accumulation. However, translational approaches between different material classes are scarce, but are required to overcome the need for labor and time-intensive pre-tests and animal studies necessary for every new particle type to come. In this work, the influence of polymeric functionalization on the biodistribution of MSN upon oral administration should be investigated and connected to literature findings for other types of materials and surface functionalities. In order to keep the sample matrix as narrow as possible, the physicochemical design of the carrier itself, as well as the types of polymers grafted were carefully chosen on studies reported in literature for different types of nanomaterials, including PLGA, silica, silicon or PS. Rod-like MSN with sizes below 200 nm should be synthesized and used as platform for further design considerations, due to the fundamental possibility of mucus-permeation of such particle

sizes as well as the potentially increased natural GIT-retention of particles with such an elongated geometry. The distribution within the GIT should be evaluated via a fluorescence-based *in vivo* imaging system (IVIS) using an *in vivo* mouse model for DSS-induced colitis and compared against particle behavior in healthy mice. With the aim of tuning the particle's fate in the GIT, the MSN should be modified with HA or PEG, two polymers which are known to exhibit decisive properties in the oral environment. The influence of the polymeric functionalization on the intestinal and systemic particle biodistribution as well as on the particle retention within the GIT depending on the health state of the animals should be studied in detail. To gain insights into the interplay between particle functionalization and biological environment on a cellular level *in vitro*, particle behavior on epithelial cell models with and without mucus producing cells should be carried out and connected to the *in vivo* results.

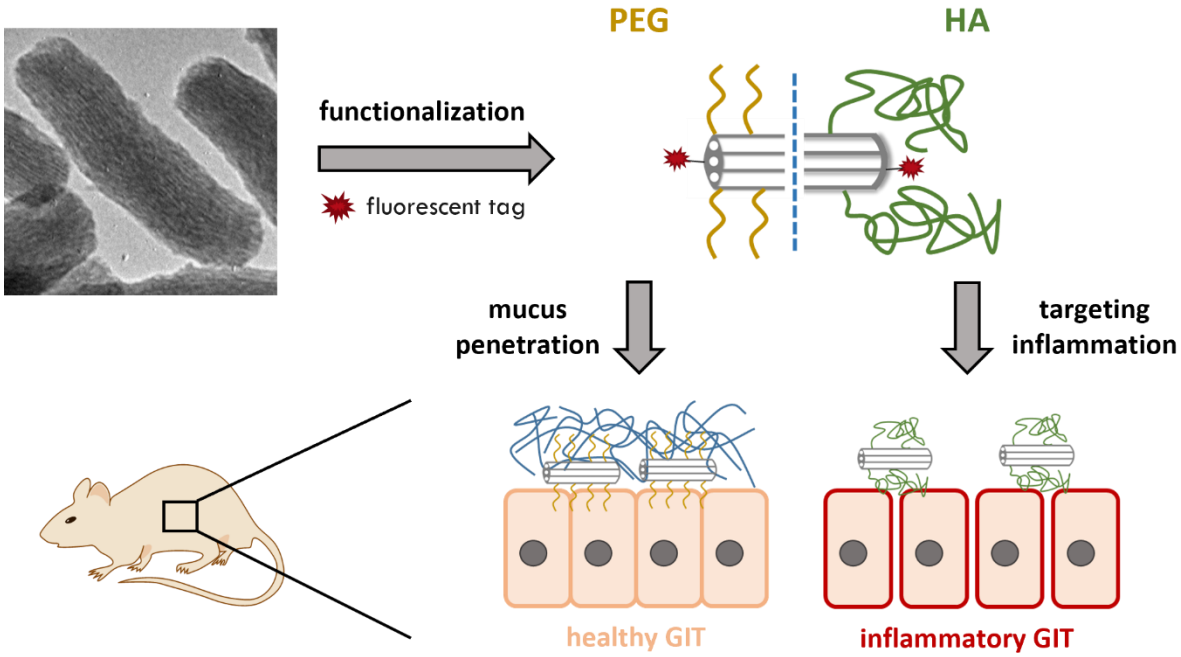

Figure 13. Schematic drawing of functionalization of rod-shaped MSN with PEG or HA for targeting healthy or inflamed intestinal tissue.

Medical relevance of new designed drug delivery platforms is mostly studied by their administration to animal models. As *in vivo* experiments are laborious, expensive, and ethically challenging, such experiments can not be exercised on a large sample matrix and other high-throughput screening methods are needed for biomaterial research. These could be utilized for the screening of a brought palette of particles with different properties, for example charge or functionalities, upon which only the most promising candidate would be used in animal trials. As

one of the main goals of drug delivery is their cell-specific uptake, this work suggests a simple cell-based screening method, to identify particles with the most promising internalization profile. The two cell lines THP-1 and PC-3 should be used to model the accumulation of particles in the host's defense system versus in the cancerous tumor, and the internalization into these cells should be evaluated by cell cytometry. The extent of internalization should be connected to the particle charge and the protein adsorption onto their surface. However, as these cell-lines can not be cultivated as a co-culture, a rating system is proposed to account for the absolute, overall balances of the particle uptake. With this ratio, prediction of which particle would be accumulating in the tumor tissue, while not being cleared by the immune system, was aimed for. The aim of this approach was to enable the screening of high numbers of particle types in a cost-effective and standardized manner *in vitro*, and to identify the most promising candidates for further *in vivo* studies smoothing the way of these materials into the clinics.

One major challenge for intravenously injected drug delivery platforms is the fast (and partly irreversible) adsorption of blood constituents leading to uptake into macrophages and accumulation in the organs of the defense system. This results in fast systemic clearance rates and narrowing of the therapeutic time frame. Strategies for inhibition of protein adsorption have been suggested, under which PEGylation is considered the gold standard and, without doubt, presents the most thoroughly explored passive biocomponent used for this purpose. However, the common approach for PEGylation is the covalent grafting of the polymer onto the drug carrier's surface, and many different synthesis routes were reported. The herein used grafting chemistries can involve high temperatures, organic solvents or coupling reagents such as frequently applied ones for amide formation in bioconjugation synthesis. Moreover, one cannot exclude that active biocomponents pre-loaded into the carrier's pores may preliminarily desorb, interact with reagents, or even get degraded under the synthesis conditions present. This risk is especially high for biological therapeutics, such as peptides. Another trade-off of covalent PEGylation, which is often not discussed in literature, is the competition between polymer and drug over available surface area. As protein adsorption inhibition is suggested to be most effective at high PEG densities, pore blocking upon PEGylation and thus limitation in drug loading degrees is possible. In order to pave the way of MSN as drug carriers into clinical use, more efficient and less labor-intensive formulation concepts are needed, optimally manageable by non-chemists, for example clinic staff. In this work, an adsorption-based formulation concept is suggested to yield densely PEGylated MSN with high drug loading degrees. For this purpose, a solvent-orthogonal adsorption-loading strategy should be used based on solubility differences of the used model drugs. As PEG is soluble in both organic and aqueous media, water and dichloromethane were used. The solvent-

dependent localization and conformation of the adsorbed PEG, as well as its influence on serum protein adsorption should be studied in detail. Successful proof of the novel formulation concept should be achieved by using either a hydrophilic peptide, or a hydrophobic dye as a model drug, loaded in the respective appropriate solvent. By selecting a solvent with orthogonal polarity, high PEG adsorption degrees without loss of the cargo was aimed for, resulting in effective protein adsorption inhibition.

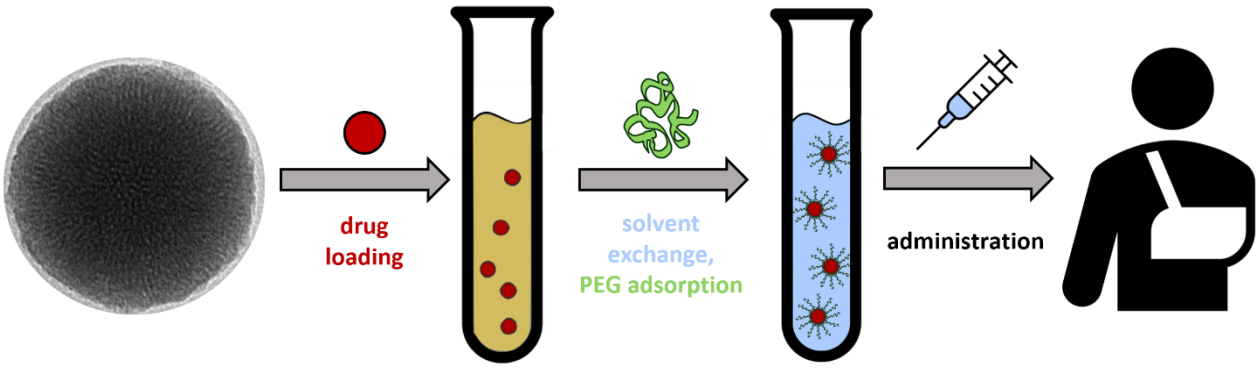

Figure 14. Schematic drawing of a straight-forward formulation process of PEGylated, drug-loaded MSN based on adsorption in solvents with orthogonal polarity.

One oft the major goals of drug delivery by nanoparticles is the effective protection of labile drugs as well as the increase of their concentration on the site of action. Therefore, high loading degrees must be attained, for which the carrier's physicochemical properties have to be adjusted according to the compound's properties, as wells as to the needs of the final therapeutic application. Additionally, drug loading and formulation of the delivery platform should be as efficient as possible with low losses of the active moiety. This applies especially for drugs which production is associated with high costs and labor, as it is often the case for innovative peptide-based compounds. To achieve this, the optimal conditions for peptide adsorption must be found and the parameters influencing the peptide-silica interactions are needed to be understood systematically. Such parameters may include pH of the loading solution (*i.e.* charge of the peptide and the particle surface), the particle's pore size and structure. Thus in this work, a model peptide (JM#21) was chosen for detailed adsorption studies onto silica nanoparticles considering all these variables. JM#21 is a derivative of the EPI-X4 peptide and was recently reported by Harms *et al*.[323] The peptide is strongly binding to the CXCR4 cell receptor and may offer the alteration of the CXCR4/CXCL12 signaling pathway, which is involved in several diseases, like cancer and inflammatory processes. By recording adsorption isotherms using particles with different pore geometries and surface hydrophilicity, as well as by variation of the peptide's net charge, the

adsorption process should be studied in detail, and connected to *in silico* modelling studies of conformational changes depending on the peptide's charged state. Finally, to exclude that such structural changes upon adsorption do not alter the functional activity of the peptide, which would be a pre-requisite for the final application in the clinics, a cell-based *in vitro* assay should be performed, to ensure that the peptide is released in its fully functional form.

III Results and discussion

The main tasks of drug delivery research are the synthesis of drug carriers with physicochemical properties suitable for specific medical applications as well as optimization of drug loading capabilities. Thus my thesis is structured into two main parts: The testing of differently functionalized silica nanoparticles in biological settings and the examination of drug loading and formulation concepts, with both parts aiming for a faster transition of drug delivery concepts into clinical applications.

Within this work, several types of silica nanoparticles were synthesized using sol-gel chemistry, varying in diameter, form, porosity and pore geometry. For some experiments, the all-silica particles were modified with carboxy- or amino-silanes to tune their physicochemical properties or to provide chemical anchor groups for further functionalization via EDC/NHS coupling chemistry. The particle characteristics were examined via a set of analytical methods. Particle sizes and pore arrangements were studied via transmission electron microscopy (TEM) and small-angle x-ray scattering (SAXS). The particles were further characterized via nitrogen sorption measurements. The specific surface areas were determined using the Brunauer-Emmett-Teller (BET) method, the pore diameters were calculated with the non-local density functional theory (NLDFT) and the external specific surface areas were estimated by the t-plot method. The zeta potential of the particles was measured using dynamic light scattering (DLS). In most cases, their functionalization degree was determined via thermogravimetric analysis (TGA). For this purpose, respective reference particles were treated under the same conditions as the functionalized particles, but without the addition of the functional motif, to exclude hydrolysis related mass losses. More experimental and methodological details can be found in the respective publication.

1. Testing of MSN in biological settings

In the field of drug delivery, the two common types of administration aimed for are the oral route and the intravenous route. As described in chapter 1, both applications exhibit different challenges on their own demanding for distinctive carrier properties to overcome these barriers. Thus, in the first part of my thesis, different MSN were synthesized and tested for their behavior in relevant *in vitro* and *in vivo* models.

The effectiveness of oral drug delivery platforms is, amongst other factors, dependent on the

intestinal residence time, i.e. the time window available for drug release. Therefore, prolongation of intestinal transit times and knowledge about the localization of the nanoparticles upon oral administration is a pre-requisite for an effective therapy. This is especially the case when treatment of local diseases, like IBD, is desired. These diseases often come with an alteration of the intestinal environment, for example inflammation, mucus depletion and faster intestinal transit times, and oppose additional challenges to drug delivery platforms. With the aim of elucidating the retention and distribution of MSN under healthy and inflammatory conditions upon their oral administration, silica nanoparticles were synthesized and further functionalized with passive biocomponents. However, as mentioned earlier, extensive pre-testing would be necessary to identify most promising candidates for further use in *in vivo* experiments, which is why the design criteria for the final particles were based on a comprehensive literature review of various other nanomaterial types. By modification of a procedure which was originally reported by Huang *et al.*,[99] rod-like MSN with an aspect ratio of 2.7, but a short mean average length of 149 nm, were successfully synthesized. The elongated form was aimed for to increase the particle's natural retentive behavior as demonstrated in literature (see chapter 1.1.1), but at the same time enabling them to diffuse through the intestinal mucus mesh due to their small diameter. After the synthesis, the structure directing surfactant was removed via calcination and the particles were post-functionalized with an amino silane to enable further functionalization steps via EDC/NHS coupling technique. The obtained particles were thoroughly characterized via TEM, nitrogen sorption measurements, zeta potential measurements and TGA. The calcined particles were found to exhibit a defined, hexagonally arranged pore structure with pore diameters of 3.2 nm and a large specific surface area of 920 $m^2 g^{-1}$ – properties which are essential to achieve high drug loadings for future drug delivery applications. The MSN were labelled with the fluorescent dyes Cy5 or ATTO647N to examine their localization *in vitro* and *ex vivo* via fluorescence imaging techniques. To tune the particle's behavior under healthy and inflammatory conditions, the MSN surface was further covalently functionalized with the passive biocomponents PEG and HA, and the final functionalization degrees were 4.7 wt% and 3.7 wt%, respectively. Both, MSN-PEG and MSN-HA, exhibited a negative zeta potential of -22 mV and -34 mV, as measured in Hepes buffer (25 mM, pH 7.4), which allowed to exclude charge specific effects in the following experiments.

The dissolution behavior of the particles was examined in a simulated intestinal buffer solution (pH 6.6) via TEM studies and fluorescence intensity measurements. Importantly, the MSN's morphological structure and fluorescence were found to be stable over 14 h, i.e. within relevant time scales for the executed mouse experiments. This finding is in accordance with human trials, where silica particles were found to be structurally intact after GIT passage, *i.e.* after much longer time scales and in a more realistic setting.[347] To gain insights into the intestinal retentive behavior

and biodistribution of the MSN upon oral uptake under healthy and inflammatory conditions, the differently functionalized particles were tested in a colitis mouse model *in vivo*. Upon oral gavage of a single particle dose of 100 mg kg^{-1} to healthy mice and mice with DSS-induced inflammation the MSN showed distinctively different accumulation behavior based on the grafted polymer type as analyzed via IVIS. The MSN were present in every region of the GIT including the colon already after 6 h, irrespective of the health condition and particle type, due to a steady particle flux from the stomach. However, a completely different picture could be drawn 14 h post-gavage: In healthy mice with an intact colonic mucus layer, the amount of MSN-PEG in the lower GIT was increasing over time, while, in contrast, MSN-HA contents decreased to a level about 3 times lower than their PEGylated analogues. Intriguingly, the opposite was the case for mice with induced intestinal inflammation. Colonic MSN-HA contents were strongly increasing over time by a factor of 3, while MSN-PEG amounts did not change, reflecting the pronounced accumulation and retention of MSN-HA under inflammatory conditions, and of MSN-PEG under healthy conditions. Moreover, the distinctive particle behavior was linked to differences in particle-mucus interactions on *in vitro* model epitheliums comprised of mucus and non-mucus producing cell co-cultures using confocal laser scanning microscopy. While MSN functionalized with mucus-penetrating PEG were abundant on epitheliums with and without mucus, MSN-HA were less abundant on mucus producing cells due to the diffusive barrier the layer represents to this particle type. This finding was further verified by comparison with MSN functionalized with the well-studied mucus-adhesive polymer chitosan, exhibiting the same behavior as MSN-HA, which explains the different accumulation behavior found for these particles in the *in vivo* experiments: Under healthy conditions, the mucus barrier was still intact, and the MSN-PEG were able to penetrate into/through the layer towards the epithelium, while the MSN-HA were not able to do so, resulting in fast clearance along with the intestinal flux as it is also described in literature for other nanomaterials (see chapter 1.1). Moreover, induction of intestinal inflammation was shown to alter the systemic uptake of the particles into systemic circulation. While nearly no MSN-HA were taken up into the organs, MSN-PEG contents were increased in kidneys, spleen, heart and lungs as compared to healthy animals, where only some minor uptake was observed for PEGylated particles, but not for MSN-HA. This makes MSN-PEG interesting candidates for the oral administration of drugs with the aim of systemic uptake and biodistribution. In addition, both particle types were shown to have no cytotoxic effects and that they were able to modulate the opening of TJ on model epitheliums. This may be utilized to achieve tissue uptake of small molecular drugs after local release at the intestinal wall from MSN with retentive behavior, i.e. increasing the drug bioavailability even under conditions where particles would be not absorbed into the tissue.

Overall, this study proved the potential of MSN for oral drug delivery applications and that the intestinal accumulation and retention of this nanomaterial can be tuned according to the health state, *i.e.* type of disease. Furthermore, the particle design criteria were successfully adopted by combining literature findings from many different nanomaterials research activities. Moreover, the *in vivo* results could be connected to the particle's behavior in *in vitro* cell experiments, which shows that such simpler experiments may serve as pre-screening for promising carrier properties. However, the reason for the accumulation of MSN-HA in inflamed intestinal tissue could not be sufficiently explained by these *in vitro* experiments. In literature, strong interaction with CD44 cell receptors resulting in increased cell uptake is described for HA and the overexpression of these receptors in inflamed intestinal tissue has been discussed as the reason for the inflammation-targeting properties of HA (see chapter 1.1.2). This assumption could not be verified in this work by the induction CD44 overexpression on the epithelial cell-cultures, as no differences in particle internalization was observed. Thus, further research is needed to elucidate the mechanism behind accumulation of HA under inflammatory conditions. Nevertheless, this work provides highly valuable knowledge about design criteria for MSN to fulfill requirements for effective oral drug delivery.

Further details can be found in publication I "**Surface functionalization affects the retention and biodistribution of orally administered mesoporous silica nanoparticles in a colitis mouse model.**"

Besides the oral route, intravenous injection is the main administration route aimed for drug delivery applications to cancerous tumors, and in general, the main challenge of limited bioavailability remains the same. However, for this route, limitations in bioavailability and fast systemic clearance are not due to excretion along with intestinal contents, but with the pronounced internalization of the carrier by immune cells followed by accumulation in the organs of the RES. Typically this would lead to low blood circulation times, and a narrow time window in which tumor cells would be able to internalize the particles. The testing of drug delivery platforms for their blood circulation and tumor accumulation must be done typically via *in vivo* experiments, which are time-consuming, laborious and ethically challenging. However, projects for the development of novel drug delivery concepts often start with the design of a wide range of carriers with different physicochemical properties, and to filter out most promising candidates, the numbers of *in vivo* experiments which would be necessary for this would be hardly justifiable. Thus, in this work a simple *in vitro* screening method is suggested with an increased sample throughput to model the accumulation of nanoparticles in tumors versus in organs of the defense system. For this purpose, PC-3 cancer cells and THP-1 cells representing a macrophage-like phenotype, were utilized as

models for tumor tissue and liver-resident macrophages. For this study, spherical MSN were synthesized, and further functionalized with amino of carboxy groups, as well as with covalently bound PEG or HA, to gain a set of particles of which *in vivo* data is available in the literature. The particles were thoroughly characterized using electron microscopy, nitrogen sorption, TGA, IR spectroscopy, and DLS. While the amino and PEG functionalized particles exhibited a positive zeta potential, the carboxy and HA particles were negatively charged. To connect the *in vitro* results with the extent of protein corona formation onto the particles, serum protein adsorption was examined using SDS-PAGE. MSN-COOH and MSN-NH2 adsorbed the most proteins, while the PEGylation of MSN-NH2 reduced protein adsorption. Interestingly, functionalization of MSN-NH2 with HA drastically decreased protein adsorption to levels much lower than PEG did. Overall, no signs of cytotoxicity were observed, irrespective of the particle type. The internalization of the MSN into PC-3 and THP-1 cells was examined using flow cytometry and laser scanning confocal microscopy. Importantly, to compensate for differences in fluorescence labelling efficiency, the particle's fluorescence intensities were measured beforehand to establish a weighting factor for uptake quantification – a parameter which is often not considered in literature. In the case of PC-3 cells, MSN-COOH, MSN-NH2 and MSN-PEG were internalized to the same extent, while only minor uptake of MSN-HA was observed. In general, cationic particles are reported to electrostatically interact with the phospholipids containing cell membrane, resulting in increased uptake into tumor cells as described in chapter 1.2.1. At the same time electrostatic screening effects by PC formation onto the MSN-COOH, in contrast to MSN-HA, possibly explained the high uptake into the cancer cells in the case of these particles. The internalization into THP-1 model macrophages, however, followed a different trend. While for MSN-COOH and MSN-HA no difference compared to PC-3 cells was seen, MSN-NH2 were taken up by a higher extent, while the uptake of MSN-PEG uptake was drastically reduced. Intriguingly, the different extents of macrophage uptake were virtually linear dependent on the extent of adsorption of medium sized proteins, of which albumin was the most prominent component. To evaluate the tumor targetability of such particles, the uptake ratio into PC-3 vs. THP-1 cells was calculated. MSN-NH2 showed the strongest affinity towards macrophages, while MSN-PEG and MSN-HA would be strongly associated with tumor cells in a similar manner. However, this ratio did not take the overall internalized particle amount into account, which is why a new key performance indicator (KPI) was proposed with a stronger weighting of tumor cell association. Here, a completely different picture could be drawn. MSN-PEG exhibited the highest KPI due to the high uptake into PC-3 cells, meaning that tumor association would be expected to be strongest. In contrast, MSN-HA had the lowest KPI reflecting the overall low cell uptake in general of these particles. This leads to the conclusion that, according to this screening assay, MSN-PEG would be the most favorable

candidate for tumor targeting – a conclusion that can also repeatedly be found in the literature. However, as this model is not quantitative, no conclusions could be drawn about the absolute particle amounts internalized, and therefore about their therapeutic efficiency. Furthermore, this approach should be verified by biodistribution studies in *in vivo* tumor models. Nevertheless, this method may be used as a simple screening technique for examining a wide range of particles and to rationalizes the decision of which promising candidates to chose from a broad set of particles for further in-depth examination.

Further details can be found in publication II "**Towards a simple in vitro surface chemistry pre-screening method for nanoparticles to be used for drug delivery to solid tumours.**"

2. Drug loading and formulation of MSN

Optimization of the carrier's properties to tune their *in vivo* behavior is without doubt essential for the development of functional drug delivery platforms, which is why in the first part of my thesis, the influence of passive biocomponents on the biodistribution and interaction of MSN within biological settings was demonstrated. However, other important aspects for the transition into clinical use are efficient drug loading processes and the applicability of the formulation concept. Thus, the second part of my thesis laid focus on examination of adsorption mechanisms of a peptide-based drug and the development of a straightforward formulation concept for MSN.

As many drug delivery platforms experience a rapid formation of protein corona after intravenous injection, followed by macrophage uptake, particle accumulation in the defense organs and decreasing drug concentrations in the blood stream, the overall reduction of non-specific protein adsorption is aimed for to increase the therapeutic efficiency of drug delivery platforms. Many strategies have been proposed for this purpose, among which PEGylation would probably be the most discussed one. Most of such functionalization approaches include the use of coupling moieties, organic solvents or high temperatures which may cross-react with pre-loaded drug molecules. On the other hand, drug loading post-functionalization was repeatedly shown to result in drastically reduced loading capacities (see chapter 1.3 and 2.4). Thus, a simple and straightforward formulation concept is presented to achieve both, high PEGylation degrees (plus low protein adsorption) and high drug loading levels, by using an adsorption-based strategy. For this purpose, spherical mesoporous (MSNc) and non-porous (NSNc) silica particles were synthesized. The particles had mean diameters of 156 nm and 190 nm respectively. The MSNc exhibited a specific surface area of 1117 $m^2\ g^{-1}$ and a pore diameter of 3.5 nm, while the NSNc had a specific surface area of 22 $m^2\ g^{-1}$ as determined by nitrogen sorption measurements. To examine the influence of surface functionalities on the PEG moieties, the MSN were further functionalized with a carboxy-silane (MSN-COOH). The adsorption of PEG with the two different molecular weights 2000 Da and 5000 Da (PEG_{2k} and PEG_{5k}) onto the silica nanoparticles was thoroughly studied using solvents with orthogonal polarities. Because of the polymer's good solubility in water and DCM, these solvents were used in this work. TGA is a standard means for the quantification of particle functionalization degrees. However, to exclude decisive inaccuracy in the TGA due to hydrolysis effects on the silica in this study, PEG quantification in water was done by implementation of a photometric assay based on the complexation of iodide ions with the polymer.

Adsorption isotherms recorded in water were steep revealing a very strong adsorptive strength

between the polymer and the silica, while the isotherm form in DCM was less steep. However, high amounts of PEG could be adsorbed for both solvents and molecular weights. In water, 0.19 mg m^{-2} for PEG_{2k} and 0.23 mg m^{-2} for PEG_{5k}, and in DCM 0.30 mg m^{-2} for PEG_{2k} and 0.28 mg m^{-2} for PEG_{5k} were found on the MSNc. Higher PEG quantities in DCM presumably resulted from deeper penetration of the polymer into the porous network enabled by the lower adsorptive strength. Interestingly, the PEG amounts on NSNc were clearly reversed for the two solvents indicating distinct differences in the adsorption geometry of the polymer in the outer particle surface. While the PEG chains were adsorbed as a rather flat layer in DCM, the polymer adapted a more upright conformation when adsorption took place in water. This conclusion was supported by the fact, that in water, but not in DCM, clearly higher adsorption degrees were obtained for PEG_{5k} than for PEG_{2k}, a finding which can only be understood if the chains on the outer particle surface are assumed to be oriented upright towards the solvent. In this case, the chain length is determining the mass fraction of adsorption. Moreover, these results are in line with the conclusion of the microcalorimetry studies by Trens *et al.*[342] (see chapter 2.4). Such a difference between PEG_{2k} and PEG_{5k} was also observed for the MSNc, but in a lower extent due to the rather low contribution of external surface area to the total specific surface area, and a more compact adsorption geometry in the confined pore space similar to DCM. Based on the detailed adsorption studies, the conformation on the outer particle surface in water could be precisely calculated as dense brush ($S/2R_F$ = 0.50 and 0.33 for PEG_{2k} and PEG_{5k}, respectively). Moreover, the PEG adsorption geometry was also dependent on the surface chemistry of the MSN. On carboxy-functionalized MSN-COOH the aqueous $S/2R_F$ values were calculated to be $S/2R_F$ = 1.02 and 0.69, *i.e.* mushroom-like PEG conformations. Based on these calculations, around 70 % and 90 % of the PEG on MSNc and MSN-COOH, respectively, were determined to reside within the pores when adsorbed from water, while this was the case for 92 % of PEG in DCM. These strong differences were reflected in extensive protein adsorption studies using SDS-PAGE. For this purpose, different amounts of PEG_{2k} and PEG_{5k} were adsorbed onto the silica nanoparticles, which were further incubated in fetal calf serum (FCS) to model serum protein adsorption. In general, protein adsorption was shown to be depending on the amount of adsorbed PEG and could be successfully inhibited to very low levels. This dependency was virtually linear for particles which were PEGylated in DCM due to the flat adsorption geometry of the polymer. Here, no conformational changes at increasing PEG amounts occurred and the inhibition of protein adsorption was solely dependent on the mass fraction of the adsorbed polymer. However, after PEGylation in aqueous media, a strong initial decrease of protein adsorption at low polymer amounts could be observed for the MSNc, indicating a conformational change of the adsorbed PEG chains towards a brush-like geometry with increasing PEG amounts. Such a strong decline

was not observed for MSN-COOH due to the coiled/mushroom-like nature of the adsorbed PEG layer. Overall, the protein adsorption studies nicely confirmed the assumptions and calculations made from the PEG adsorption isotherms. Moreover, by comparative examination of the protein adsorption onto porous and non-porous silica nanoparticles without PEG, the protein adsorption was shown to be solely driven by the extent of available outer surface area and that no protein adsorption within the pores took place.

Finally, these findings were expanded by a formulation concept based on drug solubility in polar and non-polar solvents. The peptide calcitonin was used as a water-soluble model drug, whereas the fluorescent dye DiI functioned as a DCM-soluble analogue. The peptide and the dye were loaded in various amount into MSNc reaching high loading levels of 9.2 wt% and 5 wt%, respectively. After drug loading in the respective solvent, the solvent was exchanged by its polar counterpart and PEGylation was performed herein. Due to the solvent change, no premature losses of drug load during the PEGylation steps were observed. While the PEG_{5k} amounts were more or less independent from DiI loading degrees, the total organic content, *i.e.* drug and PEG_{5k}, in the case of calcitonin was found to be constant, irrespective of the drug load, indicating that drug molecules and PEG_{5k} chains competed for the same adsorption sites in this case. However, in both settings the adsorbed PEG effectively inhibited serum protein adsorption onto the MSNc, suggesting that these particles would exhibit prolonged blood circulation times. All in all, this study successfully demonstrated the proof-of-concept of the suggested formulation strategy and provided detailed insight into adsorption mechanisms and conformations of PEG on silica surfaces. As the main portion of PEG was shown to reside within the pore space and to not contribute to protein adsorption inhibition, these findings can be transferred to literature studies in which high PEGylation degrees via covalent attachment were aimed for, and similar extents of protein adsorption inhibition were observed (see chapter 2.2). This raises the question if also in such studies, most of the PEG actually resided within the pores and whether the PEG was really covalently attached, or if the polymer was just physiosorbed onto the surface. This would also explain the low drug loading levels and differences in protein adsorption inhibition often observed for such particles in the literature. However, this work strengthens the understanding of protein adsorption onto silica nanoparticles and the inhibition thereof via PEGylation and provides an important initiative for the development of straightforward formulation concepts for clinical applications of MSN-based drug delivery systems.

Further details can be found in publication III “**Straightforward adsorption-based formulation of mesoporous silica nanoparticles for drug delivery applications.**”

The overall success of a drug delivery platform itself, and therefor of such a formulation concept, would depend on many aspects like the variability of functionalization types and the applicability of the formulation strategy, but also high drug loads to maximize the efficiency of the delivery system. In general, a broad variety of drugs and active components can be loaded into MSN and the parameters influencing the adsorptive interactions are copious (see chapter 2.3). This is especially the case for peptide-based drugs, which have gained a lot of attention in recent years. Thus, knowledge about peptide adsorption and how physicochemical particle characteristics influence the processes behind, is essential for the development of carriers with suitable drug loading capacities. In this work, detailed adsorption studies of the model peptide drug JM#21 onto a set of MSN with distinctive pore structures and surface characteristics were conducted. JM#21 is a small peptide with 12 amino acids and a pI of 11.2. As a novel CXCR4-antagonist it has recently gained increased attention due to its potential in several therapeutic applications, such as atopic dermatitis and airway inflammation,[323] but may also play a role in the treatment of IBD.[348] However, due to its short plasma half-life time of 6 min,[323] this peptide is predestined as a model peptide for drug delivery studies. Molecular dynamics simulations of JM#21 in different protonation states corresponding to the pH values of 2, 7, 10 and 11 revealed that the peptide adapts different conformations depending on its charge state. At pH 2 and a net charge state of +4 the peptide was elongated, while at a net charge of +3 (pH 7) a terminal loop structure was formed. At basic pH (10 and 11) and more neutrally net charged states (+1 and 0) the peptide adapted a compact form due to low intramolecular electrostatic repulsion and increasing hydrophobicity, raising its dimerization energy. Moreover, the cationic charge distribution along the peptide backbone shifted from being broadly distributed at a state +4 to being focused on the N-terminus at low charged states. This implied that the adsorption geometry on a surface could change from a flat/side-on towards an orthogonal/head-on scenario depending on the charge state and pH value. Such changes of peptide orientation upon adsorption onto 2D silica surfaces were proposed earlier by Su *et al*.[349]

However, to study the influence of confinement on peptide adsorption depending on conformation and charge state, a set of porous all-silica particles with distinctively different pore characteristics (MSNhex, DMSN, DMON_c) as well as non-porous silica nanoparticles (NSN) were synthesized. The particles had a diameter in the range of 120-200 nm and a negative surface charge at pH > 2 due to their superficial silanol groups. MSNhex exhibited a hexagonal arranged pore system and a pore diameter of 3.5 nm, while DMSN and DMON_c had dendritically aligned conical pores with a diameter of 4-12 nm and 3-20 nm, respectively. To elucidate the peptide interaction with the particles, detailed adsorption isotherms were recorded at different pH values using UV/Vis spectroscopy. In general, the overall maximum peptide loadings at pH 2 were neglectable, and at

pH 11 the isotherms adapted a flattened form, both due to low electrostatic attraction between the peptide and the silica surface. However, at pH 7 and 10 the isotherms were steep indicating strong adsorptive interactions of the cationic peptide with the negative silica surface underlining electrostatic forces as the main contributor to the adsorption. However, the influence of hydrophobic interactions under electrostatic unfavorable conditions, *i.e.* low electrostatic attraction (at pH 2) and/or intermolecular repulsion (at pH 7), could be facilitated by the introduction of organic moieties to the silica network of the particles with a dendritic pore structure (DMON).

By determination of the isotherm plateau for the NSN particles, the monolayer capacities on a fully available surface were examined and compared to the theoretical values based on the peptide dimensions from the *in silico* studies. At pH 2 and pH 7 maximum packing densities of 0.14 µmol m^{-2} and 0.24 µmol m^{-2} were measured, while the simulation studies resulted in theoretical values of 0.50 µmol m^{-2} and 0.58 µmol m^{-2} under the assumption of a flat, side-on adsorption geometry. Thus, the model underestimated the actual effective adsorption space of the highly cationic peptide molecules at these pH values, due to the strong intermolecular repulsion at these conditions. However, at pH 10 and 11 the theoretical monolayer capacities were calculated to be 0.59 µmol m^{-2} and 0.75 µmol m^{-2} under the assumption of an orthogonal/head-on adsorption geometry. The calculations fitted nicely to the experimentally measured maximum packing densities of 0.66 µmol m^{-2} and 0.74 µmol m^{-2}. These values were higher than at pH 2 and pH 7 due to a balanced relation between electrostatic attraction to the surface and low intra- and intermolecular repulsion, and consequently a more compact effective peptide size. The preference of a head-on adsorption geometry at basic pH can be explained by the shifted cationic charge distribution along the peptide backbone. Interestingly, the measured peptide loading at pH 11 exceeded that at pH 10 and no distinct plateau was observed despite the lower electrostatic attraction to the silica surface. This may be explained by the increased tendency of the peptide to form dimers and the possibility of higher packing densities due to the low intermolecular repulsion.

However, the different pore structures and sizes of MSN, DMSN and DMON_c altered the peptide adsorption in a distinctive manner: While the isotherms for pH ≥ 7 were again initially steep, indicating electrostatic contributions as the main force, the transition phase as well as the plateau values were different. At pH 7 the maximum loading degrees were similar, irrespective of the pore size and slightly lower than on the NSN, indicating only minor limiting effects by pore confinement in this case. Here, the packing density was mainly governed by the effective adsorption area which the peptide would require on the surface. Similar to NSN, the packing densities at pH 10 were increased compared to pH 7 due to the smaller effective size of the peptide. However, differences depending on the pore structure were observed. The small pores of MSNhex decreased the maximum packing density compared to NSN due to pronounced confinement effects on the

naturally favored head-on adsorption geometry on flat surfaces. In contrast to MSNhex, the large-pore DMSN and DMON_c particles reached no distinct adsorption plateau but showed a flat transition of the initial steep isotherm into a more linear form. Such a deviation from an ideal Langmuir isotherm may arise from conformational or orientational changes of a peptide when approaching the maximum surface coverage as previously suggested by Latour.[350] In this case, this indicated a progressive conformational re-arrangement of the adsorbed peptide as the loading concentration increased – a process which was enabled by the larger pore space. The measured packing densities for these particles were again lower than for NSN, but clearly higher than for MSNhex, and ranged between the theoretical side-on and head-on scenario. This indicated that the effect of confinement here was not as strong as for the small-pore particles, and thus was directly corelated with pore diameter and pore curvature. At pH 11 pore size limiting effects were even more pronounced as the peptide tended to aggregate due to low intermolecular repulsion, and its effective adsorption space increased. This led to strongly decreased packing densities on the porous particles as compared to the NSN, even below the theoretical side-on scenario. The large-pore particles offered higher accessibility for the peptide and its conformational changes, which was reflected by a higher packing density and a more linear isotherm form as compared to MSNhex. Moreover, for MSNhex and DMSN, but not for DMON_c, the maximum packing densities were lower than those at pH 10, potentially indicating a pore size dependent exclusion effect on the adsorption of peptide dimers/aggregates.

Furthermore, peptide adsorption was shown to be independent of the pore connectivity to the surrounding medium since spherical particles with either hexagonally (MSNhex) or radially (MSNrad) arranged pores, as well as elongated particles (MSN-rod), exhibited comparable maximum loading degrees.

Finally, the protective effect against pre-mature degradation was proven by using a cell-based activity assay. Compared to the unstable free peptide, the biological activity of the peptide when loaded into DMSN or MSNhex was increased by a factor of 2. Overall, this study combines results from modeling and experimental approaches to provide a holistic view on peptide adsorption mechanisms onto silica nanoparticles which can be influenced by many parameters, like electrostatic and hydrophobic interactions, pore confinement, peptide conformation and charge. Based on these findings, adsorption parameters and particle characteristics can be identified to enable efficient drug loading. Furthermore, this knowledge may be transferred to all kinds of different peptide-based drugs and their loading into mesoporous silica nanoparticles.

Further details can be found in publication IV "**Confinement and polarity effects on the peptide packing density on mesoporous silica nanoparticles.**"

IV Conclusion and outlook

Nano-scaled drug delivery platforms promise to overcome many barriers in the way to effective and efficient therapies, which are often limited by poor bioavailability and uncontrolled biodistribution, as well as fast systemic clearance of highly potent, and in the case of peptides, often labile drugs. In this field of research many different material types (for example metals, polymers, liposomes) have been synthesized and further modified according to the distinct requirements a drug carrier needs to fulfill dependent on the application. Typically, newly synthesized nanomaterials are studied under different aspects such as formulation and drug loading capabilities, uptake behavior in *in vitro* cell cultures, and distribution and accumulation in *in vivo* animal models. However, only few candidates make their way into clinical trials, which may be due to labor, time and cost-intensive testing necessary for every single material type. In order to accelerate this process, translational concepts are needed concerning formulation and drug loading, cell-based screening assays and design considerations for new delivery platforms.
Such a delivery platform is mesoporous silica nanoparticles. In general, this material class offers distinct benefits compared other nanoparticle types. They can be synthesized in all kinds of different sizes and shapes and their surface charge can be adjusted easily by the introduction of functional groups (for example amines or carboxylic acids) to the synthesis solution. In addition, further modification with passive biocomponents like stealth polymers according to the requirements of different fields of application can be achieved by a broad set of post-grafting and coupling chemistries. Furthermore, active biocomponents, *i.e.* therapeutic drugs, can be loaded at high capacities into the MSN due to their tunable pore size, volume and structure. Finally, silica nanoparticles are biodegradable and biocompatible, and, in general, well-tolerated.

Within this thesis four articles focusing on the synthesis, functionalization, drug loading and biological testing of MSN are presented. As oral and intravenous injection are the two most common administration routes for drug delivery systems, the first part of my thesis laid focus on the testing of various MSN in biological models thereof.
Based on translational design criteria, elongated MSN were synthesized and optimized for increased intestinal transit times through the GIT. The particle's intestinal retention and distribution were investigated using an *in vivo* mouse model and was shown to be a function of functionalization type as well as of the health status of the mice. While PEGylated MSN showed affinity towards healthy colonic tissue, HA functionalized particles were accumulating in inflamed tissue, making these particles promising candidates for the treatment of inflammatory diseases

like IBD. However, in contrast to many studies in literature, this work also focused on the particle's distribution within the internal organs after oral administration. Here, colonic inflammation promoted the uptake of the PEGylated MSN into systemic circulation indicating that a combinational therapy consisting of both particle types may be promising. Moreover, the differences in intestinal biodistribution observed in the *in vivo* experiments were reflected by *in vitro* experiments utilizing mucus and non-mucus producing cell co-cultures. The conclusive connection between *in vivo* and *in vitro* experiments demonstrates the usefulness of such cell models for testing and screening purposes and may help to reduce the number of animal experiments. Overall, this work provides a brought insight into the biodistribution of orally administered MSN and identifies particle types with high potential for oral drug delivery. However, as this study was limited to a semi-quantitative approach, no statement about absolute particle amounts and the exact localization of the particles within the intestinal tissues could be drawn. This information would be needed for future oral drug delivery experiments, including formulation and release studies – information which could be provided by more quantitative means like positron emission tomography.

To transfer novel drug delivery concepts into the clinics, extensive testing of the drug carrier must be conducted concerning different aspects of applicability, such as the exclusion of (cyto-) toxicity and unwanted side effects. To ensure the effectiveness of the carrier, knowledge about its biodistribution and blood circulation time upon intravenous injection, as well as about the internalization into the target cells/tissue is needed. For such investigations *in vivo* studies are often used, where the particle contents in the liver and the tumor upon intravenous injection would be measured as indicator for the particle's blood circulation time and tumor tissue accumulation. In this work, a simple experimental setup is proposed to screen for particles which may exhibit suitable properties for intravenous drug delivery, *i.e.* long blood circulation and at the same time high uptake by cancer cells. For this purpose, the particle internalization into the two cell lines THP-1 and PC-3 was examined. Importantly, the differences in particle uptake into the macrophage model cell line could be directly connected to differences in the extent of protein serum adsorption onto the particles, while uptake into cancer cells was mainly driven by particle charge. Moreover, by putting the extent of internalization into both cell lines in relation to each other, statements about the tumor targetability of the particles could be drawn and were compared to similar findings from previous *in vivo* studies from literature. However, as this model is not quantitative, no conclusions can be made about the absolute particle amounts, and therefore about the therapeutic efficiency of the potential drug delivery system. Furthermore, the proposed model should be complemented by detailed biodistribution studies in *in vivo* tumor models in future work.

As evident from this study, the internalization of MSN into macrophages and therefore their blood circulation time depends on serum protein adsorption, which is why avoiding protein adsorption is one of the major challenges in the field of drug delivery. However, as described in chapter 1.3 functionalization with moieties inhibiting protein adsorption often comes with loss of drug loading efficiency and effectiveness, which is critical for the success and applicability of novel drug delivery systems in the clinics. Thus in the second part of my thesis, focus was laid on the development of a straightforward adsorption-based formulation concept as well as on adsorption studies of a peptide-based drug.

First, the adsorption of PEG with two different molecular weights onto silica nanoparticles was studied in detail. By recording adsorption isotherms in water and DCM conclusions could be drawn on the conformation and adsorption geometry of the polymer depending on the solvent polarity, PEG localization, particle surface functionalization and polymer amount. While in DCM the PEG adsorbed in a flat form, an upright brush-like conformation was calculated for PEG on the outer particle surface after adsorption in aqueous media. Moreover, these differences in PEG conformation were confirmed by extensive protein adsorption studies. Intriguingly, the PEG adsorption kinetics were fast, and most of the polymer was shown to be located within the pore system. In addition, only the external PEG layer contributed to protein adsorption inhibition to levels comparable with literature findings. These findings may also explain the low drug loading degrees often reported in literature at high PEGylation degrees. To prevent preliminary drug desorption, the herein proposed formulation concept was based on cross-polarity of the used solvents. With this approach MSN were loaded with high amounts of drugs, and at the same time equipped with a PEG layer effectively shielding the carrier against serum protein adsorption, proving the functionality of this novel concept. Overall, this study elucidates the factors influencing conformational states of PEG on MSN and the consequences to protein adsorption inhibition, which has important implications on PEGylation approaches of drug carriers in general and of MSN in particular. In future work, these findings should be complemented by experiments examining the influence of the polymer conformation as well as the inside-outside PEG distribution on blood circulation times *in vivo,* as well as on drug release kinetics to transfer this formulation concept to clinical applications.

Besides applicability of formulation concepts, efficient and effective drug loading procedures are decisive for the success of a novel drug transporter. Hence, detailed adsorption studies of the peptide-based drug JM#21 onto different silica nanoparticles were conducted. Adsorption isotherms at different pH values showed that the adsorptive strength is mainly governed by electrostatic attraction between the peptide and the silica support, as well as on inter- and intramolecular charge-mediated repulsion. In addition, peptide adsorption was shown to be

dependent on the pore characteristics, indicating confinement effects on the peptide's adsorption geometry. The experimental results were supplemented by *in silico* modelling of the peptide conformation at varying charge states. Finally, the protection of the loaded peptides against enzymatic degradation was demonstrated with an *in vitro* cell assay. Here, the loaded drug outperformed the rapidly degrading free peptide. Overall these results underline the potential of MSN as carrier platform for peptide-based drugs and give guidelines for the optimization of peptide loading procedures in general. The transferability to other peptide-based drugs should be further validated by comparative studies with agents differing in size, charge, and hydrophobicity, to establish a toolbox of loading protocols adjustable to the distinctive properties of any peptide chosen for the respective drug delivery application.

All in All, the presented thesis is focused on several important aspects of drug delivery research: Optimization of carrier properties for specific applications, testing of MSN in biological settings, as well as drug loading and formulation studies. Each study provides important knowledge about these aspects, which may be transferred and applied in future work, with the goal to pave the way of MSN as a highly promising drug delivery platform into the clinics.

V References

1. Padín-González, E. *et al.* Understanding the Role and Impact of Poly (Ethylene Glycol) (PEG) on Nanoparticle Formulation: Implications for COVID-19 Vaccines. *Front. Bioeng. Biotechnol.* **10**, (2022).

2. Yetisgin, A. A. & Sibel, Cetinel; Merve, Zuvin; Ali, Kosar and Ozlem, K. *Therapeutic Nanoparticles and Their Targeted Delivery Applications*. *Molecules* vol. 25 (2020).

3. Abeer, M. M. *et al.* Silica nanoparticles: A promising platform for enhanced oral delivery of macromolecules. *J. Control. Release* **326**, 544–555 (2020).

4. Florek, J., Caillard, R. & Kleitz, F. Evaluation of Mesoporous Silica Nanoparticles for Oral Drug Delivery – Current status and perspective of MSNs drug carriers. *Nanoscale* **9**, 15252–15277 (2017).

5. Homayun, B., Lin, X. & Choi, H. J. Challenges and recent progress in oral drug delivery systems for biopharmaceuticals. *Pharmaceutics* **11**, (2019).

6. Batista, P., Castro, P. M., Madureira, A. R., Sarmento, B. & Pintado, M. Recent insights in the use of nanocarriers for the oral delivery of bioactive proteins and peptides. *Peptides* **101**, 112–123 (2018).

7. Yun, Y., Woo, Y. & Park, K. Nanoparticles for oral delivery : Targeted nanoparticles with peptidic ligands for oral protein delivery. *Adv. Drug Deliv. Rev.* **65**, 822–832 (2013).

8. González-Mariscal, L., Betanzos, A., Nava, P. & Jaramillo, B. E. Tight junction proteins. *Prog. Biophys. Mol. Biol.* **81**, 1–44 (2003).

9. Gagnon, M., Zihler Berner, A., Chervet, N., Chassard, C. & Lacroix, C. Comparison of the Caco-2, HT-29 and the mucus-secreting HT29-MTX intestinal cell models to investigate Salmonella adhesion and invasion. *J. Microbiol. Methods* **94**, 274–279 (2013).

10. Wang, F. *et al.* Interferon-γ and tumor necrosis factor-α synergize to induce intestinal epithelial barrier dysfunction by up-regulating myosin light chain kinase expression. *Am. J. Pathol.* **166**, 409–419 (2005).

11. Zolotarevsky, Y. *et al.* A membrane-permeant peptide that inhibits MLC kinase restores barrier function in in vitro models of intestinal disease. *Gastroenterology* **123**, 163–172

(2002).

12. Clayburgh, D. R. *et al.* Epithelial myosin light chain kinase-dependent barrier dysfunction mediates T cell activation-induced diarrhea in vivo. *J. Clin. Invest.* **115**, 2702–2715 (2005).

13. Turner, J. R., Buschmann, M. M., Romero-Calvo, I., Sailer, A. & Shen, L. The role of molecular remodeling in differential regulation of tight junction permeability. *Semin. Cell Dev. Biol.* **36**, 204–212 (2014).

14. Per, A., Tuulikki, L., S., D. S. & Lisbeth, I. Effects of Chitosan on the Permeability of Monolayers of Intestinal Epithelial Cells. *Pharm. Res.* **11**, 1358–1361 (1994).

15. Kotzé, A. F. *et al.* Comparison of the effect of different chitosan salts and N-trimethyl chitosan chloride on the permeability of intestinal epithelial cells (Caco-2). *J. Control. Release* **51**, 35–46 (1998).

16. Thanou, M. M. *et al.* Effect of degree of quaternization of N-trimethyl chitosan chloride for enhanced transport of hydrophilic compounds across intestinal Caco-2 cell monolayers. *J. Control. Release* **64**, 15–25 (2000).

17. Thanou, M., Florea, B. I., Langemeÿer, M. W. E., Verhoef, J. C. & Junginger, H. E. N-trimethylated chitosan chloride (tmc) improves the intestinal permeation of the peptide drug buserelin in vitro (caco-2 cells) and in vivo (rats). *Pharm. Res.* **17**, 27–31 (2000).

18. Jevprasesphant, R., Penny, J., Attwood, D., McKeown, N. B. & D'Emanuele, A. Engineering of Dendrimer Surfaces to Enhance Transepithelial Transport and Reduce Cytotoxicity. *Pharm. Res.* **20**, 1543–1550 (2003).

19. Lin, Y. *et al.* Polyamidoamine dendrimers as novel potential absorption enhancers for improving the small intestinal absorption of poorly absorbable drugs in rats. *J. Control. Release* **149**, 21–28 (2011).

20. Ranaldi, G., Marigliano, I., Vespignani, I., Perozzi, G. & Sambuy, Y. The effect of chitosan and other polycations on tight junction permeability in the human intestinal Caco-2 cell line. *J. Nutr. Biochem.* **13**, 157–167 (2002).

21. Loo, Y. *et al.* Comparative study of nanoparticle-mediated transfection in different GI epithelium co-culture models. *J. Control. Release* **160**, 48–56 (2012).

22. Cao, Y. *et al.* Virus-like silica nanoparticles enhance macromolecule permeation in vivo. *Biomater. Sci.* **13**, 4508–4521 (2023).

23. Cornu, R., Chrétien, C., Pellequer, Y., Martin, H. & Béduneau, A. Small silica nanoparticles transiently modulate the intestinal permeability by actin cytoskeleton disruption in both Caco-2 and Caco-2/HT29-MTX models. *Arch. Toxicol.* **94**, 1191–1202 (2020).

24. Lamson, N. G., Berger, A., Fein, K. C. & Whitehead, K. A. Anionic nanoparticles enable the oral delivery of proteins by enhancing intestinal permeability. *Nat. Biomed. Eng.* **4**, 84–96 (2019).

25. Lai, S. K., Wang, Y. Y. & Hanes, J. Mucus-penetrating nanoparticles for drug and gene delivery to mucosal tissues. *Adv. Drug Deliv. Rev.* **61**, 158–171 (2009).

26. Leal, J., Smyth, H. D. C. & Ghosh, D. Physicochemical properties of mucus and their impact on transmucosal drug delivery. *Int. J. Pharm.* **532**, 555–572 (2017).

27. Atuma, C., Strugala, V., Allen, A. & Holm, L. The adherent gastrointestinal mucus gel layer: Thickness and physical state in vivo. *Am. J. Physiol. - Gastrointest. Liver Physiol.* **280**, 922–929 (2001).

28. Lundquist, P. & Artursson, P. Oral absorption of peptides and nanoparticles across the human intestine: Opportunities, limitations and studies in human tissues. *Adv. Drug Deliv. Rev.* **106**, 256–276 (2016).

29. Lock, J. Y., Carlson, T. L. & Carrier, R. L. Mucus models to evaluate the diffusion of drugs and particles. *Adv. Drug Deliv. Rev.* **124**, 34–49 (2018).

30. Murgia, X. *et al.* Size-Limited Penetration of Nanoparticles into Porcine Respiratory Mucus after Aerosol Deposition. *Biomacromolecules* **17**, 1536–1542 (2016).

31. Schuster, B., Suk, J., Woodworth, G. & Hanes, J. Nanoparticle diffusion in respiratory mucus from humans without lung disease. *Biomaterials* **34**, 3439–3446 (2013).

32. Dawson, M., Wirtz, D. & Hanes, J. Enhanced Viscoelasticity of Human Cystic Fibrotic Sputum Correlates with Increasing Microheterogeneity in Particle Transport. *J. Biol. Chem.* **278**, 50393–50401 (2003).

33. Sanders, N. N. *et al.* Cystic fibrosis sputum: A barrier to the transport of nanospheres. *Am. J. Respir. Crit. Care Med.* **162**, 1905–1911 (2000).

34. Ensign, L. M. *et al.* Ex vivo characterization of particle transport in mucus secretions coating freshly excised mucosal tissues. *Mol. Pharm.* **10**, 2176–2182 (2013).

35. Bhattacharjee, S. *et al.* Nanoparticle passage through porcine jejunal mucus: Microfluidics

and rheology. *Nanomedicine Nanotechnology, Biol. Med.* **13**, 863–873 (2017).

36. Cu, Y. & Saltzman, W. Controlled surface modification with poly(ethylene)glycol enhances diffusion of PLGA nanoparticles in human cervical mucus. *Mol. Pharm.* **6**, 173–181 (2009).

37. Lai, S. K. *et al.* Rapid transport of large polymeric nanoparticles in fresh undiluted human mucus. *Proc. Natl. Acad. Sci. U. S. A.* **104**, 1482–1487 (2007).

38. Xu, Q. *et al.* Impact of Surface Polyethylene Glycol (PEG) Density on Biodegradable Nanoparticle Transport in Mucus ex Vivo and Distribution in Vivo. *ACS Nano* **9**, 9217–9227 (2015).

39. Yu, T. *et al.* Biodegradable mucus-penetrating nanoparticles composed of diblock copolymers of polyethylene glycol and poly(lactic-co-glycolic acid). *Drug Deliv. Transl. Res.* **2**, 124–128 (2012).

40. Maisel, K., Ensign, L., Reddy, M., Cone, R. & Hanes, J. Effect of surface chemistry on nanoparticle interaction with gastrointestinal mucus and distribution in the gastrointestinal tract following oral and rectal administration in the mouse. *J. Control. Release* **197**, 48–57 (2015).

41. Schneider, C. S. *et al.* Nanoparticles that do not adhere to mucus provide uniform and long-lasting drug delivery to airways following inhalation. *Sci. Adv.* **3**, (2017).

42. Popov, A., Schopf, L., Bourassa, J. & Chen, H. Enhanced pulmonary delivery of fluticasone propionate in rodents by mucus-penetrating nanoparticles. *Int. J. Pharm.* **502**, 188–197 (2016).

43. Wang, Y. Y. *et al.* Addressing the PEG mucoadhesivity paradox to engineer nanoparticles that ‘slip’ through the human mucus barrier. *Angew. Chemie - Int. Ed.* **47**, 9726–9729 (2008).

44. Murgia, X., Loretz, B., Hartwig, O., Hittinger, M. & Lehr, C. M. The role of mucus on drug transport and its potential to affect therapeutic outcomes. *Adv. Drug Deliv. Rev.* **124**, 82–97 (2018).

45. Iqbal, J. *et al.* Preactivated thiomers as mucoadhesive polymers for drug delivery. *Biomaterials* **33**, 1528–1535 (2012).

46. Mao, Y. *et al.* Thiolated polymer and Cell-Penetrating Peptide dual-surface functionalization of mesoporous silicon nanoparticles to overcome intestinal barriers. *J. Drug Deliv. Sci.*

Technol. **53**, 101184 (2019).

47. Dünnhaupt, S. *et al.* Distribution of thiolated mucoadhesive nanoparticles on intestinal mucosa. *Int. J. Pharm.* **408**, 191–199 (2011).

48. Lehr, C. M., Bouwstra, J. A., Schacht, E. H. & Junginger, H. E. In vitro evaluation of mucoadhesive properties of chitosan and some other natural polymers. *Int. J. Pharm.* **78**, 43–48 (1992).

49. Bravo-Osuna, I., Vauthier, C., Farabollini, A., Palmieri, G. F. & Ponchel, G. Mucoadhesion mechanism of chitosan and thiolated chitosan-poly(isobutyl cyanoacrylate) core-shell nanoparticles. *Biomaterials* **28**, 2233–2243 (2007).

50. Andreani, T. *et al.* Effect of mucoadhesive polymers on the in vitro performance of insulin-loaded silica nanoparticles: Interactions with mucin and biomembrane models. *Eur. J. Pharm. Biopharm.* **93**, 118–126 (2015).

51. Takeuchi, H. *et al.* Novel mucoadhesion tests for polymers and polymer-coated particles to design optimal mucoadhesive drug delivery systems. *Adv. Drug Deliv. Rev.* **57**, 1583–1594 (2005).

52. Sogias, I. A., Williams, A. C. & Khutoryanskiy, V. V. Why is chitosan mucoadhesive? *Biomacromolecules* **9**, 1837–1842 (2008).

53. Collado-González, M., Espinosa, Y. G. & Goycoolea, F. M. Interaction between Chitosan and Mucin: Fundamentals and applications. *Biomimetics* **4**, 1–20 (2019).

54. Elsayed, A., Al-Remawi, M., Maghrabi, I., Hamaidi, M. & Jaber, N. Development of insulin loaded mesoporous silica injectable particles layered by chitosan as a controlled release delivery system. *Int. J. Pharm.* **461**, 448–458 (2014).

55. Liu, W. T. *et al.* Facile and simple preparation of pH-sensitive chitosan-mesoporous silica nanoparticles for future breast cancer treatment. *Express Polym. Lett.* **9**, 1068–1075 (2015).

56. Chen, F. & Zhu, Y. Chitosan enclosed mesoporous silica nanoparticles as drug nano-carriers: Sensitive response to the narrow pH range. *Microporous Mesoporous Mater.* **150**, 83–89 (2012).

57. Popat, A., Liu, J., Lu, G. Q. (Max) & Qiao, S. Z. A pH-responsive drug delivery system based on chitosan coated mesoporous silica nanoparticles. *J. Mater. Chem.* **22**, 11173

(2012).

58. Abeer, M. M. *et al.* Rationally Designed Dendritic Silica Nanoparticles for Oral Delivery of Exenatide. *Pharmaceutics* **11**, 1–16 (2019).

59. das Neves, J., Amiji, M. & Sarmento, B. Mucoadhesive nanosystems for vaginal microbicide development: Friend or foe? *Wiley Interdiscip. Rev. Nanomedicine Nanobiotechnology* **3**, 389–399 (2011).

60. Ensign, L. M., Cone, R. & Hanes, J. Oral drug delivery with polymeric nanoparticles: The gastrointestinal mucus barriers. *Adv. Drug Deliv. Rev.* **64**, 557–570 (2012).

61. Johansson, M. E. V. Fast renewal of the distal colonic mucus layers by the surface goblet cells as measured by in vivo labeling of mucin glycoproteins. *PLoS One* **7**, (2012).

62. Lehr, C. M., Poelma, F. G. J., Junginger, H. E. & Tukker, J. J. An estimate of turnover time of intestinal mucus gel layer in the rat in situ loop. *Int. J. Pharm.* **70**, 235–240 (1991).

63. Wang, Y. *et al.* Effects of surface modification and size on oral drug delivery of mesoporous silica formulation. *J. Colloid Interface Sci.* **513**, 736–747 (2018).

64. Lautenschläger, C., Schmidt, C., Lehr, C. M., Fischer, D. & Stallmach, A. PEG-functionalized microparticles selectively target inflamed mucosa in inflammatory bowel disease. *Eur. J. Pharm. Biopharm.* **85**, 578–586 (2013).

65. Maisel, K. *et al.* Nanoparticles coated with high molecular weight PEG penetrate mucus and provide uniform vaginal and colorectal distribution in vivo. *Nanomedicine* **11**, 1337–1343 (2016).

66. Desai, D. *et al.* Targeted modulation of cell differentiation in distinct regions of the gastrointestinal tract via oral administration of differently PEG-PEI functionalized mesoporous silica nanoparticles. *Int. J. Nanomedicine* **11**, 299–313 (2016).

67. Li, L. *et al.* Biodistribution, excretion, and toxicity of mesoporous silica nanoparticles after oral administration depend on their shape. *Nanomedicine Nanotechnology, Biol. Med.* **11**, 1915–1924 (2015).

68. Zhao, Y. *et al.* A comparison between sphere and rod nanoparticles regarding their in vivo biological behavior and pharmacokinetics. *Sci. Rep.* **7**, 1–11 (2017).

69. Alatab, S. *et al.* The global, regional, and national burden of inflammatory bowel disease in 195 countries and territories, 1990–2017: a systematic analysis for the Global Burden of

Disease Study 2017. *Lancet Gastroenterol. Hepatol.* **5**, 17–30 (2020).

70. Volpato, E. *et al.* The evolution of IBD perceived engagement and care needs across the life-cycle: a scoping review. *BMC Gastroenterol.* **21**, 1–17 (2021).

71. Cai, Z., Wang, S. & Li, J. Treatment of Inflammatory Bowel Disease: A Comprehensive Review. *Front. Med.* **8**, 1–24 (2021).

72. Seyedian, S. S., Nokhostin, F. & Malamir, M. D. A review of the diagnosis, prevention, and treatment methods of inflammatory bowel disease. *J. Med. Life* **12**, 113–122 (2019).

73. Tirosh, B., Khatib, N., Barenholz, Y., Nissan, A. & Rubinstein, A. Transferrin as a luminal target for negatively charged liposomes in the inflamed colonic mucosa. *Mol. Pharm.* **6**, 1083–1091 (2009).

74. Peterson, C. G. B., Eklund, E., Taha, Y., Raab, Y. & Carlson, M. A new method for the quantification of neutrophil and eosinophil cationic proteins in feces: Establishment of normal levels and clinical application in patients with inflammatory bowel disease. *Am. J. Gastroenterol.* **97**, 1755–1762 (2002).

75. Wittig, B. M., Johansson, B., Zöller, M., Schwärzler, C. & Günthert, U. Abrogation of experimental colitis correlates with increased apoptosis in mice deficient for CD44 variant exon 7 (CD44v7). *J. Exp. Med.* **191**, 2053–2063 (2000).

76. Wittig, B. M., Stallmach, A., Zeitz, M. & Günthert, U. Functional involvement of CD44 variant 7 in gut immune response. *Pathobiology* **70**, 184–189 (2003).

77. Stenson, W. F. Hyaluronic acid and intestinal inflammation. *Curr. Opin. Gastroenterol.* **26**, 85–87 (2010).

78. Abd-Rabou, A. A., Abdelaziz, A. M., Shaker, O. G. & Ayeldeen, G. Hyaluronated nanoparticles deliver raloxifene to CD44-expressed colon cancer cells and regulate lncRNAs/miRNAs epigenetic cascade. *Cancer Nanotechnol.* **14**, 1–23 (2023).

79. Yang, C. *et al.* Hyaluronic acid nanogels with enzyme-sensitive cross-linking group for drug delivery. *J. Control. Release* **205**, 206–217 (2015).

80. Yu, M. *et al.* Hyaluronic acid modified mesoporous silica nanoparticles for targeted drug delivery to CD44-overexpressing cancer cells. *Nanoscale* **5**, 178–183 (2013).

81. Chen, Z. *et al.* Bioresponsive hyaluronic acid-capped mesoporous silica nanoparticles for targeted drug delivery. *Chem. - A Eur. J.* **19**, 1778–1783 (2013).

82. Vafaei, S. Y. *et al.* Self assembled hyaluronic acid nanoparticles as a potential carrier for targeting the inflamed intestinal mucosa. *Carbohydr. Polym.* **144**, 371–381 (2016).

83. Chiu, C. T., Kuo, S. N., Hung, S. W. & Yang, C. Y. Combined treatment with hyaluronic acid and mesalamine protects rats from inflammatory bowel disease induced by intracolonic administration of trinitrobenzenesulfonic acid. *Molecules* **22**, 1–24 (2017).

84. Xiao, B. *et al.* Orally Targeted Delivery of Tripeptide KPV via Hyaluronic Acid-Functionalized Nanoparticles Efficiently Alleviates Ulcerative Colitis. *Mol. Ther.* **25**, 1628–1640 (2017).

85. Li, W. *et al.* Hierarchical structured and programmed vehicles deliver drugs locally to inflamed sites of intestine. *Biomaterials* **185**, 322–332 (2018).

86. Xavier, M., García-Hevia, L., Amado, I. R., Pastrana, L. & Gonçalves, C. In vitro intestinal uptake and permeability of fluorescently-labelled hyaluronic acid nanogels. *Int. J. Nanomedicine* **14**, 9077–9088 (2019).

87. Blanco, E., Shen, H. & Ferrari, M. Principles of nanoparticle design for overcoming biological barriers to drug delivery. *Nat. Biotechnol.* **33**, 941–951 (2015).

88. Kulkarni, S. A. & Feng, S. S. Effects of particle size and surface modification on cellular uptake and biodistribution of polymeric nanoparticles for drug delivery. *Pharm. Res.* **30**, 2512–2522 (2013).

89. Shima, F., Uto, T., Akagi, T., Baba, M. & Akashi, M. Size effect of amphiphilic poly(γ-glutamic acid) nanoparticles on cellular uptake and maturation of dendritic cells in vivo. *Acta Biomater.* **9**, 8894–8901 (2013).

90. Li, K. & Schneider, M. Quantitative evaluation and visualization of size effect on cellular uptake of gold nanoparticles by multiphoton imaging-UV/Vis spectroscopic analysis. *J. Biomed. Opt.* **19**, 101505 (2014).

91. Arnida, Malugin, A. & Ghandehari, H. Cellular uptake and toxicity of gold nanoparticles in prostate cancer cells: A comparative study of rods and spheres. *J. Appl. Toxicol.* **30**, 212–217 (2010).

92. Chithrani, B. D., Ghazani, A. A. & Chan, W. C. W. Determining the size and shape dependence of gold nanoparticle uptake into mammalian cells. *Nano Lett.* **6**, 662–668 (2006).

93. Lu, F., Wu, S. H., Hung, Y. & Mou, C. Y. Size effect on cell uptake in well-suspended, uniform mesoporous silica nanoparticles. *Small* **5**, 1408–1413 (2009).

94. Varela, J. A., Mariana G. Bexiga, C. Å., Simpson, J. C. & Dawson, K. A. Quantifying size-dependent interactions between fluorescently labeled polystyrene nanoparticles and mammalian cells. Additional Information. *J. Nanobiotechnology* **10**, (2012).

95. Huang, J. *et al.* Effects of nanoparticle size on cellular uptake and liver MRI with polyvinylpyrrolidone-coated iron oxide nanoparticles. *ACS Nano* **4**, 7151–7160 (2010).

96. Xu, A. *et al.* A physical model for the size-dependent cellular uptake of nanoparticles modified with cationic surfactants. *Int. J. Nanomedicine* **7**, 3547–3554 (2012).

97. Dos Santos, T., Varela, J., Lynch, I., Salvati, A. & Dawson, K. A. Quantitative assessment of the comparative nanoparticle-uptake efficiency of a range of cell lines. *Small* **7**, 3341–3349 (2011).

98. He, C., Hu, Y., Yin, L., Tang, C. & Yin, C. Effects of particle size and surface charge on cellular uptake and biodistribution of polymeric nanoparticles. *Biomaterials* **31**, 3657–3666 (2010).

99. Huang, X., Teng, X., Chen, D., Tang, F. & He, J. The effect of the shape of mesoporous silica nanoparticles on cellular uptake and cell function. *Biomaterials* **31**, 438–448 (2010).

100. Huang, X. *et al.* The shape effect of mesoporous silica nanoparticles on biodistribution, clearance, and biocompatibility in vivo. *ACS Nano* **5**, 5390–5399 (2011).

101. Champion, J. A. & Mitragotri, S. Role of target geometry in phagocytosis. *Proc. Natl. Acad. Sci. U. S. A.* **103**, 4930–4934 (2006).

102. Yu, T., Hubbard, D., Ray, A. & Ghandehari, H. In vivo biodistribution and pharmacokinetics of silica nanoparticles as a function of geometry, porosity and surface characteristics. *J. Control. Release* **163**, 46–54 (2012).

103. Gentile, F. *et al.* The effect of shape on the margination dynamics of non-neutrally buoyant particles in two-dimensional shear flows. *J. Biomech.* **41**, 2312–2318 (2008).

104. Albanese, A., Tang, P. S. & Chan, W. C. W. The effect of nanoparticle size, shape, and surface chemistry on biological systems. *Annu. Rev. Biomed. Eng.* **14**, 1–16 (2012).

105. Kou, L. *et al.* Transporter-guided delivery of nanoparticles to improve drug permeation across cellular barriers and drug exposure to selective cell types. *Front. Pharmacol.* **9**, 1–

16 (2018).

106. Fröhlich, E. The role of surface charge in cellular uptake and cytotoxicity of medical nanoparticles. *Int. J. Nanomedicine* **7**, 5577–5591 (2012).

107. Alexis, F., Pridgen, E., Molnar, L. & Farokhzad, O. Factors affecting the clearance and biodistribution of polymeric nanoparticles. *Mol. Pharm.* **5**, 505–515 (2008).

108. Rosenholm, J. M. *et al.* Targeting of Porous Hybrid Silica Nanoparticles to Cancer Cells. *ACS Nano* **3**, 197–206 (2009).

109. Jambhrunkar, S. *et al.* Effect of surface functionality of silica nanoparticles on cellular uptake and cytotoxicity. *Mol. Pharm.* **11**, 3642–3655 (2014).

110. Heuts, J., Jiskoot, W., Ossendorp, F. & Maaden, K. Van Der. Cationic Nanoparticle-Based Cancer Vaccines. *Pharmaceutics* **13**, (2021).

111. Panariti, A., Miserocchi, G. & Rivolta, I. The effect of nanoparticle uptake on cellular behavior : disrupting or enabling functions ? *Nanotechnol. Sci. Appl.* **5**, 87–100 (2012).

112. Slowing, I., Trewyn, B. G. & Lin, V. S.-Y. Effect of Surface Functionalization of MCM-41-Type Mesoporous Silica Nanoparticles on the Endocytosis by Human Cancer Cells. *J. Am. Chem. Soc.* **128**, 14792–14793 (2006).

113. Thorek, D. L. J. & Tsourkas, A. Size, charge and concentration dependent uptake of iron oxide particles by non-phagocytic cells. *Biomaterials* **29**, 3583–3590 (2008).

114. Thurston, G. *et al.* Cationic liposomes target angiogenic endothelial cells in tumors and chronic inflammation in mice. *J. Clin. Invest.* **101**, 1401–1413 (1998).

115. Lunov, O. *et al.* Differential uptake of functionalized polystyrene nanoparticles by human macrophages and a monocytic cell line. *ACS Nano* **5**, 1657–1669 (2011).

116. Daigneault, M., Preston, J. A., Marriott, H. M., Whyte, M. K. B. & Dockrell, D. H. The identification of markers of macrophage differentiation in PMA-stimulated THP-1 cells and monocyte-derived macrophages. *PLoS One* **5**, (2010).

117. Bircsak, K. M. *et al.* A 3D microfluidic liver model for high throughput compound toxicity screening in the OrganoPlate®. *Toxicology* **450**, 152667 (2021).

118. Souris, J. S. *et al.* Surface charge-mediated rapid hepatobiliary excretion of mesoporous silica nanoparticles. *Biomaterials* **31**, 5564–5574 (2010).

119. Rosenholm, J. M., Sahlgren, C. & Lindén, M. Towards multifunctional, targeted drug delivery systems using mesoporous silica nanoparticles--opportunities & challenges. *Nanoscale* **2**, 1870–1883 (2010).

120. Lu, J., Liong, M., Li, Z., Zink, J. I. & Tamanoi, F. Biocompatibility, biodistribution, and drug-delivery efficiency of mesoporous silica nanoparticles for cancer therapy in animals. *Small* **6**, 1794–1805 (2010).

121. Mamaeva, V. *et al.* Mesoporous silica nanoparticles as drug delivery systems for targeted inhibition of notch signaling in cancer. *Mol. Ther.* **19**, 1538–1546 (2011).

122. Chen, F. *et al.* In vivo tumor targeting and image-guided drug delivery with antibody-conjugated, radiolabeled mesoporous silica nanoparticles. *ACS Nano* **7**, 9027–9039 (2013).

123. Goel, S. *et al.* VEGF 121 -Conjugated Mesoporous Silica Nanoparticle: A Tumor Targeted Drug Delivery System. *ACS Appl. Mater. Interfaces* **6**, 21677–21685 (2014).

124. Chakravarty, R. *et al.* Hollow mesoporous silica nanoparticles for tumor vasculature targeting and PET image-guided drug delivery. *Nanomedicine* **10**, 1233–1246 (2015).

125. Fang, J., Nakamura, H. & Maeda, H. The EPR effect: Unique features of tumor blood vessels for drug delivery, factors involved, and limitations and augmentation of the effect. *Adv. Drug Deliv. Rev.* **63**, 136–151 (2011).

126. Hussain, Z. *et al.* PEGylation: a promising strategy to overcome challenges to cancer-targeted nanomedicines: a review of challenges to clinical transition and promising resolution. *Drug Deliv. Transl. Res.* **9**, 721–734 (2019).

127. Suk, J. S., Xu, Q., Kim, N., Hanes, J. & Ensign, L. M. PEGylation as a strategy for improving nanoparticle-based drug and gene delivery. *Adv. Drug Deliv. Rev.* **99**, 28–51 (2016).

128. Song, K. *et al.* Hyaluronic Acid-Functionalized Mesoporous Silica Nanoparticles Loading Simvastatin for Targeted Therapy of Atherosclerosis. *Pharmaceutics* **14**, (2022).

129. Mishra, P., Nayak, B. & Dey, R. K. PEGylation in anti-cancer therapy: An overview. *Asian J. Pharm. Sci.* **11**, 337–348 (2016).

130. Sanchez, L., Yi, Y. & Yu, Y. Effect of partial PEGylation on particle uptake by macrophages. *Nanoscale* **9**, 288–297 (2017).

131. Walkey, C. D., Olsen, J. B., Guo, H., Emili, A. & Chan, W. C. W. Nanoparticle size and

surface chemistry determine serum protein adsorption and macrophage uptake. *J. Am. Chem. Soc.* **134**, 2139–2147 (2012).

132. Yang, Q. *et al.* Evading immune cell uptake and clearance requires PEG grafting at densities substantially exceeding the minimum for brush conformation. *Mol. Pharm.* **11**, 1250–1258 (2014).

133. Kramer, L. *et al.* Quantitative and correlative biodistribution analysis of 89Zr-labeled mesoporous silica nanoparticles intravenously injected into tumor-bearing mice. *Nanoscale* **9**, 9743–9753 (2017).

134. Meng, H. *et al.* Use of Size and a Copolymer Design Feature To Improve the Biodistribution and the Enhanced Permeability and Retention Eff ect of Doxorubicin-Loaded Mesoporous Silica Nanoparticles in a Murine Xenograft Tumor Model. *ACS Nano* **5**, 4131–4144 (2011).

135. Perrault, S. D., Walkey, C., Jennings, T., Fischer, H. C. & Chan, W. C. W. Mediating tumor targeting efficiency of nanoparticles through design. *Nano Lett.* **9**, 1909–1915 (2009).

136. Miteva, M. *et al.* Tuning PEGylation of mixed micelles to overcome intracellular and systemic siRNA delivery barriers. *Biomaterials* **38**, 97–107 (2015).

137. Mori, A., Klibanov, A. L., Torchilin, V. P. & Huang, L. Influence of the steric barrier activity of amphipathic poly(ethyleneglycol) and ganglioside GM1 on the circulation time of liposomes and on the target binding of immunoliposomes in vivo. *FEBS Lett.* **284**, 263–266 (1991).

138. Zhang, Y., Liu, A. T., Cornejo, Y. R., van Haute, D. & Berlin, J. M. A Systematic comparison of in vitro cell uptake and in vivo biodistribution for three classes of gold nanoparticles with saturated PEG coatings. *PLoS One* **15**, 1–16 (2020).

139. Klibanov, A. L., Maruyama, K., Torchilin, V. P. & Huang, L. Amphipathic polyethyleneglycols effectively prolong the circulation time of liposomes. *FEBS Lett.* **268**, 235–237 (1990).

140. Gref, R. *et al.* Biodegradable Long-Circulating Polymeric Nanospheres. *Science (80-.).* **263**, 1600–1603 (1994).

141. Gabizon, A., Shmeeda, H. & Barenholz, Y. Pharmacokinetics of pegylated liposomal doxorubicin: Review of animal and human studies. *Clin. Pharmacokinet.* **42**, 419–436 (2003).

142. Nance, E. *et al.* Non-invasive delivery of stealth, brain-penetrating nanoparticles across the

blood - Brain barrier using MRI-guided focused ultrasound. *J. Control. Release* **189**, 123–132 (2014).

143. Hu, Y., Xie, J., Tong, Y. W. & Wang, C. H. Effect of PEG conformation and particle size on the cellular uptake efficiency of nanoparticles with the HepG2 cells. *J. Control. Release* **118**, 7–17 (2007).

144. Steinmetz, N. F. & Manchester, M. PEGylated viral nanoparticles for biomedicine: The impact of PEG chain length on VNP cell interactions in vitro and Ex vivo. *Biomacromolecules* **10**, 784–792 (2009).

145. Choi, K. Y. *et al.* PEGylation of hyaluronic acid nanoparticles improves tumor targetability in vivo. *Biomaterials* **32**, 1880–1889 (2011).

146. Cai, R. & Chen, C. The Crown and the Scepter: Roles of the Protein Corona in Nanomedicine. *Adv. Mater.* **31**, 1–13 (2019).

147. Gunawan, C., Lim, M., Marquis, C. P. & Amal, R. Nanoparticle-protein corona complexes govern the biological fates and functions of nanoparticles. *J. Mater. Chem. B* **2**, 2060–2083 (2014).

148. Lesniak, A. *et al.* Effects of the presence or absence of a protein corona on silica nanoparticle uptake and impact on cells. *ACS Nano* **6**, 5845–5857 (2012).

149. Wang, S. *et al.* The role of protein corona on nanodrugs for organ-targeting and its prospects of application. *J. Control. Release* **360**, 15–43 (2023).

150. Aliyandi, A., Reker-Smit, C., Bron, R., Zuhorn, I. S. & Salvati, A. Correlating Corona Composition and Cell Uptake to Identify Proteins Affecting Nanoparticle Entry into Endothelial Cells. *ACS Biomater. Sci. Eng.* **7**, 5573–5584 (2021).

151. Möller, K. & Bein, T. Degradable Drug Carriers: Vanishing Mesoporous Silica Nanoparticles. *Chem. Mater.* **31**, 4364–4378 (2019).

152. Lin, C. Y., Yang, C. M. & Lindén, M. Dissolution and morphology evolution of mesoporous silica nanoparticles under biologically relevant conditions. *J. Colloid Interface Sci.* **608**, 995–1004 (2022).

153. Beck, M., Mandal, T., Buske, C. & Lindén, M. Serum Protein Adsorption Enhances Active Leukemia Stem Cell Targeting of Mesoporous Silica Nanoparticles. *ACS Appl. Mater. Interfaces* **9**, 18566–18574 (2017).

154. Salvati, A. *et al.* Transferrin-functionalized nanoparticles lose their targeting capabilities when a biomolecule corona adsorbs on the surface. *Nat. Nanotechnol.* **8**, 137–143 (2013).

155. Vonarbourg, A., Passirani, C., Saulnier, P. & Benoit, J. P. Parameters influencing the stealthiness of colloidal drug delivery systems. *Biomaterials* **27**, 4356–4373 (2006).

156. Walkey, C. D. & Chan, W. C. W. Understanding and controlling the interaction of nanomaterials with proteins in a physiological environment. *Chem. Soc. Rev.* **41**, 2780–2799 (2012).

157. Tenzer, S. *et al.* Nanoparticle size is a critical physicochemical determinant of the human blood plasma corona: A comprehensive quantitative proteomic analysis. *ACS Nano* **5**, 7155–7167 (2011).

158. Landsiedel, R. *et al.* Toxico-/biokinetics of nanomaterials. *Arch. Toxicol.* **86**, 1021–1060 (2012).

159. Ogawara, K. I. *et al.* Pre-coating with serum albumin reduces receptor-mediated hepatic disposition of polystyrene nanosphere: Implications for rational design of nanoparticles. *J. Control. Release* **100**, 451–455 (2004).

160. Dutta, D. *et al.* Adsorbed proteins influence the biological activity and molecular targeting of nanomaterials. *Toxicol. Sci.* **100**, 303–315 (2007).

161. Fleischer, C. C. & Payne, C. K. Nanoparticle-cell interactions: Molecular structure of the protein corona and cellular outcomes. *Acc. Chem. Res.* **47**, 2651–2659 (2014).

162. Mortimer, G. M. *et al.* Cryptic epitopes of albumin determine mononuclear phagocyte system clearance of nanomaterials. *ACS Nano* **8**, 3357–3366 (2014).

163. Jansen, R. W. *et al.* Formaldehyde treated albumin contains monomeric and polymeric forms that are differently cleared by endothelial and kupffer cells of the liver: Evidence for scavenger receptor heterogeneity. *Biochem. Biophys. Res. Commun.* **180**, 23–32 (1991).

164. Tenzer, S. *et al.* Rapid formation of plasma protein corona critically affects nanoparticle pathophysiology. *Nat. Nanotechnol.* **8**, 772–781 (2013).

165. Vroman, L. & Adams, A. L. Findings with the recording ellipsometer suggesting rapid exchange of specific plasma proteins at liquid/solid interfaces. *Surf. Sci.* **16**, 438–446 (1969).

166. Weber, C., Simon, J., Mailänder, V., Morsbach, S. & Landfester, K. Preservation of the soft

protein corona in distinct flow allows identification of weakly bound proteins. *Acta Biomater.* **76**, 217–224 (2018).

167. Rampado, R., Crotti, S., Caliceti, P., Pucciarelli, S. & Agostini, M. Recent Advances in Understanding the Protein Corona of Nanoparticles and in the Formulation of “Stealthy” Nanomaterials. *Front. Bioeng. Biotechnol.* **8**, 1–19 (2020).

168. Galdino, F. E., Picco, A. S., Capeletti, L. B., Bettini, J. & Cardoso, M. B. Inside the Protein Corona: From Binding Parameters to Unstained Hard and Soft Coronas Visualization. *Nano Lett.* **21**, 8250–8257 (2021).

169. Gessner, A. *et al.* Nanoparticles with decreasing surface hydrophobicities: Influence on plasma protein adsorption. *Int. J. Pharm.* **196**, 245–249 (2000).

170. Yoon, J. Y., Kim, J. H. & Kim, W. S. Interpretation of protein adsorption phenomena onto functional microspheres. *Colloids Surfaces B Biointerfaces* **12**, 15–22 (1998).

171. Hartvig, R. A., Van De Weert, M., Østergaard, J., Jorgensen, L. & Jensen, H. Protein adsorption at charged surfaces: The role of electrostatic interactions and interfacial charge regulation. *Langmuir* **27**, 2634–2643 (2011).

172. Meissner, J., Prause, A., Bharti, B. & Findenegg, G. H. Characterization of protein adsorption onto silica nanoparticles: influence of pH and ionic strength. *Colloid Polym. Sci.* **293**, 3381–3391 (2015).

173. Lundqvist, M. *et al.* Nanoparticle size and surface properties determine the protein corona with possible implications for biological impacts. *Proc. Natl. Acad. Sci. U. S. A.* **105**, 14265–14270 (2008).

174. Saikia, J., Yazdimamaghani, M., Hadipour Moghaddam, S. P. & Ghandehari, H. Differential Protein Adsorption and Cellular Uptake of Silica Nanoparticles Based on Size and Porosity. *ACS Appl. Mater. Interfaces* **8**, 34820–34832 (2016).

175. Lundqvist, M., Sethson, I. & Jonsson, B. H. Protein adsorption onto silica nanoparticles: Conformational changes depend on the particles’ curvature and the protein stability. *Langmuir* **20**, 10639–10647 (2004).

176. Clemments, A. M., Botella, P. & Landry, C. C. Protein Adsorption from Biofluids on Silica Nanoparticles: Corona Analysis as a Function of Particle Diameter and Porosity. *ACS Appl. Mater. Interfaces* **7**, 21682–21689 (2015).

177. Gessner, A., Lieske, A., Paulke, B. R. & Müller, R. H. Influence of surface charge density on protein adsorption on polymeric nanoparticles: Analysis by two-dimensional electrophoresis. *Eur. J. Pharm. Biopharm.* **54**, 165–170 (2002).

178. Capriotti, A. L. *et al.* Do plasma proteins distinguish between liposomes of varying charge density? *J. Proteomics* **75**, 1924–1932 (2012).

179. Gessner, A., Lieske, A., Paulke, B. R. & Müller, R. H. Functional groups on polystyrene model nanoparticles: Influence on protein adsorption. *J. Biomed. Mater. Res. - Part A* **65**, 319–326 (2003).

180. Deng, Z. J., Liang, M., Toth, I., Monteiro, M. & Minchin, R. F. Plasma protein binding of positively and negatively charged polymer-coated gold nanoparticles elicits different biological responses. *Nanotoxicology* **7**, 314–322 (2013).

181. Schlenoff, J. B. Zwitteration: Coating surfaces with zwitterionic functionality to reduce nonspecific adsorption. *Langmuir* **30**, 9625–9636 (2014).

182. Chen, S., Li, L., Zhao, C. & Zheng, J. Surface hydration: Principles and applications toward low-fouling/nonfouling biomaterials. *Polymer (Guildf).* **51**, 5283–5293 (2010).

183. Erfani, A., Seaberg, J., Aichele, C. P. & Ramsey, J. D. Interactions between Biomolecules and Zwitterionic Moieties: A Review. *Biomacromolecules* **21**, 2557–2573 (2020).

184. He, Y. *et al.* Molecular simulation studies of protein interactions with phosphorylcholine self-assembled monolayers. *LAngmui* **24**, 10358–10364 (2008).

185. Walker, J. A. *et al.* Antibody-Binding, Antifouling Surface Coatings Based on Recombinant Expression of Zwitterionic EK Peptides. *Langmuir* **35**, 1266–1272 (2019).

186. Rosenholm, J. M., Duchanoy, A. & Lindén, M. Hyperbranching surface polymerization as a tool for preferential functionalization of the outer surface of mesoporous silica. *Chem. Mater.* **20**, 1126–1133 (2008).

187. Viklund, C. & Irgum, K. Synthesis of porous zwitterionic sulfobetaine monoliths and characterization of their interaction with proteins. *Macromolecules* **33**, 2539–2544 (2000).

188. Vasantha, V. A., Junhui, C., Wenguang, Z., Van Herk, A. M. & Parthiban, A. Reversible Photo- and Thermoresponsive, Self-Assembling Azobenzene Containing Zwitterionic Polymers. *Langmuir* **35**, 1465–1474 (2019).

189. Jiang, S. & Cao, Z. Ultralow-fouling, functionalizable, and hydrolyzable zwitterionic

materials and their derivatives for biological applications. *Adv. Mater.* **22**, 920–932 (2010).

190. Carr, L. R., Xue, H. & Jiang, S. Functionalizable and nonfouling zwitterionic carboxybetaine hydrogels with a carboxybetaine dimethacrylate crosslinker. *Biomaterials* **32**, 961–968 (2011).

191. Zhang, Z. *et al.* Nonfouling behavior of polycarboxybetaine-grafted surfaces: Structural and environmental effects. *Biomacromolecules* **9**, 2686–2692 (2008).

192. Yang, W., Xue, H., Li, W., And, J. Z. & Jiang, S. Pursuing 'zero' protein adsorption of poly(carboxybetaine) from undiluted blood serum and plasma. *Langmuir* **25**, 11911–11916 (2009).

193. Kyomoto, M. *et al.* Hydrated Phospholipid Polymer Gel-Like Layer for Increased Durability of Orthopedic Bearing Surfaces. *Langmuir* **35**, 1954–1963 (2019).

194. Futamura, K., Matsuno, R., Konno, T., Takai, M. & Ishihara, K. Rapid development of hydrophilicity and protein adsorption resistance by polymer surfaces bearing phosphorylcholine and naphthalene groups. *Langmuir* **24**, 10340–10344 (2008).

195. Chen, S., Cao, Z. & Jiang, S. Ultra-low fouling peptide surfaces derived from natural amino acids. *Biomaterials* **30**, 5892–5896 (2009).

196. Ashraf, S. *et al.* Zwitterionic surface coating of quantum dots reduces protein adsorption and cellular uptake. *Nanoscale* **8**, 17794–17800 (2016).

197. Debayle, M. *et al.* Zwitterionic polymer ligands: an ideal surface coating to totally suppress protein-nanoparticle corona formation? *Biomaterials* **219**, (2019).

198. Liu, X. *et al.* Blood compatible materials: State of the art. *J. Mater. Chem. B* **2**, 5718–5738 (2014).

199. Morra, M. On the molecular basis of fouling resistance. *J. Biomater. Sci. Polym. Ed.* **11**, 547–569 (2000).

200. Robinson, S. & Williams, P. A. Inhibition of protein adsorption onto silica by polyvinylpyrrolidone. *Langmuir* **18**, 8743–8748 (2002).

201. Jin, Z., Feng, W., Zhu, S., Sheardown, H. & Brash, J. L. Protein-resistant polyurethane by sequential grafting of poly(2-hydroxyethyl methacrylate) and poly(oligo(ethylene glycol) methacrylate) via surface-initiated ATRP. *J. Biomed. Mater. Res. - Part A* **95**, 1223–1232 (2010).

202. Kumar, S., Tong, X., Dory, Y. L., Lepage, M. & Zhao, Y. A CO2-switchable polymer brush for reversible capture and release of proteins. *Chem. Commun.* **49**, 90–92 (2013).

203. Lemarchand, C. *et al.* Influence of polysaccharide coating on the interactions of nanoparticles with biological systems. *Biomaterials* **27**, 108–118 (2006).

204. Frazier, R. A. *et al.* Characterization of protein-resistant dextran monolayers. *Biomaterials* **21**, 957–966 (2000).

205. Tasaki, K. *et al.* Poly (oxyethylene) - Water Interactions : A Molecular Dynamics Study. *J. Am. Chem. Soc.* **118**, 8459–8469 (1996).

206. Alconcel, S. N. S., Baas, A. S. & Maynard, H. D. FDA-approved poly(ethylene glycol)-protein conjugate drugs. *Polym. Chem.* **2**, 1442–1448 (2011).

207. D'Avanzo, N. *et al.* Immunogenicity of Polyethylene Glycol Based Nanomedicines: Mechanisms, Clinical Implications and Systematic Approach. *Adv. Ther.* **3**, 1900170 (2020).

208. Bergström, K. *et al.* Effects of branching and molecular weight of surface-bound poly(ethylene oxide) on protein rejection. *J. Biomater. Sci. Polym. Ed.* **6**, 123–132 (1995).

209. Shi, L. *et al.* Effects of polyethylene glycol on the surface of nanoparticles for targeted drug delivery. *Nanoscale* **13**, 10748–10764 (2021).

210. Lee, H. & Larson, R. G. Adsorption of Plasma Proteins onto PEGylated Lipid Bilayers: The Effect of PEG Size and Grafting Density. *Biomacromolecules* **17**, 1757–1765 (2016).

211. Meng, F., Engbers, G. H. M. & Feijen, J. Polyethylene glycol-grafted polystyrene particles. *J. Biomed. Mater. Res. - Part A* **70**, 49–58 (2004).

212. Gref, R. *et al.* 'Stealth' corona-core nanoparticles surface modified by polyethylene glycol (PEG): Influences of the corona (PEG chain length and surface density) and of the core composition on phagocytic uptake and plasma protein adsorption. *Colloids Surfaces B Biointerfaces* **18**, 301–313 (2000).

213. Li, M. *et al.* Brush conformation of polyethylene glycol determines the stealth effect of nanocarriers in the low protein adsorption regime. *Nano Lett.* **21**, 1591–1598 (2021).

214. Peracchia, M. T., Vauthier, C., Passirani, C., Couvreur, P. & Labarre, D. Complement consumption by poly(ethylene glycol) in different conformations chemically coupled to poly(isobutyl 2-cyanoacrylate) nanoparticles. *Life Sci.* **61**, 749–761 (1997).

215. Pasche, S., Vörös, J., Griesser, H. J., Spencer, N. D. & Textor, M. Effects of ionic strength and surface charge on protein adsorption at PEGylated surfaces. *J. Phys. Chem. B* **109**, 17545–17552 (2005).

216. Zhou, H. *et al.* Dense and Dynamic Polyethylene Glycol Shells Cloak Nanoparticles from Uptake by Liver Endothelial Cells for Long Blood Circulation. *ACS Nano* **12**, 10130–10141 (2018).

217. Du, H., Chandaroy, P. & Hui, S. W. Grafted poly-(ethylene glycol) on lipid surface inhibits protein adsorption and cell adhesion. *Biochim. Biophys. Acta - Biomembr.* **1326**, 236–248 (1997).

218. Perry, J. L. *et al.* PEGylated PRINT nanoparticles: The impact of PEG density on protein binding, macrophage association, biodistribution, and pharmacokinetics. *Nano Lett.* **12**, 5304–5310 (2012).

219. de Gennes, P. G. Conformations of Polymers Attached to an Interface. *Macromolecules* **13**, 1069–1075 (1980).

220. Oesterhelt, F., Rief, M. & Gaub, H. E. Single molecule force spectroscopy by AFM indicates helical structure of poly(ethylene-glycol) in water. *New J. Phys.* **1**, (1999).

221. Damodaran, V. B., Fee, C. J., Ruckh, T. & Popat, K. C. Conformational studies of covalently grafted poly(ethylene glycol) on modified solid matrices using X-ray photoelectron spectroscopy. *Langmuir* **26**, 7299–7306 (2010).

222. Moghimi, S. M., Muir, I. S., Illum, L., Davis, S. S. & Kolb-Bachofen, V. Coating particles with a block co-polymer (poloxamine-908) suppresses opsonization but permits the activity of dysopsonins in the serum. *BBA - Mol. Cell Res.* **1179**, 157–165 (1993).

223. Selli, D., Motta, S. & Di Valentin, C. Impact of surface curvature, grafting density and solvent type on the PEGylation of titanium dioxide nanoparticles. *J. Colloid Interface Sci.* **555**, 519–531 (2019).

224. Andersson, J., Rosenholm, J., Areva, S. & Lindén, M. Influences of material characteristics on ibuprofen drug loading and release profiles from ordered micro- and mesoporous silica matrices. *Chem. Mater.* **16**, 4160–4167 (2004).

225. Hu, Q. *et al.* A low cytotoxic cationic metal-organic framework carrier for controllable drug release. *J. Med. Chem.* **57**, 5679–5685 (2014).

226. Fonseca, C., Simoes, S. & Gaspar, R. Paclitaxel-loaded PLGA nanoparticles: preparation, physicochemical characterization and in vitro anti-tumoral. *J. Control. Release* **83**, 273–286 (2002).

227. Wu, M., Wang, Q., Liu, X. & Liu, J. Highly efficient loading of doxorubicin in Prussian Blue nanocages for combined photothermal/chemotherapy against hepatocellular carcinoma. *RSC Adv.* **5**, 30970–30980 (2015).

228. Luo, B. *et al.* Mesoporous biocompatible and acid-degradable magnetic colloidal nanocrystal clusters with sustainable stability and high hydrophobic drug loading capacity. *ACS Nano* **5**, 1428–1435 (2011).

229. Wani, A. *et al.* Surface PEGylation of Mesoporous Silica Nanorods (MSNR): Effect on loading, release, and delivery of mitoxantrone in hypoxic cancer cells. *Sci. Rep.* **7**, 1–11 (2017).

230. He, C., Lu, K., Liu, D. & Lin, W. Nanoscale metal-organic frameworks for the co-delivery of cisplatin and pooled siRNAs to enhance therapeutic efficacy in drug-resistant ovarian cancer cells. *J. Am. Chem. Soc.* **136**, 5181–5184 (2014).

231. Turrina, C., Berensmeier, S. & Schwaminger, S. P. Bare iron oxide nanoparticles as drug delivery carrier for the short cationic peptide lasioglossin. *Pharmaceuticals* **14**, (2021).

232. Braun, K. *et al.* Membrane interactions of mesoporous silica nanoparticles as carriers of antimicrobial peptides. *J. Colloid Interface Sci.* **475**, 161–170 (2016).

233. Braun, K., Pochert, A., Gerber, M., Raber, H. F. & Lindén, M. Influence of mesopore size and peptide aggregation on the adsorption and release of a model antimicrobial peptide onto/from mesoporous silica nanoparticles: In vitro. *Mol. Syst. Des. Eng.* **2**, 393–400 (2017).

234. Beitzinger, B. *et al.* Delivery by Dendritic Mesoporous Silica Nanoparticles Enhances the Antimicrobial Activity of a Napsin-Derived Peptide Against Intracellular Mycobacterium tuberculosis. *Adv. Healthc. Mater.* **10**, 1–13 (2021).

235. Kim, J. H., Shin, D. H. & Kim, J. S. Preparation, characterization, and pharmacokinetics of liposomal docetaxel for oral administration. *Arch. Pharm. Res.* **41**, 765–775 (2018).

236. Khosravian, P. *et al.* Mesoporous silica nanoparticles functionalized with folic acid/methionine for active targeted delivery of docetaxel. *Onco. Targets. Ther.* **9**, 7315–7330 (2016).

237. Sakhi, M. *et al.* Design and Characterization of Paclitaxel-Loaded Polymeric Nanoparticles Decorated With Trastuzumab for the Effective Treatment of Breast Cancer. *Front. Pharmacol.* **13**, 1–15 (2022).

238. Wang, J. *et al.* Synthesis and antitumor efficacy of daunorubicin-loaded magnetic nanoparticles. *Int. J. Nanomedicine* **6**, 203–211 (2011).

239. Halley, P. D. *et al.* Daunorubicin-Loaded DNA Origami Nanostructures Circumvent Drug-Resistance Mechanisms in a Leukemia Model. *Small* **12**, 308–320 (2016).

240. Du, Y. *et al.* Synthesis and Evaluation of Doxorubicin-Loaded Gold Nanoparticles for Tumor-Targeted Drug Delivery. *Bioconjug. Chem.* **29**, 420–430 (2018).

241. Norouzi, M. *et al.* Doxorubicin-loaded iron oxide nanoparticles for glioblastoma therapy: a combinational approach for enhanced delivery of nanoparticles. *Sci. Rep.* **10**, 1–18 (2020).

242. Regier, M. C., Taylor, J. D., Borcyk, T., Yang, Y. & Pannier, A. K. Fabrication and characterization of DNA-loaded zein nanospheres. *J. Nanobiotechnology* **10**, 1–13 (2012).

243. Lin, J. *et al.* PEGylated Lipid bilayer coated mesoporous silica nanoparticles for co-delivery of paclitaxel and curcumin: Design, characterization and its cytotoxic effect. *Int. J. Pharm.* **536**, 272–282 (2018).

244. Nicholas, A. R., Scott, M. J., Kennedy, N. I. & Jones, M. N. Effect of grafted polyethylene glycol (PEG) on the size, encapsulation efficiency and permeability of vesicles. *Biochim. Biophys. Acta - Biomembr.* **1463**, 167–178 (2000).

245. De Leo, V. *et al.* Preparation of drug-loaded small unilamellar liposomes and evaluation of their potential for the treatment of chronic respiratory diseases. *Int. J. Pharm.* **545**, 378–388 (2018).

246. Kanamaru, T., Sakurai, K. & Fujii, S. Impact of Polyethylene Glycol (PEG) Conformations on the in Vivo Fate and Drug Release Behavior of PEGylated Core-Cross-Linked Polymeric Nanoparticles. *Biomacromolecules* **23**, 3909–3918 (2022).

247. Hashizaki, K. *et al.* Effects of poly(ethylene glycol) (PEG) concentration on the permeability of PEG-grafted liposomes. *Chem. Pharm. Bull.* **53**, 27–31 (2005).

248. Edwards, K. & Almgren, M. Surfactant-Induced Leakage and Structural Change of Lecithin Vesicles: Effect of Surfactant Headgroup Size. *Langmuir* **8**, 824–832 (1992).

249. Lin, T. T. *et al.* Development and characterization of sorafenib-loaded PLGA nanoparticles

for the systemic treatment of liver fibrosis. *J. Control. Release* **221**, 62–70 (2016).

250. Liu, Y., Yang, G., Jin, S., Xu, L. & Zhao, C. X. Development of High-Drug-Loading Nanoparticles. *Chempluschem* **85**, 2143–2157 (2020).

251. Trzeciak, K., Chotera-ouda, A., Bak-sypien, I. I. & Potrzebowski, M. J. Mesoporous silica particles as drug delivery systems—the state of the art in loading methods and the recent progress in analytical techniques for monitoring these processes. *Pharmaceutics* **13**, (2021).

252. Stöber, W., Fink, A. & Bohn, E. Controlled growth of monodisperse silica spheres in the micron size range. *J. Colloid Interface Sci.* **26**, 62–69 (1968).

253. Brinker, J. C. & Scherer, G. W. *Sol-Gel Science - The Physics and Chemistry of Sol-Gel Processing*. (Academic Press, 1990). doi:10.1186/1471-2105-8-444.

254. LaMer, V. K. & Dinegar, R. H. Theory, Production and Mechanism of Formation of Monodispersed Hydrosols. *J. Am. Chem. Soc.* **72**, 4847–4854 (1950).

255. Matsoukas, T. & Gulari, E. Dynamics of growth of silica particles from ammonia-catalyzed hydrolysis of tetra-ethyl-orthosilicate. *J. Colloid Interface Sci.* **124**, 252–261 (1988).

256. Engineering, C. Uniform silica particle precipitation: An aggregative growth model. *J. Colloid Interface Sci.* **142**, 19–34 (1991).

257. Carcouët, C. C. M. C. *et al.* Nucleation and growth of monodisperse silica nanoparticles. *Nano Lett.* **14**, 1433–1438 (2014).

258. Bogush, G. H., Tracy, M. A. & Zukoski, I. Preparation of Monodisperse Silica Particles: Control of Size and Mass Fraction. *J. Non. Cryst. Solids* **104**, 95–106 (1988).

259. Beck, M. Mesoporöse Silikananopartikel als Transportsysteme für miRNA und Wirkstoffmoleküle für die Therapie von Krebsstammzellen. (Universität Ulm, 2018). doi:10.18725/OPARU-5444.

260. Björk, E. M., Söderlind, F. & Odén, M. Tuning the shape of mesoporous silica particles by alterations in parameter space: From rods to platelets. *Langmuir* **29**, 13551–13561 (2013).

261. Fang, A., Gosse, C., Gaillard, C., Zhao, X. & Davy, J. Tuning silica particle shape at fluid interfaces. *Lab Chip* **12**, 4960–4963 (2012).

262. Schüth, F. Endo- und Exotemplate zur Erzeugung von anorganischen Materialien mit

großer spezifischer Oberfläche. *Angew. Chemie* **115**, 3730–3750 (2003).

263. Li, W., Zhang, M., Zhang, J. & Han, Y. Self-assembly of cetyl trimethylammonium bromide in ethanol-water mixtures. *Front. Chem. China* **1**, 438–442 (2006).

264. Monnier, A. *et al.* Cooperative formation of inorganic-organic interfaces in the synthesis of silicate mesostructures. *Science (80-.).* **261**, 1299–1303 (1993).

265. Mandal, M., Farid, G. & Kruk, M. Swollen mixed Pluronic surfactant micelles as templates for mesoporous nanotubes with diverse bridged-organosilica frameworks. *J. Colloid Interface Sci.* **524**, 445–455 (2018).

266. Yano, K. & Fukushima, Y. Synthesis of mono-dispersed mesoporous silica spheres with highly ordered hexagonal regularity using conventional alkyltrimethylammonium halide as a surfactant. *J. Mater. Chem.* **14**, 1579–1584 (2004).

267. Gu, J. *et al.* Sub-150nm mesoporous silica nanoparticles with tunable pore sizes and well-ordered mesostructure for protein encapsulation. *J. Colloid Interface Sci.* **407**, 236–242 (2013).

268. Möller, K. & Bein, T. Talented mesoporous silica nanoparticles. *Chem. Mater.* **29**, 371–388 (2017).

269. Spitzmüller, L. *et al.* Dissolution control and stability improvement of silica nanoparticles in aqueous media. *J. Nanoparticle Res.* **25**, 1–17 (2023).

270. Rosenholm, J. M. & Lindén, M. Wet-chemical analysis of surface concentration of accessible groups on different amino-functionalized mesoporous SBA-15 silicas. *Chem. Mater.* **19**, 5023–5034 (2007).

271. Hoffmann, F., Cornelius, M., Morell, J. & Fröba, M. Silica-based mesoporous organic-inorganic hybrid materials. *Angew. Chemie - Int. Ed.* **45**, 3216–3251 (2006).

272. Radu, D. R., Lai, C. Y., Huang, J., Shu, X. & Lin, V. S. Y. Fine-tuning the degree of organic functionalization of mesoporous silica nanosphere materials via an interfacially designed co-condensation method. *Chem. Commun.* 1264–1266 (2005) doi:10.1039/b412618a.

273. Rahman, I. A., Jafarzadeh, M. & Sipaut, C. S. Synthesis of organo-functionalized nanosilica via a co-condensation modification using γ-aminopropyltriethoxysilane (APTES). *Ceram. Int.* **35**, 1883–1888 (2009).

274. Gabrielli, L. *et al.* Epoxide opening versus silica condensation during sol-gel hybrid

biomaterial synthesis. *Chem. - A Eur. J.* **19**, 7856–7864 (2013).

275. Putz, A. M., Almásy, L., Len, A. & Ianăşi, C. Functionalized silica materials synthesized via co-condensation and post-grafting methods. *Fullerenes Nanotub. Carbon Nanostructures* **27**, 323–332 (2019).

276. Rivas, M. V. *et al.* Revisiting carboxylic groups functionalization of silica sol-gel materials. *J. Mater. Chem. B* (2023) doi:10.1039/d2tb02279f.

277. Trouvé, A., Batonneau-Gener, I., Valange, S., Bonne, M. & Mignard, S. Tuning the hydrophobicity of mesoporous silica materials for the adsorption of organic pollutant in aqueous solution. *J. Hazard. Mater.* **201**–**202**, 107–114 (2012).

278. Hatton, B., Landskron, K., Whitnall, W., Perovic, D. & Ozin, G. A. Past, present, and future of periodic mesoporous organosilicas - The PMOs. *Acc. Chem. Res.* **38**, 305–312 (2005).

279. Johann Kecht, Axel Schlossbauer, T. B. Selective Functionalization of the Outer and Inner Surfaces in Mesoporous Silica Nanoparticles. *Chem. Mater.* **20**, 7207–7214 (2008).

280. Cauda, V., Argyo, C. & Bein, T. Impact of different PEGylation patterns on the long-term bio-stability of colloidal mesoporous silica nanoparticles. *J. Mater. Chem.* **20**, 8693 (2010).

281. Cauda, V., Schlossbauer, A. & Bein, T. Bio-degradation study of colloidal mesoporous silica nanoparticles: Effect of surface functionalization with organo-silanes and poly(ethylene glycol). *Microporous Mesoporous Mater.* **132**, 60–71 (2010).

282. Park, J. W., Park, Y. J. & Jun, C. H. Post-grafting of silica surfaces with pre-functionalized organosilanes: New synthetic equivalents of conventional trialkoxysilanes. *Chem. Commun.* **47**, 4860–4871 (2011).

283. Estevão, B. M., Miletto, I., Hioka, N., Marchese, L. & Gianotti, E. Mesoporous Silica Nanoparticles Functionalized with Amino Groups for Biomedical Applications. *ChemistryOpen* **10**, 1251–1259 (2021).

284. Baumann, B., Wittig, R. & Linden, M. Mesoporous silica nanoparticles in injectable hydrogels: Factors influencing cellular uptake and viability. *Nanoscale* (2017) doi:10.1039/C7NR02015E.

285. Shui, Y. *et al.* Facile and controllable synthesis of hybrid silica nanoparticles densely grafted with poly(ethylene glycol). *Polym. Int.* **66**, 1395–1401 (2017).

286. Issa, S. *et al.* Poly(ethylene oxide) grafted silica nanoparticles: efficient routes of synthesis

with associated colloidal stability. *Soft Matter* **17**, 6552–6565 (2021).

287. Millot, Y. *et al.* Revisiting Alkoxysilane Assembly on Silica Surfaces: Grafting versus Homo-Condensation in Solution. *J. Am. Chem. Soc.* **145**, 6671–6681 (2023).

288. Ma, J. *et al.* Efficient proteolysis using a regenerable metal-ion chelate immobilized enzyme reactor supported on organic-inorganic hybrid silica monolith. *Proteomics* **11**, 991–995 (2011).

289. Ojea-Jiménez, I. *et al.* Highly Flexible Platform for Tuning Surface Properties of Silica Nanoparticles and Monitoring Their Biological Interaction. *ACS Appl. Mater. Interfaces* **8**, 4838–4850 (2016).

290. Neises, B. & Steglich, W. Simple Method for the Esterification of Carboxylic Acids. *Angew. Chemie Int. Ed. English* **17**, 522–524 (1978).

291. Von Baeckmann, C., Guillet-Nicolas, R., Renfer, D., Kählig, H. & Kleitz, F. A Toolbox for the Synthesis of Multifunctionalized Mesoporous Silica Nanoparticles for Biomedical Applications. *ACS Omega* **3**, 17496–17510 (2018).

292. Lin, B. & Zhou, S. Poly(ethylene glycol)-grafted silica nanoparticles for highly hydrophilic acrylic-based polyurethane coatings. *Prog. Org. Coatings* **106**, 145–154 (2017).

293. Quignard, S., Masse, S., Laurent, G. & Coradin, T. Introduction of disulfide bridges within silica nanoparticles to control their intra-cellular degradation. *Chem. Commun.* **49**, 3410–3412 (2013).

294. Li, W., Zhou, Y., Ma, W., Wang, S. & Dai, Y. Cleaved disulfide cross-linking functionalized silica nanoparticles for enrichment of Cd (II). *Colloids Surfaces A Physicochem. Eng. Asp.* **395**, 18–23 (2012).

295. Schiestel, T., Brunner, H. & Tovar, G. E. M. Controlled surface functionalization of silica nanospheres by covalent conjugation reactions and preparation of high density streptavidin nanoparticles. *J. Nanosci. Nanotechnol.* **4**, 504–511 (2004).

296. Mohammadi Ziarani, G., Hassanzadeh, Z., Gholamzadeh, P., Asadi, S. & Badiei, A. Advances in click chemistry for silica-based material construction. *RSC Adv.* **6**, 21979–22006 (2016).

297. Hermanson, G. *Bioconjugate Techniques 2nd Edition*. (2008).

298. Staros, J. V., Wright, R. W. & Swingle, D. M. Enhancement by N-hydroxysulfosuccinimide

of water-soluble carbodiimide-mediated coupling reactions. *Anal. Biochem.* **156**, 220–222 (1986).

299. Xiao, Y. *et al.* Enzyme and voltage stimuli-responsive controlled release system based on β-cyclodextrin-capped mesoporous silica nanoparticles. *Dalt. Trans.* **44**, 4355–4361 (2015).

300. Kunc, F., Moore, C. J., Sully, R. E., Hall, A. J. & Gubala, V. Polycarboxylated Dextran as a Multivalent Linker: Synthesis and Target Recognition of the Antibody-Nanoparticle Bioconjugates in PBS and Serum. *Langmuir* **35**, 4909–4917 (2019).

301. von Baeckmann, C., Kählig, H., Lindén, M. & Kleitz, F. On the importance of the linking chemistry for the PEGylation of mesoporous silica nanoparticles. *J. Colloid Interface Sci.* **589**, 453–461 (2021).

302. Gao, Y. *et al.* The Architecture and Function of Monoclonal Antibody-Functionalized Mesoporous Silica Nanoparticles Loaded with Mifepristone: Repurposing Abortifacient for Cancer Metastatic Chemoprevention. *Small* **12**, 2595–2608 (2016).

303. Tsai, C.-P., Chen, C.-Y., Hung, Y., Chang, F.-H. & Mou, C.-Y. Monoclonal antibody-functionalized mesoporous silica nanoparticles (MSN) for selective targeting breast cancer cells. *J. Mater. Chem.* **19**, 5737 (2009).

304. Bouchoucha, M., Béliveau, É., Kleitz, F., Calon, F. & Fortin, M. A. Antibody-conjugated mesoporous silica nanoparticles for brain microvessel endothelial cell targeting. *J. Mater. Chem. B* **5**, 7721–7735 (2017).

305. Watermann, A. *et al.* Fluorescein- and EGFR-antibody conjugated silica nanoparticles for enhancement of real-time tumor border definition using confocal laser endomicroscopy in squamous cell carcinoma of the head and neck. *Nanomaterials* **9**, 1–16 (2019).

306. Peng, X., Lin, G., Zeng, Y., Lei, Z. & Liu, G. Mesoporous Silica Nanoparticle-Based Imaging Agents for Hepatocellular Carcinoma Detection. *Front. Bioeng. Biotechnol.* **9**, 1–12 (2021).

307. Yuan, D., Ellis, C. M. & Davis, J. J. Mesoporous silica nanoparticles in bioimaging. *Materials (Basel).* **13**, 16–18 (2020).

308. Li, Z., Guo, J., Zhang, M., Li, G. & Hao, L. Gadolinium-Coated Mesoporous Silica Nanoparticle for Magnetic Resonance Imaging. *Front. Chem.* **10**, 1–10 (2022).

309. Pochert, A., Vernikouskaya, I., Pascher, F., Rasche, V. & Lindén, M. Cargo-influences on

the biodistribution of hollow mesoporous silica nanoparticles as studied by quantitative 19F-magnetic resonance imaging. *J. Colloid Interface Sci.* **488**, 1–9 (2017).

310. Taylor, K. M. L. *et al.* Mesoporous silica nanospheres as highly efficient MRI contrast agents. *J. Am. Chem. Soc.* **130**, 2154–2155 (2008).

311. Cheng, C. A., Chen, W., Zhang, L., Wu, H. H. & Zink, J. I. A Responsive Mesoporous Silica Nanoparticle Platform for Magnetic Resonance Imaging-Guided High-Intensity Focused Ultrasound-Stimulated Cargo Delivery with Controllable Location, Time, and Dose. *J. Am. Chem. Soc.* **141**, 17670–17684 (2019).

312. Pan, L. *et al.* Nuclear-targeted drug delivery of tat peptide-conjugated monodisperse mesoporous silica nanoparticles. *J. Am. Chem. Soc.* **134**, 5722–5725 (2012).

313. Yoo, J., Park, C., Yi, G., Lee, D. & Koo, H. Active targeting strategies using biological ligands for nanoparticle drug delivery systems. *Cancers (Basel).* **11**, 1–13 (2019).

314. De Oliveira, L. F. *et al.* Functionalized Silica Nanoparticles As an Alternative Platform for Targeted Drug-Delivery of Water Insoluble Drugs. *Langmuir* **32**, 3217–3225 (2016).

315. Di Paola, M. *et al.* Human Hepatocarcinoma Cell Targeting by Glypican-3 Ligand Peptide Functionalized Silica Nanoparticles: Implications for Ultrasound Molecular Imaging. *Langmuir* **33**, 4490–4499 (2017).

316. Zhou, S. *et al.* Intracellular pH-responsive and rituximab-conjugated mesoporous silica nanoparticles for targeted drug delivery to lymphoma B cells. *J. Exp. Clin. Cancer Res.* **36**, 1–14 (2017).

317. Rosenholm, J. M. *et al.* Cancer-cell-specific induction of apoptosis using mesoporous silica nanoparticles as drug-delivery vectors. *Small* **6**, 1234–1241 (2010).

318. Mortera, R. *et al.* Cell-induced intracellular controlled release of membrane impermeable cysteine from a mesoporous silica nanoparticle-based drug delivery system. *Chem. Commun.* 3219–3221 (2009) doi:10.1039/b900559e.

319. Popat, A. *et al.* Enzyme-responsive controlled release of covalently bound prodrug from functional mesoporous silica nanospheres. *Angew. Chemie - Int. Ed.* **51**, 12486–12489 (2012).

320. Castillo, R. R., Lozano, D. & Vallet-Regí, M. Mesoporous silica nanoparticles as carriers for therapeutic biomolecules. *Pharmaceutics* **12**, 1–42 (2020).

321. Otvos, L. & Wade, J. D. Current challenges in peptide-based drug discovery. *Front. Chem.* **2**, 1–4 (2014).

322. Böttger, R., Hoffmann, R. & Knappe, D. Differential stability of therapeutic peptides with different proteolytic cleavage sites in blood, plasma and serum. *PLoS One* **12**, 1–15 (2017).

323. Harms, M. *et al.* An optimized derivative of an endogenous CXCR4 antagonist prevents atopic dermatitis and airway inflammation. *Acta Pharm. Sin. B* (2020) doi:10.1016/j.apsb.2020.12.005.

324. Zhao, X. *et al.* Preparation, characterization, and evaluation in vivo of Ins-SiO 2-HP55 (insulin-loaded silica coating HP55) for oral delivery of insulin. *Int. J. Pharm.* **454**, 278–284 (2013).

325. Guha, A., Biswas, N., Bhattacharjee, K., Sahoo, N. & Kuotsu, K. pH responsive cylindrical MSN for oral delivery of insulin-design, fabrication and evaluation. *Drug Deliv.* **23**, 3552–3561 (2016).

326. Juère, E., Caillard, R., Marko, D., Del Favero, G. & Kleitz, F. Smart Protein-Based Formulation of Dendritic Mesoporous Silica Nanoparticles: Toward Oral Delivery of Insulin. *Chem. - A Eur. J.* **26**, 5195–5199 (2020).

327. Tenland, E. *et al.* Effective delivery of the anti-mycobacterial peptide NZX in mesoporous silica nanoparticles. *PLoS One* **14**, 1–16 (2019).

328. Yu, Q., Deng, T., Lin, F. C., Zhang, B. & Zink, J. I. Supramolecular Assemblies of Heterogeneous Mesoporous Silica Nanoparticles to Co-deliver Antimicrobial Peptides and Antibiotics for Synergistic Eradication of Pathogenic Biofilms. *ACS Nano* **14**, 5926–5937 (2020).

329. Ndayishimiye, J. *et al.* Engineering mesoporous silica nanoparticles towards oral delivery of vancomycin. *J. Mater. Chem. B* **9**, 7145–7166 (2021).

330. Braun, K., Stürzel, C. M., Kirchhoff, F. & Lindén, M. In vitro evaluation of a peptide-mesoporous silica nanoparticle drug release system against hiv-1. *Inorganics* **8**, 1–10 (2020).

331. Patwardhan, S. V. *et al.* Chemistry of aqueous silica nanoparticle surfaces and the mechanism of selective peptide adsorption. *J. Am. Chem. Soc.* **134**, 6244–6256 (2012).

332. Deere, J., Magner, E., Wall, J. G. & Hodnett, B. K. Mechanistic and structural features of

protein adsorption onto mesoporous silicates. *J. Phys. Chem. B* **106**, 7340–7347 (2002).

333. Boehnke, N., Dolph, K. J., Juarez, V. M., Lanoha, J. M. & Hammond, P. T. Electrostatic Conjugation of Nanoparticle Surfaces with Functional Peptide Motifs. *Bioconjug. Chem.* **31**, 2211–2219 (2020).

334. Puddu, V. & Perry, C. C. Peptide adsorption on silica nanoparticles: Evidence of hydrophobic interactions. *ACS Nano* **6**, 6356–6363 (2012).

335. Zhu, Y., Fang, Y., Borchardt, L. & Kaskel, S. PEGylated hollow mesoporous silica nanoparticles as potential drug delivery vehicles. *Microporous Mesoporous Mater.* **141**, 199–206 (2011).

336. Zhang, Y. & Xu, J. Mesoporous silica nanoparticle-based intelligent drug delivery system for bienzyme-responsive tumour targeting and controlled release. *R. Soc. Open Sci.* **5**, (2018).

337. Xiong, L., Du, X., Kleitz, F. & Qiao, S. Z. Cancer-Cell-Specific Nuclear-Targeted Drug Delivery by Dual-Ligand-Modified Mesoporous Silica Nanoparticles. *Small* **11**, 5919–5926 (2015).

338. Parray, Z. A., Hassan, M. I., Ahmad, F. & Islam, A. Amphiphilic nature of polyethylene glycols and their role in medical research. *Polym. Test.* **82**, (2020).

339. Chang, C. Y., Tsai, W. T., Ing, C. H. & Chang, C. F. Adsorption of polyethylene glycol (PEG) from aqueous solution onto hydrophobic zeolite. *J. Colloid Interface Sci.* **260**, 273–279 (2003).

340. Liu, H. & Xiao, H. Adsorption of poly(ethylene oxide) with different molecular weights on the surface of silica nanoparticles and the suspension stability. *Mater. Lett.* **62**, 870–873 (2008).

341. Wiśniewska, M., Szewczuk-Karpisz, K. & Ostolska, I. Temperature effect on the adsorption equilibrium at the silica-polyethylene glycol solution interface. *Fluid Phase Equilib.* **360**, 10–15 (2013).

342. Trens, P. & Denoyel, R. Conformation of Poly(ethylene glycol) Polymers at the Silica/Water Interface: A Microcalorimetric Study. *Langmuir* **9**, 519–522 (1993).

343. Janjua, T. I., Cao, Y., Yu, C. & Popat, A. Clinical translation of silica nanoparticles. *Nat. Rev. Mater.* **6**, 1072–1074 (2021).

344. Bukara, K. *et al.* Ordered mesoporous silica to enhance the bioavailability of poorly water-

soluble drugs: Proof of concept in man. *Eur. J. Pharm. Biopharm.* **108**, 220–225 (2016).

345. Phillips, E. *et al.* Clinical translation of an ultrasmall inorganic optical-PET imaging nanoparticle probe. *Sci. Transl. Med.* **6**, 1–10 (2014).

346. Zanoni, D. K. *et al.* Use of Ultrasmall Core-Shell Fluorescent Silica Nanoparticles for Image-Guided Sentinel Lymph Node Biopsy in Head and Neck Melanoma: A Nonrandomized Clinical Trial. *JAMA Netw. Open* **4**, 1–14 (2021).

347. Iqbal, M. N. *et al.* Mesoporous Silica Particles Retain Their Structure and Function while Passing through the Gastrointestinal Tracts of Mice and Humans. *ACS Appl. Mater. Interfaces* **15**, 9542–9553 (2022).

348. Xia, X. M. *et al.* CXCR4 antagonist AMD3100 attenuates colonic damage in mice with experimental colitis. *World J. Gastroenterol.* **16**, 2873–2880 (2010).

349. Su, T. J., Lu, J. R., Thomas, R. K., Cui, Z. F. & Penfold, J. The effect of solution pH on the structure of lysozyme layers adsorbed at the silica-water interface studied by neutron reflection. *Langmuir* **14**, 438–445 (1998).

350. Latour, R. A. The Langmuir isotherm: A commonly applied but misleading approach for the analysis of protein adsorption behavior. *J. Biomed. Mater. Res. - Part A* **103**, 949–958 (2015).

VI Publications

1. Declaration of authorship

1.1. Publication I

Roman Schmid developed methodology and experimental design, performed material synthesis and characterization, and the *in vivo* experiments. Roman Schmid conducted data analysis, interpretation, and visualization of all experiments. Roman Schmid wrote the original manuscript draft. Zhi Qu contributed to the *in vivo* experiments, and data analysis and interpretation thereof. Dr. Stephan Fischer performed *in vitro* cell viability measurements and contributed to data analysis and interpretation thereof. Dr. Meta Volcic developed methodology and experimental design of the *in vitro* experiments on the epithelial cell co-culture models, performed these experiments, and contributed to data analysis and interpretation thereof. Prof. Holger Barth, Prof. Amirali Popat, Prof. Frank Kirchhoff and Prof. Mika Lindén acquired financial support, developed, and supervised the work. All authors contributed to the article, reviewed, and edited the manuscript.

1.2. Publication II

Roman Schmid developed methodology and experimental design, performed material synthesis and characterization, as well as data analysis, interpretation, and visualization of all experiments. Roman Schmid wrote the original manuscript draft. Juliane Kaiser, Ramona Willbold, Nomusa Walther and Dr. Rainer Wittig developed methodology and experimental design of the *in vitro* experiments and performed the *in vitro* cell experiments, as well as data analysis and interpretation thereof. Dr. Rainer Wittig has written parts of the original manuscript draft. Dr. Rainer Wittig and Prof. Mika Lindén acquired financial support, and developed and supervised the work, as well as reviewed and edited the manuscript. All authors contributed to the article. Roman Schmid, Nomusa Walther, Dr. Rainer Wittig and Prof. Mika Lindén reviewed and edited the manuscript.

1.3. Publication III

The article was published under shared co-authorship and the experimental work was equally distributed between Nathalie Neffgen and Roman Schmid. Nathalie Neffgen and Roman Schmid developed methodology and experimental design and performed material synthesis and

characterization. Nathalie Neffgen and Roman Schmid performed protein adsorption and drug loading experiments, as well as data analysis, interpretation, visualization, and writing of the original manuscript draft. Aqueous PEGylation of MSN and their testing was conducted by Roman Schmid. PEGylation of MSN in DCM and their testing was performed by Nathalie Neffgen. Prof. Mika Lindén acquired financial support, and developed, conceptualized, and supervised the work. All authors contributed to the article and have reviewed and edited the manuscript.

1.4. Publication IV

The article was published under shared co-authorship and the experimental work was equally distributed between Bastian Beitzinger and Roman Schmid. Bastian Beitzinger and Roman Schmid developed methodology and experimental design, synthesized, and characterized the MSN, and performed peptide adsorption experiments. Bastian Beitzinger and Roman Schmid conducted data analysis, interpretation, visualization, and writing of the original manuscript draft. Roman Schmid conducted peptide adsorption experiments onto NSN, MSNrad, MSNhex, MSNrod. Bastian Beitzinger conducted peptide adsorption experiments onto DMSN, DMON, DMON_c. Dr. Christoph Jung conducted the computational peptide modelling studies. Dr. Kanishka Tiwary performed the *in vitro* cell experiments, as well as data analysis, interpretation, and visualization thereof. Prof. Timo Jacob, Prof. Patrick Hermann, and Prof. Mika Lindén acquired financial support, developed, conceptualized, and supervised the work. All authors contributed to the article and have reviewed and edited the manuscript.

.

2. Publication I

Surface functionalization affects the retention and biodistribution of orally administered mesoporous silica nanoparticles in a colitis mouse model.

Roman Schmid, Meta Volcic, Stephan Fischer, Zhi Qu, Holger Barth, Amirali Popat, Frank Kirchhoff, Mika Lindén

Scientific Reports, 2023, 13, 20175.
https://doi.org/10.1038/s41598-023-47445-6

Published by Springer Nature, Copyright © 2023.
This is an open access article under the CC BY 4.0 license
(https://creativecommons.org/licenses/by/4.0/).

scientific reports

Check for updates

OPEN

Surface functionalization affects the retention and bio-distribution of orally administered mesoporous silica nanoparticles in a colitis mouse model

Roman Schmid[1], Meta Volcic[2], Stephan Fischer[4], Zhi Qu[3], Holger Barth[4], Amirali Popat[3], Frank Kirchhoff[2] & Mika Lindén[1]✉

Besides the many advantages of oral drug administration, challenges like premature drug degradation and limited bioavailability in the gastro-intestinal tract (GIT) remain. A prolonged residence time in the GIT is beneficial for enhancing the therapeutic outcome when treating diseases associated with an increased intestinal clearance rate, like inflammatory bowel disease (IBD). In this study, we synthesized rod-shaped mesoporous silica nanoparticles (MSNs) functionalized with polyethylene glycol (PEG) or hyaluronic acid (HA) and investigated their bio-distribution upon oral administration in vivo. The negatively charged, non-toxic particles showed different accumulation behavior over time in healthy mice and in mice with dextran sulfate sodium (DSS)-induced intestinal inflammation. PEGylated particles were shown to accumulate in the lower intestinal tract of healthy animals, whereas inflammation promoted retention of HA-functionalized particles in this area. Overall systemic absorption was low. However, some particles were detected in organs of mice with DSS-induced colitis, especially in the case of MSN-PEG. The in vivo findings were connected to surface chemistry-related differences in particle adhesion on Caco-2/Raji and mucus-producing Caco-2/Raji/HT29 cell co-culture epithelial models in vitro. While the particle adhesion behavior in vivo was mirrored in the in vitro results, this was not the case for the resorption results, suggesting that the in vitro model does not fully reflect the erosion of the inflamed epithelial tissue. Overall, our study demonstrates the possibility to modulate accumulation and retention of MSNs in the GIT of mice with and without inflammation through surface functionalization, which has important implications for the formulation of nanoparticle-based delivery systems for oral delivery applications.

Oral drug delivery offers many advantages over other administration routes in terms of patient compliance, cost effectiveness, and avoidance of infection and pain. However, oral delivery is also challenging, especially when it comes to administration of macromolecular drugs, due to the harsh conditions prevailing in the GIT, like varying pH, and enzymatic activity. Additional challenges include reduced exposure of cells to the therapeutics due to shielding through the mucosal barrier and consequently fast transportation off-site along with intestinal contents resulting in low overall bioavailability[1–3]. Approaches to overcome the latter include the development of long-lasting drug delivery platforms accumulating at the intestinal wall[4]. Such delivery platforms may be based on mesoporous silica nano- or microparticles, which offer distinct benefits due to their high porosity and specific surface area, as well as their tunable size, shape and charge. Especially interesting is their straightforward surface functionalization. With the aim to increase their oral bio-availability, mesoporous silica particles (MSNs) have been loaded with a variety of therapeutics, for example insulin[5,6], budesonide[7], 5-amino salicylic acid[8], paclitaxel[9], antitubercular agents[10], antibiotics[11] or notch inhibitors[12]. In general, silica is considered to

[1]Inorganic Chemistry II, Ulm University, 89081 Ulm, Germany. [2]Institute of Molecular Virology, Ulm University Medical Center, Ulm, Germany. [3]School of Pharmacy, The University of Queensland, Brisbane, QLD, Australia. [4]Institute of Experimental and Clinical Pharmacology, and Toxicology and Pharmacology of Natural Products, Ulm University Medical Center, Ulm, Germany. ✉email: mlinden@uni-ulm.de

be safe by the US Food and Drug Administration (FDA) and the European Food Safety Authority (EFSA)[13] and oral administration of mesoporous silica particles at doses of 9 g per day was well tolerated in human trials[14,15].

A pre-requisite for accumulation at the intestinal epithelium is that the carrier itself should show a pro-longed retention in the GIT, and that transportation off-site either via intestinal absorption or via excretion along with the luminal contents is low. A previous study by Li et al.[16] examined how the shape of MSNs influences their bio-distribution upon oral administration. Here, negatively charged, all-silica particles with different aspect ratios (AR) of 1 (= spherical particles), 1.75 and 5 and a particle length of 85 nm, 146 nm and 483 nm, respectively, were examined. The particles were absorbed into systemic circulation already after 2 h and were detected in defense organs (spleen and liver) up to 72 h whereas the elongated particles (AR 5) were overall less abundant in internal organs over the time periods studied. Furthermore, the spherical particles were excreted both via feces and the urine, while elongated particles were almost exclusively cleared through the feces, and at a rate which was slower than that of the spherical counterparts. Similar results were reported by Zhao et al.[17], where systemic absorption and accumulation in defense organs was pronounced for spherical particles, and these exhibited shorter circulation times as compared to long-rod MSNs (AR 4). 7 days post-administration, concentrations of elongated MSNs (AR 4) were still elevated in the organs and in the feces. The same study reported that elongated MSNs were more retained in the colon at 12 h post-administration as compared to spherical particles. Overall, systemic absorption of rod-like particles seemed to be low, but at the same time, residence times in the GIT were prolonged.

One major obstacle a drug transporter encounters on its path to the epithelium is the mucus barrier of which the main component is glycosylated mucin-2 proteins forming a dense hexagonal mesh-like hydrogel. These mucus layers act as natural diffusion barrier against pathogens, bacteria as well as drug carriers leading to their entrapment and fast clearance from the GIT[18,19]. An important factor influencing the interaction of potential drug carriers with the mucus barrier and therefore their availability at the intestinal wall is their size. The ability of particles to diffuse through mucus is inversely correlated with their size, and hardly occurs for particles having diameters exceeding 200 nm[20,21].

Another key parameter influencing the interaction of nanoparticles with mucus is their surface chemistries. For example, it is well known that surface functionalization with PEG reduces particle-mucin interactions, therefore enabling the particles to penetrate easily through the mucus[22–24]. The effect is more pronounced for high PEG packing densities, and can be affirmed over a wide molecular weight range[25–27]. On the other hand, mucus-adhesiveness is characterized by strong interactions with mucins, a property well-known for polymers like chitosan[2]. However, other than the term suggests, mucus-adhesiveness might actually be counteractive when it comes to delivery of therapeutics towards the healthy intestinal epithelium[19]. Mucus-adhesive particles are unlikely to penetrate through the mucosal barrier towards the epithelium, and are therefore more prone to be transported off-site due to rapid mucus turnover rates[28]. A comparative study of the translocation of PLGA micro- and nanoparticles, either coated with mucus-adhesive chitosan or mucus-penetrating PEG, across colonic tissue ex vivo, demonstrated that chitosan coated particles did not enter the mucosa, but negatively charged PEGylated particles did, and were eventually found translocated across the mucosa[29]. Increased translocation and permeation in vivo has also been reported for positively charged PEGylated MSNs loaded with PEI-coated carbon dots[30].

In vitro models of the intestinal epithelium are widely used to study toxic effects on epithelial integrity, drug permeation or internalization of drug carriers. These models are typically comprised of a dense Caco-2 cell layer cultivated on permeable membranes and can be further refined by introducing additional cell lines as co-cultures, such as mucus producing HT29 cells, as well as Raji cells in order to promote differentiation into M-cells. This results in triple-co-cultures closely mimicking the intact intestinal epithelium in a healthy state[31–37]. However, the intactness of the intestinal mucosa can be affected by a variety of diseases, especially in the case of IBD. IBD is a generic term for Crohn's disease and ulcerative colitis, both resulting in chronic inflammation of the GIT and disruption of the mucosal integrity followed by infiltration of immune cells and pathogens, which typically results in symptoms like diarrhea, weight loss, abdominal pain and ulceration[38]. While Crohn's disease can affect the whole GIT, inflammation and ulceration in ulcerative colitis is mostly limited to the lower parts of the GIT[39]. Additionally, ulcerative colitis is accompanied with faster colonic transit times[40], pronouncing the urge for the design of a drug delivery platform exhibiting accumulation and prolonged retention at the intestinal wall. While the healthy intestinal epithelium may be modelled in vitro to some extent, in vivo models are widely used to mimic the conditions present in IBD. A well-established in vivo model to reassemble the clinical picture of ulcerative colitis is dextran sulfate sodium (DSS)-induced colitis, which results in reproducible alteration of the mucosal barrier, as well as in the formation of inflamed lesions caused by infiltration of bacteria and recruitment of immune cells, such as macrophages and granulocytes[41,42]. Promising drug release profiles in DSS-induced colitis in mice with MSNs surface functionalized with the anionic, carboxylic acid group-containing hydrophilic polymer Eudragit S100 and loaded with Budesonide were recently demonstrated by Qu et al.[7]. Distribution and retention of silica particles with sizes of 200–300 nm after a single oral dose in healthy and DSS-treated mice was reported by Tam et al.[43]. The particles reached the distal colon, but no differences in accumulation between the DSS and control groups were observed, reinforcing the need for particle modifications which increase retention times in inflamed GIT. Furthermore, inflamed GIT regions are reported to be rich in cationic proteins[44,45], and anionic liposomes are reported to adhere stronger in inflamed colonic mucosa than their cationic counterparts[46]. HA is a negatively charged bio-polymer which has been shown to potentially accumulate in GIT under inflammatory conditions when used in rather complex multi-stage co-formulation approaches[47,48].

Encouraged by these findings, this work aimed at the comprehensive, direct comparison of mucus-penetrative or inflammation-targeted MSNs functionalized with either PEG or HA via well-established synthesis protocols and the influence of these polymers on the intestinal and organ-specific bio-distribution in vivo upon oral administration under both, healthy and inflammatory conditions. In order to increase their retention time, rod-shaped MSNs were synthesized exhibiting an AR of 3. The length of the particles was kept below 200 nm to enable potential penetration through the mucosal mesh. Bio-distribution of MSNs in GIT and organs were

investigated via fluorescence imaging after oral gavage of a single dose and was connected to particle accumulation on cell-based epithelial models in the presence and absence of mucus producing cells.

Experimental section

Chemicals and materials

Tetraethyl orthosilicate (TEOS), (3-aminopropyl) triethoxysilane (APTES), dry toluene, *N*-(3-dimethylaminopropyl)-*N'*-ethylcarbodiimide hydrochloride (EDC), N-hydroxysuccinimide (NHS), hyaluronic acid sodium salt from *Streptococcus Equi* (HA, 1.5–1.8 × 10^3 kDa), low molecular weight chitosan (50–190 kDa, 75–85% deacetylated), triethylamine, 3-(triethoxysilyl) propyl isocyanate, dichloromethane, IL-1β and LPS were purchased from Sigma-Aldrich Chemie GmbH, Schnelldorf, Germany. Cetyltrimethylammonium bromide (CTAB), ammonium hydroxide (28% and 32% in water), sodium hydroxide, acetic acid, methanol, ethanol, acetone and ethylene glycol were purchased from VWR International GmbH, Darmstadt, Germany. Ammonium nitrate and dialysis tubing were purchased from Carl Roth GmbH & Co. KG, Karlsruhe, Germany. (4-(2-hydroxyethyl)-1-piperazineethanesulfonic acid) (HEPES), sodium taurocholate, sodium chloride, L-α-lecithin (Egg Yolk), Immobilon-FL PVDF membranes and disodium maleate were purchased from Merck KgaA, Darmstadt, Germany. Cy5-NHS was purchased from Lumiprobe GmbH, Hannover, Germany. DMSO (amine free), Phosphate buffered saline (PBS), BCA protein assay kit and N-hydroxysulfosuccinimide (sulfo-NHS) were purchased from Thermo Fisher Scientific, Karlsruhe, Germany. ATTO647N-NHS, ATTO647N-NH2 and ATTO565-NHS were purchased from ATTO-TEC GmbH, Siegen, Germany. α-methoxy-ω-NHS polyethylene glycol with a molecular weight of 5056 Da (PEG_{5k}) was purchased from Rapp Polymere, Tübingen, Germany. Human colon adenocarcinoma Caco-2 cells (Acc No. 86010202), human colon HT29-MTX-E12 cells (Acc No. 12040401) and human lymph Raji cells (Acc No: 85011429) cells were obtained from the European Collection of Authenticated Cell Cultures (ECACC), Porton Down, United Kingdom. DMEM, RPMI, fetal bovine serum (FBS) and MEM non-essential amino acid solution were purchased from Gibco, Carlsbad, USA. L-glutamine and penicillin–streptomycin solutions were purchased from PAN-Biotech GmbH, Aidenbach, Germany. 0.4 µm 12 well PET TC-Inserts were purchased from Sarstedt AG & Co. KG, Nümbrecht, Germany. Alexa Fluor™488-Phalloidin was purchased from Invitrogen, Carlsbad, USA. 96-well plates were purchased from Corning Incorporated, New York, USA. CellTiter 96® AQ_{ueous} One Solution Cell Proliferation Assay (MTS) was purchased from Promega, Fitchburg, USA. Fluorescence-free diet Teklad Global Diet 2019S was purchased from Inotiv, Lafayette, USA. Lysis buffer (50 mM Tris pH 7,4, 150 mM NaCl, 2 mM EGTA, 2 mM EDTA, 25 mM NaF, 25 mM β-glycerophosphate, 0.1 mM NaV and proteinase inhibitor) was purchased from Roche, Mannheim, Germany. Protein sample loading buffer was purchased from Li-COR, Lincoln, USA. Anti-CD44 ab254530 Abcam and anti-actin ab8227 were purchased from Abcam, Cambridge, United Kingdom.

Synthesis of elongated, rod-shaped mesoporous silica nanoparticles

Elongated mesoporous silica nanoparticles with an aspect ratio of 2.7 were synthesized according to a modified synthesis of that originally reported by Huang et al.[49] CTAB (2.2 g, 6 mmol) was dissolved in a mixture of water (285 mL), ammonium hydroxide solution (32 wt%, 16.6 M, 5.9 mL, 98 mmol) and ethylene glycol (27.8 mL, 0.4 mol) in a 0.5 L round-bottomed flask at 60 °C. After cooling to room temperature (RT), TEOS (4.7 mL, 21.2 mmol) was added to the mixture at a stirring rate of 600 rpm and the reaction proceeded for 4 h. The particles were precipitated with ammonium nitrate (30 g, 23.5 mmol), separated via centrifugation and thoroughly washed with ethanol twice and acetone once in an ultrasonic bath for 1 h each. After drying at 60 °C in vacuo, the particles were calcined at 550 °C for 7 h (heating rate 1.5°C min^{-1}) yielding all-silica, rod-shaped mesoporous silica nanoparticles, entitled "MSN-c".

Post-functionalization of MSNs with amino groups

Calcined "MSN-c" were dried at 100 °C in vacuo overnight. After dispersing the particles (300 mg, 4.6 mg mL^{-1}) in dry toluene using a focused ultrasonic bath (Covaris S220) the dispersion was transferred in a 0.25 L round-bottomed flask and stirred at 250 rpm. Upon addition of APTES (0.175 mL, 0.75 mmol), the mixture was stirred for 20 h at 85 °C. After centrifugation, the MSN were washed thoroughly with ethanol twice and acetone once in an ultrasonic bath for 30 min each. Finally, the particles were dried in vacuo at 50 °C overnight to yield "MSN-NH2".

Labelling of MSNs with a fluorescent dye

For in vivo imaging, the amino-functionalized particles (MSN-NH2) were fluorescently labeled with a Cy5-NHS dye. The particles were dispersed in 25 mM HEPES buffer (270 mg, 22 mg mL^{-1}) at pH 7.2. Subsequently, a stock solution of Cy5-NHS in DMSO (7.49 µM, 2.16 mL, 16.179 µmol) was added, as well as additional EDC (76.6 mg, 401.072 µmol) and Sulfo-NHS (89.7 mg, 413.463 µmol) to compensate for potential hydrolysis-related loss of NHS ester. After agitation for 17 h on ice, the particles were separated via centrifugation and thoroughly washed with water once and ethanol ten times in an ultrasonic bath until complete absence of fluorescence in the washing media was observed. Finally, the particles were dried in vacuo at 60 °C overnight to yield fluorescently labeled "MSN-NH2-Cy5".

For in vitro imaging, the amino-functionalized particles were fluorescently labeled with an ATTO647N dye. MSN-NH2 were dispersed in 25 mM HEPES buffer (270 mg, 10 mg mL^{-1}) pH 7.2. Subsequently, 270 µl of ATTO647N-NHS in DMSO (1.555 µM, 0.420 µmol) and 208 µl of an aqueous stock solution of EDC (7.32 µM, 1.523 µmol) and NHS (15.4 µM, 3.203 µmol) were added. After agitation at RT for 1 h the particles were separated via centrifugation and thoroughly washed with water once, ethanol thrice and methanol twice in an

ultrasonic bath until complete absence of fluorescence in the washing media was observed. Finally, the particles were dried in vacuo at 60 °C overnight to yield fluorescently labeled MSN-NH2.

The calcined MSN-c particles were fluorescently labeled with an ATTO647N dye via silane grafting as previously described by Beitzinger et al.[50] Briefly, DMSO stock solutions of ATTO647N-NH2 (1.092 µM, 0.551 mL, 0.602 µmol), triethylamine (53.256 µM, 0.015 mL, 0.799 µmol) and 3-(triethoxysilyl) propyl isocyanate (29.916 µM, 0.027 mL, 0.796 µmol) were mixed in 30 mL dichloromethane in a dry Teflon tube under argon atmosphere. The mixture was stirred at 45 °C for 17 h. Subsequently, 20 mL of dichloromethane and a dispersion of dried (in vacuo, 100 °C, 24 h) MSN-c (150 mg, 15 mg mL^{-1}) was added and the mixture was stirred at 45 °C for another 17 h. The solvent was removed with a rotary evaporator and the particles were thoroughly washed four times with ethanol and three times with methanol using an ultrasonic bath until complete absence of fluorescence in the washing media was observed. Finally, the particles were dried in vacuo at 60 °C overnight to yield fluorescently labeled MSN-c.

Grafting of PEG onto MSNs

MeO-PEG_{5k}-NHS (2.373 mM, 7.5 mL, 17.8 µmol) was dissolved in 25 mM HEPES buffer pH 7.2. To compensate for potential hydrolysis-related loss of NHS ester, EDC (17.3 mg, 90 µmol) and sulfo-NHS (39.1 mg, 180 µmol) were added, and the mixture was agitated for 35 min at RT. PEG-NHS solution (2.373 mM, 3 mL, 7.1 µmol) was mixed with a dispersion of fluorescently labeled MSN-NH2 (90 mg, 12.9 mg mL^{-1}) and the reaction proceeded for another 3 h. Upon centrifugation, the particles were thoroughly washed with water once and ethanol thrice in an ultrasonic bath for 20 min each and dried in vacuo at 60 °C overnight to yield fluorescently labeled "MSN-PEG". The amount of PEG grafted to the particles was determined by TGA. To correct for hydrolysis related mass losses, reference particles without the addition of PEG were analyzed as well.

Grafting of HA onto MSNs

HA (6 mg mL^{-1}, 10 mL) was dissolved in 25 mM HEPES buffer at pH 7.2 under agitation overnight. After the addition of EDC (192 mg, 1 mmol) and sulfo-NHS (325 mg, 1.5 mmol), the mixture was agitated for 40 min at RT. Activated HA solution (6 mg mL^{-1}, 3 mL, 18 mg) was mixed with a dispersion of fluorescently labeled MSN-NH2 (90 mg, 12.9 mg mL^{-1}) and the reaction proceeded for another 3 h. Upon centrifugation, the particles were thoroughly washed with water once and ethanol thrice in an ultrasonic bath for 20 min each and dried in vacuo at 60 °C overnight to yield fluorescently labeled "MSN-HA". The amount of HA grafted to the particles was determined by TGA. To correct for hydrolysis related mass losses, reference particles without the addition of HA were analyzed as well.

Fluorescence labelling of chitosan and adsorption onto MSNs

Chitosan was fluorescently labeled with an ATTO565 dye based on a procedure described by Huang et al.[51]. Briefly, an aqueous stock solution of chitosan in 0.1 M acetic acid (5 mg mL^{-1}, 10 mL, 50 mg) was mixed with a stock solution of ATTO565-NHS in DMSO (1.412 µM, 0.5 mL, 0.706 µmol) in 10 mL methanol. To compensate for potential hydrolysis-related loss of NHS-dye ester, EDC (0.7 mg, 3.65 µmol) and NHS (0.8 mg, 6.95 µmol) were added, and the mixture was agitated at 40 °C for 4 h, and dialyzed in 4 L of distilled water for 40 h. The fluorescently labeled chitosan was precipitated with 0.1 M sodium hydroxide solution and separated via centrifugation at 4 °C. The precipitate was thoroughly washed six times with water until complete absence of fluorescence in the washing media was observed, and finally freeze-dried to yield "Chit-565".

Functionalization of particles with ATTO565 labeled chitosan was achieved via adsorption of the polymer onto ATTO647N labeled MSN-c in 1 M sodium acetate buffer at pH 5. A stock solution of fluorescently labeled Chit-565 (4 mg mL^{-1}, 0.45 mL, 1.8 mg) was mixed with a dispersion of fluorescently labeled MSN-c (30 mg, 5.4 mg mL^{-1}) and the mixture was agitated for 2 h at RT. Upon centrifugation, the particles were thoroughly washed with water once, ethanol twice and methanol once until complete absence of fluorescence in the washing media was observed. The particles were dried in vacuo at 60 °C overnight to yield fluorescently labeled "MSN-Chit". The amount of chitosan adsorbed onto the particles was determined by fluorescence intensity measurements of the adsorption supernatant.

Characterization of silica nanoparticles

Thermogravimetric analysis (TGA) was performed at a heating rate of 10 °C min^{-1} in nitrogen/oxygen (70%/30%) atmosphere on a TG209 F1 Libra (Netzsch, Germany). Nitrogen sorption measurements were conducted on a Quadrasorb-1 (Quantachrome Instruments, Germany) at −196 °C after drying the particles in vacuo at 100 °C for 22 h. The specific surface areas were determined using the BET method. Pore diameters and pore volumes were calculated via equilibrium NLDFT kernel (silica, cylindrical pores) in a relative pressure range of $p\,p_0^{-1} = 0–0.9$. The external surface areas were estimated by t-plot method in the relative pressure range of 0.62–0.78. Zeta potentials were measured three times with a Zetasizer NanoZS Zen3600 (Malvern Panalytical, Germany) in aqueous 1 mM KCl solution or 25 mM HEPES buffer (pH 7.4) and a particle concentration of 0.1 mg mL^{-1}. Particle shape and size were examined with a Jeol 1200 (Jeol, Germany) transmission electron microscope (TEM) using a HT voltage of 120 kV and beam current of 65 µA. Electron micrographs of thin section were recorded after embedding the MSNs in Epon® resin and cutting with a microtome. Fluorescence intensities of the labelled particles were measured with a Spark 10 M microplate reader (Tecan, Crailsheim, Germany).

Dissolution experiments

Dissolution of MSNs were examined in fasted state intestinal fluid (FaSSiF) buffer composed of sodium taurocholate (3 mM), disodium maleate (19.12 mM), sodium chloride (68.6 mM) and lecithin (0.2 mM) adjusted

with hydrochloric acid to a pH of 6.5[52]. The particles were dispersed in the buffer at a concentration of 1 mg mL^{-1} using a focused ultrasonic bath and diluted 1:1 resulting in a concentration of 500 µg mL^{-1} (normalized on rest mass at 600 °C). The dispersions were agitated for 14 h at 37 °C and centrifuged at 20,000 rpm for 15 min. Fluorescence intensities of supernatants and non-incubated dispersions were measured in 96 well plates. After centrifugation, the particles were briefly washed with acetone, centrifuged, re-dispersed in acetone, and finally pipetted onto TEM grids for electron microscopy.

Cell cultures

Human colon adenocarcinoma cell line Caco-2 (Acc No. 86010202) and HT29-MTX-E12 ("HT29") cells (Acc No. 12040401) were obtained from the European Collection of Authenticated Cell Cultures (ECACC, UK) and cultured in DMEM containing 20% FBS, 1% MEM non-essential amino acid solution, 1% L-Glutamine and 1% penicillin–streptomycin solution in a humidified atmosphere of 5% CO_2 at 37 °C. Human lymphoma cell line Raji (Acc No: 85011429) was purchased from ECACC and grown in RPMI medium containing 10% FBS, 1% L-Glutamine and 1% penicillin–streptomycin solution in a humidified atmosphere of 5% CO_2 at 37 °C.

Evaluation of cellular toxicity

1.1×10^6 Caco-2 cells were seeded in a 96-well plate for 48 h. The particles were dispersed in DMEM/10% FCS with a focused ultrasonic bath at different concentrations and added to the cells by diluting them 1:1, resulting in particle concentrations of 500 µg mL^{-1}, 250 µg mL^{-1}, 100 µg mL^{-1} and 50 µg mL^{-1} (normalized on silica rest mass at 600 °C), respectively. Then, cells were incubated with the respective components for either 6 h or 24 in serum containing medium for cytotoxicity measurements. After the defined time points, the medium was removed, and the cells were washed once with 100 µL PBS. 100 µL of fresh medium was added to each well and cell viability was measured using the CellTiter 96® AQ_{ueous} One Solution Cell Proliferation Assay (MTS) according to the manufacturer's instruction. In short, a volume of the MTS substrate equal to 10% of the volume of cell culture medium present in each well was added, cells were further incubated for 2 h at 37 °C and absorbance was measured at 490 nm using a TriStar² LB 942 plate reader (Berthold Technologies, Bad Wildbad, Germany). Untreated medium only containing cells or cells treated with 20% DMSO served as negative and positive controls respectively. To visualize morphological changes, images before treatment and before addition of the MTS substrate were acquired using a LEICA DMi1 microscope connected to a LEICA MC170 HD camera (both Leica Microsystems GmbH, Wetzlar, Germany).

In vitro co-culture model of the intestinal epithelium

For the development of the intestinal epithelium model, 5×10^4 Caco-2 cells alone or Caco-2 and HT29 cells in a ratio of 7:3 were seeded on permeable PET membrane inserts. Cell culture medium was changed every second day. On day 14, 0.5×10^6 Raji cells were added to the lower compartment. Cells were further cultivated for another 6 days while the Raji cells density was monitored and kept at 0.5×10^6. For monitoring of the trans-epithelial electrical resistance (TEER), the medium was substituted with fresh cell culture medium and the electrode was inserted at a fitted depth and position. All TEER values were measured at RT using an EVOM3 Trans Epithelial Electrical Resistance meter (World precision instruments, Friedberg, Germany). Only co-cultures with comparable TEER values (> 300 Ω cm^{-2}) were used for further experiments.

For particle treatment, the MSNs were dispersed in xvivo15 medium with a focused ultrasonic bath at a concentration of 100 µg mL^{-1} (normalized on silica rest mass at 600 °C) and added to the cell cultures (n = 3) by diluting them 1:1 with xvivo15, resulting in a particle concentration of 50 µg mL^{-1}. At distinct time points, the TEER values were measured as described before. For immunostaining, the particle containing media were removed and the cells were washed with PBS, fixed with PBS/4% PFA for 20 min, washed again with PBS and permeabilized with PBS/0.5% Triton for 15min. Afterwards, the cells were washed, incubated with 0.5 µL Alexa Fluor™ 488-Phalloidin in 200 µL for 1 h, washed again and incubated with 1 µg mL^{-1} DAPI in PBS for 10 min. After another washing step, the membrane was cut out and molded onto the microscopy glass for confocal fluorescence microscopy.

CD44 overexpression was induced according to a previous report[53]. Briefly, co-cultures of Caco-2 and Raji cells were cultured as described before. At day 21, the cells were treated with IL-1β and LPS (50 ng mL^{-1} and 1000 ng mL^{-1}) for 48 h. To confirm the overexpression of CD44, western blot analysis was conducted.

The cells were lysed in lysis buffer for 20 min on ice and centrifuged at 14,000 rpm for 20 min. The protein concentrations were determined using a BCA protein assay kit. The samples were mixed with protein sample loading buffer with 10% β-mercaptoethanol, heated at 95 °C for 5 min and 60–80 µg of protein was loaded onto 8–15% SDS–PAGE gels. The electrophoresed protein samples were blotted onto Immobilon-FL PVDF membranes using the antibodies anti-CD44 (ab254530) and anti-Actin (ab8227).

Confocal laser scanning microscopy

Confocal laser scanning microscopy was conducted with a Zeiss LSM 710 (Zeiss, Jena, Germany) equipped with an EC Plan-Neofluar 40x/1.30 oil objective and four lasers (405 nm, 488 nm, 561 nm, 633 nm). Images were acquired of randomly selected areas of the cell layers with a pixel scaling of 0.69 µm × 0.69 µm × 0.30 µm, an image size of 354.25 µm × 354.25 µm and a bit depth of 16 bit. All instrument settings were kept constant for image acquisition. Image analysis and post-processing was performed with ZenBlue software (version 3.7.97.0400). Black/white values were adjusted for each channel (nuclei: 1400/44,000, actin: 2000/50,000, MSN: 2800/65,500, chitosan: 2800/65,500) and were kept constant for all acquired images. Maximal intensity projections and 3D rendered projections of on-top views were created using the software-specific tools.

Oral administration of MSNs in vivo

All animal-related experimental procedures and protocols in this study were approved by the Animal Ethics Committee of the University of Queensland, Brisbane, Australia and conducted according to National Health and Medical Research Council guidelines (AEC approval number: MRI-UQ/TRI/058/17), and are in accordance with ARRIVE guidelines. 6 weeks old, male C57BL/6J mice (n = 36) were randomized in groups of three individuals and held under standard laboratory conditions and with a 12 h light/dark cycle. After 7 days of settling, the animals were re-caged and their initial body weight was determined. For one half of the population water supply was replaced by an aqueous 1.5% dextran sulfate sodium solution (DSS) and the diet was changed to a fluorescence-free diet (Teklad Global Diet 2019S). The body weight and health score (diarrhea, rectal bleeding) of the numbered animals were daily monitored for another 7 days during which access to water was provided over the whole course. 12 h prior to administration the mice were set on a fasted state to minimize influence of food matter and feces and DSS containing water was replaced by regular water. The particles were dispersed in PBS at a concentration of 20 mg mL^{-1} using an ultrasonic probe and administered via careful oral gavage to the stomach using gavage needles. The single particle dose of 100 mg kg^{-1} was normalized on the current body weight, and 110 µL of PBS served as negative control. For each treatment/duration/health state combination three animals were used (n = 3). Sample blinding was not considered in this study as dosage determination and administration was dependent on health status and body weight of each individual numbered animal. The animals were placed back in their cages and provided with fresh water. After 6 h and 14 h, the mice were sacrificed, and the organs and GITs were immediately retrieved. All handling of live animals and organ excisions were performed by the same two investigators to ensure consistency in animal handling and reduction of stress. Particle gavage was carried out by a single researcher to ensure standardized experimental procedure. Fluorescence intensities were immediately measured using the in vivo imaging system IVIS (PerkinElmer, Waltham, USA) by placing the organs on black paper sheets. Imaging was conducted at an excitation wavelength of 570 nm (autofluorescence correction) and 640 nm and an emission wavelength of 670 nm. Image analysis was conducted with Living Image 4.8.0 (PerkinElmer, Waltham, USA). Background fluorescence subtraction for all images was conducted in order to exclude light reflection off stage. Regions of interest (ROI) were defined for each organ and the total radiant efficiencies were measured. In order to account for tissue related autofluorescence an organ specific correction factor ($k_{HC/DC} = ROI_{640nm}/ROI_{570nm}$) was calculated for healthy (HC) and DSS (DC) control animals (i.e. animals treated with PBS only) respectively for each image sequence recorded and the treated samples were corrected with the respective correction factors (fluorescence intensity $= ROI_{640nm} - (k_{HC/DC} \cdot ROI_{570nm})$).

Data analysis

The reported data are either individual values or mean values ± standard deviation (SD). The sample size (n) is specified in the respective figure legends and table captions. Particle size was determined using Zeiss ZenBlue 3.7 and a total number of 40 particles or higher was measured.

Results

Silica nanoparticle characterization

Rod-shaped mesoporous silica nanoparticles with a length of 149 ± 46 nm and a width of 54 ± 7 nm resulting in an aspect ratio of 2.7 were synthesized. Exemplary transmission electron micrographs (TEM) of the particles and ultra-thin sections are shown in Fig. 1. The particles exhibited a 2D hexagonal, MCM-41-like pore system which was aligned longitudinal to the particle's axis. CTAB used as the porogen was removed by calcination at 550 °C. The resulting all-silica particles ("MSN-c") exhibited a specific surface area of 920 $m^2 g^{-1}$ as well as a pore size and pore volume of 3.2 nm and 0.58 $cm^3 g^{-1}$. The external surface area was 157 $m^2 g^{-1}$ as calculated by the t-plot method. Nitrogen sorption isotherms and pore size distribution obtained by NLDFT calculations can be seen in Supplementary Fig. S1. The calcined particles were further covalently post-functionalized with an amino-silane

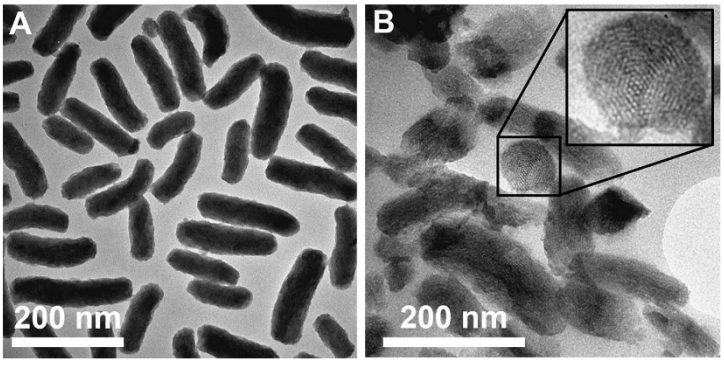

Figure 1. Transmission electron microscopy images of MSNs. (**A**) TEM image of representative basic calcined MSN-c particles. (**B**) TEM image of thin sections display the porous structure of MSNs.

("MSN-NH_2"), which led to a change in the zeta potential from a negative (−32 mV) to a positive (+15 mV) as measured in HEPES buffer at pH 7.2 (Table 1). Further functionalization through covalent attachment of a Cy5 fluorophore via EDC/NHS coupling ("MSN-NH2_Cy5") shifted the zeta potential back to a negative value of −26 mV due to the dominating extent of free silanol groups compared to decreasing amounts of primary amino groups after the dye attachment. The presence of free amino-groups after dye attachment was evident by a zeta-potential of +28 mV as measured in non-buffered 1 mM KCl (pH 5.7) (Supplementary Figure S2). The free amino groups were utilized to further covalently functionalize the particles with HA ("MSN-HA") and PEG ("MSN-PEG"). The degree of functionalization was measured via thermogravimetric analysis (TGA) (Supplementary Fig. S3), where the mass loss in the temperature range of 150°C to 700°C of each particle was normalized on the particle weight at 150 °C. Additionally, the mass loss was corrected for silica condensation-connected mass loss, by use of a reference sample which was treated under the same synthesis conditions, but without the addition of polymer. The quantity of HA and PEG attached to the MSNs were rather low (3.7 wt% and 4.7 wt%), which may be caused by partial obstruction of the external amino functions by the fluorophore and/or diffusion limitation of polymers into the porous space, where the latter would result in predominant functionalization of the outer particle surface. Nevertheless, the amount of grafted polymer was sufficient to further shift the zeta potential of MSN-HA towards more negative values as compared to the fluorescently labeled particles. Contrary to that, no change of absolute zeta potential was observed upon PEGylation.

Mesoporous silica nanoparticles do not dissolve under simulated GIT conditions

Silica nanoparticles are well-known for their ability to dissolve in aqueous media which is an important key parameter for biodegradability and biocompatibility. Mesoporous all-silica nanoparticles have been reported to completely dissolve in simulated body fluid at neutral pH within hours[54]. However, therapeutic platforms intended for oral administration of drugs need to be intact long enough to ensure the delivery of their cargo to the site of therapeutic action, e.g. the colonic wall. To assess whether our particles could withstand premature dissolution under dilute conditions, the MSNs were incubated under agitation in FaSSIF buffer (pH 6.5) at 37 °C, and a rest mass-normalized silica concentration of 500 µg mL^{-1} for 14 h. After incubation, the particles were recovered by centrifugation, and their structural integrity was examined via TEM (Fig. 2). The functionalized MSNs showed only minor signs of dissolution in the aqueous buffer, and the pore structure was still intact. Also, no alteration of particle length or width was observed. Thus, it can be concluded that structural integrity is preserved over time courses relevant for oral administration of MSNs. Moreover, fluorescence measurements of the dissolution supernatants revealed that around 85% of the dye were still attached to MSN-HA and MSN-PEG

	Functionalization degree (wt.%)	Functionalization degree (µmol g^{-1} SiO_2)	Zeta potential (mV)
MSN-c	–	–	− 32 ± 5
MSN-NH2	9.1	56.29	+ 15 ± 3
MSN-NH2_Cy5	–	–	− 26 ± 5
MSN-PEG	4.7	11.68	− 22 ± 4
MSN-HA	3.7	0.03	− 34 ± 4

Table 1. Zeta-potentials measured in 25 mM HEPES buffer (pH 7.4) and functionalization degrees measured via TGA of synthesized MSNs (zeta potentials: mean ± SD, n = 3).

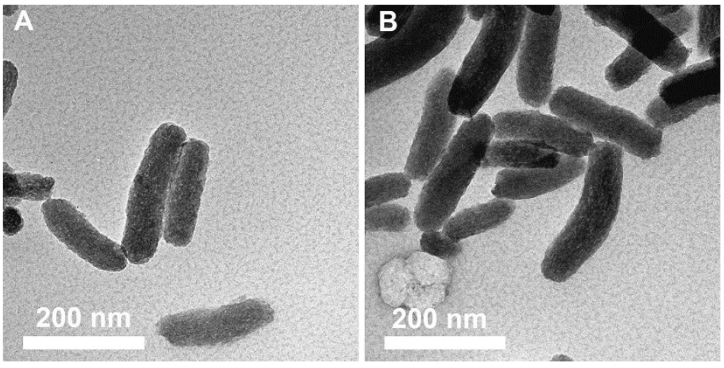

Figure 2. Transmission electron microscopy of (**A**) MSN-HA and (**B**) MSN-PEG after dissolution experiments. The particles were incubated in FaSSIF buffer (pH 6.5) for 14 h under agitation at 37 °C, and at a rest mass-normalized silica concentration of 500 µg mL^{-1}.

respectively after incubation (Supplementary Fig. S4) confirming that the particle's fluorescent label and polymeric functionalization can withstand this treatment. However, the conditions simulated here are of course not fully mimicking the conditions the particles would encounter under in vivo conditions, where the composition of the intestinal fluid is much more complex and is comprised of a wide variety of constituents, e.g. proteins, fatty acids or food particles. In general, adsorption of biological compounds is known to decrease the dissolution kinetics of mesoporous silica[55–57]. Recently, Iqbal et al.[58] demonstrated that elongated mesoporous silica particles with a length of 1 µm were not degraded after complete passage through the whole GIT in mice as well as in human trials and that the pore structure remained unaffected even under the strongly varying pH values present in the GIT. In the present study, the particles were orally administered in mice as a single particle dose of 100 mg kg^{-1}. Considering the body weight and overall gastrointestinal volume of average mice to be approximately 20 mg and 1.34 mL respectively[59], this would result in a mean concentration along the GIT of 1.5 mg mL^{-1}. This is much higher than the reported silica solubility limit of roughly 120 µg mL^{-1} under low salt conditions[60], and the particle concentrations used in our in vitro dissolution experiments, which were conducted under even more dilute conditions in compliance with a more fluid gastro intestinal content as it is typical for diseases affecting the GIT (e.g. IBD). This gives further support that the particles used in this study are stable against dissolution under the in vivo conditions.

Intestinal distribution of MSNs depends on functionalization type

To investigate the local distribution within the GIT depending on the state of inflammation, a well-established in vivo mouse model to mimic the alteration of the mucosal barrier was used[41,42,61,62]. Erosion of the mucosal barrier is one of the symptoms of inflammatory diseases like ulcerative colitis. DSS containing water was orally administered to mice over a course of seven days, and the state of inflammation was indicated by the development of diarrhea and bloody stool consistency. In general, DSS-related effects are limited to the lower GIT (colon and cecum) epithelium resulting in reproducible alteration of the mucosal barrier, decreasing epithelial structures, as well as formation of inflamed lesions caused by recruitment of immune cells such as macrophages and granulocytes. Fluorescently labeled MSN-HA and MSN-PEG were dispersed in PBS and orally administered to healthy and DSS-treated mice via gavage as a single dose of 100 mg kg^{-1}, which corresponded to approximately 2 mg per mouse. Fluorescence intensities of both particle types were similar as shown in Supplementary Fig. S5. After 6 h and 14 h mice were sacrificed, and GITs as well as organs were excised. Fluorescence intensities were measured using an in vivo imaging system (IVIS) with an excitation/emission wavelength of 640/670 nm. Representative fluorescence images of GITs are shown in Supplementary Fig. S6. Tissue-related autofluorescence was corrected for by recording additional images with an excitation/emission wavelength of 570/670 nm for control animals that had not been treated with MSNs (see experimental for details). Autofluorescence-corrected intensities of stomach, small intestine, cecum and colon 6 h and 14 h after gavage are shown in Fig. 3.

At 6 h post-administration, particles were already present in the lower GIT regions (cecum and colon) irrespective of the health state and particle surface chemistry. This finding is in line with reported transit times of 6–8 h in healthy mice[63]. Thus, the 6 h time point was used as a reference for further analysis of different particle behavior over time within one model. However, a direct cross-comparison of particle retention at fixed timepoints between models is difficult due to increased gastro-intestinal transit times during the acute phase of DSS-induced colitis[64,65]. Thus, we based our discussion on comparison of results obtained for a given mouse model.

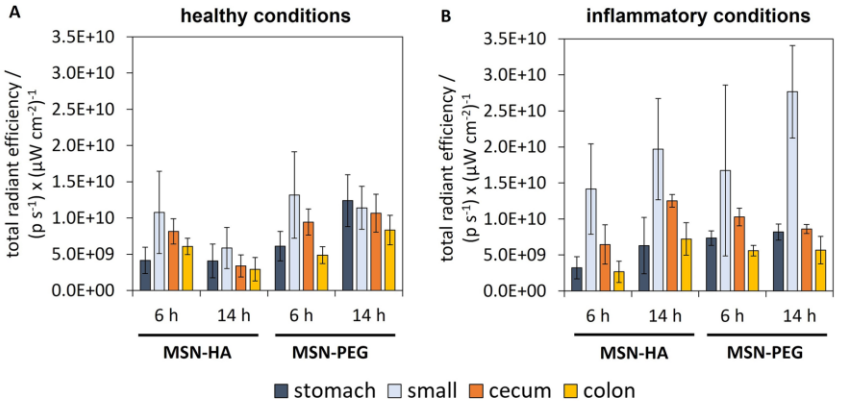

Figure 3. Gastro-intestinal distribution of fluorescently labeled MSNs. GITs were excised from (**A**) healthy mice and (**B**) mice with DSS-induced inflammation 6 h and 14 h after oral gavage of a single dose of 100 mg kg^{-1}. Fluorescence intensities were measured via IVIS with an excitation/emission wavelength of 640/670 nm and were corrected for tissue-related autofluorescence based on control animals. (mean ± SD, n = 3).

14 h after gavage of MSN-PEG to healthy animals, the intensity in the small intestine was very similar to that measured after 6 h. This would indicate a steady particle influx from the stomach. The role of the stomach as long-lasting particle reservoir is in line with results reported in a recent study, where solid lipid nanoparticles were found in the stomach even 12 h post-gavage[66]. However, the MSN-PEG particles were more abundant in the lower GIT at 14 h as compared to 6 h post-gavage, indicating some level of particle retention in this region. Interestingly, the exact opposite was the case for MSN-HA in healthy mice, for which particle-related fluorescence was decreased by a factor of around 2 for the small intestine, the cecum and the colon between the 6 h and the 14 h time-point, highlighting the GIT clearance of these MSNs. In mice with DSS-induced inflammation, the amount of MSN-PEG present in the GIT remained unchanged over time, again indicating particle influx from the stomach. Intriguingly, a completely different picture can be drawn for MSN-HA in DSS-treated mice. A strong increase in particle fluorescence over time was observed for the cecum and the colon by a factor of about 2 and 3 respectively.

In addition to the particle distribution in the GIT, we examined if the particles could permeate through the epithelium and be absorbed into systemic circulation. Therefore, the internal organs were excised 6 h and 14 h post-gavage and analyzed for particle-related fluorescence. Exemplary fluorescence images of organs recorded via IVIS can be seen in Supplementary Fig. S7. Figure 4 shows autofluorescence-corrected intensities measured for the excised organs 6 h and 14 h post-gavage. Tissue-related autofluorescence levels were high, especially for large organs rich in blood like the liver, which produced unreliable data after correction for autofluorescence based on the control animals as described in the experimental section. This data was therefore omitted in the analysis. At 6 h, no MSN-HA particles were detected in the organs irrespective of the health status of mice. MSN-PEG content in organs of healthy animals was neglectable and high mouse-to-mouse variation impeded detailed data analysis. However, fluorescence levels of MSN-PEG measured after 6 h in DSS-treated mice were evident and notably increased by a factor of 18 and 2.5 for the heart/lungs and the spleen, respectively. In a previous study by Kramer et al.[67], PEGylated MSNs were found to have a pro-longed blood retention time when injected intravenously, and accumulation thereof preferentially happened in the organs of the immune system, mainly in the spleen. In the same study, high particle contents were also found in blood-rich organs like the heart/lungs due to high MSN concentrations in the blood, which could be allegedly misinterpreted as actual accumulation. Presumably, this was also the case in the present study, supported by the fact that MSN-PEG contents in diseased animals changed from 6 to 14 h. While the intensity in the heart/lungs decreased by a factor of 0.7, fluorescence levels in the kidneys and the spleen were further increased by a factor of 1.6 and 1.1, respectively. This indicates the beginning of particle clearance from the blood circulation. Weak fluorescence levels of MSN-HA were only found in the kidneys and the spleen of DSS-treated mice 14 h post-gavage, in contrast to the fit animals. In healthy mice, MSN-PEG concentrations were low indicating that PEGylated particles were able to permeate through the healthy epithelium to some minor extent. Nevertheless, particle absorption in the GIT was clearly influenced by the treatment with DSS suggesting that inflammation and disruption of the epithelial barrier can promote particle uptake into the system. However, overall organ-related intensities were minor compared to intensities measured in the GIT, indicating that the vast majority of particles remained in the GIT and were not absorbed into systemic circulation. This indicates that rod-like MSNs would be promising candidates for local, prolonged drug delivery within the GIT.

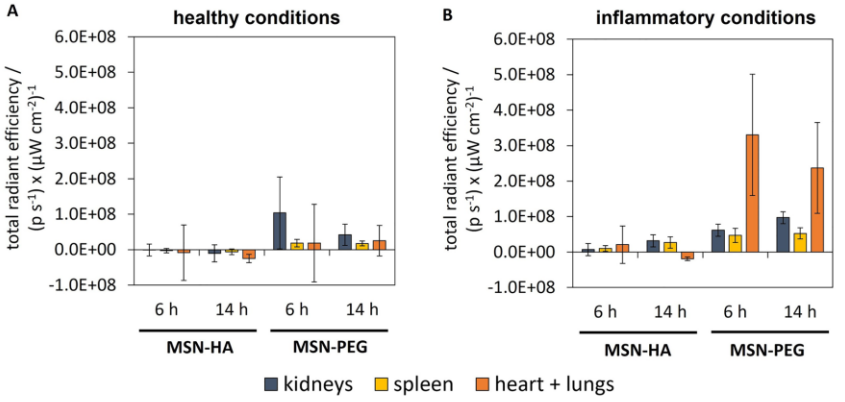

Figure 4. Bio-distribution of fluorescently labeled MSNs in organs. The organs were excised from (**A**) healthy mice and (**B**) mice with DSS-induced inflammation of the GIT 6h and 14h after oral gavage of a single dose of 100 mg kg^{-1}. Fluorescence intensities were measured via IVIS with an excitation wavelength of 640 nm and an emission wavelength of 670 nm. Auto-fluorescence correction was conducted as stated in the experimental section. (mean ± SD, n = 3).

Presence of mucus influences accumulation of MSNs on epithelial cell models

To further investigate the influence of particle surface chemistry on trans-epithelial localization and resorption, epithelial cell models with and without a mucus layer were used. Cell co-cultures comprised of Caco-2/Raji ("no mucus") or mucin producing Caco-2/Raji/HT29 ("mucus") were cultivated on permeable membranes. Fluorescently labeled MSNs were added to the apical chamber at a silica concentration of 50 µg mL^{-1} and incubated for different periods of time. After several washing steps, the cells were fixed, fluorescently stained and examined via laser scanning confocal microscopy. On-top views of maximum projections of the samples as well as rendered 3D projections and side views after incubation for 14 h are shown in Fig. 5 and additional time points can be found in Supplementary Fig. S8.

Both negatively charged MSN-HA and MSN-PEG were present on cells without mucus, and the increase of particle fluorescence intensity over time was more pronounced for MSN-PEG. Overall intensities for MSN-PEG were higher as compared to MSN-HA. However, we cannot fully exclude that sedimentation effects may also played a role for this observation. Thus, in the following we compared results obtained for mucus vs. no mucus conditions. Both studied MSNs were located on top of the epithelium and close to the cell membranes. In all cases, neither cellular uptake nor permeation of the particles into or through the cell layer were observed. Impermeability of Caco-2-based epithelial models for silica nanoparticles has been previously reported for particles with an even smaller size of 50 nm[5]. With regards to reported CD44 overexpression in inflamed intestinal regions, which can act as a potential target for HA-based drug transporters[47,68], we asked ourselves if modelling these conditions in vitro would have a pronouncing effect on particle uptake. In connection to this, self-assembling HA-based nanoparticles were reported to be internalized into CD44 expressing cells[53]. However, CD44 overexpression induced by treatment with pro-inflammatory IL-1β and LPS of Caco-2 mono-cultures had no effect on particle internalization or permeation across the model epitheliums (Supplementary Fig. S9), whether for MSN-PEG nor MSN-HA. This is advantageous if extracellular release of therapeutic drugs at the site of inflammation is desired.

However, also no particle internalization was observed in the mucin producing epithelial cell model irrespective of surface functionality, and even less MSN-HA was located on the epithelium as compared to the cell model without mucus. In contrast, the abundance of MSN-PEG was still high and less affected by the presence of mucus. We hypothesized that this was due to MSN-HA particles being unable to penetrate through the mucin layer and eventually accumulate, while MSN-PEG could penetrate the mucus. Hu et al.[66] reported that the adherence of solid lipid nanoparticles on Caco-2 and Caco-2/HT29 cell co-cultures was strongly compromised by the presence of the mucus layer because of their inability to penetrate through the layer, which is why they were easily washed away during further staining procedures. We speculated that this was also the case for MSN-HA in the present study. To verify this hypothesis, fluorescently labeled MSNs having surface silanol groups (zeta potential = − 35 mV) and comparable in size to the other MSNs studied, were further functionalized with chitosan, a polymer well-known for its mucus-impermeable properties, through adsorption from aqueous solution. The chitosan loading degree was 5.3 wt%. These particles are denoted MSN-Chit in the following. The pK_a-value of protonated chitosan is around 6.1–6.3[69], which is why the MSN-Chit exhibited a negative zeta potential of −27 mV at physiological pH. Analogous to MSN-HA and MSN-PEG, the MSN-Chit particles showed no signs of dissolution or premature dye detachment in FaSSIF buffer, nor cytotoxicity (Supplementary Figs. S4, S10, S11). In order to study potential detachment of chitosan under physiological conditions, the chitosan itself was fluorescently labeled. The fluorescence originating from chitosan co-localized with fluorescence originating from the MSN, giving proof for the stability of the adsorptive polymer functionalization. The in vitro results obtained for MSN-Chit are shown in Fig. 6. No internalization of MSN-Chit was observed, and the particles were abundant on the mucus-lacking cell layer. However, on mucin-producing cells, the particles exhibited a similar behavior to that of MSN-HA. Almost no chitosan-functionalized particles were observed in this case, emphasizing the obstructing effect mucins exercise on diffusion and accumulation of such particles.

Overall, the in vitro results fit well to the observed GIT clearance of MSN-HA in the in vivo experiments. The intact mucus layer represents a diffusion barrier for HA-functionalized particles leading them to stay localized more towards the center of the lumen, and to be readily transported off-site along with intestinal flux. On the other side, diffusion limitation does not apply to MSN-PEG to the same extent, causing pronounced permeation towards the intestinal wall, eventually leading to slower clearance in healthy animals alongside with the possibility of (low) particle resorption. However, the comparison with the in vivo results also shows the limitation of cell-based in vitro models when it comes to modelling of diseases causing complex tissue alterations. No internalization into or permeation through the cell layers were observed, in contrast to notable increases in particle content in organs for MSN-PEG in mice under inflammatory conditions.

The epithelium integrity was retained upon exposure to MSNs in vitro

To exclude toxicity or epithelial damage caused by the administration of MSNs, viability of the colonic cell line Caco-2 was assessed via MTS assay after exposure to MSN-HA and MSN-PEG for 6 h and 24 h at varying particle concentrations. Figure 7A shows that no signs of cytotoxicity were observed at both incubation times and high particle concentrations of up to 500 µg mL^{-1}, i.e. values exceeding those typically used for in vitro toxicity studies. Furthermore, cell morphology was not affected by incubation with the different MSNs as demonstrated by light microscopy images (Supplementary Fig. S12). The influence of therapeutics on the epithelial integrity as well as their accumulation and/or permeation through the epithelium are important key parameters to consider when designing promising therapy platforms intended for oral administration. Co-culture cell models comprised of the three different cell lines Caco-2, Raji and HT-29 can be utilized to draw conclusions about epithelial integrity and permeability to drugs or drug carriers by measuring the trans-epithelial electrical resistance (TEER) between the apical and basal side of the cellular layer[36,37]. MSNs were incubated on epithelial models comprised of Caco-2/Raji cells as well as cell cultures additionally including mucin producing HT-29 cells for up to 14 h

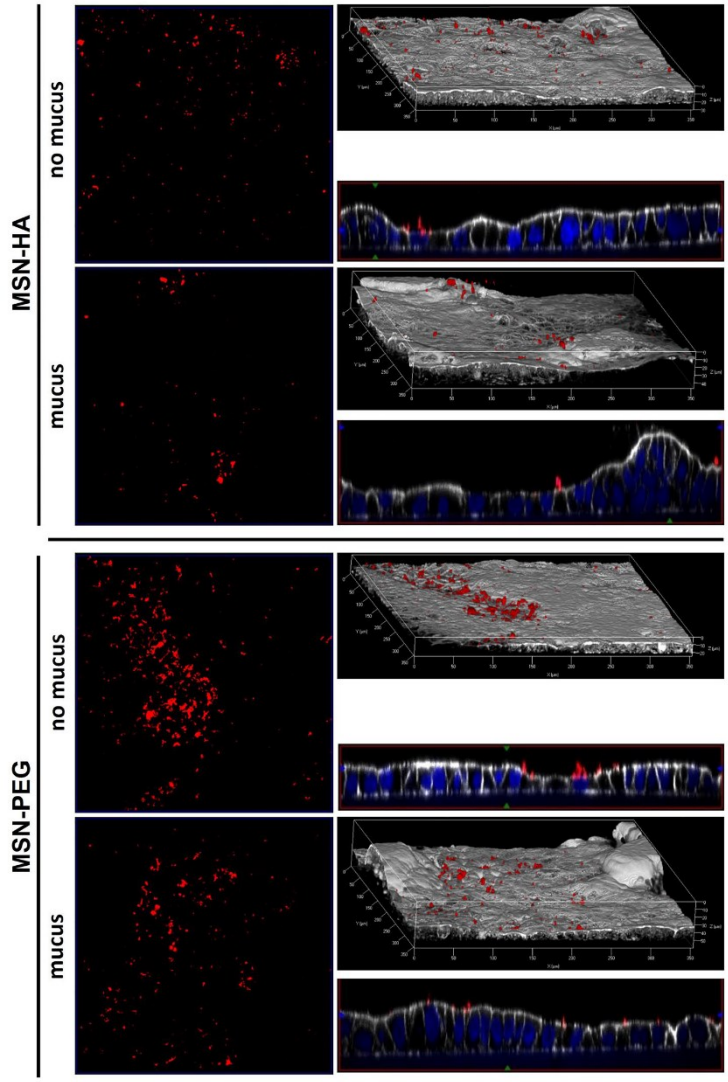

Figure 5. Adherence of MSN-PEG and MSN-HA to epithelial cell models. Representative confocal laser scanning microscopy images of random areas of Caco-2/Raji ("no mucus") or Caco-2/HT28/Raji ("mucus") co-culture cell models after incubation with MSN-PEG or MSN-HA at a silica concentration of 50 µg mL^{-1} for 14 h at 37 °C. Left column: maximal intensity projection of on-top views of the epithelial model. Right column: channel overlay of 3D rendered projections and cross-sectional Y/Z side views of channel overlays. MSNs (red), cell membrane (white), nuclei (blue). (n = 3).

at a silica concentration of 50 µg mL^{-1}. The TEER were measured at distinct times and were normalized on the TEER values measured for each sample before the beginning of the incubation period. Figure 7B shows the particle-related effects on the TEER upon addition of MSNs. In the case of MSN-HA, Caco-2 TEER values were continuously increasing and reached a level after 14 h which was 139% higher than the original resistance levels. Rising TEER levels were also observed for control cultures without particles as well as for samples including MSN-PEG in the same extent (126% of t_0), indicating that proliferation and consolidation of the Caco-2 epithelium continued. However, in the case of Caco-2/Raji/HT29 co-cultures, no continued condensing of the cellular

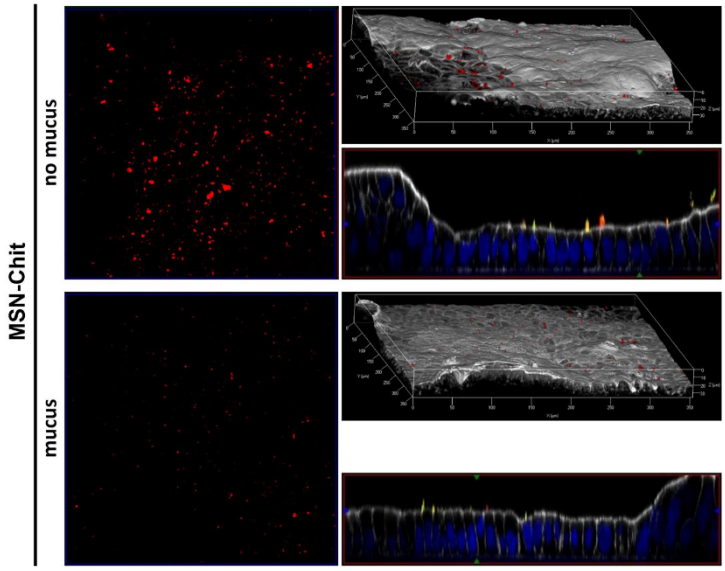

Figure 6. Adherence of MSN-Chit to epithelial cell models. Representative confocal laser scanning microscopy images of random areas of Caco-2/Raji ("no mucus") or Caco-2/HT28/Raji ("mucus") co-culture cell models after incubation with chitosan-functionalized MSNs at 50 µg mL^{-1} for 14 h at 37 °C. Left column: maximal intensity projection of on-top views of the epithelial model. Right column: 3D rendered projections and cross-sectional Y/Z side views of channel overlays. MSNs (red), Chitosan (green), cell membrane (white), nuclei (blue) (n = 3).

layer was observed, but rather a decrease in TEER values to about 80% within 1 h upon addition of both particle types. Similar observations were previously reported in a study by Lamson et al.[5] for the incubation of Caco-2 monolayers with silica nanoparticles at a concentration of 2 mg mL^{-1}, and was shown to be inversely correlated with particle size, as particles with a diameter of 20 nm and 200 nm caused a drop in TEER to about 10% and 70% of initial values respectively within the first 3 h of incubation. A recent study by Cao et al.[6] reported a decrease in TEER of Caco-2 mono-cultures and Caco-2/HT-29 co-cultures upon incubation with virus-like silica nanoparticles resulting in increased permeability of macromolecular therapeutics in vitro and in vivo. These findings were ascribed to a temporal and reversible opening of inter-cellular tight junctions, which could eventually be utilized to increase permeability of drugs through the epithelial layer. In the same studies, particle concentration dependency of TEER development was reported, and this may be the reason why no TEER drop was observed for Caco-2/Raji cell cultures in our experiments conducted at much lower particle concentrations. Compared to Caco-2 mono-cultures, permeability values for Caco-2/HT-29/Raji co-cultures are reported to be higher due to larger tight junctions[70], rendering them more prone to particle related changes in TEER values even at low concentrations. Nevertheless, the TEER values of Caco-2/Raji/HT-29 co-cultures recovered to pre-treatment levels within the next 5 h, and finally reached a level identical to the control samples after 14 h of incubation. Overall, it can be concluded that the MSNs were non-toxic over a wide concentration range, and that there were no negative effects on the integrity of complex epithelial models in vitro.

Discussion

Major challenges of oral drug delivery, *e.g.* decreased bioavailability, are supposed to be overcome by the development of delivery platforms. This would be especially the case for diseases altering the gastro-intestinal physiology and environment. To fulfill these high promises, long residence times in the GIT are a pre-requisite. Thus, this work aimed for the in-depth analysis of the intestinal and organ-specific biodistribution and retention of orally administered MSNs to mice with healthy and inflamed GIT over time. Size and shape of the particles were rationally chosen based on findings reported in literature and further expanded by the influence of surface functionality on the particle distribution in organs and GIT depending on the health status of the animals. Moreover, the obtained results from in vivo experiments were connected to differences in particle adhesion in vitro on cell models in the presence and absence of mucus.

In the lower GIT of healthy mice, increasing fluorescence intensities over time were detected in the case of MSN-PEG, whereas fluorescence intensities of MSN-HA decreased, indicating slower clearance of the PEGylated particles. Additionally, in our co-culture cell models adherence of MSN-PEG has been shown to be less affected

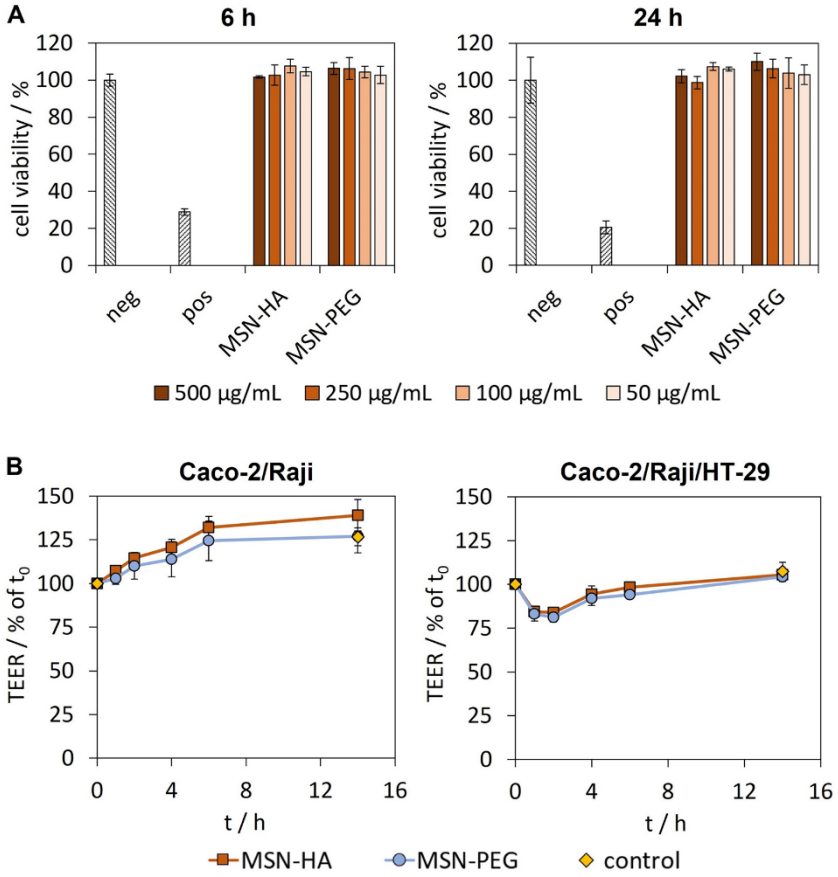

Figure 7. Toxicological evaluation of MSN-HA and MSN-PEG. (**A**) Cell viability of Caco-2 cells after incubation with varying particle concentrations after 6 h and 14 h as well as DMSO treated cells (pos) was measured with MTS-assay and was normalized on cells without treatment (neg). (**B**) Measurement of the TEER of Caco-2/Raji (left) and Caco-2/Raji/HT29 (right) epithelial models upon incubation with MSN-PEG or MSN-HA at 50 µg mL^{-1}. TEER values were measured at distinct time points and calculated as percentage of TEER before the addition of the particles (mean ± SD, n = 3).

by the presence of mucus. On the other hand, MSN-HA were less abundant on mucus-secreting cell layers as compared to the cell cultures without mucus, which was also the case for MSN-Chit. This implicates, that the different bio-distributions in vivo were based on alteration of mucus-penetrability by the polymeric functionalization leading to different luminal localization and excretion rates. Maisel et al.[24] reported pronounced deposition of mucus-penetrating polystyrene particles at the intestinal wall via analysis of intestinal cross-sections. In contrast, their mucus-adhesive analogues were localized within the intestinal lumen unable to penetrate through the mucus towards the epithelium, resulting in transportation off-site along with the intestinal flux. However, no statements about differences regarding retention and resorption of such particles were made. Additionally, it was previously demonstrated that PEGylation of PLGA particles can inhibit mucin binding followed by increased particle mobility, as well as coverage on mucosal tissues, and effective penetration close towards the epithelium in vaginal and colorectal tissues in vivo[25,71]. These effects were reported to be dependent on the surface density of the PEG chains which were in the range of 0.07 to 0.1 chains/nm^{-2}, i.e. values comparable to the MSN-PEG used in this study (0.05 chains/nm^{-2}). In DSS-treated mice with damaged mucosal barriers a completely different trend was observed for the HA-functionalized particles as compared to MSN-PEG. Intensities in the cecum and the colon strongly increased over time, indicating high affinity towards the disrupted mucosa and potential accumulation of MSN-HA in the inflamed tissue. This finding fits well to a previous study where complex hierarchically structured 35 µm vehicles (AP@PSi-HA@HPMCAS) based on HA-functionalized silicon nanoparticles showed

greater retention (but no tissue resorption) in mice with DSS-induced colitis as compared to healthy mice 2 h and 5 h post-administration, a result which was mainly ascribed to the negative particle charge[48]. Furthermore, it is reported that positively charged proteins such as transferrin or eosinophil are abundant on the surface of damaged epithelia which could potentially offer increased affinity of drug delivery platforms with a negative surface charge[44,45]. In another study, rectally administered HA-based hydrogels (without particles) showed increased affinity towards inflammatory regions of the GIT induced by TNBS treatment[72]. However, electrostatic interaction of such proteins is not expected to account for anionic PEGylated MSNs due to the well-known inhibiting effect PEG exerts on protein adsorption.

In general, resorption of bare silica nanoparticles by healthy intestinal tissue is reported to result in accumulation in the organs of the RES, where rod-shaped particles remained longer in the systemic circulation than spherical particles[16,17]. This stands in contrast to a study demonstrating increased drug permeability through opening of tight junctions by incubation with 50 nm spherical silica particles in vitro, but where no intestinal particle resorption was observed in vivo[5]. In the present study, mucosal inflammation and erosion in mice treated with DSS resulted in steady MSN-PEG amounts in the GIT, but the amounts in organs like kidneys, spleen and heart/lungs were increased. PEGylation has been reported as a means to increase the translocation and infiltration of nanoparticles on/into inflamed mucosal biopsies of IBD patients[29], which explains their pronounced resorption into the system in our case and thus steady fluorescence intensities in the GIT. Additionally, colonic permeability in general has been demonstrated to be increased in DSS-induced colitis due to alteration of the tight junction protein ZO-1[73,74].

Cell-based epithelial models (mono- and co-cultures) are a widely used means for toxicity and drug permeability studies[5,6,70,75,76], and are also utilized to examine the epithelial transport of drug delivery platforms. Schimpel et al.[37] compared the uptake of 50 and 200 nm polystyrene particles on Caco-2 mono-cultures as well as on mucus producing co-cultures. Internalization of particles was observed for Caco-2 cell layers. However, their uptake was strongly reduced by the presence of mucus which led to immobilization of the particles. Integration of M-cells into the epithelium again promoted internalization in all cases, and the uptake was pronounced for the 50 nm particles, whereas the 200 nm NP were found to be accumulated on top of the cell layers to a higher extent. In contrast, neglectable particle internalization and translocation of 50 nm MSNs on Caco-2 mono-cultures were reported by Ye et al.[77], where the majority of particles adhered on top of the cell layer. In the present study, no internalization into Caco-2 mono- or co-cultures was observed, whereas accumulation of MSN-PEG in organs of DSS-treated mice was found, thus pointing out the need for more advanced in vitro models to simulate intestinal resorption especially in cases of epithelial erosion and inflammation. Therefore, multi-layer co-cultures including macrophages and dendritic cells to study inflammatory responses and the role of macrophage infiltration on particle uptake and therapeutic effects[78,79] or in vitro models with realistic 3D environments, for example organoids or tissue engineered architectures[80–83], have been proposed in order to minimize in vivo studies. However, these models have drawbacks on their own, e.g. work-intensiveness and time-consumption, omitting high-throughput screening of components and parameters, and may be reserved for most promising candidates. Nevertheless, we demonstrated here the suitability of such epithelial models to simulate accumulation depending on the presence of mucus from which predictions regarding intestinal retention could eventually be made.

Conclusions

In the present study, rod-shaped mesoporous silica nanoparticles were synthesized and further functionalized with PEG or HA. Upon oral administration of the particles to healthy mice and animals exhibiting DSS-induced colitis, the biodistribution in the GIT and organs over time was investigated via in vivo fluorescence imaging. In all cases, MSNs were found to be localized in all compartments of the GIT already 6 h after administration and to be still present after 14 h. While MSN-PEG remained abundant in the lower GIT of healthy animals over time, MSN-HA experienced continuous clearance. This was shown to be caused by differences in adherence of the polymer-functionalized particles to cell-based epithelial models in vitro. In the presence of a mucus layer, which acted as a diffusion barrier for MSN-HA, diminishing particle accumulation on the cell layers was observed. However, in mice with DSS-colitis, the MSN-HA particles were shown to accumulate in the lower compartments of the GIT, *i.e.* in the cecum and in the colon. Moreover, the possibility of particles to be taken up into the body and their biodistribution in other organs was examined. Particle resorption was found to be strongly dependent on animal health status and particle functionalization type. No MSNs were observed in organs of healthy mice, but intestinal inflammation promoted resorption of the particles, which was especially the case for MSN-PEG. Here, particles were found in the kidneys, the spleen and the heart/lungs 6 h post-administration, and signs of beginning blood clearance were found. Systemic uptake of MSNs could not be predicted by in vitro experiments where no internalization or permeation was observed, demonstrating the need for more ingenious in vitro systems to model the complex environment present in the inflamed GIT.

Overall, this work provides valuable information on particle accumulation and uptake under different conditions in vitro and in vivo. Although only semi-quantitative statements about particle biodistribution can be drawn from these results, this study serves as basis for further research to elucidate the quantitative portions of these MSN types present in the GIT under healthy and inflammatory conditions. The pronounced differences in particle accumulation dependent on the functionalization with PEG or HA are evident, underlining the high potential of MSNs as long-lasting delivery platform for oral drug delivery applications.

Data availability

The datasets generated during and/or analyzed during the current study are available from the corresponding author on reasonable request.

Received: 29 June 2023; Accepted: 14 November 2023
Published online: 17 November 2023

References

1. Florek, J., Caillard, R. & Kleitz, F. Evaluation of mesoporous silica nanoparticles for oral drug delivery—Current status and perspective of MSNs drug carriers. *Nanoscale* **9**, 15252–15277 (2017).
2. Nunes, R., das Neves, J. & Sarmento, B. Nanoparticles for the regulation of intestinal inflammation: Opportunities and challenges. *Nanomedicine* **14**, 2631–2644 (2019).
3. Raza, A. *et al.* Solid nanoparticles for oral antimicrobial drug delivery: A review. *Drug Discov. Today* **24**, 858–866 (2019).
4. Date, A. A., Hanes, J. & Ensign, L. M. Nanoparticles for oral delivery: Design, evaluation and state-of-the-art. *J. Control. Release* **240**, 504–526 (2016).
5. Lamson, N. G., Berger, A., Fein, K. C. & Whitehead, K. A. Anionic nanoparticles enable the oral delivery of proteins by enhancing intestinal permeability. *Nat. Biomed. Eng.* **4**, 84–96 (2019).
6. Cao, Y. *et al.* Virus-like silica nanoparticles enhance macromolecule permeation in vivo. *Biomater. Sci.* **13**, 4508–4521 (2023).
7. Qu, Z. *et al.* One-pot synthesis of pH-responsive Eudragit-mesoporous silica nanocomposites enable colonic delivery of glucocorticoids for the treatment of inflammatory bowel disease. *Adv. Ther.* **4**, 1–11 (2021).
8. Moulari, B., Pertuit, D., Pellequer, Y. & Lamprecht, A. The targeting of surface modified silica nanoparticles to inflamed tissue in experimental colitis. *Biomaterials* **29**, 4554–4560 (2008).
9. Wang, Y. *et al.* Overcoming multiple gastrointestinal barriers by bilayer modified hollow mesoporous silica nanocarriers. *Acta Biomater.* **65**, 405–416 (2018).
10. Ang, C. W. *et al.* Mesoporous silica nanoparticles improve oral delivery of antitubercular bicyclic nitroimidazoles. *ACS Biomater. Sci. Eng.* **8**, 4196–4206 (2022).
11. Ndayishimiye, J. *et al.* Engineering mesoporous silica nanoparticles towards oral delivery of vancomycin. *J. Mater. Chem. B* **9**, 7145–7166 (2021).
12. Desai, D. *et al.* Targeted modulation of cell differentiation in distinct regions of the gastrointestinal tract via oral administration of differently PEG-PEI functionalized mesoporous silica nanoparticles. *Int. J. Nanomed.* **11**, 299–313 (2016).
13. Diab, R. *et al.* Silica-based systems for oral delivery of drugs, macromolecules and cells. *Adv. Colloid Interface Sci.* **249**, 346–362 (2017).
14. Baek, J. *et al.* Engineered mesoporous silica reduces long-term blood glucose, HbA1c, and improves metabolic parameters in prediabetics. *Nanomedicine* **17**, 9–22 (2022).
15. Hagman, E. *et al.* Oral intake of mesoporous silica is safe and well tolerated in male humans. *PLoS One* **15**, 1–13 (2020).
16. Li, L. *et al.* Biodistribution, excretion, and toxicity of mesoporous silica nanoparticles after oral administration depend on their shape. *Nanomed. Nanotechnol. Biol. Med.* **11**, 1915–1924 (2015).
17. Zhao, Y. *et al.* A comparison between sphere and rod nanoparticles regarding their in vivo biological behavior and pharmacokinetics. *Sci. Rep.* **7**, 1–11 (2017).
18. Murgia, X., Loretz, B., Hartwig, O., Hittinger, M. & Lehr, C. M. The role of mucus on drug transport and its potential to affect therapeutic outcomes. *Adv. Drug Deliv. Rev.* **124**, 82–97 (2018).
19. Lundquist, P. & Artursson, P. Oral absorption of peptides and nanoparticles across the human intestine: Opportunities, limitations and studies in human tissues. *Adv. Drug Deliv. Rev.* **106**, 256–276 (2016).
20. Ensign, L. M. *et al.* Ex vivo characterization of particle transport in mucus secretions coating freshly excised mucosal tissues. *Mol. Pharm.* **10**, 2176–2182 (2013).
21. Yildiz, H. M., McKelvey, C. A., Marsac, P. J. & Carrier, R. L. Size selectivity of intestinal mucus to diffusing particulates is dependent on surface chemistry and exposure to lipids. *J. Drug Target.* **23**, 768–774 (2015).
22. Andreani, T. *et al.* Effect of mucoadhesive polymers on the in vitro performance of insulin-loaded silica nanoparticles: Interactions with mucin and biomembrane models. *Eur. J. Pharm. Biopharm.* **93**, 118–126 (2015).
23. Yoncheva, K., Lizarraga, E. & Irache, J. M. Pegylated nanoparticles based on poly(methyl vinyl ether-co-maleic anhydride): Preparation and evaluation of their bioadhesive properties. *Eur. J. Pharm. Sci.* **24**, 411–419 (2005).
24. Maisel, K., Ensign, L., Reddy, M., Cone, R. & Hanes, J. Effect of surface chemistry on nanoparticle interaction with gastrointestinal mucus and distribution in the gastrointestinal tract following oral and rectal administration in the mouse. *J. Control. Release* **197**, 48–57 (2015).
25. Maisel, K. *et al.* Nanoparticles coated with high molecular weight PEG penetrate mucus and provide uniform vaginal and colorectal distribution in vivo. *Nanomedicine* **11**, 1337–1343 (2016).
26. Wang, Y. Y. *et al.* Addressing the PEG mucoadhesivity paradox to engineer nanoparticles that 'slip' through the human mucus barrier. *Angew. Chem.-Int. Ed.* **47**, 9726–9729 (2008).
27. Pereira De Sousa, I., Moser, T., Steiner, C., Fichtl, B. & Bernkop-Schnürch, A. Insulin loaded mucus permeating nanoparticles: Addressing the surface characteristics as feature to improve mucus permeation. *Int. J. Pharm.* **500**, 236–244 (2016).
28. Huckaby, J. T. & Lai, S. K. PEGylation for enhancing nanoparticle diffusion in mucus. *Adv. Drug Deliv. Rev.* **124**, 125–139 (2018).
29. Lautenschläger, C., Schmidt, C., Lehr, C. M., Fischer, D. & Stallmach, A. PEG-functionalized microparticles selectively target inflamed mucosa in inflammatory bowel disease. *Eur. J. Pharm. Biopharm.* **85**, 578–586 (2013).
30. Wang, Y. *et al.* Effects of surface modification and size on oral drug delivery of mesoporous silica formulation. *J. Colloid Interface Sci.* **513**, 736–747 (2018).
31. Shah, P., Jogani, V., Bagchi, T. & Misra, A. Role of Caco-2 cell monolayers in prediction of intestinal drug absorption. *Biotechnol. Prog.* **22**, 186–198 (2006).
32. Ungell, A. L. B. Caco-2 replace or refine?. *Drug Discov. Today Technol.* **1**, 423–430 (2004).
33. Hilgendorf, C. *et al.* Caco-2 versus Caco-2/HT29-MTX co-cultured cell lines: Permeabilities via diffusion, inside- and outside-directed carrier-mediated transport. *J. Pharm. Sci.* **89**, 63–75 (2000).
34. Wikman-Larhed, A. & Artursson, P. Co-cultures of human intestinal goblet (HT29-H) and absorptive (Caco-2) cells for studies of drug and peptide absorption. *Eur. J. Pharm. Sci.* **3**, 171–183 (1995).
35. Araújo, F. & Sarmento, B. Towards the characterization of an in vitro triple co-culture intestine cell model for permeability studies. *Int. J. Pharm.* **458**, 128–134 (2013).
36. García-Rodríguez, A., Vila, L., Cortés, C., Hernández, A. & Marcos, R. Exploring the usefulness of the complex in vitro intestinal epithelial model Caco-2/HT29/Raji-B in nanotoxicology. *Food Chem. Toxicol.* **113**, 162–170 (2018).
37. Schimpel, C. *et al.* Development of an advanced intestinal in vitro triple culture permeability model to study transport of nanoparticles. *Mol. Pharm.* **11**, 808–818 (2014).
38. Guan, Q. A Comprehensive review and update on the pathogenesis of inflammatory bowel disease. *J. Immunol. Res.* **2019** (2019).
39. Seyedian, S. S., Nokhostin, F. & Malamir, M. D. A review of the diagnosis, prevention, and treatment methods of inflammatory bowel disease. *J. Med. Life* **12**, 113–122 (2019).
40. Hebden, J. M., Blackshaw, P. E., Perkins, A. C., Wilson, C. G. & Spiller, R. C. Limited exposure of the healthy distal colon to orally-dosed formulation is further exaggerated in active left-sided ulcerative colitis. *Aliment. Pharmacol. Ther.* **14**, 155–161 (2000).

41. Kiesler, P., Fuss, I. J. & Strober, W. Experimental models of inflammatory bowel diseases. *Cell. Mol. Gastroenterol. Hepatol.* **1**, 154–170 (2015).
42. Chassaing, B., Aitken, J. D., Malleshappa, M. & Vijay-Kumar, M. Dextran sulfate sodium (DSS)-induced colitis in mice. *Curr. Protoc. Immunol.* **104** (2014).
43. Tam, S. Y. J. *et al.* Intestinal accumulation of silica particles in a rat model of dextran sulfate sodium-induced colitis. *Ann. Gastroenterol.* **32**, 584–592 (2019).
44. Tirosh, B., Khatib, N., Barenholz, Y., Nissan, A. & Rubinstein, A. Transferrin as a luminal target for negatively charged liposomes in the inflamed colonic mucosa. *Mol. Pharm.* **6**, 1083–1091 (2009).
45. Peterson, C. G. B., Eklund, E., Taha, Y., Raab, Y. & Carlson, M. A new method for the quantification of neutrophil and eosinophil cationic proteins in feces: Establishment of normal levels and clinical application in patients with inflammatory bowel disease. *Am. J. Gastroenterol.* **97**, 1755–1762 (2002).
46. Jubeh, T. T., Barenholz, Y. & Rubinstein, A. Differential adhesion of normal and inflamed rat colonic mucosa by charged liposomes. *Pharm. Res.* **21**, 447–453 (2004).
47. Xiao, B. *et al.* Orally targeted delivery of tripeptide KPV via hyaluronic acid-functionalized nanoparticles efficiently alleviates ulcerative colitis. *Mol. Ther.* **25**, 1628–1640 (2017).
48. Li, W. *et al.* Hierarchical structured and programmed vehicles deliver drugs locally to inflamed sites of intestine. *Biomaterials* **185**, 322–332 (2018).
49. Huang, X., Teng, X., Chen, D., Tang, F. & He, J. The effect of the shape of mesoporous silica nanoparticles on cellular uptake and cell function. *Biomaterials* **31**, 438–448 (2010).
50. Beitzinger, B. *et al.* Delivery by dendritic mesoporous silica nanoparticles enhances the antimicrobial activity of a napsin-derived peptide against intracellular *Mycobacterium tuberculosis*. *Adv. Healthc. Mater.* **10**, 1–13 (2021).
51. Huang, M., Ma, Z., Khor, E. & Lim, L. Uptake of FITC-chitosan by A549 cells. *Pharm. Res.* **19**, 1489–1494 (2002).
52. Jantratid, E., Janssen, N., Reppas, C. & Dressman, J. B. Dissolution media simulating conditions in the proximal human gastrointestinal tract: An update. *Pharm. Res.* **25**, 1663–1676 (2008).
53. Vafaei, S. Y. *et al.* Self assembled hyaluronic acid nanoparticles as a potential carrier for targeting the inflamed intestinal mucosa. *Carbohydr. Polym.* **144**, 371–381 (2016).
54. Braun, K. *et al.* Dissolution kinetics of mesoporous silica nanoparticles in different simulated body fluids. *J. Sol-Gel Sci. Technol.* **79**, 319–327 (2016).
55. Bindini, E. *et al.* Following in situ the degradation of mesoporous silica in biorelevant conditions: At last, a good comprehension of the structure influence. *ACS Appl. Mater. Interfaces* **12**, 13598–13612 (2020).
56. Lin, C. Y., Yang, C. M. & Lindén, M. Dissolution and morphology evolution of mesoporous silica nanoparticles under biologically relevant conditions. *J. Colloid Interface Sci.* **608**, 995–1004 (2022).
57. Möller, K. & Bein, T. Degradable drug carriers: Vanishing mesoporous silica nanoparticles. *Chem. Mater.* **31**, 4364–4378 (2019).
58. Iqbal, M. N. *et al.* Mesoporous silica particles retain their structure and function while passing through the gastrointestinal tracts of mice and humans. *ACS Appl. Mater. Interfaces* **15**, 9542–9553 (2022).
59. Casteleyn, C., Rekecki, A., Van Der Aa, A., Simoens, P. & Van Den Broeck, W. Surface area assessment of the murine intestinal tract as a prerequisite for oral dose translation from mouse to man. *Lab. Anim.* **44**, 176–183 (2010).
60. Hamrouni, B. & Dhahbi, M. Analytical aspects of silica in saline waters—Application to desalination of brackish waters. *Desalination* **136**, 225–232 (2001).
61. Okayasu, I. *et al.* A novel method in the induction of reliable experimental acute and chronic ulcerative colitis in mice. *Gastroenterology* **98**, 694–702 (1990).
62. Gancarcikova, S. *et al.* Innovative animal model of DSS-induced ulcerative colitis in pseudo germ-free mice. *Cells* **9**, 1–28 (2020).
63. Padmanabhan, P., Grosse, J., Asad, A. B. M. A., Radda, G. K. & Golay, X. Gastrointestinal transit measurements in mice with 99mTc-DTPA-labeled activated charcoal using NanoSPECT-CT. *EJNMMI Res.* **3**, 1–8 (2013).
64. Kodani, M. *et al.* Association between gastrointestinal motility and macrophage/mast cell distribution in mice during the healing stage after DSS-induced colitis. *Mol. Med. Rep.* **17**, 8167–8172 (2018).
65. Lu, C. *et al.* Colonic transit disorder mediated by downregulation of interstitial cells of cajal/anoctamin-1 in dextran sodium sulfate-induced colitis mice. *J. Neurogastroenterol. Motil.* **25**, 316–331 (2019).
66. Hu, X. *et al.* Evidence does not support absorption of intact solid lipid nanoparticles via oral delivery. *Nanoscale* **8**, 7024–7035 (2016).
67. Kramer, L. *et al.* Quantitative and correlative biodistribution analysis of 89Zr-labeled mesoporous silica nanoparticles intravenously injected into tumor-bearing mice. *Nanoscale* **9**, 9743–9753 (2017).
68. Stenson, W. F. Hyaluronic acid and intestinal inflammation. *Curr. Opin. Gastroenterol.* **26**, 85–87 (2010).
69. Collado-González, M., Espinosa, Y. G. & Goycoolea, F. M. Interaction between chitosan and mucin: Fundamentals and applications. *Biomimetics* **4**, 1–20 (2019).
70. Lozoya-Agullo, I. *et al.* Usefulness of Caco-2/HT29-MTX and Caco-2/HT29-MTX/Raji B coculture models to predict intestinal and colonic permeability compared to Caco-2 monoculture. *Mol. Pharm.* **14**, 1264–1270 (2017).
71. Xu, Q. *et al.* Impact of surface polyethylene glycol (PEG) density on biodegradable nanoparticle transport in mucus ex vivo and distribution in vivo. *ACS Nano* **9**, 9217–9227 (2015).
72. Chiu, C. T., Kuo, S. N., Hung, S. W. & Yang, C. Y. Combined treatment with hyaluronic acid and mesalamine protects rats from inflammatory bowel disease induced by intracolonic administration of trinitrobenzenesulfonic acid. *Molecules* **22**, 1–24 (2017).
73. Poritz, L. S. *et al.* Loss of the tight junction protein ZO-1 in dextran sulfate sodium induced colitis. *J. Surg. Res.* **140**, 12–19 (2007).
74. Yan, Y. *et al.* Temporal and spatial analysis of clinical and molecular parameters in dextran sodium sulfate induced colitis. *PLoS One* **4**, 1–8 (2009).
75. Silva, D. S. *et al. N*-(2-hydroxy)-propyl-3-trimethylammonium, *o*-mysristoyl chitosan enhances the solubility and intestinal permeability of anticancer curcumin. *Pharmaceutics* **10**, 1–18 (2018).
76. Abeer, M. M. *et al.* Rationally designed dendritic silica nanoparticles for oral delivery of exenatide. *Pharmaceutics* **11**, 1–16 (2019).
77. Ye, D. *et al.* Low uptake of silica nanoparticles in Caco-2 intestinal epithelial barriers. *Beilstein J. Nanotechnol.* **8**, 1396–1406 (2017).
78. Leonard, F., Collnot, E. M. & Lehr, C. M. A three-dimensional coculture of enterocytes, monocytes and dendritic cells to model inflamed intestinal mucosa in vitro. *Mol. Pharm.* **7**, 2103–2119 (2010).
79. Leonard, F. *et al.* Design and in vitro characterization of multistage silicon-PLGA budesonide particles for inflammatory bowel disease. *Eur. J. Pharm. Biopharm.* **151**, 61–72 (2020).
80. Creff, J., Malaquin, L. & Besson, A. In vitro models of intestinal epithelium: Toward bioengineered systems. *J. Tissue Eng.* **12**, 1–16 (2021).
81. Cruz-Acuña, R. *et al.* Synthetic hydrogels for human intestinal organoid generation and colonic wound repair. *Nat. Cell Biol.* **19**, 1326–1335 (2017).
82. Wang, Y. *et al.* A microengineered collagen scaffold for generating a polarized crypt-villus architecture of human small intestinal epithelium. *Biomaterials* **128**, 44–55 (2017).
83. Brassard, J. A., Nikolaev, M., Hübscher, T., Hofer, M. & Lutolf, M. P. Recapitulating macro-scale tissue self-organization through organoid bioprinting. *Nat. Mater.* **20**, 22–29 (2021).

Acknowledgements
The authors want to thank Cornelia Egger and Kea Fedke for nitrogen sorption and thermogravimetric, measurements. The authors acknowledge the funding from the Deutsche Forschungsgemeinschaft (DFG, German Research Foundation) as part of the CRC 1279 "Exploiting the human peptidome for novel antimicrobial and anticancer agents"-project ID 316249678 and the Deutscher Akademiker Austauschdienst (DAAD, German Academic Exchange Service)-project ID RM2018001723. The work in the Barth group was supported by the German Research Foundation (DFG) as part of the CRC 1279 (C02)-project ID 316249678.

Author contributions
R.S.: Formal analysis, Investigation, Methodology, Validation, Visualization, Writing-original draft. M.V.: Formal analysis, Investigation, Methodology, Validation, Visualization, Writing-review & editing. S.F.: Formal analysis, Investigation, Methodology, Validation, Writing-review & editing. Z.Q.: Formal analysis, Investigation, Methodology, Validation, Writing-review & editing. H.B.: Conceptualization, Funding acquisition, Investigation, Project administration, Resources, Supervision, Validation, Writing-review & editing. A.P.: Conceptualization, Funding acquisition, Investigation, Project administration, Resources, Supervision, Validation, Writing-review & editing. F.K.: Conceptualization, Funding acquisition, Investigation, Project administration, Resources, Supervision, Validation, Writing-review & editing. M.L.: Conceptualization, Funding acquisition, Investigation, Project administration, Resources, Supervision, Validation, Writing-review & editing.

Funding
Open Access funding enabled and organized by Projekt DEAL.

Competing interests
The authors declare no competing interests.

Additional information
Supplementary Information The online version contains supplementary material available at https://doi.org/10.1038/s41598-023-47445-6.

Correspondence and requests for materials should be addressed to M.L.

Reprints and permissions information is available at www.nature.com/reprints.

Publisher's note Springer Nature remains neutral with regard to jurisdictional claims in published maps and institutional affiliations.

Open Access This article is licensed under a Creative Commons Attribution 4.0 International License, which permits use, sharing, adaptation, distribution and reproduction in any medium or format, as long as you give appropriate credit to the original author(s) and the source, provide a link to the Creative Commons licence, and indicate if changes were made. The images or other third party material in this article are included in the article's Creative Commons licence, unless indicated otherwise in a credit line to the material. If material is not included in the article's Creative Commons licence and your intended use is not permitted by statutory regulation or exceeds the permitted use, you will need to obtain permission directly from the copyright holder. To view a copy of this licence, visit http://creativecommons.org/licenses/by/4.0/.

© The Author(s) 2023

3. Publication II

Towards a simple in vitro surface chemistry pre-screening method for nanoparticles to be used for drug delivery to solid tumours.

Roman Schmid, Juliane Kaiser, Ramona Willbold, Nomousa Walther, Rainer Wittig, Mika Lindén

Biomaterials Science, 2023,11, 6287-6298.
https://doi.org/10.1039/D3BM00966A

Published by Royal Society of Chemistry, Copyright © 2023.
This is an open access article under the CC BY-NC 3.0 license
(https://creativecommons.org/licenses/by-nc/3.0/).

Biomaterials Science

ROYAL SOCIETY OF CHEMISTRY

PAPER

View Article Online
View Journal | View Issue

Check for updates

Cite this: *Biomater. Sci.*, 2023, **11**, 6287

Towards a simple *in vitro* surface chemistry pre-screening method for nanoparticles to be used for drug delivery to solid tumours†

Roman Schmid, [a] Juliane Kaiser, [b] Ramona Willbold, [b] Nomusa Walther, [b] Rainer Wittig *[b] and Mika Lindén *[a]

An efficient nanoparticulate drug carrier intended for chemotherapy based on intravenous administration must exhibit a long enough blood circulation time, a good penetrability into the tumour volume, as well as an efficient uptake by cancer cells. Limiting factors for the therapeutic outcome *in vivo* are recognition of the nanoparticles as foreign objects, which triggers nanoparticle uptake by defence organs rich in macrophages, *e.g.* liver and spleen, on the time-scale of accumulation and uptake in/by the tumour. However, the development of nanomedicine towards efficient nanoparticle-based delivery to solid tumours is hampered by the lack of simple, reproducible, cheap, and predictive means for early identification of promising nanoparticle formulations. The surface chemistry of nanoparticles is known to be the most important determinant for the biological fate of nanoparticles, as it influences the extent of serum protein adsorption, and also the relative composition of the protein corona. Here we preliminarily evaluate an extremely simple screening method for nanoparticle surface chemistry pre-optimization based on nanoparticle uptake *in vitro* by PC-3 cancer cells and THP-1 macrophages. Only when both selectivity for the cancer cells as well as the extent of nanoparticle uptake are taken into consideration do the *in vitro* results mirror literature results obtained for small animal models. Furthermore, although not investigated here, the screening method does also lend itself to the study of actively targeted nanoparticles.

Received 6th June 2023,
Accepted 2nd August 2023

DOI: 10.1039/d3bm00966a

rsc.li/biomaterials-science

Open Access Article. Published on 02 August 2023. Downloaded on 9/30/2023 4:21:47 PM.
This article is licensed under a Creative Commons Attribution-NonCommercial 3.0 Unported Licence.

Introduction

Nanoparticle-based drug delivery is seen as one of the most promising means for enhancing the therapeutic outcome due to enhanced specificity, improved drug bioavailability, and biodistribution. This is of special importance in oncology, where side-effects related to non-specific drug delivery in combination with the need for high systemic drug doses are severe problems. In the case of solid tumours, the enhanced permeability and retention (EPR) effect is supposed to help nanoparticles accumulate in the tumour.[1] Further enhancement of the cellular specificity can be attempted through linking of ligands to the outer surface of the nanoparticles, which addresses receptors that are overexpressed on the target cells. However, a large fraction of intravenously injected nanoparticles are typically removed from the blood circulation very soon after administration through immune response-triggered nanoparticle uptake by the mononuclear phagocyte system (MPS, also known as the reticuloendothelial system, RES) consisting of phagocytic cells, typically monocytes and macrophages.[2] Organs rich in phagocytotic cells are the liver and spleen, and therefore nanoparticle accumulation in these organs with time is observed upon intravenous administration of nanoparticles. Thus, in order to enhance the portion of particles getting accumulated in the tumour area, the blood circulation time should be long enough. Here, the surface chemistry of the nanoparticles naturally plays an important role. Although there is no clear consensus about the relationship between the composition of the protein corona and the biodistribution, the commonly accepted paradigm is that the recognition of nanoparticles by the MPS system correlates with the extent of opsonin binding to the nanoparticles.[3] Therefore, nanoparticles intended for intravenous administration are typically surface functionalized by a hydrophilic polymer, in most cases poly(ethylene glycol), PEG, in order to decrease the extent of serum protein adsorption.[4–7] As can be expected, not only the surface polarity but also the surface charge influences the extent of protein adsorption, and also which proteins adsorb.[8,9] Nanoparticles exhibiting a low effective charge typi-

[a]*Inorganic Chemistry II, Albert-Einstein-Allee 11, Ulm University, 89081 Ulm, Germany. E-mail: mlinden@uni-ulm.de*
[b]*Institute for Laser Technologies in Medicine & Metrology (ILM) at Ulm University, Helmholtzstrasse 12, 89081 Ulm, Germany. E-mail: rainer.wittig@ilm-ulm.de*
† Electronic supplementary information (ESI) available. See DOI: **https://doi.org/10.1039/d3bm00966a**

Open Access Article. Published on 02 August 2023. Downloaded on 9/30/2023 4:21:47 PM.
This article is licensed under a Creative Commons Attribution-NonCommercial 3.0 Unported Licence.

cally adsorb less serum proteins, which explains why zwitterionic nanoparticle coatings in addition to non-ionic polymers can be used to minimize protein adsorption.[10] Highly charged particles, on the other hand, are typically removed quickly from the blood stream by RES upon intravenous injection,[11–14] which can be attributed to enhanced protein adsorption to such particles.

However, escaping RES and thus prolonging the nanoparticle circulation time is not the only important aspect concerning the therapeutic outcome. The nanoparticles should also be able to invade the tumour and also be efficiently internalized by the target cells in order to serve as efficient drug carriers, as most anticancer drugs are active intracellularly. For example, it has been shown that a zwitterionic coating that reduces protein adsorption also lead to a lower nanoparticle uptake by HeLa cancer cells *in vitro*.[15] It has also been reported that the cell-specificity (targetability) of antibody-tagged nanoparticles towards acute myeloid leukaemia stem cells depends on the exact composition of the protein corona,[16] suggesting that a total suppression of protein adsorption may be counterproductive when aiming for high cell-specificity *in vivo*, even in the case that such nanoparticles may exhibit a prolonged blood circulation time. Cationic nanoparticles, on the other hand, are known to be internalized much more efficiently by cancer cells as compared to anionic nanoparticles,[17–20] and lead to enhanced therapeutic outcomes.[21,22] Thus, it is clear that this is a classic optimization problem, but the mutual influences of this multitude of parameters remain largely unknown, and any attempts to establish such links are associated with an immense experimental effort even when only a very small number of nanoparticles would be considered. From a nanoparticle development point of view, simple screening means would therefore be highly beneficial in order to speed up the surface chemistry optimization, and to allow focusing the detailed studies on the most promising particles for a given application. Although simple *in vitro* measurements can never fully replace *in vivo* characterizations, it is also clear that broad *in vivo* screenings are not feasible, neither from an economical nor an ethical point of view. Finding a surface chemistry that allow for a high specificity towards the target cells in combination with a fast uptake kinetics is preferable. Mesoporous silica nanoparticles (MSNs) are attracting considerable interest as drug carrier systems due to their easy functionalization, high drug loading capacities, and flexible tuning of particle size and shape. However, their biodistribution characteristics still need optimization. An increasing number of small animal *in vivo* studies have been published recently, using MSNs with different types of surface functionalities. This allows some conclusions concerning the relation between the MSN surface chemistry, the general biodistribution, and tumour accumulation of intravenously injected particles. In a recent study, hyaluronic acid-functionalized MSNs with a particle diameter of about 180 nm were shown to exhibit a long blood circulation time, much longer than corresponding cationic amino-functionalized particles.[23] In another study, an increase on the blood circulation time and in the tumour targetability of pure hyaluronic acid-based nanoparticles *via* PEGylation was demonstrated *in vivo*, where these effects were dependent on the degree of PEGylation.[24] A fast accumulation of amino-functionalized MSNs in the liver upon intravenous injection is in agreement with previous reports.[14,25] All-silica MSNs as well as carboxy-silane functionalized MSNs have also been shown to accumulate fast in liver and spleen.[26–28] PEGylation has been shown to decrease uptake in the liver in several cases, as compared to corresponding non-PEGylated particles.[24,26,29,30] On the other hand, as discussed above, amino-functionalized MSNs have repeatedly been shown to be efficiently taken up by cancer cells *in vitro* and to accumulate in solid tumours, leading to efficient tumour-directed drug delivery.[31–33]

Inspired by these literature reports, we conducted a study in order to investigate if we could mirror these results by a simple and reproducible *in vitro* uptake study involving THP-1 cells as models for naïve macrophages, and PC-3 prostate cancer cells as a cancer model. Both the selectivity at a given time-point as well as the relative amount of particles taken up by the cells are evaluated, in order to allow for classification of the particles. In addition, the results are complemented by preliminary protein corona analysis using SDS-PAGE. It is shown that the simple *in vitro* evaluation nicely mirrors the *in vivo* responses that have been seen for such particles, and this approach could potentially as such or in modified form serve as a fast pre-screening method for surface chemistry optimization of nanoparticles intended for drug delivery to solid tumours.

Experimental

Chemicals and materials

Tetramethyl orthosilicate (TMOS), (3-aminopropyl) trimethoxysilane (APTMS), 1-ethyl-3-(3-dimethylaminopropyl)carbodiimide (EDC), *N*-(3-dimethylaminopropyl)-*N*′-ethylcarbodiimide hydrochloride (EDC-HCl), *N*-hydroxysuccinimide (NHS), glycerine, hyaluronic acid sodium salt from *Streptococcus equi* (1.5–1.8 × 10^3 kDa), *O*-[2-(Fmoc-amino)-ethyl]-*O*′-(2-carboxyethyl)polyethylene glycol 3000 (Fmoc-NH-PEG3k-COOH), piperidine, dimethylformamide (DMF), 4′,6-diamidino-2-phenylindole dihydrochloride (DAPI), propidium iodide (PI) and phalloidin-TRITC were purchased from Sigma-Aldrich Chemie GmbH, Schnelldorf, Germany. cetyltrimethylammonium bromide (CTAB), sodium hydroxide, acetone, ethanol, methanol and hydrochloric acid were purchased from VWR International GmbH, Darmstadt, Germany. Carboxyethylsilanetriol di-sodium salt (CES, 25 wt% in water, 1.49 M) was purchased from ABCR GmbH & Co. KG, Karlsruhe, Germany. Ammonium nitrate, sodium dodecyl sulfate (SDS) sodium dodecyl sulfate (SDS), tris(hydroxymethyl)aminomethane (TRIS) and glycine were purchased from Carl Roth GmbH & Co. KG, Karlsruhe, Germany. (4-(2-Hydroxyethyl)-1-piperazineethanesulfonic acid) (HEPES) and Accutase were purchased from Merck KGaA, Darmstadt,

 This journal is © The Royal Society of Chemistry 2023

Open Access Article. Published on 02 August 2023. Downloaded on 9/30/2023 4:21:47 PM.
This article is licensed under a Creative Commons Attribution-NonCommercial 3.0 Unported Licence.

Germany. *N*-Hydroxysulfosuccinimide (Sulfo-NHS), phosphate buffered saline (PBS), PageRuler™ Broad range unstained protein ladder and black 96-well microplates were purchased from Thermo Fisher Scientific, Karlsruhe, Germany, fetal calf serum (FCS) was purchased from Cytiva HyClone™. ATTO647N-NH2 and ATTO647N-NHS were purchased from ATTO-TEC GmbH, Siegen, Germany. THP-1 monocyte cell line was purchased from Cell Lines Service, Eppelheim, Germany. RPMI 1640 medium, streptomycin/penicillin, glutamine, sodium pyruvate and Trypsin-EDTA were purchased from Life Technologies, Darmstadt, Germany. Fetal bovine serum was purchased from Applichem, Darmstadt, Germany. Ibitreat dishes were purchased from ibidi, Munich, Germany. The Cell Titer Blue assay was purchased from Promega, Mannheim, Germany. The FCS was heat inactivated, all other chemicals were used as supplied by the manufacturer without further purification.

Synthesis of mesoporous silica nanoparticles

Mesoporous silica nanoparticles (MSN) were synthesized as described by Rosenholm *et al.*[20] In a 2 L round-bottomed flask, 7.88 g of the surfactant CTAB (7.88 g, 21.6 mmol) was dissolved in a mixture of water (922 mL), methanol (849 mL) and sodium hydroxide solution (1 M, 4.56 mL, 4.6 mmol). A mixture of the silica precursors TMOS (2.18 mL, 14.7 mmol) and APTMS (0.36 mL, 2.1 mmol) was added at a stirring rate of 500 rpm. The solution was stirred for 45 min and consecutively reduced to 300 rpm. After 18 h, the particles were precipitated with ammonium nitrate (25 g, 19.6 mmol) and separated *via* centrifugation. In order to yield all-silica nanoparticles, the precipitate was washed with ethanol twice and with acetone once by dispersing them for 1 h each step in an ultrasonic bath. Finally, the dried particles were calcined at 550 °C for 5.5 h (heating rate 1.5 °C min^{-1}). These particles are denoted "MSN-c" in the following. For preservation of amino-functionalities the separated as-synthesized nanoparticles were, instead of calcination, washed with ethanol and the surfactant was extracted by dispersing the particles with acidic ethanol (4 g 32% HCl in 1 L ethanol) for 1 h. Consecutive to a final washing step in ethanol, the particles were dried at 60 °C overnight to yield amino-functionalized "MSN-NH_2". The amount of amino groups on the particles was determined by TGA in the temperature range 150 °C–700 °C.

Carboxy-functionalization of mesoporous silica particles

A solution of 25 wt% CES in water (1.49 M, 336 μL, 0.5 mmol) was added to a dispersion of MSNc particles in methanol (7.5 mg mL^{-1}, 20 mL). The mixture was agitated for 3 h at RT. Finally, the particles were centrifuged, washed with methanol and acetone in an ultrasonic bath and dried at 60 °C overnight. These particles are denoted "MSN-COOH" in the following. The amount of carboxy groups on the particles was determined by TGA in the temperature range of 250 °C to 700 °C. The contribution of silanol condensation to the mass loss was accounted for by using non-functionalized particles that had otherwise been exposed to the same conditions as reference.

Fluorescence dye-attachment

Carboxy-functionalized particles were dispersed in HEPES buffer (10 mg mL^{-1}, 10 mL). Particulate carboxy groups were activated with EDC (5.649 M, 89 μL, 0.5 mmol) and an aqueous NHS solution (0.434 M, 2.3 mL, 1 mmol). After agitation for 30 min the particles were centrifuged, briefly washed and re-dispersed in HEPES buffer (10 mg mL^{-1}, 10 mL). The activated MSN-COOH were fluorescently labelled with a solution of ATTO647N-NH_2 in DMSO (1.092 mM, 100 μL, 0.109 μmol) for 1 h at RT. The particles were centrifuged and washed thoroughly with water once and methanol twice and dried *in vacuo* at 60 °C overnight to yield fluorescence labelled "MSN-COOH". To a dispersion of amino-functionalized particles in HEPES buffer (10 mg mL^{-1}, 10 mL) a solution of ATTO647N-NHS ester in DMSO (1.186 mM, 100 μL, 0.119 μmol) was added and the mixture was agitated for 1.5 h at RT. Upon centrifugation, the particles were thoroughly washed with water once and methanol twice and dried *in vacuo* at 60 °C overnight. These particles are denoted "MSN-NH_2" in the following.

Functionalization of MSN-NH_2 with PEG

EDC-HCl (16 mg, 83 μmol) and NHS (19 mg, 165 μmol) were dissolved in a HEPES-buffered aqueous solution of Fmoc-NH-PEG_{3k}-COOH (0.83 mM, 19 mL, 15.7 μmol) and agitated for 45 min at RT. NHS-activated PEG solution (0.83 mM, 6.375 mL, 5.3 μmol) was mixed with a dispersion of amino-functionalized MSN-NH_2 (8.8 mg mL^{-1}, 9.1 mL) and reacted for 2 h at room temperature (RT). The particles were separated *via* centrifugation and washed with water and acetone in an ultrasonic bath. After drying the particles at 60 °C for 40 h, the PEGylated MSNs were labelled with an ATTO647N-COOH dye as described above. The cleavage of the Fmoc protection group was achieved by dispersing the particles in a 25 wt% solution of piperidine in DMF (5 mg mL^{-1}, 5 mL) and agitation for 15 min. The particles were separated *via* centrifugation and the cleavage procedure was repeated once again. Finally, the particles were thoroughly washed with DMF and acetone and dried at 60 °C overnight to yield fluorescence labelled "MSN-PEG". The amount of PEG on the particles was determined by TGA in the temperature range of 150 °C to 700 °C. The contribution of silanol condensation and aminopropyl-functions to the mass loss was accounted for by using non-functionalized particles that had otherwise been exposed to the same conditions as a reference.

Functionalization of MSN-NH_2 with hyaluronic acid

EDC-HCl (6.4 mg, 33 μmol) and sulfo-NHS (14.6 mg, 67 μmol) were dissolved in a HEPES-buffered (25 mM, pH = 7.2) aqueous solution of hyaluronic acid (2 mg mL^{-1}, 1 mL) and agitated for 45 min at RT. Upon addition of a dispersion of amino-functionalized MSN-NH_2 (20 mg mL^{-1}, 1 mL) the coupling reaction proceeded for another 3.5 h. The particles were separated *via* centrifugation and thoroughly washed with water once and MeOH twice in an ultrasonic bath and finally dried

Open Access Article. Published on 02 August 2023. Downloaded on 9/30/2023 4:21:47 PM.
This article is licensed under a Creative Commons Attribution-NonCommercial 3.0 Unported Licence.

in vacuo at 60 °C overnight yielding particles denoted "MSN-HA". The amount of hyaluronic acid bound to the MSN-HA particles was determined by TGA in the temperature range of 150 °C to 700 °C corrected by the mass loss measured for reference particles that had not been exposed to hyaluronic acid, but otherwise had undergone the same treatment conditions as the MSN-HA particles.

Nanoparticle characterization

Amounts of functionalities bound to the particles was measured *via* thermogravimetric analysis (TGA) using a TG209 F1 Libra (Netzsch, Germany) at a heating rate of 10 °C min^{-1} in nitrogen/oxygen (70%/30%) atmosphere and normalized on the silica rest mass at 1000 °C. Upon nitrogen sorption measurements of the dried particles (*in vacuo*, 100 °C, 22 h) on a Quadrasorb-1 (Quantachrome Instruments, Germany) at −196 °C, the specific surface areas, pore diameters and volumes were determined *via* BET model and equilibrium NLDFT kernel calculations (silica, cylindrical pores, relative pressure range of 0–0.9). Zeta potentials of MSNs were measured with a Zetasizer NanoZS Zen3600 (Malvern Panalytical, Germany) in an aqueous HEPES buffer (25 mM, pH 7.2, particle concentration: 0.1 mg mL^{-1}). Particle morphology and size was examined *via* transmission electron microscope (TEM) with a Jeol 1200 (Jeol, Germany) using a HT voltage of 120 kV and a beam current of 65 μA. Mean fluorescence intensities (MFIs) of ATTO-dye labelled particles were determined in an aqueous 10% sucrose solution (particle concentration: 0.1 mg mL^{-1}) using black 96-well microplates and a Spark 10M microplate reader (Tecan, Crailsheim, Germany). In order to account for different fluorescence labelling efficiencies, the MFI of each particle type was measured at a constant concentration of 100 μg mL^{-1} in aqueous 10% sucrose solution and normalized to the MFI of "MSN-NH_2" resulting in conversion factors ("rMFIs") which were used to calculate "rated GMFIs" (rGMFIs) in flow cytometry experiments. ATR-IR spectra were measured on a Tensor 27 (Bruker, USA) with a total of 200 scans per sample. Depending on the coupling chemistry used for surface functionalization, either a spectrum measured for MSN-c or for MSN-NH_2 was used as a background spectrum.

Protein adsorption onto silica nanoparticles from FCS

Formation of protein corona on the set of different functionalized MSNs was examined by dispersing the particles in PBS with a focused ultrasonic bath. The dispersions were mixed with pure, heat inactivated FCS in 2 mL Eppendorf tubes resulting in 10 vol% FCS and a silica concentration of 5 mg mL^{-1}. Note, that the silica concentration was normalized on the rest mass at 700 °C (TGA) in order to account for different functionalization degrees. After protein adsorption for 24 h at 37 °C under agitation, the particles were centrifuged (21 100 rcf, 10 min) and the supernatants were discharged. Upon briefly washing the particles with purified water thrice, the protein corona was eluted by dispersing the samples in an aqueous solution of 10 wt% SDS (0.39 M), doubling the initial silica concentration, and further incubation at 95 °C for 30 min. Finally, the particles were centrifuged again (21 100 rcf, 10 min), and the SDS supernatants were stored at −80 °C until further use.

SDS-PAGE of SDS supernatants

Upon thawing and another centrifugation step (21 100 rcf, 10 min), 40 μL of SDS supernatant was mixed with 8 μL Laemmli buffer (Tris-HCl buffer (0.5 M; pH 6.8 (adjusted with HCl); 1.2 mL), SDS (1.2 g), bromophenol blue (6 mg), glycerine (4.7 mL), water (2.9 mL) and 1,4-dithiothreitol (0.9 g). Additionally, as controls, solutions containing SDS buffer (150 μL) and Laemmli buffer (30 μL; "SDS") as well as FCS (25 μL), SDS buffer (185 μL) and Laemmli buffer (90 μL; "FCS") were prepared. The protein samples and controls were incubated at 95 °C for 5 min. Consecutively, 5 μL broad range unstained protein ladder, 7.5 μL of protein sample, 15 μL of SDS control and 2.5 μL of FCS control were loaded into Mini-PROTEAN TGX Stain-Free Precast Gels (Bio-Rad Laboratories GmbH, Germany). SDS-PAGE was run at a voltage of 300 V in an aqueous electrophoresis buffer (SDS (3.5 mM), Tris (49.5 mM), glycine (383.6 mM)) with a Mini-PROTEAN Tetra Vertical Electrophoresis Cell and a PowerPac Universal Power Supply. Gel documentation and analysis was performed with a Gel Doc™ EZ Imager (Bio-Rad Laboratories GmbH, Germany) and Image Lab software version 6.0.1. The lanes on every gel were divided into three protein molecular mass regions: high molecular weight (>88 kDa), medium molecular weight (88–47 kDa) and low molecular weight proteins (<47 kDa). The overall absolute grey values of each of the band regions were first normalized on the 70 kDa band of the broad range ladder to obtain staining-normalized intensities. Finally, the band region intensities were normalized on the respective intensities of the MSN-NH_2 particles.

Cell culture

Cells were cultivated using standard conditions (37 °C, 5% CO_2, >95% relative humidity). The THP-1 monocyte cell line was originally isolated from peripheral blood of a one year old boy suffering from acute monocytic leukemia.[34] THP-1 cells were grown in RPMI 1640 medium supplemented with 10% fetal bovine serum, 1% streptomycin/penicillin, 2 mM glutamine, and 1 mM sodium pyruvate. Differentiation to macrophages (M0) was conducted using Phorbol-12-myristat-13-acetate (PMA) as described previously.[35] PC-3 prostate cancer (PCa) cells were cultivated in RPMI 1640 medium supplemented with 10% fetal bovine serum, and 1% streptomycin/penicillin. To retain the option of using the current dataset in a context of molecular targeting analysis in the future, experiments were conducted using a genetically engineered subclone of PC-3[36] (PC3L1) which was further engineered for doxycycline inducible expression of the FOLH1/PSMA targeting ligand (resulting in PC3L1-FOLH1) using a vector system described previously.[37] However, since the transgene was not induced the clone was phenotypically identical to the original PC-3 cell line.

 This journal is © The Royal Society of Chemistry 2023

Open Access Article. Published on 02 August 2023. Downloaded on 9/30/2023 4:21:47 PM.
This article is licensed under a Creative Commons Attribution-NonCommercial 3.0 Unported Licence.

Evaluation of cellular particle uptake

Nanoparticle internalization was assessed qualitatively *via* confocal laser scanning fluorescence microscopy, as well as quantitatively using flow cytometry. A constant particle concentration of 10 μg mL^{-1} was used. THP-1 cells were seeded at a density of 268 mm^{-2} and grown for 72 h in presence of PMA, followed by a 24 h incubation period in MSN-containing growth medium. PC-3 cells were seeded at a density of 150–200 mm^{-2} and grown for 24 to 48 h prior to a 24 h incubation period in MSN-containing growth medium.

Flow cytometry

Flow cytometry was conducted using a CyFlow Space instrument (Sysmex-Partec, Görlitz, Germany) and FloMax 3.0 software (Sysmex-Partec). Cells were detached using Trypsin-EDTA (for THP-1) or Accutase (for PC3L1-FOLH1), washed with PBS/1% BSA and subsequently resuspended in PBS/1% BSA. For detection of dead cells, propidium iodide (PI) was added at 2 μg mL^{-1}. A total of 30 000 to 50 000 events was acquired, respectively. Debris and dead cells were identified by scattering characteristics (FSC, SSC) and/or enhanced PI-mediated fluorescence and excluded from further analysis. Quantification of internalization efficiencies was performed using the geometric mean fluorescence intensity (GMFI) data for ATTO647N-mediated fluorescence of particle-treated cells *vs.* controls from flow cytometry (n = 3 for each cell type and particle, respectively).

Confocal laser scanning fluorescence microscopy

Confocal laser scanning fluorescence microscopy (CLSM) was conducted using a Leica TCS SP8 system (Leica Microsystems, Wetzlar, Germany). Cells were seeded in ibitreat dishes and grown in presence of nanoparticles for 24 h. At the end of the incubation period, cells were fixed using PBS-buffered formaldehyde (4%) for 10 min at RT. Cells were washed with PBS and subsequently stained using DAPI (0.1 μg mL^{-1} in PBS for visualization of nuclei) during 5 min at RT, followed by phalloidin-TRITC (50 nM in PBS/1% BSA for visualization of actin cytoskeleton) during 30 min at RT. Subsequent to washing, cells were kept in PBS for confocal microscopy. Here, excitation of DAPI, TRITC and ATTO647N was achieved using integrated laser emitting at 405 nm, 552 nm and 638 nm, respectively. DAPI-mediated fluorescence was detected at 410–601 nm, TRITC-mediated fluorescence was detected at 557–713 nm, and ATTO647N-mediated fluorescence was detected at 643–795 nm using a HP CL APO 63×/1.40 OIL CS2 oil immersion objective (Leica Microsystems) and a pinhole setting of 1 Airy unit.

Evaluation of cell viability

For cytotoxicity studies, PC-3 cells were seeded at 200 cells per mm^2 in 96-well microplates. THP-1 cells were seeded at 268 cells per mm^2 to 96 well microplates and differentiated to macrophages during 72 h. Nanoparticles were added after 24 h in case of PC-3 cells and after 72 h in case of THP-1 macrophages at various concentrations, and incubated for further 24 h. Subsequently, cell viability was determined using the Cell Titer Blue assay. Resorufin-mediated fluorescence (excitation: 544 nm, detection: 590 nm), the intensity of which correlates to the number of viable cells per well, was quantified using a Fluostar Omega microplate reader (BMG Labtech, Ortenberg, Germany). Fluorescence intensity values were blank corrected and viability was calculated as a percentage of an untreated control. For each sample, four independent experiments were performed in triplicates.

Results and discussion

Monodisperse MSNs with a mean particle diameter of 190 nm and a radially aligned pore system were synthesized. The surfactant was removed either by acidic extraction yielding amino-functionalized particles (MSN-NH_2) or by calcination. Calcined particles were further covalently functionalized with a carboxysilane resulting in MSN-COOH particles. Further covalent functionalization of the MSN-NH_2 particles with PEG_{3k} (MSN-PEG) or hyaluronic acid (MSN-HA) resulted in altogether four different sets of particles. Key physicochemical characteristics of the particles are summarized in Table 1, and a representative transmission electron microscopy (TEM) image of the MSN-NH_2 particles is shown in Fig. 1. TEM images of MSN-COOH, MSN-PEG and MSN-HA are shown in Fig. S1.† The high specific surface areas and pore volumes of the basic particles are in agreement with what is to be expected for this kind of particles (see Fig. S2 and Table S1†). Successful surface functionalization was proven by thermogravimetric analysis, zeta-potential, and ATR-IR spectroscopy measurements. Exemplary thermogravimetric measurements of both the native and the functionalized particles are depicted in ESI Fig. S3,† and the ATR-IR spectra including peak assignments are shown in Fig. S4.† While the MSN-NH_2 and MSN-PEG particles exhibited an unaltered, positive zeta potential at pH 7.2, functionalization with hyaluronic acid led to a shift towards a

Table 1 Summary of key nanoparticle physiochemical and morphological characteristics. Zeta potentials were measured in aqueous HEPES buffer (25 mM, pH 7.2)

	MSN-NH_2	MSN-PEG	MSN-HA	MSN-COOH
Mean diameter ± SD/nm	176 ± 16	176 ± 16	211 ± 19	184 ± 17
Functional groups/mg g^{-1} (silica)	116	110	108	16
Functional groups/mmol g^{-1} (silica)	2.00	1.90	7.19×10^{-5}	0.22
Zeta potential (HEPES) ± SD/mV	+14 ± 3.2	+10 ± 3.6	−27 ± 4.3	−44 ± 6.5

Open Access Article. Published on 02 August 2023. Downloaded on 9/30/2023 4:21:47 PM.
This article is licensed under a Creative Commons Attribution-NonCommercial 3.0 Unported Licence.

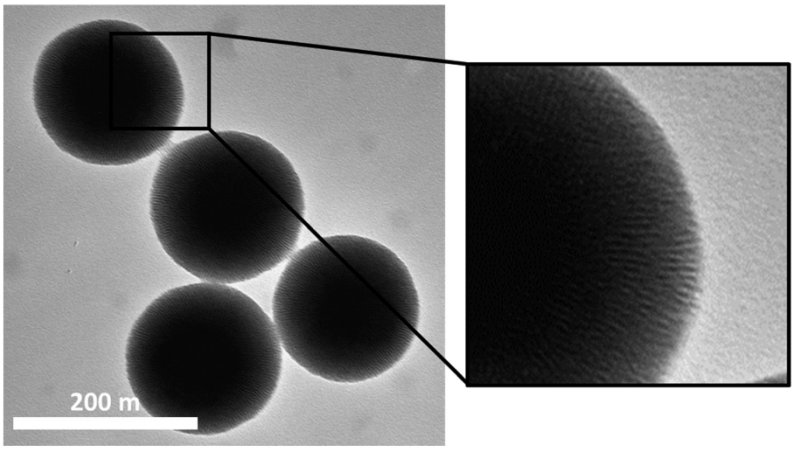

Fig. 1 Exemplary transmission electron microscopy image of the MSN-NH_2 particles.

negative zeta potential. The MSN-COOH particles exhibited strongly negative zeta potentials as expected.

As a simple but informative MPS model we used THP-1 monocytes,[34] which were differentiated to an adherently growing naïve macrophage-like phenotype (M0) by incubation with the phorbol ester phorbol-12-myristate-13-acetate (PMA). Particularly liver macrophages may be best represented by the M0 phenotype,[38] and in line with this argumentation THP-1 M0 cells were recently used as a liver-resident macrophage model in an organ-on-chip application.[39] M0-differentiated THP-1 cells can be further polarized to pro-inflammatory (M1) and tissue repair (M2) phenotypes and are as such a well-accepted *in vitro* model for the evaluation of the effects of nanomaterials on the immune system.[35,40–42] Although some researchers prefer primary *ex vivo* models such as (human) peripheral blood mononuclear cells (PBMC), these bear significant disadvantages such as the requirement of chemokine supplementation for prolonged growth and considerable batch-to-batch/donor variation, which particularly impedes data interpretation in repetitive screening approaches. In contrast, THP-1 cells have been demonstrated to retain a relatively stable genetic background and monocyte/macrophage-like phenotype over several passages, which facilitates the reproducibility of results from screening approaches.[43]

Successful nanoparticle dispersability, and dispersion stability in cell medium supplemented with 10% FCS was proven by dynamic light-scattering. Hydrodynamic diameters of about 200 nm was measured for all particles (10 μg mL^{-1} concentration) apart from for the MSN-HA particles, for which a hydrodynamic diameter of about 300–400 nm was measured, suggesting some slight particle aggregation in this case (see ESI S5†). No loss of viability compared to untreated controls could be observed subsequent to incubation with MSNs under investigation at doses up to 25 μg mL^{-1} for THP-1 cells and up to 50 μg mL^{-1} for PC-3 cells, respectively (ESI Fig. S6†). The internalization of the particles by THP-1 M0 macrophages and the prostate cancer cell line PC-3 was investigated subsequent to a 24 h incubation at a particle concentration of 10 μg mL^{-1} *via* both confocal laser scanning fluorescence microscopy (CLSM) and flow cytometry. Intracellular localization of the particles as well as the distribution patterns observed in flow cytometry were verified by CLSM (Fig. 2). Particle uptake could be visualized in both cell lines irrespective of particle type, but variation in signal intensities were evident. However, the particle-related fluorescence signals were narrowly localized and clearly distinguishable within the cells, indicating that the fluorescence dye was still attached to the MSNs and that neither particle dissolution nor diffusion of free dye into the cytosol impacted further analysis *via* flow cytometry. The low contribution of particle dissolution effects can be attributed to the fact that most of the particle internalization occur during the first 1–2 hours of incubation under these conditions.[44]

Exemplary histograms of ATTO647N-mediated fluorescence of viable cells in response to MSN treatment obtained from flow cytometry experiments are shown in Fig. 3. Gaussian-like distributions demonstrate a relatively homogeneous uptake of MSN-COOH, MSN-NH_2 and MSN-HA in PC-3 cells, whereas the internalization of MSN-PEG was rather inhomogeneous, resulting in a broader distribution in the histogram (Fig. 3a). THP-1 cells revealed an overall broader distribution of fluorescence intensities in the flow cytometry measurements for all MSNs tested (Fig. 3b). The bar plots shown in Fig. 2 show the quantitation of MSN uptake, where the mean of the geometric mean relative fluorescence intensities resulting from triplicate flow cytometry measurements were weighted with a particle specific factor reflecting the ATTO647N-labelling efficiency, as recently suggested[45] (see Fig. S6†).

Rated GMFI values for particle internalization to both cell lines are shown in Fig. 4 as a function of zeta potential measured

 This journal is © The Royal Society of Chemistry 2023

Open Access Article. Published on 02 August 2023. Downloaded on 9/30/2023 4:21:47 PM.
This article is licensed under a Creative Commons Attribution-NonCommercial 3.0 Unported Licence.

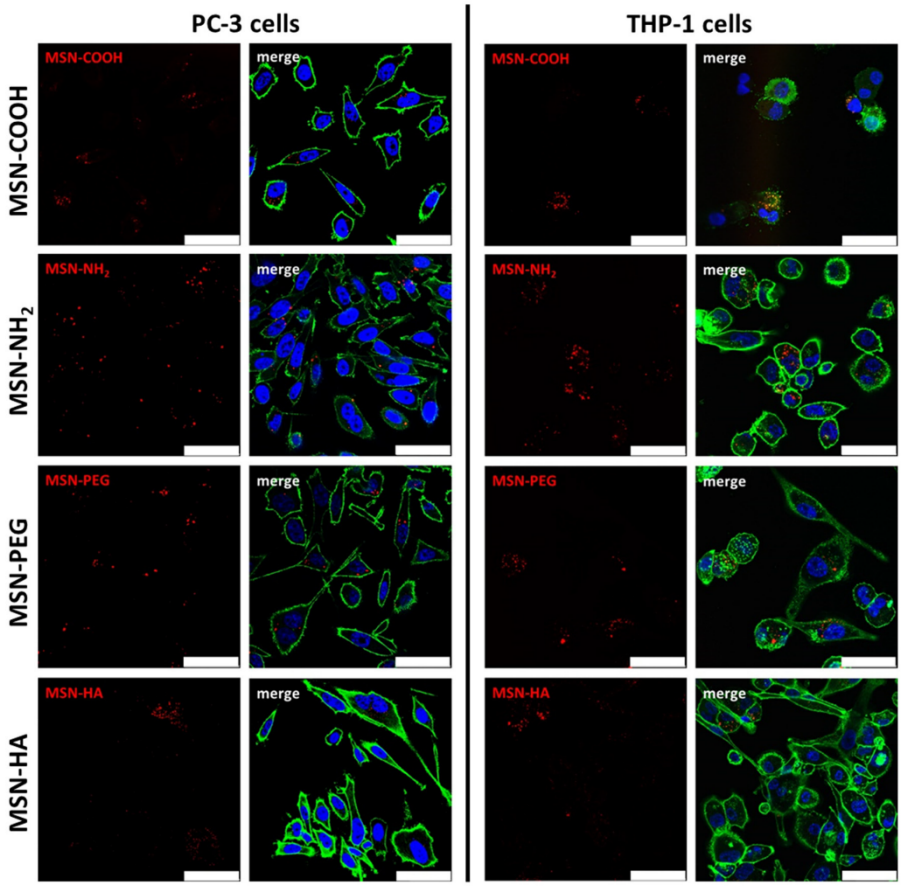

Fig. 2 Exemplary micrographs of PC-3 (left column) and THP-1 (right column) cells treated with 10 μg ml^{-1} of MSNs for 24 h. Subsequent to fixation, cells were stained with fluorescent probes indicative for the actin cytoskeleton (Phalloidin-TRITC, green) and the nucleus (DAPI, blue). The nanoparticles are ATTO647N-labelled and depicted red in the images (scale bar: 50 μm).

in HEPES buffer (pH = 7.2). In PC-3 cells, the positively charged MSN-NH_2 and MSN-PEG particles are taken up to the same extent as the negatively charged MSN-COOH, and their cellular uptake is much higher (by a factor of ~7) than that of the likewise negative MSN-HA particles. At first sight, this seems to contradict the expected influence of particle charge on the uptake of nanoparticles by endocytotic cells, as electrostatic attraction between positively charged particles with negatively charged phospholipids present in the outer cell membrane are assumed to be beneficial for cellular uptake efficiency.[46,47] However, it was previously reported[48] that considerable serum protein adsorption, as observed here for the MSN-COOH particles (see Fig. 5), can partially shield a negative surface charge resulting in elevated, endocytosis-driven nanoparticle uptake into human osteoblasts as compared to their positively charged counter-parts. With the low protein adsorption levels on MSN-HA (as discussed later) in mind, the strongly reduced uptake of these particles into PC-3 cells can be understood.

The corresponding nanoparticle uptake by adherently growing macrophage-like THP-1 cells (M0) as determined by flow cytometry measurements are also summarized in Fig. 4. No correlation between particle charge (positive *vs.* negative particle charge) and uptake was observed, as highlighted by the almost 20 times higher rGMFI values measured for the anionic MSN-COOH as compared to anionic MSN-HA particles, and the approximately two-fold higher uptake of MSN-COOH *vs.* cationic MSN-PEG particles. The by far highest particle uptake was observed for the MSN-NH_2 particles, although the MSN-PEG exhibited a virtually identical, positive zeta potential. Thus, in the case of THP-1 cells other factors than particle

Open Access Article. Published on 02 August 2023. Downloaded on 9/30/2023 4:21:47 PM.
This article is licensed under a Creative Commons Attribution-NonCommercial 3.0 Unported Licence.

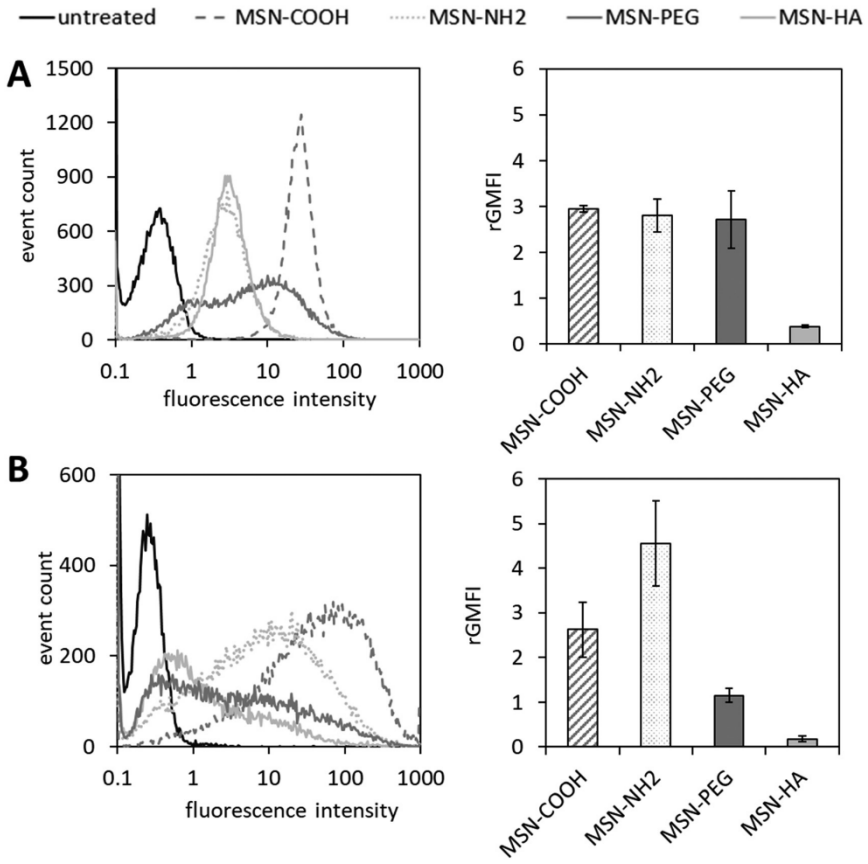

Fig. 3 Analysis of MSN internalization by (A) PC-3 cells and (B) THP-1 cells *via* flow cytometry. Cell lines were treated with ATTO647N-labelled MSNs at 10 μg mL^{-1} for 24 h at 37 °C. Surface functionalities are color coded, respectively. Exemplary histograms of one out of three replicate measurements with similar outcomes are shown on the left side. For quantitation of internalization characteristics for each MSN species to a certain cell type, geometric mean fluorescence intensities (GMFIs) of MSN-treated cell populations were blank corrected (*i.e.* the geometric MFI of the corresponding untreated control populations was subtracted), rated with a particle-specific factor which reflects the ATTO647N-labelling efficiency (see Fig. S6†) and plotted as bar graphs (n = 3, error bars are SD).

charge strongly influenced particle uptake. Nanoparticle uptake into macrophages have been repeatedly linked to protein corona formation. We therefore studied the composition of the protein corona of the different nanoparticles by SDS-PAGE. A representative gel is shown in Fig. 4.

Indeed, already based on visual inspection it is evident that the MSN-HA particles adsorbed by far the least amounts of serum proteins of all studied particles, and only for 26 kDa a strong band is seen, which can be ascribed to Apolipoprotein A-1 (Apo-A1),[49] and a clearly fainter band in the range of 68 kDa ascribable to BSA can be seen. Albumin has previously been shown to interact weakly with HA-coated silica surfaces at neutral pH.[50] Apo-A1 and serum albumin are common constituents of the protein corona of various nanoparticles subsequent to plasma exposition.[51] Clearly stronger band intensities in the same molecular weight regions, and additionally in the molecular weight range >88 kDa, were seen for both MSN-COOH and MSN-PEG particles, and the band intensities were very similar for both sets of particles. By far the highest band intensities were observed for the MSN-NH_2 particles, which is not surprising keeping in mind that most plasma proteins have a pI < 7.4.[52] Thus, it is evident that the order of nanoparticle uptake by the THP-1 cells followed the order to serum protein adsorption to the particles.

We have previously shown that the integrated band intensities can be used for a semi-quantitative comparison of the relative amounts of protein adsorbed.[53] In Fig. 6(a), integrated intensities obtained from three separate molecular weight

 This journal is © The Royal Society of Chemistry 2023

Open Access Article. Published on 02 August 2023. Downloaded on 9/30/2023 4:21:47 PM.
This article is licensed under a Creative Commons Attribution-NonCommercial 3.0 Unported Licence.

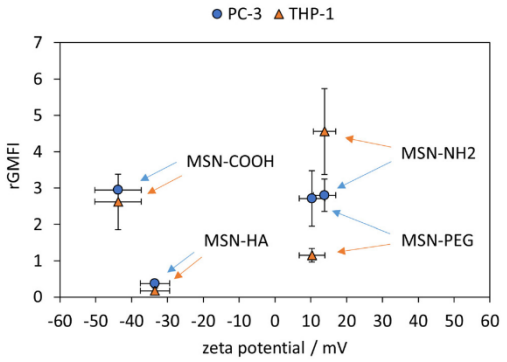

Fig. 4 rGMFIs measured for PC-3 cells and THP-1 after incubation with 10 μg mL^{-1} particles for 24 h as a function of the MSN zeta potential. Zeta potentials were measured in aqueous HEPES buffer (25 mM, pH 7.2) (n = 3, error bars are SD).

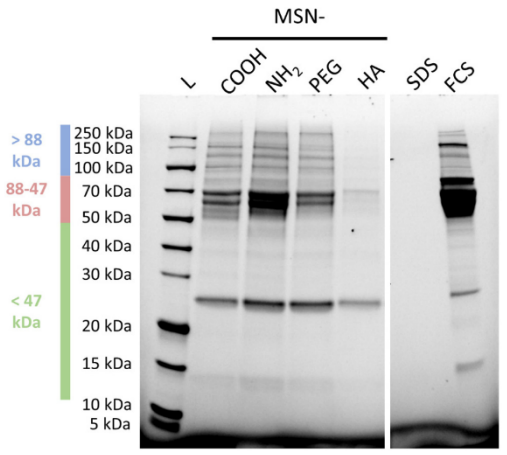

Fig. 5 Representative SDS-PAGE of SDS supernatants after adsorption of serum proteins from 10% FCS in PBS onto MSNs at a silica concentration of 5 mg mL^{-1} for 24 h at 37 °C. L: broad range protein ladder, SDS: SDS control, FCS: 8% FCS control.

windows (>88 kDa (high), 88–47 kDa (medium), and <47 kDa (low)), are shown, where the intensities have been normalized to those obtained for the respective molecular weight windows of the MSN-NH_2 particles. As can be seen, the smaller molecular weight proteins, mainly corresponding to the strong band attributed to Apolipoprotein A-I, adsorb to all particles, while pronounced particle-dependent differences were observed for the heavier proteins, and especially so for the proteins with molecular weights in the medium range, mainly ascribed to BSA. While the correlation between the extent of adsorption of neither the heavy proteins nor of the lighter proteins showed a direct correlation with the particle uptake by the THP-1 cells, (ESI Fig. S7†) an almost perfectly linear correlation was observed between the relative amounts of medium molecular weight proteins and the cellular uptake, as shown in Fig. 6. These results suggest an active role of the protein corona, and more specifically albumin, in mediating the nanoparticle uptake by the THP-1 cells. A direct connection between serum protein adsorption,[54] and specifically BSA,[8,55] and nanoparticle uptake has also been demonstrated previously, and our preliminary results imply an even quantitative connection between these parameters.

Having determined the nanoparticle uptake in the two model cell lines, the next step was to investigate how the uptakes can be converted into a general measure by which the nanoparticles can be classified in terms of their potential ability to most efficiently deliver drugs to tumours. The most straightforward means for grading the nanoparticles would be in terms of their selectivity towards the cancer cells. The selectivity was therefore defined simply as the ratio between the corresponding relative uptakes, $\text{uptake}_{\text{PC-3}}/\text{uptake}_{\text{THP-1}}$. The corresponding ratios obtained for the studied nanoparticles are shown in Fig. 7. The selectivity for the cancer cells is the highest for the MSN-PEG particles, closely followed by the MSN-HA particles.

Surface charge of nanocarriers generally plays a critical role for tumour targeting *in vivo*. However, findings reported in the literature are heterogeneous and suggest that a combination of surface charge extent, size and shape of the nanocarrier determines its fate in the organism.[56] Different studies suggest that a modest negative surface charge appears to be favourable for circumvention of MPS clearance and improved blood compatibility, thereby extending blood circulation time and improving tumour delivery.[57,58] On the other hand, cationic nanocarriers were recently used for the improvement of tumour immunosurveillance[59] as well as, more specifically, the administration of cancer vaccines which preferentially target antigen presenting cells.[18] These findings were reflected by our *in vitro* system: whereas internalization of anionic MSN-COOH particles was still slightly higher in PC-3 *vs.* THP-1 cells, cationic MSN-NH_2 particles had a preference for THP-1 cells.

To further account for the overall amount of nanocarrier internalization, a key parameter for reaching a high intracellular drug concentration in the target cells, we define a new value for comparison, specifically focusing on this aspect, as $\text{uptake}_{\text{PC-3}}$ x the selectivity, *i.e.* $(\text{uptake}_{\text{PC-3}})^2/\text{uptake}_{\text{THP-1}}$. This is equivalent to an activity times selectivity-measure for catalyst classification. The so obtained values are shown in Fig. 8. As can be seen, the MSN-PEG particle is clearly the most promising one according to this analysis. This result is in full agreement with what is to be expected for the drug delivery efficiency of the studied particles to solid tumours if administered intravenously.

Naturally this simple means for analysis is not quantitative, but can serve as a simple preliminary tool for grading particles during *in vitro* particle screenings for identifying the most promising nanoparticle surface chemistries for further more

Open Access Article. Published on 02 August 2023. Downloaded on 9/30/2023 4:21:47 PM.
This article is licensed under a Creative Commons Attribution-NonCommercial 3.0 Unported Licence.

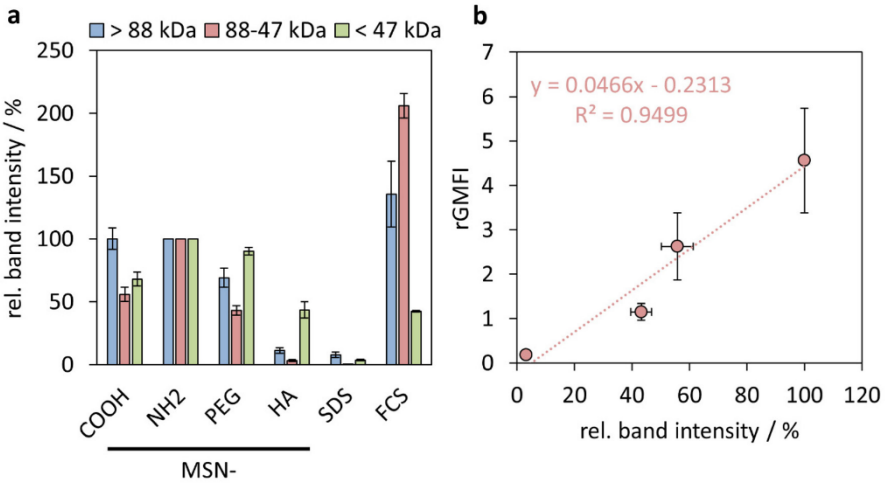

Fig. 6 (a) Relative band intensities for the three protein mass windows: high molecular weight (>88 kDa), medium molecular weight (88–47 kDa) and low molecular weight (<47 kDa). Band intensities were normalized on the respective intensities of MSN-NH_2. (b) rGMFIs measured for THP-1 cells after particle treatment for 24 h as a function of relative band intensities of medium molecular weight proteins (n = 3, error bars = SD).

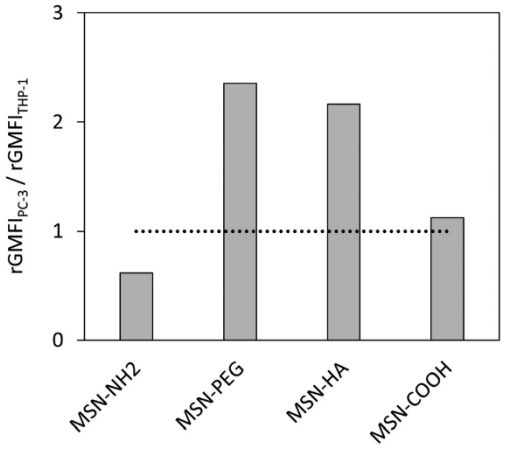

Fig. 7 Nanoparticle uptake ratio calculated as $rGMFI_{PC\text{-}3}/rGMFI_{THP\text{-}1}$.

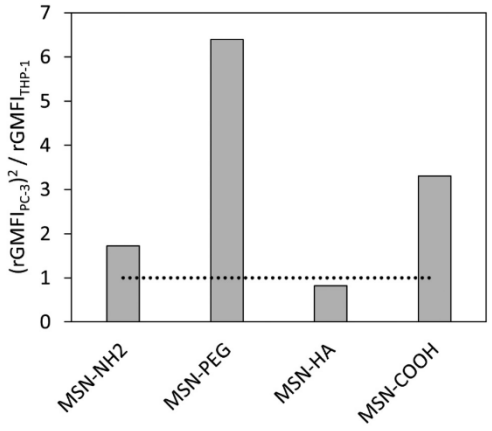

Fig. 8 Nanoparticle uptake ratio calculated as $(rGMFI_{PC\text{-}3})^2/rGMFI_{THP\text{-}1}$.

detailed *in vitro* and *in vivo* evaluations. We are well aware that the model is oversimplified, but encouraged by the fact that the outcome appears to be reasonable. Experimental parameters like incubation time, particle concentration or cell lines could be varied but were chosen based on some consideration. A low particle concentration of 10 μg mL^{-1} was chosen in order to minimize potential contributions from particle aggregation and sedimentation on the cellular uptake, as well as to avoid potential cellular saturation effects. The used incubation time of 24 h is within relevant *in vivo* time-scale, and minimizes potential influences of different nanoparticle internalization kinetics. The cancer cell line can naturally be varied at will, based on the application aimed for, and particles intended for active targeting can also easily be screened with the suggested methodology. We emphasize that the main aim of the suggested screening is to identify the most promising surface chemistries for efficient drug delivery to solid tumours through intravenous (or intraperitoneal) administration, and the model is probably relatively insensitive to other important parameters for *in vivo* responses of nanoparticles, like particle size and shape.

 This journal is © The Royal Society of Chemistry 2023

Open Access Article. Published on 02 August 2023. Downloaded on 9/30/2023 4:21:47 PM.
This article is licensed under a Creative Commons Attribution-NonCommercial 3.0 Unported Licence.

Conclusions

The identification of the most promising nanoparticle formulations for drug delivery to solid tumours is a bottleneck in the field of bionanomedicine. Chemists can synthesize a battery of different particles within a time-frame of weeks and months, and testing of all those particles *in vivo* is expensive and time-consuming, and also not ethically acceptable. Here we propose a very simple *in vitro* nanoparticle surface chemistry screening methodology based on established cell-lines that ensures reproducibility and comparability of the results. As the efficiency of the drug delivery is dependent both upon the possibility of the nanoparticles to escape the RES as well as on the extent of which they are accumulating in the tumour area and internalized by the cancer cells, a macrophage model cell line, THP-1, as well as a model cancer cell line, PC-3, was used for the screening. Realistic mirroring of *in vivo* results obtained by intravenous administration of comparable particles was achieved only when taking into account both the selectivity of the nanoparticles for the cancer cells, as well as the extent of nanoparticle uptake by the cancer cells. The screening method can naturally easily be modified to account for other cancer cell types, and is also suitable for screening of nanoparticles where active, receptor-mediated cell targeting is aimed for. While the screening method promises to be suitable for early identification of promising nanoparticle surface chemistries, it seems less suitable for the optimization of other important nanoparticle characteristics like size and probably also shape. When increasingly more data becomes available, the predictability of the screening method can be judged, and further optimized.

Conflicts of interest

There are no conflicts to declare.

Acknowledgements

The financial support from the DFG funded projects WI3868/6-1 as well as SFB 1279 is gratefully acknowledged. The authors want to thank Cornelia Egger for nitrogen sorption measurements, Petra Kruse and Eva Winkler for technical assistance in cell culture experiments, as well as Kea Fedke and Lionel Kroner for TG measurements.

References

1 Y. Matsumura and H. Maeda, *Cancer Res.*, 1986, **46**, 6387–6392.
2 Y. N. Zhang, W. Poon, A. J. Tavares, I. D. McGilvray and W. C. W. Chan, *J. Controlled Release*, 2016, **240**, 332, DOI: 10.1016/j.jconrel.2016.01.020.
3 W. P. Caron, S. Rawal, G. Song, P. Kumar, J. C. Lay and W. C. Zamboni, *J. Pharmacol. Exp. Ther.*, 2013, **347**, 599–606, DOI: 10.1124/jpet.113.208801.
4 J. D. Friedl, V. Nele, G. de Rosa and A. Bernkop-Schnürch, *Adv. Funct. Mater.*, 2021, **31**, 2103347, DOI: 10.1002/adfm.202103347.
5 R. Gref, M. Lück, P. Quellec, M. Marchand, E. Dellacherie, S. Harnisch, T. Blunk and R. H. Müller, *Colloids Surf., B*, 2000, **18**, 301, DOI: 10.1016/S0927-7765(99)00156-3.
6 W. R. Gombotz, W. Guanghui, T. A. Horbett and A. S. Hoffman, *J. Biomed. Mater. Res.*, 1991, **25**, 1547, DOI: 10.1002/jbm.820251211.
7 D. E. Owens and N. A. Peppas, *Int. J. Pharm.*, 2006, **307**, 93, DOI: 10.1016/j.ijpharm.2005.10.010.
8 J. A. Champion, S. M. Pustulka, K. Ling and S. L. Pish, *ACS Appl. Mater. Interfaces*, 2020, **12**, 48284, DOI: 10.1021/acsami.0c12341.
9 C. D. Walkey, J. B. Olsen, H. Guo, A. Emili and W. C. W. Chan, *J. Am. Chem. Soc.*, 2012, **134**, 2139, DOI: 10.1021/ja2084338.
10 C. Yao, P. Wang, L. Zhou, R. Wang, X. Li, D. Zhao and F. Zhang, *Anal. Chem.*, 2014, **86**, 9749, DOI: 10.1021/ac5023259.
11 E. Blanco, H. Shen and M. Ferrari, *Nat. Biotechnol.*, 2015, **33**, 941, DOI: 10.1038/nbt.3330.
12 L. Kou, Y. D. Bhutia, Q. Yao, Z. He, J. Sun and V. Ganapathy, *Front. Pharmacol.*, 2018, **9**, DOI: 10.3389/fphar.2018.00027.
13 F. Alexis, E. Pridgen, L. K. Molnar and O. C. Farokhzad, *Mol. Pharm.*, 2008, **5**, 505–15, DOI: 10.1021/mp800051m.
14 J. S. Souris, C. H. Lee, S. H. Cheng, C. T. Chen, C. S. Yang, J. an A. Ho, C. Y. Mou and L. W. Lo, *Biomaterials*, 2010, **31**, 5564, DOI: 10.1016/j.biomaterials.2010.03.048.
15 S. Ashraf, J. Park, M. A. Bichelberger, K. Kantner, R. Hartmann, P. Maffre, A. H. Said, N. Feliu, J. Lee, D. Lee, G. U. Nienhaus, S. Kim and W. J. Parak, *Nanoscale*, 2016, **8**, 17794, DOI: 10.1039/c6nr05805a.
16 M. Beck, T. Mandal, C. Buske and M. Lindén, *ACS Appl. Mater. Interfaces*, 2017, **9**, 18566, DOI: 10.1021/acsami.7b04742.
17 A. Panariti, G. Miserocchi and I. Rivolta, *Nanotechnol., Sci. Appl.*, 2012, 7, 87, DOI: 10.2147/NSA.S25515.
18 J. Heuts, W. Jiskoot, F. Ossendorp and K. van der Maaden, *Pharmaceutics*, 2021, **13**, 596, DOI: 10.3390/pharmaceutics13050596.
19 S. Jambhrunkar, Z. Qu, A. Popat, J. Yang, O. Noonan, L. Acauan, Y. Ahmad Nor, C. Yu and S. Karmakar, *Mol. Pharm.*, 2014, **11**, 3642, DOI: 10.1021/mp500385n.
20 J. M. Rosenholm, A. Meinander, E. Peuhu, R. Niemi, J. E. Eriksson, C. Sahlgren and M. Lindén, *ACS Nano*, 2009, **3**, 19, DOI: 10.1021/nn800781r.
21 H. X. Wang, Z. Q. Zuo, J. Z. Du, Y. C. Wang, R. Sun, Z. T. Cao, X. D. Ye, J. L. Wang, K. W. Leong and J. Wang, *Nano Today*, DOI: 10.1016/j.nantod.2016.04.008.
22 R. Wittig, J. M. Rosenholm, E. von Haartman, J. Hemming, F. Genze, L. Bergman, T. Simmet, M. Lindén and C. Sahlgren, *Nanomedicine*, 2014, **9**, DOI: 10.2217/nnm.13.62.
23 K. Song, Z. Tang, Z. Song, S. Meng, H. Guo, Y. Zhu and X. Wang, *Pharmaceutics*, 2022, **14**, 1265, DOI: 10.3390/pharmaceutics14061265.

Open Access Article. Published on 02 August 2023. Downloaded on 9/30/2023 4:21:47 PM.
This article is licensed under a Creative Commons Attribution-NonCommercial 3.0 Unported Licence.

24 K. Y. Choi, K. H. Min, H. Y. Yoon, K. Kim, J. H. Park, I. C. Kwon, K. Choi and S. Y. Jeong, *Biomaterials*, 2011, **32**, 1880, DOI: 10.1016/j.biomaterials.2010.11.010.
25 P. Dogra, N. L. Adolphi, Z. Wang, Y. S. Lin, K. S. Butler, P. N. Durfee, J. G. Croissant, A. Noureddine, E. N. Coker, E. L. Bearer, V. Cristini and C. J. Brinker, *Nat. Commun.*, 2018, **9**, DOI: 10.1038/s41467-018-06730-z.
26 X. He, H. Nie, K. Wang, W. Tan, X. Wu and P. Zhang, *Anal. Chem.*, 2008, **80**, 9597, DOI: 10.1021/ac801882g.
27 L. Miller, G. Winter, B. Baur, B. Witulla, C. Solbach, S. Reske and M. Lindén, *Nanoscale*, 2014, **6**, 4928, DOI: 10.1039/c3nr06800e.
28 M. Xie, Y. Xu, H. Shen, S. Shen, Y. Ge and J. Xie, *Int. J. Pharm.*, 2014, **474**, 223, DOI: 10.1016/j.ijpharm.2014.08.027.
29 L. Kramer, G. Winter, B. Baur, A. J. Kuntz, T. Kull, C. Solbach, A. J. Beer and M. Lindén, *Nanoscale*, DOI: 10.1039/c7nr02050c.
30 Q. He, Z. Zhang, F. Gao, Y. Li and J. Shi, *Small*, DOI: 10.1002/smll.201001459.
31 Y. He, L. Luo, S. Liang, M. Long and H. Xu, *J. Biomater. Appl.*, 2017, **32**, DOI: 10.1177/0885328217724638.
32 V. Mamaeva, R. Niemi, M. Beck, E. Ozliseli, D. Desai, S. Landor, T. Gronroos, P. Kronqvist, I. K. N. Pettersen, E. McCormack, J. M. Rosenholm, M. Linden and C. Sahlgren, *Mol. Ther.*, 2016, **24**, 926, DOI: 10.1038/mt.2016.42.
33 R. Wittig, J. M. Rosenholm, E. von Haartman, J. Hemming, F. Genze, L. Bergman, T. Simmet, M. Lindén and C. Sahlgren, *Nanomedicine*, 2014, **9**, DOI: 10.2217/nnm.13.62.
34 S. Tsuchiya, M. Yamabe, Y. Yamaguchi, Y. Kobayashi, T. Konno and K. Tada, *Int. J. Cancer*, 1980, **26**, 171, DOI: 10.1002/ijc.2910260208.
35 Z. Zhu, C. Scalfi-Happ, A. Ryabova, S. Gräfe, A. Wiehe, R. U. Peter, V. Loschenov, R. Steiner and R. Wittig, *J. Photochem. Photobiol., B*, 2018, **185**, 215, DOI: 10.1016/j.jphotobiol.2018.06.015.
36 S. M. Wittig-Blaich, L. A. Kacprzyk, T. Eismann, M. Bewerunge-Hudler, P. Kruse, E. Winkler, W. S. L. Strauss, R. Hibst, R. Steiner, M. Schrader, D. Mertens, H. Sültmann and R. Wittig, *Neoplasia*, 2011, **13**, 579, DOI: 10.1593/neo.11294.
37 S. Wittig-Blaich, R. Wittig, S. Schmidt, S. Lyer, M. Bewerunge-Hudler, S. Gronert-Sum, O. Strobel-Freidekind, C. Müller, M. List, A. Jaskot, H. Christiansen, M. Hafner, D. Schadendorf, I. Block and J. Mollenhauer, *Oncotarget*, 2017, **8**, 23760, DOI: 10.18632/oncotarget.15863.
38 C. Wang, C. Ma, L. Gong, Y. Guo, K. Fu, Y. Zhang, H. Zhou and Y. Li, *Front. Immunol.*, 2021, **12**, DOI: 10.3389/fimmu.2021.803037.
39 K. M. Bircsak, R. DeBiasio, M. Miedel, A. Alsebahi, R. Reddinger, A. Saleh, T. Shun, L. A. Vernetti and A. Gough, *Toxicology*, 2021, **450**, 152667, DOI: 10.1016/j.tox.2020.152667.
40 T. Brzicova, E. Javorkova, K. Vrbova, A. Zajicova, V. Holan, D. Pinkas, V. Philimonenko, J. Sikorova, J. Klema, J. Topinka and P. Rossner, *Nanomaterials*, 2019, **9**, 687, DOI: 10.3390/nano9050687.
41 Y. Matsuoka, Y. Kawauchi, K. Kawauchi, A. Takiyama, S. Kojima, Y. Kuroda and N. Kojima, *Glycoconjugate J.*, 2019, **36**, 185, DOI: 10.1007/s10719-019-09870-6.
42 A. D. Schoenenberger, A. Schipanski, V. Malheiro, M. Kucki, J. G. Snedeker, P. Wick and K. Maniura-Weber, *ACS Biomater. Sci. Eng.*, 2016, **2**, 908, DOI: 10.1021/acsbiomaterials.6b00006.
43 W. Chanput, J. J. Mes and H. J. Wichers, *Int. Immunopharmacol.*, 2014, **23**, 37, DOI: 10.1016/j.intimp.2014.08.002.
44 M. Fisichella, H. Dabboue, S. Bhattacharyya, G. Lelong, M. L. Saboungi, F. Warmont, P. Midoux, C. Pichon, M. Guérin, T. Hevor and J. P. Salvetat, *J. Nanosci. Nanotechnol.*, 2010, **10**.
45 B. Baumann, R. Wittig and M. Lindén, *Nanoscale*, 2017, **9**, 12379, DOI: 10.1039/c7nr02015e.
46 O. Harush-Frenkel, N. Debotton, S. Benita and Y. Altschuler, *Biochem. Biophys. Res. Commun.*, 2007, **353**, 26, DOI: 10.1016/j.bbrc.2006.11.135.
47 A. Verma and F. Stellacci, *Small*, 2010, **6**, 12, DOI: 10.1002/smll.200901158.
48 S. Shahabi, L. Treccani, R. Dringen and K. Rezwan, *ACS Appl. Mater. Interfaces*, 2015, 7, 13821, DOI: 10.1021/acsami.5b01900.
49 A. Pochert, I. Vernikouskaya, F. Pascher, V. Rasche and M. Lindén, *J. Colloid Interface Sci.*, 2017, **488**, 1, DOI: 10.1016/j.jcis.2016.10.085.
50 I. Berts, G. Fragneto, L. Porcar, M. S. Hellsing and A. R. Rennie, *J. Colloid Interface Sci.*, 2017, **504**, 315, DOI: 10.1016/j.jcis.2017.05.037.
51 S. Winzen, S. Schoettler, G. Baier, C. Rosenauer, V. Mailaender, K. Landfester and K. Mohr, *Nanoscale*, 2015, 7, 2992, DOI: 10.1039/c4nr05982d.
52 C. D. Walkey and W. C. W. Chan, *Chem. Soc. Rev.*, 2012, **41**, 2780, DOI: 10.1039/c1cs15233e.
53 C.-Y. Lin, C.-M. Yang and M. Lindén, *RSC Adv.*, 2019, **9**, 33912, DOI: 10.1039/c9ra05585a.
54 O. Lunov, T. Syrovets, C. Loos, J. Beil, M. Delacher, K. Tron, G. U. Nienhaus, A. Musyanovych, V. Mailänder, K. Landfester and T. Simmet, *ACS Nano*, 2011, **5**, 1657, DOI: 10.1021/nn2000756.
55 Y. Yan, K. T. Gause, M. M. J. Kamphuis, C. S. Ang, N. M. O'Brien-Simpson, J. C. Lenzo, E. C. Reynolds, E. C. Nice and F. Caruso, *ACS Nano*, 2013, 7, 10960, DOI: 10.1021/nn404481f.
56 X. Duan and Y. Li, *Small*, 2013, **9**, 1521, DOI: 10.1002/smll.201201390.
57 Y. Yamamoto, Y. Nagasaki, Y. Kato, Y. Sugiyama and K. Kataoka, *J. Controlled Release*, 2001, 77, 27–38, DOI: 10.1016/s0168-3659(01)00451-5.
58 K. Xiao, Y. Li, J. Luo, J. S. Lee, W. Xiao, A. M. Gonik, R. G. Agarwal and K. S. Lam, *Biomaterials*, 2011, **32**, 3435, DOI: 10.1016/j.biomaterials.2011.01.021.
59 R. Smith, E. I. Wafa, S. M. Geary, S. H. Alhaj-Suliman and A. K. Salem, *Sci. Adv.*, 2022, **8**, DOI: 10.1126/sciadv.abk3150.

 This journal is © The Royal Society of Chemistry 2023

4. Publication III

Straightforward adsorption-based formulation of mesoporous silica nanoparticles for drug delivery applications.

Roman Schmid*, Nathalie Neffgen*, Mika Lindén
(*equal contribution)

Journal of Colloid Interface and Science, 2023, 640, 961-974.
https://doi.org/10.1016/j.jcis.2023.03.012

Published by Elsevier, Copyright © 2023.
This is an open access article under the CC BY NC 4.0 license
(https://creativecommons.org/licenses/by-nc/4.0/).

Journal of Colloid and Interface Science 640 (2023) 961–974

Contents lists available at ScienceDirect

Journal of Colloid and Interface Science

journal homepage: www.elsevier.com/locate/jcis

Straightforward adsorption-based formulation of mesoporous silia nanoparticles for drug delivery applications

Roman Schmid [1], Nathalie Neffgen [1], Mika Lindén *

Department of Inorganic Chemistry II, Ulm University, Albert-Einstein-Allee 11, 89081 Ulm, Germany

GRAPHICAL ABSTRACT

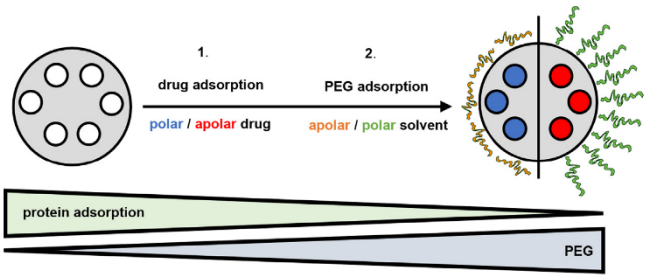

ARTICLE INFO

Article history:
Received 6 December 2022
Revised 28 February 2023
Accepted 2 March 2023
Available online 8 March 2023

Keywords:
Mesoporous silica
Nanomedicine
Protein corona
PEGylation
Drug formulation

ABSTRACT

Mesoporous silica nanoparticles (MSNs) have emerged as a very promising drug delivery platform. However, multi-step synthesis and surface functionalization protocols rise the hurdle for translation of this promising drug delivery platform to the clinic. Furthermore, surface functionalization aiming at enhancing the blood circulation time, typically through surface functionalization with poly(ethylene glycol) (PEG) (PEGylation), has repeatedly been shown to be detrimental for the drug loading levels that can be achieved. Here, we present results related to sequential adsorptive drug loading and adsorptive PEGylation, where the conditions can be chosen so that the drug desorption during PEGylation is minimized. At the heart of the approach is the high solubility of PEG both in water and in apolar solvents, which makes it possible to use a solvent for PEGylation in which the drug exhibits a low solubility, as demonstrated here for two model drugs, one being water soluble and the other not. Analysis of the influence of PEGylation on the extent of serum protein adsorption underline the promise of the approach, and the results also allow the adsorption mechanisms to be elaborated. Detailed analysis of the adsorption isotherms enables determination of the fractions of PEG residing on the outer particle surfaces in comparison to inside the mesopore systems, and also makes it possible to determine the PEG conformation on the outer particle surfaces. Both parameters are directly reflected in the extent of protein adsorption to the particles. Finally, the PEG coating is shown to be stable on time-scales compatible with intravenous drug administration, which is why we are convinced that the presented approach or modifications thereof will pave the way for faster translation of this drug delivery platform to the clinic.

© 2023 The Author(s). Published by Elsevier Inc.

* Corresponding author.
E-mail address: mlinden@uni-ulm.de (M. Lindén).
[1] equal contribution.

https://doi.org/10.1016/j.jcis.2023.03.012
0021-9797/© 2023 The Author(s). Published by Elsevier Inc.

1. Introduction

Nanoparticle-based drug delivery promises to overcome limitations related to conventional delivery through enhancement of drug stability, improving blood-circulation time and bioavailability, as well as through providing possibilities for targeting to specific cells and organelles.[1,2,3] A nanoparticulate drug delivery system that has attracted a lot of recent interest is mesoporous silica nanoparticles, MSNs. These highly porous particles consisting of amorphous silica are generally considered biocompatible,[4,5] and are biodegradable at a rate which is mainly controlled by the surface area and degree of silica condensation.[6–8] The particle size and shape, as well as the pore size and pore connectivity, can be rationally controlled, and the pore sizes are compatible with both small molecule drugs, and with bioactive macromolecules, like DNA and peptides. [9–11] The high surface area and mesopore volume allow high drug loading levels to be achieved.[12–14] This, in combination with straightforward means for surface functionalization based on well-established bioconjugation protocols, allows for optimization of the particle properties for a certain administration route, and also for modulation of the interactions between the drug and the particles, as well as between the particles and the biological system. In most *in vivo* studies intravenous, intraperitoneal or intratumoral injections have been the modes of administration. As also observed for other nanoparticle systems, native particles are typically immediately recognized by the reticuloendothelial system (RES) as foreign, and are therefore virtually immediately removed from circulation through uptake by macrophages in defence organs like liver and spleen.[15–17] The composition of the protein corona forming on the nanoparticles upon contact with serum has been shown to be important for triggering RES response. Recent studies suggest a special role of serum albumin, the most abundant protein in serum, for mediating the uptake by macrophages.[18–20] In order to enhance the blood circulation time, the nanoparticles are typically surface functionalized through covalent attachment of hydrophilic, charge-neutral polymers, in most cases poly(ethylene glycol) (PEG) before drug loading.[21–24] This coating serves to decrease the extent of serum protein adsorption, and therefore to render the particles with "stealth"-properties. However, several studies have reported that PEGylation of the MSNs lead to a decrease in the drug loading levels that can be achieved, as the particle surfaces become increasingly inaccessible for adsorption of drugs with increasing degree of PEGylation.[25,26] If the drug is introduced into the pore system of the MSNs before PEGylation, there is a risk that the drug is prematurely released from the pore system during PEGylation, and/or that the drug cannot withstand the conditions needed for efficient PEGylation. Furthermore, the complicated multistep synthesis and functionalization protocols typically employed, decrease the possibility for translation of this promising drug delivery platform to the clinic due to high costs for both synthesis and product quality control. Thus, there is an urgent need for the development of more straightforward and reproducible means that allow for both high drug loading levels and appropriate surface functionalization. Furthermore, as many drugs of interest are either hydrophobic, small molecule drugs or hydrophilic peptides, the approach should be useable for cargos exhibiting different polarities.

Here we report results related to adsorptive PEGylation of model drug-loaded MSNs. As PEG exhibits a high solubility in water and in apolar solvents, we first studied adsorptive PEGylation of all-silica and surface functionalized MSNs, respectively, from both (4-(2-hydroxyethyl)-1-piperazineethanesulfonic acid) (HEPES) buffer and from dichloromethane (DCM). In both cases, successful PEGylation reaching high mass-loadings could be achieved. Furthermore, serum protein adsorption was studied for all particle/solvent combinations, and serum protein adsorption generally decreased with increasing degree of PEGylation as expected. However, clear differences between proteins of different mass-fractions were observed, suggesting that the relative composition of the protein corona was PEGylation-degree dependent. The results are discussed based on differences in PEG location and conformation as well as hydrolytic particle stability. PEGylation of MSNs pre-loaded with either a hydrophobic small molecule or with a peptide was also successful under conditions where no premature drug release was observed. Again, PEGylation resulted in a strong decrease of serum protein adsorption as compared to the non-PEGylated particles. Taken together, our results suggest that adsorptive PEGylation is a highly promising means for straightforward and reproducible drug loading and PEGylation of MSNs, allowing for a more cost-effective formulation of MSNs for drug delivery applications.

2. Experimental details

2.1. Chemicals and materials

Tetramethyl orthosilicate (TMOS; 98 %), (3-aminopropyl) trimethoxysilane (APTMS; 97 %), tetraethyl orthosilicate (TEOS; ≥ 99 %), dichloromethane (DCM; ≥ 99.9 %), iodine (≥99.99 %), glycerine (99 % – 101 %), tetramethylethyldiamin (TEMED; 99 %), cyclohexane, 1,1'-dioctadecyl-3,3,3'3'-tetramethy lindocarbocyanine perchlorate (DiI) and sodium azide (≥99,5 %) were purchased from Sigma-Aldrich Chemie GmbH, Schnelldorf, Germany. Cetyltrimethylammonium bromide (CTAB; ≥ 99 %) and ammonium hydroxide (28 % in water), sodium hydroxide, potassium iodide, ethanol, methanol and hydrochloric acid were purchased from VWR International GmbH, Darmstadt, Germany. Carboxyethylsilanetriol di-sodium salt (CES, 25 wt% in water, 1.49 M) was purchased from abcr GmbH & Co. KG, Karlsruhe, Germany. α-Methoxy-ω-amino poly(ethylene glycol) with a molecular weight of 1964 Da and 5516 Da (PEG_{2k} (>95 %), PEG_{5k} (>95 %)) were purchased from Rapp Polymere, Tübingen, Germany. Ammonium nitrate (≥99), sodium dodecyl sulfate (SDS; ≥ 99 %), tris(hydroxy methyl)aminomethane (TRIS; ≥ 99 %), glycine (≥99 %), 1,4-dithiothreitol (≥99 %), agarose (low melt), acrylamide (≥98 %), N, N'-methylen-bis-acrylamide (≥98 %), ammonium peroxodisulfate (APS; ≥ 98 %), and Coomassie® Brilliant Blue G-250 were purchased from Carl Roth GmbH & Co. KG, Karlsruhe, Germany. (4-(2-hydroxyethyl)-1-piperazineethanesulfonic acid) (HEPES) and bromophenol blue were purchased from Merck KGaA, Darmstadt, Germany. Phosphate buffered saline (PBS), and PageRuler™ Broad range unstained protein ladder and HyClone™ fetal calf serum (FCS) were purchased from Thermo Fisher Scientific, Karlsruhe, Germany. The FCS was heat-inactivated (76 °C, 1 h), all other chemicals were used as supplied by the manufacturer without further purification. Calcitonin was purchased from PolyPeptide, Zug, Switzerland.

2.2. Synthesis of mesoporous silica nanoparticles

Mesoporous silica nanoparticles (MSNs) were synthesized according to Rosenholm *et al.*[27] Briefly, the structure directing agent CTAB (7.88 g, 21.6 mmol) was dissolved in a mixture of methanol (890 mL), water (879 mL) and sodium hydroxide solution (1 M, 4.56 mL, 4.6 mmol) in a 2 L round-bottomed flask. Upon equilibrating to room temperature (RT), a mixture of the precursors TMOS (2.19 mL, 14.7 mmol) and APTMS (0.37 mL, 2.1 mmol) was added dropwise at a stirring rate of 500 rpm. After 45 min the stirring rate was reduced to 300 rounds per minute (rpm) and the reaction proceeded for another 16 h. The particles were

precipitated with ammonium nitrate (35 g, 27.4 mmol), separated via centrifugation, and subsequently washed once with water and twice with ethanol by dispersing them in an ultrasonic bath for 1 h. Finally, the particles were dried at 80 °C and calcined at 550 °C for 5.5 h (heating rate 1.8 °C min^{-1}). Such particles will be referred to as MSNc in the following.

2.3. Synthesis of non-porous silica particles

Non-porous silica particles (NSNs) were synthesized according to a modified Stöber synthesis,[28] as previously reported.[29] To a mixture of ethanol (55.8 mL), water (44 mL) and ammonium hydroxide solution (28 wt%, 14.8 M, 6 mL, 100.7 mmol) in a 0.5 L round-bottomed flask, the silica precursor TEOS (3 mL, 13.5 mmol) was added at a stirring rate of 450 rpm. The reaction took place at RT for 19 h. After centrifugation, the obtained particles were washed with ethanol in an ultrasonic bath for 1 h and dried at 60 °C. Finally, the particles were calcined as described above and are denoted NSNc in the following.

2.4. Functionalization of mesoporous silica particles

For functionalization with carboxy groups, MSNc were dispersed in methanol using a focused ultrasonic bath (Covaris S220) and mixed with an aqueous solution of CES (25 wt%, 1.49 M) in a 50 mL centrifugation tube. The final concentration of MSNc and functional silane were 5 mg mL^{-1} and 20 μmol mL^{-1}. After agitation for 3 h at RT, the particles were centrifuged and washed thoroughly once with water and twice with acetone in an ultrasonic bath. The functionalized particles were dried *in vacuo* at 80 °C for 17 h. Such particles are denoted MSN-COOH in the following.

2.5. Characterization of silica nanoparticles

Thermogravimetric analysis (TGA) was performed on a TG209 F1 Libra (Netzsch, Germany) at a heating rate of 10 °C min^{-1} in nitrogen/oxygen (70 % / 30 %) atmosphere. After the particles were dried *in vacuo* at 100 °C for 22 h, nitrogen sorption measurements were conducted on a Quadrasorb–1 (Quantachrome Instruments, Germany) at −196 °C. The specific surface areas were determined using the Brunauer, Emmett and Teller (BET) method, pore diameters were determined using the equilibrium non-local density functional theory (NLDFT) kernel (silica, cylindrical pores) in a relative pressure range of 0–0.9. The external surface areas were estimated by the *t*-plot method in the relative pressure range of 0.75–0.95. Pore volumes were determined at a relative pressure value of 0.9 p p_0^{-1}. Zeta potentials were measured three times with a Zetasizer NanoZS Zen3600 (Malvern Panalytical, Germany) in aqueous HEPES buffer (25 mM, pH 7.2) using a particle concentration of 0.1 mg mL^{-1}. Particle shape and diameter were examined with a Jeol 1200 (Jeol, Germany) transmission electron microscope (TEM) using a HT voltage of 120 kV and a beam current of 65 μA. Grey-scale images of the electron diffraction patterns were obtained via fast Fourier transformation (FFT) using the FFT plug-in of ImageJ version 1.52n. Electron diffracting structures were visualized by filtering different frequency ranges via selection of grey values ranging from 142 to 255 or from 142 to 149 and subsequent inverse FFT. Small-angle X-ray diffraction measurements were performed on a Bruker Nanostar (Bruker, USA) using Cu Kα radiation (λ = 1.5406 Å) at an angle from 0.3° to 3.3° (2θ). ATR-IR measurements were conducted on a Tensor 27 (Bruker, USA) with a total of 200 scans per sample. Raman spectra were recorded on a UHTS-300 spectrometer utilizing a 532 nm WITech laser and a WITec alpha 300R microscope (WITech, Germany) with a 50x/0.7NA objective (Zeiss, Germany).

2.6. Loading of a hydrophobic model drug (DiI)

MSNc particles were dried at 100 °C *in vacuo* for 16 h. The particles (5.5 mg mL^{-1}) were dispersed with a focused ultrasonic bath and mixed with different amounts of a DiI stock solution in cyclohexane (2 mg mL^{-1}, 2.14 mM). The final DiI concentrations were 0, 1 and 5 mg mL^{-1} respectively. After 3 h of agitation in the dark, the particles were separated via centrifugation and briefly washed with cyclohexane in an ultrasonic bath. The particles loaded with different amounts of DiI were dried at 80 °C *in vacuo* for 3 h prior further PEG adsorption in HEPES buffer (as described below). The DiI loading degree was quantified via UV/Vis spectroscopy of the adsorption supernatants and the washing media at a wavelength of λ = 563 nm.

2.7. Loading of a hydrophilic peptide-based drug (calcitonin)

For calcitonin loading onto MSNc, the particles were dispersed in PBS using a focused ultrasonic bath. A stock solution of the calcitonin in PBS (5 mg mL^{-1}) was added to the particle dispersion leading to a final peptide concentration of 0.25 mg mL^{-1} or 1.5 mg mL^{-1} and a final particle concentration of 5 mg mL^{-1}. After 1 h of agitation at RT, the particles were collected by centrifugation, washed with acetone and dried at 37 °C. PEGylation was then carried out in DCM as described above. The peptide loading degree was quantified by TGA.

2.8. Adsorption of PEG onto silica nanoparticles

Adsorptive PEGylation was caried out either in aqueous HEPES buffer (25 mM) at pH 7.2 or in dichloromethane (DCM). Stock solutions (10 mg mL^{-1}) containing α-methoxy-ω-amino polyethylene glycol with a molecular weight of either 1964 Da (PEG_{2k}) or 5516 Da (PEG_{5k}) were prepared. The particles were dispersed with a focused ultrasonic bath and mixed with different amounts of diluted PEG stock solutions in 2 mL tubes resulting in a particle concentration of 5 mg mL^{-1} and PEG concentrations ranging from 0 mg mL^{-1} to 2 mg mL^{-1}. After 2 h of agitation at RT, the particles were separated via centrifugation, washed briefly with pure solvent and finally with acetone, followed by drying at 60 °C *in vacuo*. The PEG loading was determined via TGA (PEGylation in DCM) or photometrically via an iodine based photometric assay [30] (PEGylation in water). For the latter, 15 μL of an aqueous potassium iodide (20 mg mL^{-1}) / iodine (10 mg mL^{-1}) solution was added to 1 mL of sample. The absorbance was measured at λ = 589 nm (PEG_{2k}) or λ = 541 nm (PEG_{5k}) using a Nanodrop 2000 UV/Vis spectrometer (Thermo Scientific). The adsorbed PEG amounts were further normalized to the specific surface area of the native particles used, yielding the respective surface mass excess values (mg m^{-2}).

2.9. Estimation of the portion of PEG adsorbed on the outer surface vs. inside the mesopores

The Flory radii, R_f, of the used PEGs were calculated according to equation (1), where N is the number of monomer units per chain (45 and 125 for PEG_{2k} and PEG_{5k} respectively), l the length of an ethylene glycol monomer (0.278 nm), and ν the Flory exponent for the expanded coil state (0.6).[31]

$$R_f = 1N^{\nu} \quad (1)$$

This results in Flory radii of 2.68 nm and 5.02 nm for PEG_{2k} and PEG_{5k}, respectively. Thus, neither PEG could fit into the mesopores of the MSNs unless the PEG chains adopt a more stretched config-

uration. We therefore assumed that the mass of PEG adsorbed into the mesopores, x, at the adsorption plateau is independent of PEG molar mass, *i.e.*

$$x_{2k} = x_{5k} \quad (2)$$

Under this assumption, any differences in total adsorbed mass (z) then arise from differences in portion of PEG adsorbed on the outer particle surfaces, y. Here, an influence of the PEG molecular mass can be expected. In order to account for this, we used the ratio of the respective PEG masses adsorbed per m^2 onto the NSNc particles at the adsorption plateau as basis for the calculations. For PEG adsorbed from DCM, the m_{PEG5k}/m_{PEG2k} value was 1.07, while the corresponding value was 1.77 when the adsorption was carried out from water. Under these assumptions, the total adsorbed masses of PEG_{2k} and PEG_{5k} onto MSNc or MSN-COOH particles are then given by equation (3) and (4), respectively, in the case of adsorption from water.

$$z_{2k} = x_{2k} + y_{2k} \quad (3)$$

$$z_{5k} = x_{2k} + 1.77\, y_{2k} \quad (4)$$

Inserting equation (3) in equation (4) leads to the external and internal mass of PEG_{2k} (equation (5) and (6)) as well as the external mass of PEG_{5k} (equation (7)).

$$y_{2k} = \frac{z_{5k} - z_{2k}}{0.77} \quad (5)$$

$$x_{2k} = z_{2k} - y_{2k} \quad (6)$$

$$y_{5k} = z_{5k} - x_{2k} \quad (7)$$

Calculations of external portions of PEG, chain densities and conformations on the different particles depending on the outer surface, as determined by *t*-plot method, are summarized in Table S1. The spatial distance between adsorbed PEG chains, S, was calculated based on the chain density of the portion of adsorbed PEG located on the outer particle surface, under the assumption of a circular adsorption area using the respective values of the Flory radii.

2.10. Protein adsorption onto silica nanoparticles from FCS

Protein corona formation was examined by incubation of silica nanoparticles with and without adsorbed PEG in FCS. In order to account for hydrolysis of the silica surface while PEG adsorption under aqueous conditions, experiments were also carried out for native MSNc and MSN-COOH that had been pre-incubated in HEPES buffer under the same conditions used for PEGylation, but in the absence of PEG. Such particles are referred to as "pre-incubated". Native, pre-incubated and PEGylated particles were dispersed thoroughly in PBS with a focused ultrasonic bath and added to FCS in 2 mL Eppendorf tubes resulting in a normalized (rest mass at 600 °C) silica concentration of 5 mg mL^{-1} and 10 vol% of FCS. The protein corona was allowed to form for 24 h at 37 °C under agitation. After separation via centrifugation (21100 rcf, 10 min), the supernatants were discharged, and the particles were briefly washed three times with purified water. For protein elution, an aqueous SDS solution (10 wt%, 0.39 M) was added, doubling the particle concentration initially used for FCS adsorption. The samples were dispersed in an ultrasonic bath and incubated at 95 °C for 30 min. Upon centrifugation (21100 rcf, 10 min), the particles were discharged and the SDS supernatants were stored at −80 °C until further use.

Direct comparison of protein adsorption onto differently functionalized porous and non-porous particles was conducted as described above but the amounts of particles used was normalized to the outer surface area (*t*-plot method) of the respective native particles resulting in a fixed surface area of 0.525 m^2 mL^{-1}, which corresponds to 19.2 mg mL^{-1} (NSNc), 19.3 mg mL^{-1} (PEG_{5k}@NSNc in water), 9.2 mg mL^{-1} (MSN–COOH), 10.8 mg mL^{-1} (PEG_{5k}@MSN-COOH in water), 5 mg mL^{-1} (MSNc) and 6 mg mL^{-1} (PEG_{5k}@MSNc in water).

The protein adsorption kinetics were investigated with a silica and FCS concentration of 5 mg mL^{-1} and 10 vol%, respectively. Corona formation was conducted at 37 °C for 5 min, 10 min, 30 min, 1 h, 2 h, 4 h, 6 h or 24 h. Further sample preparation was carried out as described above. Finally, obtained SDS supernatants were examined via gel electrophoresis using manually casted polyacrylamide gels.

2.11. SDS-PAGE of SDS supernatants

Upon thawing, the SDS supernatants were once again centrifuged (21100 rcf, 10 min), and 40 µL of sample was mixed with 8 µL Laemmli buffer (Tris-HCl buffer (0.5 M; pH 6.8 (adjusted with HCl); 1.2 mL), SDS (1.2 g), bromophenol blue (6 mg), glycerine (4.7 mL), water (2.9 mL) and 1,4-dithiothreitol (0.9 g)). Additionally, mixtures of 100 µL SDS buffer and 20 µL Laemmli buffer ("SDS") as well as 25 µL FCS, 185 µL SDS buffer and 90 µL Laemmli buffer ("FCS") were prepared as controls. All samples and controls were incubated at 95 °C for 5 min. Afterwards, 5 µL protein ladder, 7.5 µL of protein sample, 15 µL of SDS control and 2.5 µL of FCS control were loaded into Mini-PROTEAN TGX Stain-Free Precast Gels (Bio-Rad Laboratories GmbH, Germany), and SDS-PAGE was run in an aqueous electrophoresis buffer, comprised of SDS (3.5 mM), Tris (49.5 mM) and glycine (383.6 mM), using a Mini-PROTEAN Tetra Vertical Electrophoresis Cell and a PowerPac Universal Power Supply at a voltage of 300 V. Gel documentation and analysis was carried out using a Gel Doc™ EZ Imager (Bio-Rad Laboratories GmbH, Germany) and Image Lab software version 6.0.1. For every gel, the absolute grey values of each band region were first normalized against the 70 kDa band intensity of the ladder. Finally, the band intensities were normalized against the band intensities measured for the native, non-pre-incubated MSNc.

SDS-PAGE was performed using a Biorad PROTEAN II XL electrophoresis chamber. 10 µL protein ladder, 15 µL protein sample, 30 µL SDS control and 5 µL of FCS control were separated using 15 % separation gels (acrylamide/N,N'-methylene-bis-acrylamide (2.1 M/ 26 mM) (20 mL); Tris-HCl buffer (1.5 M; pH 8.8 (adjusted with HCl); 10 mL), ultrapure water (9.8 mL); APS (10 % in water; 200 µL); TEMED (20 µL)) and 5 % stacking gels (acrylamide/N,N'-methylene-bis-acrylamide (2.1 M/ 26 mM) (2 mL); Tris-HCl buffer (0.5 M; pH = 6.8 (adjusted with HCl); 3 mL), ultrapure water (7 mL); APS (10 % in water; 120 µL); TEMED (24 µL)). SDS–PAGE was run in aqueous lower buffer, containing SDS (3.5 mM), Tris (49.5 mM), glycine (383.6 mM) and sodium azide (3 mM) and aqueous upper buffer, comprising SDS (3.5 mM), Tris (49.5 mM) and glycine (383.6 mM), applying constantly 300 V (900 Vh). After separation, the gels were washed three times with ultrapure water and stained for 2 h with Coomassie staining solution as described by Kang *et al.*,[34] After washing with ultrapure water and destaining in ultrapure water over night, a Biorad GelDoc System was used for visualization and Image Lab software version 6.0.1 (Bio-Rad Laboratories GmbH, Germany) for analysis.

3. Results

3.1. Particle characterization

MSNs were synthesized using established protocols, and will be denoted by MSNc (c = calcined) in the following.[27] Carboxy-

silane-functionalized MSNc particles are referred to as MSN-COOH. The silanization degree was 0.24 mmol g^{-1} silica as determined by thermogravimetric analysis (TGA) (see Figure S1). Transmission electron microscopy (TEM) images taken of the two sets of particles are shown in Fig. 1. The radial mesopore structure of the mesoporous particles is evident, but there is no long-range ordered porosity. This conclusion is also supported by FFT analyses of the TEM image as well as by small-angle X-raydiffraction results shown in Figure S2. The mean particle size was around 152 nm with a narrow particle size distribution. Further characterization of the particles was carried out by nitrogen sorption, and the results are summarized in Fig. 2 and Table 1. The specific surface areas were high for both particles, but slightly lower for the surface functionalized particles as expected (1117 m^2 g^{-1} vs 861 m^2 g^{-1}), and the corresponding external surface areas as determined using the *t*-plot method were 76 m^2 g^{-1} and 85 m^2 g^{-1}, respectively. The mean mesopore diameter was slightly smaller for the MSN-COOH particles as compared to the MSNc particles (3.5 nm vs 3.2 nm). In addition, non-porous silica nanoparticles, denoted by NSNc, having similar but slightly higher mean particle diameters (190 nm) were synthesized using the Stöber method followed by calcination. The absence of mesoporosity in these particles was confirmed by nitrogen sorption (see Fig. 2), and their specific BET surface area was 22 m^2 g^{-1}. All particles exhibited similar negative zeta potential values of −34 to −51 mV measured in HEPES buffer (25 mM, pH = 7.2), in good agreement with literature values.[32].

Table 1
Physicochemical characteristics of the starting particles. See text and experimental for details. Zeta potentials were measured in 25 mM HEPES buffer at pH 7.2 (mean ± SD; n = 3).

	MSNc	MSN-COOH	NSNc
diameter / nm (mean ± SD; N > 100)	156 ± 20	152 ± 16	190 ± 19
functionalization degree / mmol · g^{-1}	–	0.30 ± 0.04	–
surface area (BET) / m^2 · g^{-1}	1117 ± 52	861 ± 2	22 ± 4
outer surface area (*t*-plot) / m^2 · g^{-1}	76 ± 8	85 ± 2	22 ± 2
pore diameter / nm	3.5 ± 0.15	3.2 ± 0.1	–
pore volume / cm^3 · g^{-1}	0.80 ± 0.04	0.60 ± 0.04	–
zeta potential / mV	−34 ± 6.6	−38 ± 4.5	−51 ± 4.7

3.2. Solvent polarity determines PEG localization and conformation

Adsorption of PEG_{2k} and PEG_{5k} onto the different particles were determined from aqueous HEPES buffer, in the following referred to as 'water', as well as from DCM. The amount of PEG adsorbed from water was determined by iodide-titration of PEG in the supernatant after adsorption. As the iodide assay does not work in DCM, the amount of PEG adsorbed onto the particles from DCM was determined by TGA. As silica is not soluble in DCM, potential influence of partial silica dissolution during PEGylation on the TGA results can be excluded. Exemplary thermogravimetric analysis of MSNs PEGylated in water or DCM can be found in Figures S3

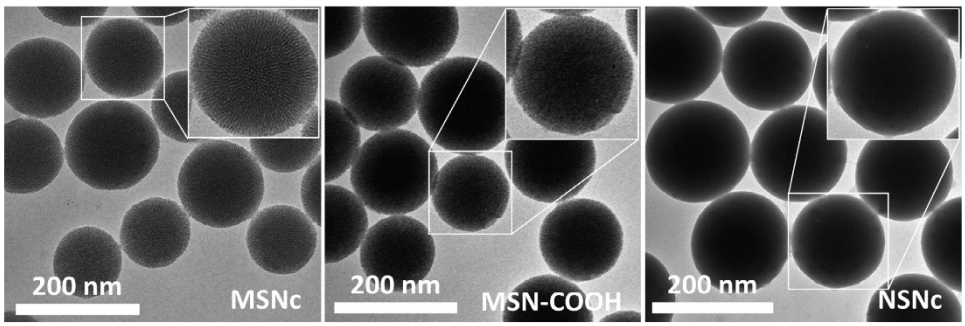

Fig. 1. Transmission electron micrographs of MSNc (left), MSN-COOH (middle) and NSNc (right) particles.

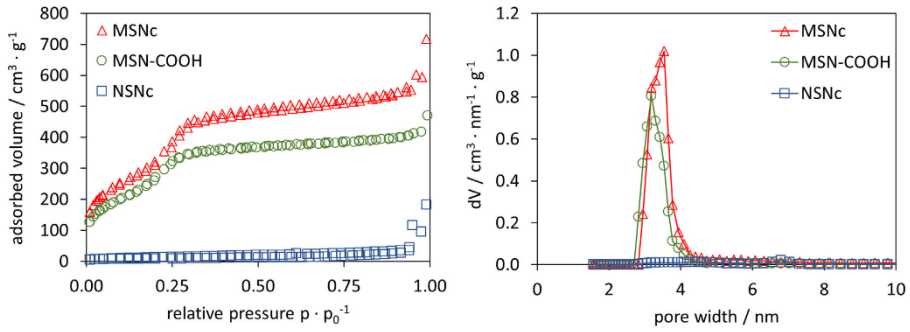

Fig. 2. Nitrogen sorption isotherms (left) measured at −196 °C for MSNc, MSN-COOH and NSNc particles, and the corresponding pore-size distribution curves (right) calculated using the equilibrium NLDFT kernel developed for silica.

and S4. Successful PEGylation was also demonstrated by ATR-IR- and Raman spectroscopy (See Figure S5). The intensities of the PEG related bands on the PEGylated particles were diminished because of the overall relatively low PEG masses in the samples. The IR bands at 1341 cm^{-1}, 1466 cm^{-1} and 2880 cm^{-1} could be assigned to C—H bending and stretching of the adsorbed PEG compound.[33] Raman bands corresponding to PEG were identified at 850 cm^{-1} (CH_2 rocking, C—O stretching, C—C stretching), 1144 cm^{-1} (CH rocking, C—O stretching), 1280 cm^{-1} (CH_2 wagging), 1470 cm^{-1} (CH_2 scissoring) and 2880 cm^{-1} (C—H stretching).[34,35] BET surface area-normalized adsorption isotherms for PEG_{2k} and PEG_{5k} are shown in Fig. 3 for MSNc and NSNc particles and in Fig. 4 for MSN-COOH. The adsorption isotherms measured in water for MSNc were steep for both PEGs studied, in agreement with literature data for PEG adsorption onto silica where the PEGs have comparable molecular weights,[36] and reached a plateau at about 0.19 mg m^{-2} for PEG_{2k} and at about 0.23 mg m^{-2} for PEG_{5k}.

Through PEGylation in DCM, higher PEG loadings mounting to around 0.30 mg m^{-2} (PEG_{2k}) and 0.28 mg m^{-2} (PEG_{5k}) for MSNc (Fig. 3) could be achieved. These isotherms were S-shaped, suggesting co-operative adsorption.

In order to shed some more light on the location and adsorption geometry of the PEG molecules after adsorption onto the MSNs, the adsorption isotherms of the two PEGs onto non-porous NSNc in water were determined (Fig. 3, right). Opposite to what was observed for MSNc, the amount of PEG_{5k} adsorbed (mass/surface area) from water was clearly higher with a factor of roughly 2 as compared to PEG_{2k} at a given solution concentration, *i.e.* about corresponding to the mass and length ratio between the two PEGs. This can be understood if the PEG molecules adapt a conformation which is extended towards the solvent. The ratio range is in good agreement with that previously observed for the adsorption of PEG_{2k} and PEG_{5k} from water onto a macroporous silica gel for which confinement effects can be excluded.[37] If it is assumed that the PEG orientation on the non-porous particles is identical to that on the outer surface of porous particles, the higher plateau values observed for PEG_{5k} as compared to PEG_{2k} in water can be understood. Such differences cannot be expected for the PEG portion located inside the mesopore system, as PEG chains present inside the mesopores have to adapt a more elongated form in order to fit into the confined geometry of the mesopores. If the mass ratios of PEG adsorbed onto the outer surface of the studied MSNs are identical to that observed for the non-porous NSNc particles,

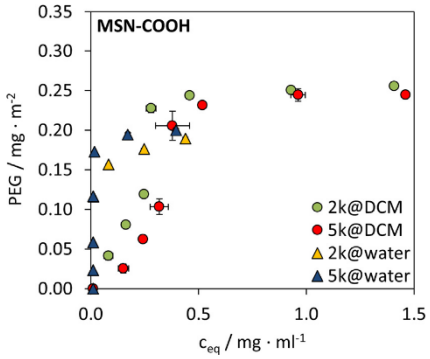

Fig. 4. Adsorption isotherms of PEG_{2k} and PEG_{5k} measured in water and DCM for porous MSN–COOH. Surface concentrations were calculated based on the specific surface areas (BET) of the respective particles (mean ± SD, n = 3).

and if the packing densities of PEG_{2k} and PEG_{5k} located inside the confined mesopore system are identical for both molar masses, the portions of PEG adsorbed into the pore system versus onto the particle's surfaces can be estimated, as outlined in the experimental section. Based on the adsorption experiments onto NSNc, the determined PEG_{5k}/PEG_{2k} mass ratio of 1.77 is also assumed to hold for the portion of the PEG molecules adsorbed from water onto the outer surface of MSNc particles. Under these assumptions, the calculations suggest that about 77 % (PEG_{2k}) and 65 % (PEG_{5k}) of the PEG mass would be located within the mesopore system of the MSNc at the adsorption plateau when adsorbed from water. This is important, as PEG present inside the mesopore system will not influence the protein adsorption onto the particles (see later). With the estimated outer surface portions in combination with the total amount adsorbed as determined based on the adsorption isotherms, the conformation of the PEG molecules present on the outer particle surfaces can be estimated, as the outer surface area can be estimated based on the *t*-plot. Generally, the PEG chain conformation can be calculated using the theory of de Gennes.[31] Here, the distance between the chains (S) which can be obtained from the number of chains/spherical adsorption area, is related to the Flory radius (R_F) of the polymer. If the value of $S/2R_f$ is ≅ 1, the polymer is expected to adopt a close-packed mushroom

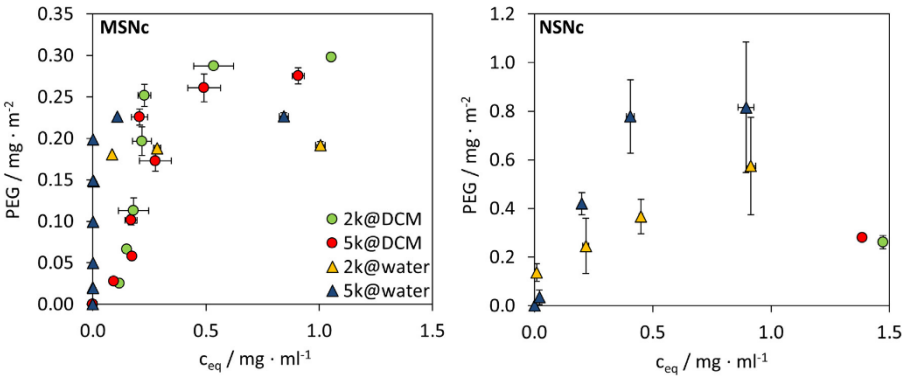

Fig. 3. Adsorption isotherms of PEG_{2k} and PEG_{5k} measured in water and DCM for porous MSNc (left), and non-porous NSNc (right). Surface concentrations were calculated based on the specific surface areas (BET) of the respective particles (mean ± SD, n = 3).

conformation, for values < 1 a dilute brush conformation, and for values ≅ 0.5 a dense brush conformation.[31,38] Many studies suggest that a dense brush PEG layer is beneficial for minimizing protein adsorption,[20,39,40] although also less dense brush conformations have been reported to effectively reduce protein adsorption.[20] The calculated $S/2R_f$ values for the different particle/solvent/molecular weight combinations at the highest PEG loadings are given in Table 2 and further error estimates are given in Table S1. For NSNc particles PEGylated in water we obtained $S/2R_f$ values of 0.63 (PEG_{2k}) and 0.39 (PEG_{5k}). The corresponding values for MSNc were 0.50 (PEG_{2k}) and 0.33 (PEG_{5k}). Thus, this suggests that the PEG chains adopt a dense brush conformation on MSNc when adsorbed from water.

For PEGylation from DCM, the surface concentrations of PEG were identical for MSNc and NSNc particles, suggesting an identical PEG conformation inside the mesopore system and on the outer particle surface. Thus, the results imply a relatively flat PEG conformation on the outer particle surface in this case. Based on a PEG_{5k}/PEG_{2k} mass ratio of 1.07 observed for NSNc, the portion of PEG inside the mesopore system of MSNc at the adsorption plateau when adsorbed from DCM was estimated to be 92 %, *i.e.* higher than in water. In order to estimate the inside/outside distribution of PEG at lower adsorbed amounts and as a function of PEG loading degree, nitrogen sorption measurements of particles PEGylated in DCM were carried out, and the results are summarized in Figure S6 and Table S2. A shift of the mesopore filling step towards lower relative pressures for the PEGylated particles was seen in all cases, indicative of a decrease in the mesopore size upon PEGylation. The decrease in the values for the PEG mass-corrected pore volumes for particles PEGylated through adsorption from DCM showed a linear dependency on the PEG content which suggests a constant ratio between PEG adsorbed on the outer and inner parts of the particles irrespective of the PEG loading in this case (Figure S7). These results give further support for the presence of PEG molecules inside the mesopore system of the MSNs for both molecular weights. Corresponding data is not shown for particles PEGylated in water as the pore volume values were influenced by partial silica dissolution-re-precipitation processes during PEGylation.

In order to investigate the influence of surface functionalization on the adsorptive PEGylation, corresponding adsorption experiments using MSN-COOH were conducted. The isotherms are shown in Fig. 4. Again, steep adsorption isotherms were observed when PEGylation was carried out from water, with plateau values of about 0.19 mg m^{-2} (PEG_{2k}) and 0.20 mg m^{-2} (PEG_{5k}). The very similar plateau values for both PEG molecular weights suggest either a relatively flat PEG conformation or a high fraction of the PEG molecules being present inside the mesopore system as compared to the MSNc particles. Based on a similar argumentation to the one presented for the MSNc particles, *i.e.* assuming that the differences in plateau values reflect the inside/outside location of the PEG molecules, suggests that around 90 % of the PEG resided within the mesopore system at the adsorption plateau when adsorbed from water. As the main polymer-silica interaction is based on hydrogen bonding between silanol groups and the oxygens in the ethylene oxide groups of the PEG molecules,[41] potentially mediated by water molecules, a lower attractive PEG-MSN interaction can be expected for the MSN-COOH particles as compared to the MSNc particles. It has repeatedly been shown that post-functionalization of small-pore mesoporous silicas by functional silanes lead to a higher concentration of functional groups closer to the particle surface due to diffusion limitation effects.[42–44] We therefore tentatively ascribe the higher degree of intrapore PEG adsorption for MSN-COOH as compared to MSNc to a higher carboxy-silane functionalization degree in the outer region of the particles as compared to inside the particles, and to a more preferential PEG-silica interaction inside the mesopore system. A lower outer surface concentration of PEG naturally leads to higher $S/2R_f$ values, being 1.02 for PEG_{2k} and 0.69 for PEG_{5k}, suggesting a more mushroom-like PEG conformation on the outer particle surface as compared to the MSNc particles PEGylated in water.

The PEG masses adsorbed from DCM were virtually identical for both PEG molecular masses studied, mounting to 0.25 mg m^{-2}, which transforms to an estimated mesopore PEG fraction of 89 %. The similarity between the PEG distribution between the inner mesopore system and the outer particle surface estimated for MSNc and MSN-COOH when adsorbed from DCM can be explained based on the same argumentation as above in terms of PEG adsorption conformation, *i.e.* a rather collapsed/flat PEG conformation on the outer surface of the particles.

Zeta potentials measured in HEPES buffer at pH 7.2 for different PEG loadings were very similar to that of the starting particles, being more negative than −26 mV in all cases (see Figure S8).

3.3. Protein corona composition depends on PEG conformation

Next, the capability of adsorbed PEG to decrease serum protein adsorption onto the MSNs under timescales of relevance for intravenous administration, *i.e.* up to 24 h, was investigated. We first investigated the kinetics of serum protein adsorption onto MSNc and MSNc-PEG_{5k} (DCM) (0.22 mg m^{-2}). After given incubation times, the particles were thoroughly washed, and then the strongly adsorbed proteins were desorbed by treatment of the particles in SDS-containing solution. Finally, the proteins were separated according to mass by gel electrophoresis. Two representative gels are shown in Figure S9, where the protein adsorption time has been varied between 5 min and 24 h. As shown in Figure S9 A), the as-synthesized MSNc particles adsorb a range of proteins, and the protein concentration and molecular weight distribution are almost independent of incubation time, suggesting very fast adsorption kinetics in agreement with previous reports. [45] For the PEGylated particles (Figure S9 B), radically lower protein band

Table 2
Conformations of externally adsorbed PEG_{2k} and PEG_{5k} onto non-porous NSNc and porous MSNc and MSN-COOH were normalized on the outer surface area as determined by *t*-plot method. Calculations for NSNc are based on the data range given by both, the third and fourth isotherm point.

	NSNc@water		MSNc@water		MSN-COOH@water	
	PEG_{2k}	PEG_{5k}	PEG_{2k}	PEG_{5k}	PEG_{2k}	PEG_{5k}
external PEG portion / %	100		23	35	7	12
chain density (*t*-plot) / 1 · nm^{-2}	0.11–0.18	0.09	0.18	0.11	0.04	0.03
distance S (*t*-plot) / nm	3.4–2.7	3.9–3.8	2.7	3.3	5.5	6.9
$S/2R_f$ (*t*-plot)	0.63–0.50	0.39–0.38	0.50	0.33	1.02	0.69
	NSNc@DCM		MSNc@DCM		MSN-COOH@DCM	
	PEG_{2k}	PEG_{5k}	PEG_{2k}	PEG_{5k}	PEG_{2k}	PEG_{5k}
external portion PEG / %	100		8	8	11	11
chain density (*t*-plot) / 1 · nm^{-2}	0.08	0.03	0.08	0.03	0.08	0.03

intensities were observed for each time-point, suggesting a stable and effective PEG layer against serum protein adsorption, at least on this time scale. Only some reminiscent, low intensity bands, presumably corresponding to BSA and Apolipoprotein A-I,[46] and some additional high molecular weight bands of unknown origin can be observed even after 24 h of incubation, with a slow but clear increase in band intensities within the first 2 h. Based on these results, it is concluded that the adsorbed PEG layer was kinetically stable, and the 24 h time-point was chosen for further experiments.

The next step was to investigate the protein adsorption as a function of PEG loading for MSNc and MSN-COOH particles. Selected SDS-PAGE gels are shown in Fig. 5. In all cases, an overall decrease in the amount of serum protein adsorbed with increasing PEG loading was observed as compared to the corresponding non-PEGylated particles. Note, that the non-PEGylated MSN-COOH particles adsorbed clearly less proteins than the non-PEGylated MSNc particles did, in agreement with previous reports showing that carboxylated MSNs show low serum protein adsorption levels.[47] However, this was not true for the high molecular weight proteins. There were clear differences in the protein adsorption behaviour as a function of PEG loading between different protein masses, as well as between the two different MSN types at intermediate and low PEG loadings. Therefore, in Fig. 6 the results are presented separated into three protein molecular weight classes, representing high molecular weight proteins (>88 kDa), medium molecular weight proteins (47–88 kDa), and low molecular weight proteins (<47 kDa). The results are presented relative to the amount of corresponding protein masses adsorbed onto the non-PEGylated as-synthesized MSNc particles. For MSNc and MSN-COOH particles PEGylated in DCM, a virtually linear decrease in protein adsorption was observed with increasing PEGylation degree for both PEG molecular weights, and the influence of PEG molecular weight was minor. This was especially true for the medium weight proteins, while substantial amounts of low and high molecular weight proteins adsorbed to these particles even at the highest PEG loadings. All in all, these results are perfectly in line with the conclusions made based on the adsorption isotherms: An increasing amount of PEG is present on the outer surface with increasing PEG loading, but the PEG conformation never reaches a brush conformation when adsorbed from DCM, and thus a gradual decrease in protein adsorption is observed with increasing PEGylation degree. Furthermore, the PEG molecular weight dependency was minor, as expected based on the discussion above.

For particles PEGylated in water, a very different behaviour was observed. For the MSNc particles, the decrease in protein adsorption with increasing PEGylation degree was very strong for the medium weight proteins already at low PEGylation levels,

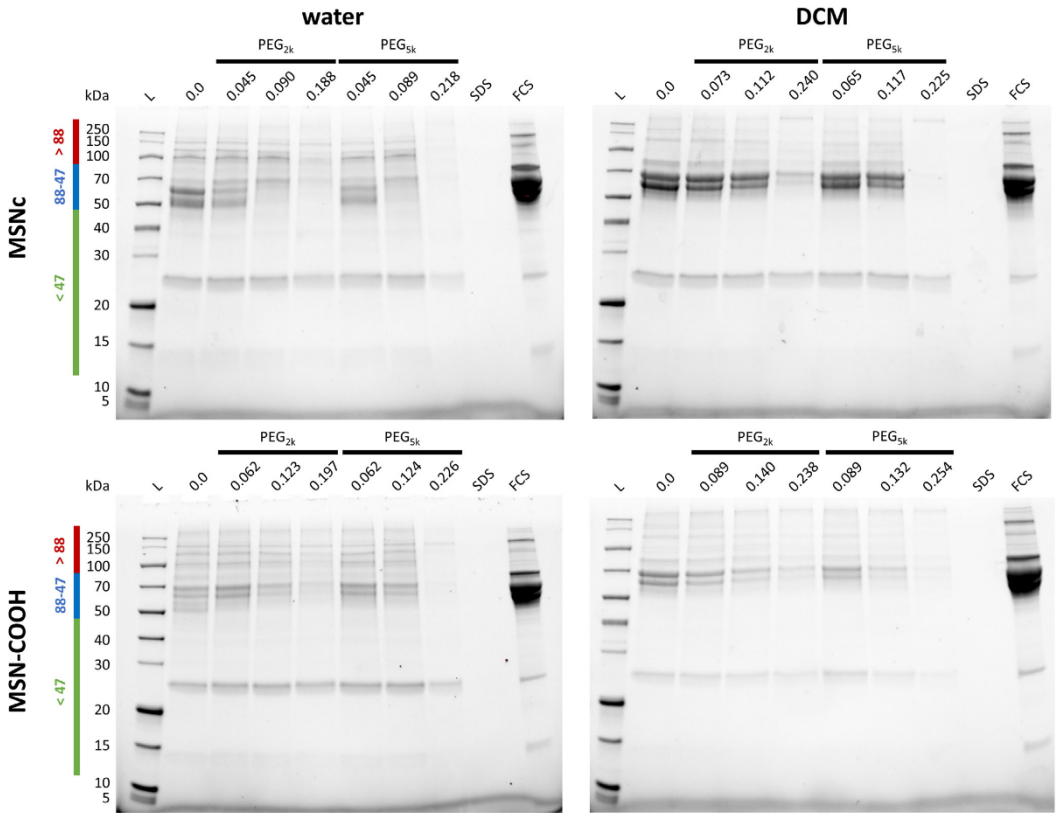

Fig. 5. SDS-PAGE of supernatants after incubation of MSNc and MSN-COOH PEGylated in water or DCM with 10 % FCS in PBS at 37 °C and 5 mg mL^{-1} for 24 h. The indicated PEG loadings are expressed as mg m^{-2} calculated based on the corresponding BET surface areas. Note, that the non-PEGylated, as-synthesized particles were not pre-incubated in water.

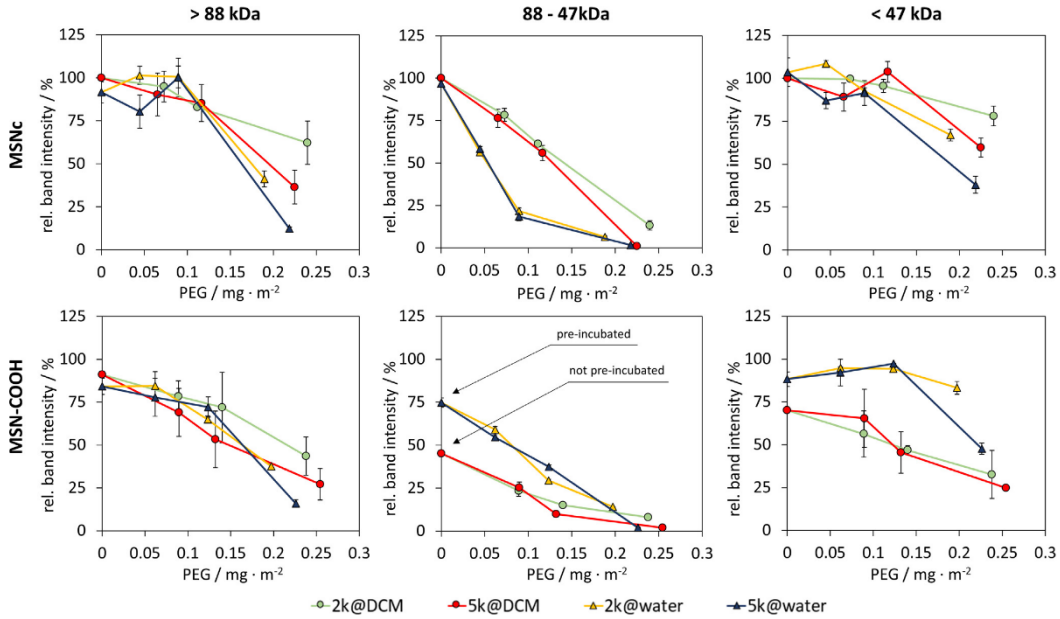

Fig. 6. Integrated SDS band intensities for different PEGylation-solvent/particle combinations as a function of MSN PEGylation level. Integrated band intensities within three molecular weight ranges (>88 kDa, 88–47 kDa, and < 47 kDa) were normalized to the integrated intensities measured for corresponding as-synthesized, non-PEGylated MSNc. The exact molecular weight ranges of the analyzed bands of each gel are highlighted on the gels shown in Fig. 6. Protein adsorption was performed for 24 h in 10 % FCS in PBS at a temperature of 37 °C and at a particle concentration of 5 mg mL^{-1} (mean ± SD, n = 3).

and this was also the case for the high and low protein weight fractions at high PEGylation levels. The difference between PEG_{5k} and PEG_{2k} was more pronounced here, especially so at high PEGylation degrees, as compared to when PEGylation was carried out from DCM. PEG_{5k} led to a more effective protein adsorption inhibition than PEG_{2k} especially at high PEG loading levels, in full agreement with what is to be expected based on the estimated differences in the packing for these particles (see above). Also, for high and low molecular weight proteins high PEGylation levels were needed for effective protein adsorption inhibition. However, for the MSN-COOH particles, an increase in the adsorption of medium molecular weight proteins was observed onto particles PEGylated with low amounts of polymer as compared to the as-synthesized MSN-COOH particles, as also seen in Fig. 5, and with respect to the protein adsorption to the as-synthesized MSN-COOH in Fig. 6. We speculated that this anomalous protein adsorption dependency on the PEGylation level could originate from a partial loss of carboxy-silane through dissolution during PEGylation. The as-synthesized MSN-COOH particles had not been exposed to water before the protein adsorption experiments. However, for the particles PEGylated in water, this was the case. If there is some detachment of carboxy-silane during PEGylation, the protein adsorption pattern would become more like that observed for the MSNc particles. Thus, we pre-incubated MSNc and MSN-COOH particles for 2 h in water in the absence of PEG, and measured the protein adsorption to such particles (Fig. 7). Indeed, the amount of medium molecular weight proteins increased substantially as compared to that of the native particles for the MSN-COOH particles, while the adsorption of high and low molecular weight proteins was hardly affected. For the MSNc particles the influence of pre-incubation on the protein adsorption was negligible. These results suggest that the results obtained for the MSN-COOH particles indeed can be connected to a partial loss of carboxy-silane during PEGylation in water. Such a partial loss of carboxy-functions during PEGylation cannot occur when the PEGylation is carried out from DCM, which is why the protein adsorption dependency on the PEGylation degree was similar for both MSN-COOH and MSNc particles in this case, being a virtually linear decrease in the amount of protein adsorbed with increasing PEGylation level. However, the carboxylate-effect was not completely lost, as evidenced by an overall lower protein adsorption level for the MSN-COOH particles as compared to the MSNc particles also in this case. Nevertheless, for the highest PEGylation levels a clear difference in the extent of protein adsorption was observed between PEG_{2k} and the PEG_{5k} particles for the MSN-COOH particles PEGylated in water, reflecting the difference in PEG conformation, as discussed earlier.

As it has recently been suggested that small proteins can enter in the mesopores of MSNs,[48,49] we carried out protein adsorption experiments under conditions where the outer surface areas of the particles, as determined by *t*-plot method, were held constant. Here, particles functionalized with 0.20 mg m^{-2} of PEG_{5k} adsorbed from water were used. The corresponding results are summarized in Fig. 8.

As can be seen, the as-synthesized MSN-COOH particles adsorb about half of the amount of protein as compared to the MSNc particles irrespective of the protein mass fraction. PEGylation of the MSNc particles in water lead to a clear decrease in the amount of adsorbed protein for all protein mass fractions, and especially so for the medium molecular mass fraction. MSN-COOH particles PEGylated in water show a similar adsorption pattern as that of the MSNc particles, as expected based on the discussion above. Interestingly, the NSNc particles adsorbed virtually identical amounts of medium and low molecular weight proteins as the MSNc particles, while the amount of high molecular weight proteins adsorbed was almost twice as high for the NSNc particles.

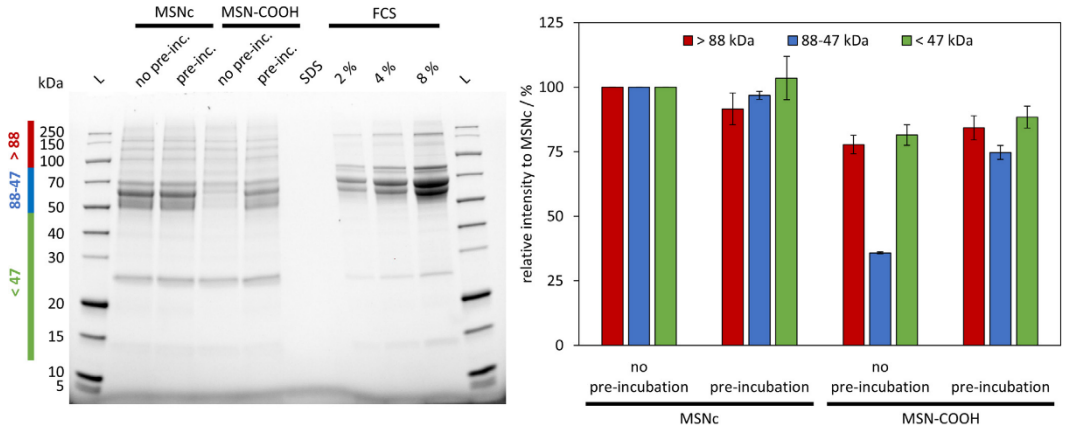

Fig. 7. Left: SDS-PAGE of supernatants, and right: corresponding relative band intensities measured for supernatants isolated after protein adsorption from FCS onto as-synthesized MSNc and MSN–COOH and corresponding particles pre-incubated ('pre-Inc.') for 2 h in water. Protein adsorption was performed for 24 h in 10 % FCS in PBS at a temperature of 37 °C and at a particle concentration of 5 mg mL^{-1}. The band intensities were normalized to the band intensities measured for as-synthesized MSNc (mean ± SD, n = 3).

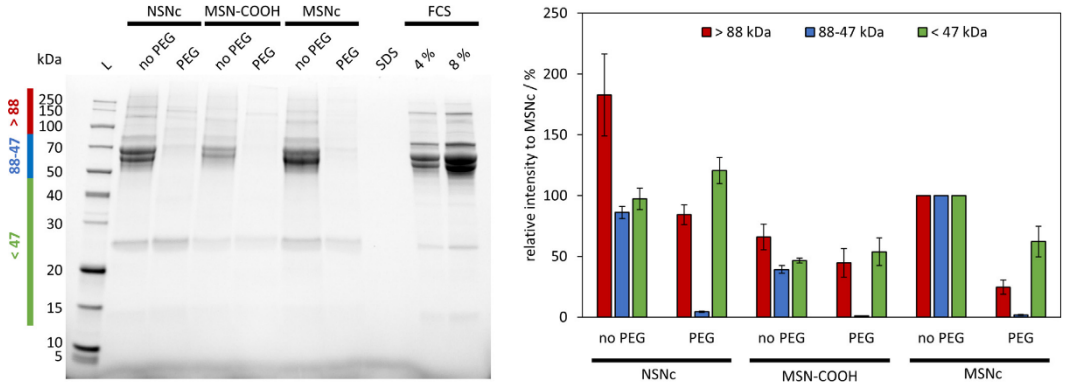

Fig. 8. Left: SDS-PAGE measured for supernatants isolated after 24 h of incubation with 10 % FCS in PBS at a temperature of 37 °C and at a constant outer particle surface area of 0.525 m^2 mL^{-1} (*t*-plot method). Right: Integrated band intensities within three molecular weight ranges (>88 kDa, 88–47 kDa, and < 47 kDa) were normalized to the integrated intensities measured for corresponding as-synthesized, non-PEGylated MSNc (mean ± SD, n = 3).

The reason for the latter observation is not fully clear, but may be related to the larger, continuous silica-protein contact area that is available on the NSNc particles as compared to the MSN particles, and that this could favour the adsorption of heavier weight proteins. PEGylation of the NSNc particles decreased the amount of high molecular weight proteins by about half, to levels corresponding to those observed for the non-PEGylated MSNc particles, while the adsorption of medium weight proteins was almost completely inhibited. For the low molecular weight proteins, no decrease in the extent of protein adsorption, rather an increase, was observed upon PEGylation. Importantly, as shown in Fig. 8, already a PEGylation level of 2 wt% was enough to decrease the adsorption of medium molecular weight proteins to NSNc particles to similar levels as those observed for mesoporous particles exhibiting PEGylation levels exceeding 16 wt%, giving further support for the conclusion that the vast majority of the PEG molecules is located inside the mesopore system for the mesoporous particles at least at high PEG loading levels. However, the very efficient inhibition of medium weight protein adsorption observed for MSNc particles already at low PEGylation levels as seen in Fig. 6, may suggest that the PEG molecules preferentially adsorb on the outer particle surface under these conditions. Taken together, we can exclude any pronounced adsorption of low molecular weight proteins into our MSNs. Furthermore, it appears that the extent of adsorption of large proteins is depending on the fraction of available outer surface of silica (higher on non-porous particles as compared to mesoporous particles), which can be understood.

3.4. Adsorbed PEG effectively shields drug loaded MSNs against protein corona formation

Finally, we wanted to demonstrate the possibility of drug loading prior to adsorptive PEGylation, without leaching of the drug during PEGylation. As PEGylation can be carried out both from water and from apolar solvents, the solvent used for PEGylation can be chosen such that the drug molecule exhibits a low solubility. As a model for a hydrophilic drug we chose the cationic peptide calcitonin (3.4 kDa, pI = 10.4), while the fluorophore DiI was cho-

sen as a model for a small, hydrophobic drug. PEG_{5k} was used in all cases. DiI adsorption onto the MSNc was carried out from cyclohexane to mount to 1 wt% or 5 wt% loading degree, followed by PEGylation with the maximum PEG amount from water. The results are summarized in Fig. 9. While no loss of cargo was observed upon PEGylation, the PEG mass slightly decreased with increasing DiI content from 20 wt% to 19 wt% mirroring the reduced silica surface available for PEG adsorption. Nevertheless, these PEG masses were similar to those of the adsorption isotherm plateau of the empty MSNc particles. The amount of serum proteins adsorbing onto the DiI-loaded MSNc increased with increasing DiI loading, and can be explained by the increasing particle hydrophobicity with increasing DiI loading. Adsorptive PEGylation dramatically diminished the extent of protein adsorption by large and medium sized proteins to an extent comparable to empty MSNc, leading to the conclusion of similar PEG conformations on both empty and DiI-loaded particles. However, slightly more proteins did adsorb on the DiI-containing particles at higher DiI-loadings, presumably due to DiI occupying some adsorption sites on the outer surface of the particles. Adsorption of small-sized proteins was found to be favoured by DiI loading, and was also less affected by PEGylation than large and medium proteins. The reason for this is not fully clear, but might be due to the predominant role of hydrophobic interactions in the adsorption process of these proteins. Interestingly, no DiI desorbed during the FCS adsorption over 24 h suggesting no premature release of the cargo (Figure S10). Taken together, the efficient decrease in the amount of adsorbed serum albumin upon PEGylation suggests that these particles could exhibit stealth properties *in vivo*.

Corresponding results obtained for calcitonin are summarized in Fig. 10. Calcitonin was loaded onto/into MSNc from water followed by PEGylation in DCM. The drug-loading levels ranged from

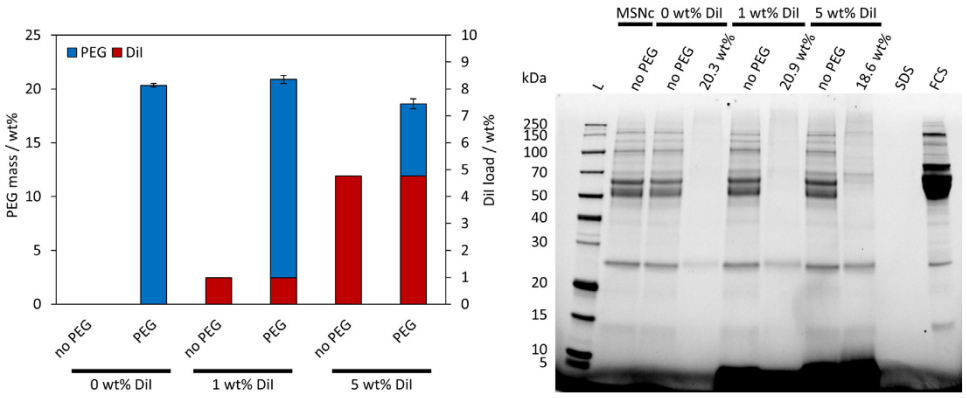

Fig. 9. Left: Loading degrees of hydrophobic DiI into MSNc in Cyclohexane and amounts of PEG_{5k} subsequently adsorbed in water. Right: SDS-PAGE measured for supernatants isolated after 24 h of incubation with 10 % FCS in PBS at a temperature of 37 °C (mean ± SD, n = 3).

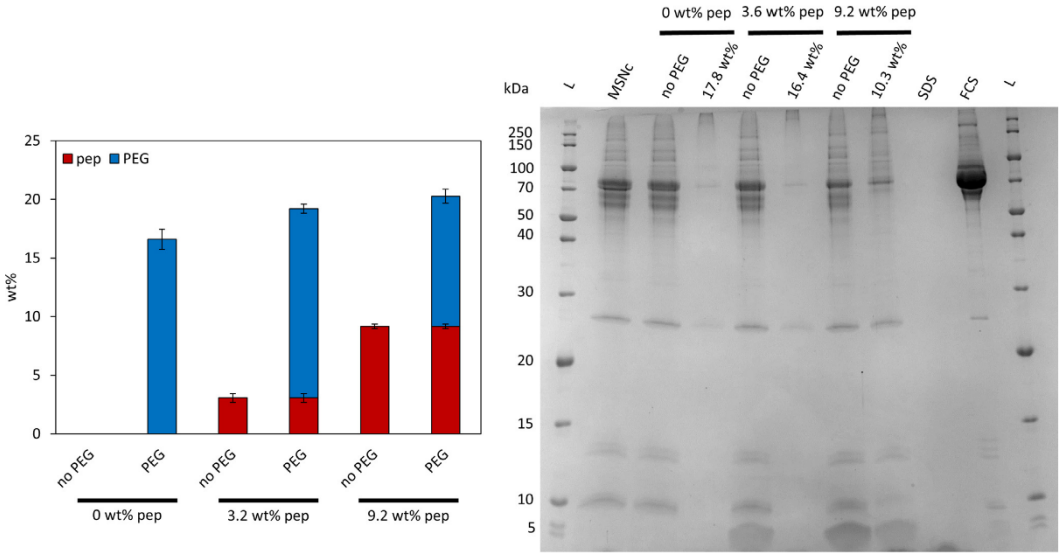

Fig. 10. Left: Loading degrees of hydrophilic calcitonin (pep) into MSNc in PBS and amounts of PEG_{5k} subsequently adsorbed in DCM. Right: SDS-PAGE measured for supernatants isolated after 24 h of incubation with 10 % FCS in PBS at a temperature of 37 °C. (mean ± SD, n = 3).

0 to 9.2 wt%. With increasing calcitonin loading the achievable PEG loadings decreased from 18 wt% to 10 wt%. The total mass loading of calcitonin + PEG was virtually constant, suggesting that calcitonin and PEG compete for the same adsorption sites on the silica. No desorption of calcitonin occurred during PEGylation, in agreement with the insolubility of calcitonin in DCM (data not shown). PEGylation led to a very efficient inhibition of especially high and medium molecular weight proteins, while a slightly less efficient inhibition of protein adsorption was observed at the highest calcitonin loading studied. As for the PEGylated DiI-loaded particles, the inhibition of low molecular weight proteins (mainly Apolipoprotein A-I) was not as efficient for the drug model-containing particles as compared to corresponding empty particles. However, as discussed previously, serum albumin adsorption inhibition is most important for decreasing the extent of nanoparticle uptake by macrophages, and therefore one can expect a clear effect of PEGylation on the blood circulation time also for these particles.

4. Discussion

Our results clearly demonstrate the possibility for straightforward, adsorption-based formulation of drug-containing MSNs followed by PEGylation, where little or no premature leakage of the cargo occurs during PEGylation. Furthermore, the PEGylation is stable on time-scales fully compatible with intravenous administration. Thus, the formulation procedure can be radically shortened as compared to covalent drug loading and/or PEGylation, as no unreacted coupling chemicals need to be removed through thorough washing, saving both time and money. Furthermore, adsorption-based functionalization makes drug loading before PEGylation possible, as there is no risk that coupling chemicals react with functional groups on the drug molecules during PEGylation, and therefore higher drug loadings can be achieved. A higher drug loading level also implies lower nanoparticle doses needed, and therefore also increased safety. Thus, adsorption-based formulation of MSNs appears to be an important step towards translation of this promising drug delivery platform to the clinic.

On a mechanistic level, our results clearly show that the PEG molecules can enter into the mesopores of the MSNs, and compete with the drug molecules for adsorption sites on the silica surface. These results thus readily explain why the drug loading levels that can be achieved for PEGylated MSNs typically are much lower than those that are observed for corresponding non-PEGylated particles. At first sight, the entry of PEG into the mesopore system having pore dimensions in the range of 3.3 nm may appear surprising. Using 2.78 Å as the monomer length,[50] gives Flory radii of 2.68 nm for PEG_{2k}, and 5.02 nm for PEG_{5k} in water. Thus, the PEG molecules cannot enter the mesopores unless a conformation change from coil to more elongated structures occurs, at least not when adsorbed from water. On this note, diffusion into the micropore system of a zeolite with a pore diameter of 1.58 nm has been demonstrated during adsorption of PEG_{6k} from water.[51] Here, the critical molecular dimension was related to the cross-section diameter of PEG and stated to be approximately 0.55 nm, which was about 1/3 of the pore diameter of the zeolite, and 1/6 of the mean mesopore diameter of the MSNs in this study. Thus, based on this argumentation, adsorption of elongated PEG chains into the mesopore system of the MSNs can be understood. Adaptation of a more elongated, stretched configuration comes at an energy cost, which has to be balanced through attractive PEG-silica interactions and/or entropy gain related to the release of hydration water upon adsorption. This also implies that the adsorption energetic parameters are solvent-dependent, as clearly seen in the different adsorption isotherm shapes obtained in water versus in DCM. Solvation-effects are clearly less important in DCM as in water, which we suggest is a main reason for the differences in PEG adsorption behaviour in the two solvents. A lower attractive PEG-support energy can also allow for deeper penetration of PEG into the mesopore system. On this note, our results thus also indirectly imply that the balance between transport and reaction limitation is an important parameter also for covalent PEGylation, and that fast coupling reaction kinetics, *i.e.* reaction limited attachment, is preferable for a preferential localization of the PEG molecules on the outer surface of the particles as previously suggested.[52] In turn, this would lead to the most efficient modulation of the serum protein adsorption characteristics of the particles. Here we want to also highlight the connection of the present study to a recent study by von Baeckmann *et al.*,[24] where it was shown that different covalent PEGylation strategies lead to pronounced differences in the PEGylation efficiencies in terms of decreasing protein adsorption to MSNs. Furthermore, care must be taken when covalent attachment of PEG is aimed for, that not a fair amount of the PEG molecules is just physisorbed to the particle surface, not to mention that a fair amount of the PEG molecules may reside inside the mesopore system regardless of the means of attachment. That also implies that the PEG molecules may exhibit different outer surface conformations even at similar total loading degrees, which will have direct implications for the protein adsorption to such particles. Thus, a true connection between serum protein adsorption and degree of PEGylation can only be obtained using often employed bulk-analysis techniques if presence of PEG molecules inside the mesopore system of MSNs can be excluded.

5. Conclusions

We have carried out sequential adsorptive cargo loading and PEGylation of MSNs in order to establish a straightforward and reproducible means for particle formulation for drug delivery applications. The method allows for PEGylation without premature release of the cargo, as the solvent used for PEGylation can be chosen so that the cargo exhibits low solubility, which was exemplarily demonstrated in this work with a water-insoluble hydrophobic dye and a water-soluble peptide-based drug. Interestingly, we observe that the PEG molecules compete with the cargo molecules for the adsorption sites, and the total gravimetric loading level of organics (model drug + PEG) remains relatively constant at about 18–23 wt% for the used model drugs. This also implies that a fair part of the PEG resides inside the mesopore system. Our results can therefore explain that high PEGylation levels (often > 30 wt%) are often accompanied by a clear decrease in drug loading levels.[25, 26] Although the maximum PEGylation levels decreased upon pre-loading of the drug models, a pronounced decrease in the serum protein adsorption was observed also in this case. Detailed analysis of PEG adsorption isotherms allowed the distribution of PEG between the outer particle surfaces and the mesopore system to be determined, which in turn made it possible to determine the PEG conformation on the outer surface of the particles. A striking 60–90 % of the PEG resided within the mesopore system depending on the solvent used, and on the polarity of the surface. The PEG affinity for silane-functionalized surfaces was lower as compared to that of bare silica surfaces. This result explains recent literature reports concerning the influence of surface functionalities on the maximum degree of PEGylation for mesoporous silica particles, [24] and highlights surface functionalization as a means for minimizing PEG adsorption into the mesopores during PEGylation. Both the extent of protein adsorption and the relative composition of the protein corona were clearly influenced by the PEGylation degree, as well as by the PEG conformation on the outer surface of the particles. In addition, our results also indicate a lower PEG affinity for carboxy-functionalized silica surfaces when the adsorp-

tion is carried out from water, highlighting the importance of attractive PEG-silanol interactions in water. A similar effect was, however, not observed in DCM, which on the other hand implies that hydration water also mediates the PEG-silica interaction. The PEG layer remained stable and bio-functional for at least 24 h in the presence of serum proteins, and is therefore stable on time-scales which are compatible with intravenous administration. Adsorption-based formulation therefore represents an important step towards a faster translation of this drug delivery platform to the clinic. Future work should focus on further elucidating the influence of PEG molecular weight and PEG structure (linear, branched, starlike) and of the mesopore size on the inside-outside distribution of PEG and on the serum protein adsorption modulation. Furthermore, the connection between the established PEG adsorption geometries and inside-outside distribution on the blood circulation time of intravenously injected particles should be established.

CRediT authorship contribution statement

Roman Schmid: Formal analysis, Investigation, Methodology, Validation, Visualization, Formal analysis, Investigation, Methodology, Validation, Visualization, Writing – original draft. **Nathalie Neffgen:** Formal analysis, Investigation, Methodology, Validation, Visualization, Writing – original draft. **Mika Lindén:** Conceptualization, Funding acquisition, Investigation, Project administration, Resources, Supervision, Validation, Writing – review & editing.

Data availability

Data will be made available on request.

Declaration of Competing Interest

The authors declare that they have no known competing financial interests or personal relationships that could have appeared to influence the work reported in this paper.

Acknowledgements

The assistance of Ms. Jasmin Sin Yi Trung related to quantification of PEG in aqueous solution is gratefully acknowledged. The authors want to thank Cornelia Egger, Kea Fedke and Lionel Kroner for nitrogen sorption, thermogravimetric, and small-angle X-ray diffraction measurements, and M.Sc. Simon Schauer for Raman measurements. The authors acknowledge the funding from the Deutsche Forschungsgemeinschaft (DFG, German Research Foundation)– Project-ID 316249678 – SFB 1279 project "Exploiting the human peptidome for novel antimicrobial and anticancer agents".

Appendix A. Supplementary material

Supplementary data to this article can be found online at https://doi.org/10.1016/j.jcis.2023.03.012.

References

[1] J. Shi, P.W. Kantoff, R. Wooster, O.C. Farokhzad, Cancer nanomedicine: progress, challenges and opportunities, Nat. Rev. Cancer 17 (2017), https://doi.org/10.1038/nrc.2016.108.
[2] A.C. Anselmo, S. Mitragotri, Nanoparticles in the clinic: an update, Bioeng. Transl. Med. 4 (2019), https://doi.org/10.1002/btm2.10143.
[3] R. van der Meel, E. Sulheim, Y. Shi, F. Kiessling, W.J.M. Mulder, T. Lammers, Smart cancer nanomedicine, Nat. Nanotechnol. 14 (2019), https://doi.org/10.1038/s41565-019-0567-y.
[4] T. Asefa, Z. Tao, Biocompatibility of mesoporous silica nanoparticles, Chem. Res. Toxicol. 25 (2012), https://doi.org/10.1021/tx300166u.
[5] S. Jafari, H. Derakhshankhah, L. Alaei, A. Fattahi, B.S. Varnamkhasti, A.A. Saboury, Mesoporous silica nanoparticles for therapeutic/diagnostic applications, Biomed. Pharmacother. 109 (2019), https://doi.org/10.1016/j.biopha.2018.10.167.
[6] C.Y. Lin, C.M. Yang, M. Lindén, Dissolution and morphology evolution of mesoporous silica nanoparticles under biologically relevant conditions, J. Colloid Interface Sci. 608 (2022), https://doi.org/10.1016/j.jcis.2021.09.164.
[7] K. Möller, T. Bein, Degradable drug carriers: vanishing mesoporous silica nanoparticles, Chem. Mater. 31 (2019), https://doi.org/10.1021/acs.chemmater.9b00221.
[8] J.L. Paris, M. Colilla, I. Izquierdo-Barba, M. Manzano, M. Vallet-Regí, Tuning mesoporous silica dissolution in physiological environments: a review, J. Mater. Sci. 52 (2017), https://doi.org/10.1007/s10853-017-0787-1.
[9] J. Zhang, W. Sun, L. Bergman, J.M. Rosenholm, M. Lind?n, G. Wu, H. Xu, H.-C. Gu, Magnetic mesoporous silica nanospheres as DNA/drug carrier, Mater Lett. 67 (2012). https://doi.org/10.1016/j.matlet.2011.09.086.
[10] B. Beitzinger, F. Gerbl, T. Vomhof, R. Schmid, R. Noschka, A. Rodriguez, S. Wiese, G. Weidinger, L. Ständker, P. Walther, J. Michaelis, M. Lindén, S. Stenger, Delivery by dendritic mesoporous silica nanoparticles enhances the antimicrobial activity of a napsin-derived peptide against intracellular mycobacterium tuberculosis, Adv. Healthc. Mater. 10 (2021), https://doi.org/10.1002/adhm.202100453.
[11] K. Braun, A. Pochert, M. Gerber, H.F. Raber, M. Lindén, Influence of mesopore size and peptide aggregation on the adsorption and release of a model antimicrobial peptide onto/from mesoporous silica nanoparticles: In vitro, Mol. Syst. Des. Eng. 2 (2017), https://doi.org/10.1039/c7me00059f.
[12] Y. Zhang, Z. Zhi, T. Jiang, J. Zhang, Z. Wang, S. Wang, Spherical mesoporous silica nanoparticles for loading and release of the poorly water-soluble drug telmisartan, J. Control. Release 145 (2010), https://doi.org/10.1016/j.jconrel.2010.04.029.
[13] Y. You, L. He, B. Ma, T. Chen, Correction to: High-Drug-Loading Mesoporous Silica Nanorods with Reduced Toxicity for Precise Cancer Therapy against Nasopharyngeal Carcinoma (Advanced Functional Materials, (2017), 27, 42, (1703313), 10.1002/adfm.201703313), Adv Funct Mater. 30 (2020). https://doi.org/10.1002/adfm.202004479.
[14] R.M. Sábio, A.B. Meneguin, T.C. Ribeiro, R.R. Silva, M. Chorilli, New insights towards mesoporous silica nanoparticles as a technological platform for chemotherapeutic drugs delivery, Int. J. Pharm. 564 (2019), https://doi.org/10.1016/j.ijpharm.2019.04.067.
[15] F. Alexis, E. Pridgen, L.K. Molnar, O.C. Farokhzad, Factors affecting the clearance and biodistribution of polymeric nanoparticles, Mol. Pharm. (2008), https://doi.org/10.1021/mp800051m.
[16] M. Lindén, Biodistribution and Excretion of Intravenously Injected Mesoporous Silica Nanoparticles: Implications for Drug Delivery Efficiency and, Safety (2018), https://doi.org/10.1016/bs.enz.2018.07.007.
[17] C. Gunawan, M. Lim, C.P. Marquis, R. Amal, Nanoparticle-protein corona complexes govern the biological fates and functions of nanoparticles, J. Mater. Chem. B 2 (2014), https://doi.org/10.1039/c3tb21526a.
[18] O. Lunov, T. Syrovets, C. Loos, J. Beil, M. Delacher, K. Tron, G.U. Nienhaus, A. Musyanovych, V. Mailänder, K. Landfester, T. Simmet, Differential uptake of functionalized polystyrene nanoparticles by human macrophages and a monocytic cell line, ACS Nano 5 (2011), https://doi.org/10.1021/nn2000756.
[19] Y. Yan, K.T. Gause, M.M.J. Kamphuis, C.S. Ang, N.M. O'Brien-Simpson, J.C. Lenzo, E.C. Reynolds, E.C. Nice, F. Caruso, Differential roles of the protein corona in the cellular uptake of nanoporous polymer particles by monocyte and macrophage cell lines, ACS Nano 7 (2013), https://doi.org/10.1021/nn404481f.
[20] J.L. Perry, K.G. Reuter, M.P. Kai, K.P. Herlihy, S.W. Jones, J.C. Luft, M. Napier, J.E. Bear, J.M. Desimone, PEGylated PRINT nanoparticles: the impact of PEG density on protein binding, macrophage association, biodistribution, and pharmacokinetics, Nano Lett. 12 (2012), https://doi.org/10.1021/nl302638g.
[21] J. Kim, H.S. Kim, N. Lee, T. Kim, H. Kim, T. Yu, I.C. Song, W.K. Moon, T. Hyeon, Multifunctional uniform nanoparticles composed of a magnetite nanocrystal core and a mesoporous silica shell for magnetic resonance and fluorescence imaging and for drug delivery, Angewandte Chemie – Int. Ed. 47 (2008), https://doi.org/10.1002/anie.200802469.
[22] R. Tavano, L. Gabrielli, E. Lubian, C. Fedeli, S. Visentin, P. Polverino De Laureto, G. Arrigoni, A. Geffner-Smith, F. Chen, D. Simberg, G. Morgese, E.M. Benetti, L. Wu, S.M. Moghimi, F. Mancin, E. Papini, C1q-Mediated Complement Activation and C3 Opsonization Trigger Recognition of Stealth Poly(2-methyl-2-oxazoline)-Coated Silica Nanoparticles by Human Phagocytes, ACS Nano 12 (2018), https://doi.org/10.1021/acsnano.8b01806.
[23] Q. He, Z. Zhang, F. Gao, Y. Li, J. Shi, In vivo Biodistribution and Urinary Excretion of Mesoporous Silica Nanoparticles: effects of Particle Size and PEGylation, Small 7 (2011), https://doi.org/10.1002/smll.201001459.
[24] C. von Baeckmann, H. Kählig, M. Lindén, F. Kleitz, On the importance of the linking chemistry for the PEGylation of mesoporous silica nanoparticles, J. Colloid Interface Sci. 589 (2021), https://doi.org/10.1016/j.jcis.2020.12.004.
[25] H. Meng, M. Xue, T. Xia, Z. Ji, D.Y. Tarn, J.I. Zink, A.E. Nel, Use of size and a copolymer design feature to improve the biodistribution and the enhanced permeability and retention effect of doxorubicin-loaded mesoporous silica nanoparticles in a murine xenograft tumor model, ACS Nano 5 (2011), https://doi.org/10.1021/nn200809t.
[26] A. Wani, G.H.L. Savithra, A. Abyad, S. Kanvinde, J. Li, S. Brock, D. Oupický, Surface PEGylation of Mesoporous Silica Nanorods (MSNR): effect on loading, release, and delivery of mitoxantrone in hypoxic cancer cells, Sci. Rep. 7 (2017), https://doi.org/10.1038/s41598-017-02531-4.

[27] J.M. Rosenholm, A. Meinander, E. Peuhu, R. Niemi, J.E. Eriksson, C. Sahlgren, M. Lindén, Targeting of porous hybrid silica nanoparticles to cancer cells, ACS Nano 3 (2009), https://doi.org/10.1021/nn800781r.
[28] W. Stöber, A. Fink, E. Bohn, Controlled growth of monodisperse silica spheres in the micron size range, J. Colloid Interface Sci. 26 (1968), https://doi.org/10.1016/0021-9797(68)90272-5.
[29] B. Baumann, R. Wittig, M. Lindén, Mesoporous silica nanoparticles in injectable hydrogels: factors influencing cellular uptake and viability, Nanoscale 9 (2017), https://doi.org/10.1039/c7nr02015e.
[30] M. Francois, R. de Neve, Determination of polyethylene glycols by precipitation with iodine, Talanta 32 (1985), https://doi.org/10.1016/0039-9140(85)80262-9.
[31] P.G. de Gennes, Conformations of Polymers Attached to an Interface, Macromolecules 13 (1980), https://doi.org/10.1021/ma60077a009.
[32] H. Yang, E.M. Akinoglu, F. Lisi, L. Wu, S. Shen, M. Jin, G. Zhou, M. Giersig, L. Shui, P. Mulvaney, A versatile strategy for loading silica particles with dyes and quantum dots, Colloids Interface Sci. Commun. 47 (2022), https://doi.org/10.1016/j.colcom.2022.100594.
[33] K. Shameli, M. bin Ahmad, S.D. Jazayeri, S. Sedaghat, P. Shabanzadeh, H. Jahangirian, M. Mahdavi, Y. Abdollahi, Synthesis and characterization of polyethylene glycol mediated silver nanoparticles by the green method, Int J Mol Sci. 13 (2012). https://doi.org/10.3390/ijms13066639.
[34] E.A. Sagitova, K.A. Prokhorov, G.Y. Nikolaeva, A. v. Baimova, P.P. Pashinin, A.Y. Yarysheva, D.I. Mendeleev, Raman analysis of polyethylene glycols and polyethylene oxides, in: J Phys Conf Ser, 2018. https://doi.org/10.1088/1742-6596/999/1/012002.
[35] V. v. Kuzmin, V.S. Novikov, L.Y. Ustynyuk, K.A. Prokhorov, E.A. Sagitova, G.Y. Nikolaeva, Raman spectra of polyethylene glycols: Comparative experimental and DFT study, J Mol Struct. 1217 (2020). https://doi.org/10.1016/j.molstruc.2020.128331.
[36] H. Liu, H. Xiao, Adsorption of poly(ethylene oxide) with different molecular weights on the surface of silica nanoparticles and the suspension stability, Mater. Lett. 62 (2008), https://doi.org/10.1016/j.matlet.2007.06.079.
[37] P. Trens, R. Denoyel, Conformation of Poly(ethylene glycol) polymers at the silica/water interface: a microcalorimetric study, Langmuir 9 (1993), https://doi.org/10.1021/la00026a026.
[38] X. Liu, L. Yuan, D. Li, Z. Tang, Y. Wang, G. Chen, H. Chen, J.L. Brash, Blood compatible materials: State of the art, J. Mater. Chem. B 2 (2014), https://doi.org/10.1039/c4tb00881b.
[39] M. Li, S. Jiang, J. Simon, D. Paßlick, M.L. Frey, M. Wagner, V. Mailander, D. Crespy, K. Landfester, Brush conformation of polyethylene glycol determines the stealth effect of nanocarriers in the low protein adsorption regime, Nano Lett. 21 (2021), https://doi.org/10.1021/acs.nanolett.0c03756.
[40] D. Bazile, C. Prud'homme, M. -T Bassoullet, M. Marlard, G. Spenlehauer, M. Veillard, Stealth Me.PEG-PLA nanoparticles avoid uptake by the mononuclear phagocytes system, J Pharm Sci. 84 (1995). https://doi.org/10.1002/jps.2600840420.
[41] J. Rubio, J.A. Kitchener, The mechanism of adsorption of poly(ethylene oxide) flocculant on silica, J. Colloid Interface Sci. 57 (1976), https://doi.org/10.1016/0021-9797(76)90182-X.
[42] G. Wang, A.N. Otuonye, E.A. Blair, K. Denton, Z. Tao, T. Asefa, Functionalized mesoporous materials for adsorption and release of different drug molecules: a comparative study, J. Solid State Chem. 182 (2009), https://doi.org/10.1016/j.jssc.2009.03.034.
[43] I. Slowing, B.G. Trewyn, V.S.Y. Lin, Effect of surface functionalization of MCM-41-type mesoporous silica nanoparticles on the endocytosis by human cancer cells, J. Am. Chem. Soc. 128 (2006), https://doi.org/10.1021/ja0645943.
[44] M. Kruk, T. Asefa, M. Jaroniec, G.A. Ozin, Synthesis and characterization of methyl- and vinyl-functionalized ordered mesoporous silicas with high organic content, Stud. Surf. Sci. Catal. (2002), https://doi.org/10.1016/s0167-2991(02)80542-0.
[45] S. Tenzer, D. Docter, J. Kuharev, A. Musyanovych, V. Fetz, R. Hecht, F. Schlenk, D. Fischer, K. Kiouptsi, C. Reinhardt, K. Landfester, H. Schild, M. Maskos, S.K. Knauer, R.H. Stauber, Rapid formation of plasma protein corona critically affects nanoparticle pathophysiology, Nat. Nanotechnol. 8 (2013), https://doi.org/10.1038/nnano.2013.181.
[46] A. Pochert, I. Vernikouskaya, F. Pascher, V. Rasche, M. Lindén, Cargo-influences on the biodistribution of hollow mesoporous silica nanoparticles as studied by quantitative 19F-magnetic resonance imaging, J. Colloid Interface Sci. 488 (2017), https://doi.org/10.1016/j.jcis.2016.10.085.
[47] M. Beck, T. Mandal, C. Buske, M. Lindén, Serum protein adsorption enhances active leukemia stem cell targeting of mesoporous silica nanoparticles, ACS Appl. Mater. Interfaces 9 (2017), https://doi.org/10.1021/acsami.7b04742.
[48] A.M. Clemments, P. Botella, C.C. Landry, Spatial mapping of protein adsorption on mesoporous silica nanoparticles by stochastic optical reconstruction microscopy, J. Am. Chem. Soc. 139 (2017), https://doi.org/10.1021/jacs.7b01118.
[49] A.M. Clemments, P. Botella, C.C. Landry, Protein adsorption from biofluids on silica nanoparticles: corona analysis as a function of particle diameter and porosity, ACS Appl. Mater. Interfaces 7 (2015), https://doi.org/10.1021/acsami.5b07631.
[50] F. Oesterhelt, M. Rief, H.E. Gaub, Single molecule force spectroscopy by AFM indicates helical structure of poly(ethylene-glycol) in water, New J. Phys. 1 (1999), https://doi.org/10.1088/1367-2630/1/1/006.
[51] C.Y. Chang, W.T. Tsai, C.H. Ing, C.F. Chang, Adsorption of polyethylene glycol (PEG) from aqueous solution onto hydrophobic zeolite, J. Colloid Interface Sci. 260 (2003), https://doi.org/10.1016/S0021-9797(02)00174-1.
[52] M. Bouchoucha, R. C.-Gaudreault, M.-A. Fortin, F. Kleitz, Mesoporous Silica Nanoparticles: Selective Surface Functionalization for Optimal Relaxometric and Drug Loading Performances, Adv Funct Mater. 24 (2014). https://doi.org/10.1002/adfm.201400524.

5. Publication IV

Confinement and polarity effects on the peptide packing density on mesoporous silica nanoparticles.

Bastian Beitzinger*, Roman Schmid*, Christoph Jung, Kanishka Tiwary, Patrick Hermann, Timo Jacob, Mika Lindén

(*equal contribution)

Langmuir 2024, 40, 8, 4294–4305.
https://doi.org/10.1021/acs.langmuir.3c03513

Copyright © 2024 The Authors. Published by American Chemical Society.
This is an open access article under the CC BY 4.0 license
(https://creativecommons.org/licenses/by/4.0/).

LANGMUIR

Open Access
This article is licensed under CC-BY 4.0

pubs.acs.org/Langmuir Article

Confinement and Polarity Effects on the Peptide Packing Density on Mesoporous Silica Nanoparticles

Bastian Beitzinger,[#] Roman Schmid,[#] Christoph Jung, Kanishka Tiwary, Patrick Hermann, Timo Jacob, and Mika Lindén*

Cite This: *Langmuir* 2024, 40, 4294−4305 Read Online

ACCESS | Metrics & More | Article Recommendations | Supporting Information

ABSTRACT: The adsorption of cationic peptide JM21 onto different mesoporous silica nanoparticles (MSNs) from an aqueous solution was studied as a function of pH. In agreement with the literature, the highest loading degrees could be achieved at pH close to the isoelectric point of the peptide where the peptide−peptide repulsion is minimum. However, mesopore size, mesopore geometry, and surface polarity all had an influence on the peptide adsorption in terms of both affinity and maximum loading at a given pH. This adsorption behavior could largely be explained by a combination of pH-dependent electrostatic interactions and confinement effects. It is demonstrated that hydrophobic interactions enhance the degree of peptide adsorption under pH conditions where the electrostatic attraction was absent in the case of mesoporous organosilica nanoparticles (MONs). The lower surface concentration of silanol groups for MON led to a lower level of peptide adsorption under optimum pH conditions compared to all-silica particles. Finally, the study confirmed the protective role of MSNs in preserving the biological activity of JM#21 against enzymatic degradation, even for large-pore MSNs, emphasizing their potential as nanocarriers for therapeutic peptides. By integrating experimental findings with theoretical modeling, this research elucidates the complex interplay of factors that influence peptide−silica interactions, providing vital insights for optimizing peptide loading and stabilization in biomedical applications.

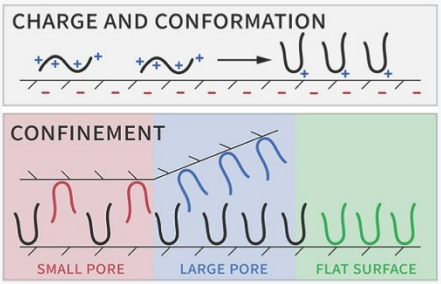

INTRODUCTION

The potential of mesoporous silica nanoparticles, MSNs, for applications within the biomedical domain has been extensively demonstrated, especially in relation to diagnostics, biosensing, and theranostics during the last two decades.[1−4] Their high surface area and customizable pore system facilitate adsorption of various therapeutics ranging from small-molecular drugs to macromolecular entities like peptides, proteins, and nucleic acids.[5−9] Particularly, peptide and protein encapsulation within MSNs has been demonstrated to give protection against enzymatic degradation, hence prolonging their functional viability.[10−13]

In the realm of drug delivery, the diverse physical and chemical properties of peptides and proteins necessitate a versatile carrier system for optimal loading and release profiles. Consequently, numerous studies have delved into understanding the various factors influencing peptide and protein adsorption onto silica-based materials.[8,14−17] For ideally flat silica surfaces, this exploration essentially pivots on the interactions between the adsorbent and adsorptive, which can encompass van der Waals forces, hydrogen bonds, and notably, electrostatic forces—the strongest short-range forces in this context.[18] Surface silanol groups of amorphous silica have pK_a values in the range of about 4.5−8.5, and consequently, the silica surface is negatively charged over a broad pH range. Therefore, electrostatic attraction between positively charged peptide side chains and deprotonated silanol groups is a primary driver for adsorption.[19−21] Another factor which can influence peptide adsorption is the hydrophilicity/hydrophobicity of the silica support itself, which can be induced by either post-grafting an alkyl silane onto the surface or co-condensation of an organic-bridge-containing bisilane. For both cases, it is known that the silica surface can turn very hydrophobic and may offer the possibility of attractive interactions with hydrophobic side-chain functionalities of the peptide.[15,22]

An attractive experimental setting for studying adsorption onto silica is to use a macromolecule adsorbate, like a peptide, that exhibits moieties of differing base strength, as the effective charge of the adsorbate then can easily be fine-tuned through pH changes. Literature data suggest that such molecules will

Received: November 16, 2023
Revised: January 16, 2024
Accepted: January 22, 2024
Published: February 12, 2024



ACS Publications
© 2024 The Authors. Published by American Chemical Society

https://doi.org/10.1021/acs.langmuir.3c03513
Langmuir 2024, 40, 4294−4305

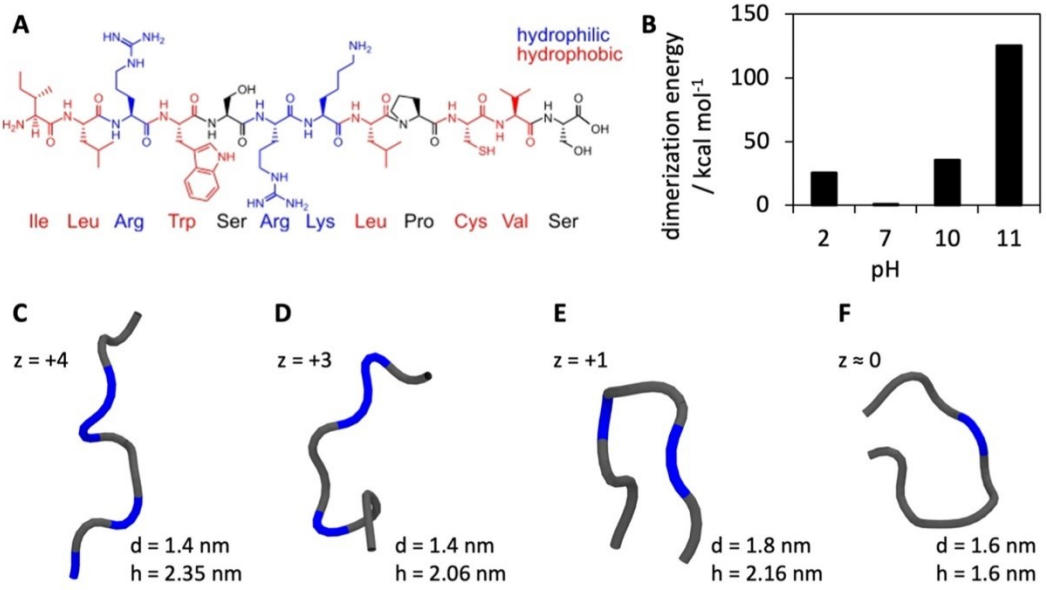

Figure 1. (A) Amino acid sequence of JM#21 with hydrophobic and hydrophilic amino acids indicated. (B) pH-dependent peptide dimerization energies calculated via molecular dynamics simulations. (C–F) Rendered structures of JM#21 obtained by molecular dynamics simulations in dependency of the peptide charge state/pH. The location of the positively charged amino acids giving rise to the net-charge z is indicated in blue.

likely show high loading capacities close to the peptide's isoelectric point (pI), i.e., at low peptide/protein charge conditions, where the intermolecular electrostatic repulsion at the surface is low. It is known that peptide–peptide interactions play a pivotal role over peptide–surface interactions when it comes to the packing density reached.[23] While it is often very intriguing to compare peptide and protein adsorption data with model isotherms like Langmuir, Freundlich, or Brunauer–Emmett–Teller (BET) models, Latour[24] pointed out in an extensive study that most of the main assumptions underlying such models are not met for peptide/protein adsorption. He suggested that the points on the adsorption isotherm do not represent equilibrium states of surface coverage but rather concentration-dependent changes in areal density of the adsorbed peptide layer. Surely, under the consideration of curved surfaces and restricted space of a porous adsorbent, additional effects on the adsorption may arise.

A commonly used model introduced by Sang, Vinu, and Coppens (SVC) for estimating maximum peptide and protein uptake on porous adsorbents assumes that the entire pore volume can be ascribed to cylindrical pores with a uniform diameter into which peptide molecules can be fitted depending on the reduced pore diameter (ratio of pore diameter and peptide diameter).[25] While the SVC model provides foundational understanding of the adsorption of proteins into mesopores, it yet falls short when applied to materials with nonuniform pore systems and shapes, as well as for proteins and peptides undergoing conformational transitions during adsorption. Meissner et al. enhanced this model by accounting for parts of the pore volume being inaccessible to the peptide, improving predictions for the experimental adsorption of lysozyme on SBA-15 materials by considering the secondary (micro)porosity of the material.[26] A macroscopic effect of physically excluding adsorptive from interaction with the surface due to pore entry size constraints was demonstrated by Katiyar et al. by the adsorption of bovine serum albumin (BSA) onto SBA-15 with different pore sizes.[27] They found that BSA adsorption was strongly depending on the pore diameter with very low loading for pore diameters <10 nm, but which increased by a factor of about 10 for 25 nm pores. It is expected that there might be pH-dependent alterations in the peptide's behavior due to charge modulation, especially near its pI, which may include dimerization/aggregation and conformation-dependent changes in hydrophilicity.[8] A confinement-related effect influencing the surface coverage of peptides and proteins is the increase in surface area the adsorbate occupies on convex-curved surfaces as compared to flat surfaces, as demonstrated by Yin et al. for the adsorption of an amyloid-β peptide onto graphene.[28] Furthermore, Su et al. found that depending on the loading concentration and peptide charge, elliptical peptides like lysozyme tend to adsorb in different orientations, like head-on, side-on, or in a tilted orientation to achieve high surface coverage.[23] These factors, beyond fundamental electrostatic or hydrophobic interactions, add a great deal of complexity to the adsorption on a plain silica surface and even more to the adsorption on curved surfaces within confined pore spaces. Our analysis aims to account for this multitude of factors, offering a nuanced understanding of peptide adsorption onto mesoporous silica. Unlike preceding studies predominantly focused on rigid proteins and a narrow range of MSNs, our research focuses specifically on peptides, employing theoretically modeled structures to elucidate adsorption variances across different pore systems.

https://doi.org/10.1021/acs.langmuir.3c03513
Langmuir 2024, 40, 4294–4305

Table 1. Characterization of the MSNs[a]

	NSN	MSNhex	DMSN	DMON	DMONc
diameter/nm	206 ± 18	121 ± 12	158 ± 7	128 ± 11	128 ± 11
surface area/m^2 g^{-1}	23	1148	475	662	567
pore diameter/nm		3.5	4–12	3–20	3–20
pore volume (0.9 p p0–1)/cm^3 g^{-1}		0.82	0.51	0.89	0.91
zeta potential/mV	−58 ± 5	−35 ± 8	41 ± 8	−19 ± 3	−29 ± 4

[a]Specific surface areas were determined by BET analysis of nitrogen sorption measurements at 77 K. The particles' pore diameter and pore volume were determined by NLDFT analysis for silica (equilibrium model) in the relative pressure range from 0 to 0.9. Zeta potentials were measured in aqueous hepes buffer (pH 7.2, 25 mM). The particle diameter was determined by TEM.

Table 2. Maximum Packing Densities (PD_{max}) of JM#21 Adsorption onto a Nonporous NSN and Theoretical Packing Densities (PD_{mono}) of a Monolayer Based on Modeled Peptide Dimensions for the Peptide Adsorbing Head-On (hdp of Cylinder Base) or Side-On (Cylinder Side, Rectangular Representation) at Different pH Values[a]

	pH 2	pH 7	pH 10	pH 11
peptide net charge	+4	+3	+1	0
c_{eq}/mM	0.97 ± 0.01	1.07 ± 0.01	1.02 ± 0.02	1.02 ± 0.01
PD_{max}/μmol m^{-2}	0.14 ± 0.05	0.24 ± 0.1	0.66 ± 0.15	0.74 ± 0.1
PD_{mono} (head-on)/μmol m^{-2}	0.98	0.98	0.59	0.75
PD_{mono} (side-on)/μmol m^{-2}	0.5	0.58	0.43	0.65

[a]The BET surface area of the NSN was 23 m^2 g^{-1}, and the initial peptide loading concentration was 1.5 mM.

In this study, we conducted pH-dependent adsorption trials using the cationic, low molecular weight peptide JM#21[29] and a variety of MSNs characterized by differing pore size, geometry, and surface properties. Force field computations of the peptide were carried out in relation to the peptide charge at adsorption pH values to provide a theoretical framework for interpreting our findings. Particularly at pH levels near the peptide's pI, which facilitate optimal peptide adsorption, we observed noteworthy variations in the peptide loading capacity across MSNs of different pore sizes. Comparing hydrophobic MSNs with their all-silica counterparts, we found enhanced adsorption onto hydrophobic MSNs under loading conditions devoid of electrostatic interactions, whereas under optimal adsorption conditions where electrostatic interactions prevail, the adsorption was diminished. To follow up, we conducted a functional cell assay for the peptide, effectively demonstrating its protection under serum conditions, i.e., environments where the peptide would typically exhibit a short half-life time. This understanding, integrated with the capability to predict loading based on peptide charge profile and potentially its conformation, unveils a pathway toward optimizing loading conditions and maximizing loading degrees. By aligning the suitable silica particle characteristics with the peptide attributes, this study lays a cornerstone for tailoring MSN systems, enhancing their potential for diverse therapeutic applications.

RESULTS AND DISCUSSION

Physicochemical and Theoretically Modeled Properties of Peptide JM#21. JM#21 is a novel optimized derivative of the endogenous, peptide-based CXCR4 antagonist, EPI-X4, isolated from human hemofiltrate.[29] While not being an antimicrobial peptide (AMP) itself, JM#21 is a good representative of typical AMPs from a chemical standpoint, enabling the transfer of the adsorption data of JM#21 onto silica to a whole class of widely applied therapeutic peptides. JM#21 shows rapid degradation in human plasma, resulting in a short half-life of 6 min. The peptide is composed of 12 amino acids (H_2N-ILRWSRKLPCVS-COOH) of which six can be classified as hydrophobic and three as positively charged and hydrophilic at neutral pH (Figure 1A). The amino acid sequence results in a molecular mass of 1457 Da and a pI of 11.2 with a net charge of +3 at pH 7. Upon increasing the pH value, the overall peptide net charge gradually decreases to +1 at pH 10 and to a neutral state at a pH of around 11 (Figure S1A). The distribution of basic amino acids within the peptide sequence shows that at maximum charge, four positive charges are distributed among the first seven amino acids, while the remaining five carry no charge. Among the charge-carrying amino acids, the terminal alpha-NH_3^+ group typically has a pK_a value of around nine, and the side chains of lysine and arginine have pK_a values of 10.3 and 12, respectively. Consequently, upon reduction of the peptide net charge to +1, the charge distribution shifts toward the amino terminus with charges at amino acids three and six. Approaching the pI of the peptide, the remaining positive charge is either located at amino acid three or six, which in the case of three implies an even stronger shift of the positive charge toward the amino terminus. It is important to consider that these different charge states may not only be induced by the pH of the adsorption solution but also partial charge screening effects that occur upon interaction of the peptide with the negatively charged silica surface. Furthermore, we conducted theoretical calculations of the peptide's 3D structure and its tendency to form aggregates at different charge states, which were representative for the pH values used for the adsorption study (Figure 1B). At a high charge (z = +4), the structure tends to be elongated (Figure 1C), while at a lower charge of +3, a loop structure is formed at the C-terminus (Figure 1D). At an effective charge of +1 and 0, the peptide transitions into a more compact conformation as a result of further loss of charged amino acid side chains, rendering the peptide more hydrophobic (Figure 1E,F). Furthermore, we examined these structures regarding their potential to dimerize and found that conditions close to the pI of the peptide energetically favor this process. The dimerization energies were calculated for the peptide under vacuum and should be lower by a factor of 4−12 for water, assuming the same conditions as for hydrogen bonds in

https://doi.org/10.1021/acs.langmuir.3c03513
Langmuir 2024, 40, 4294−4305

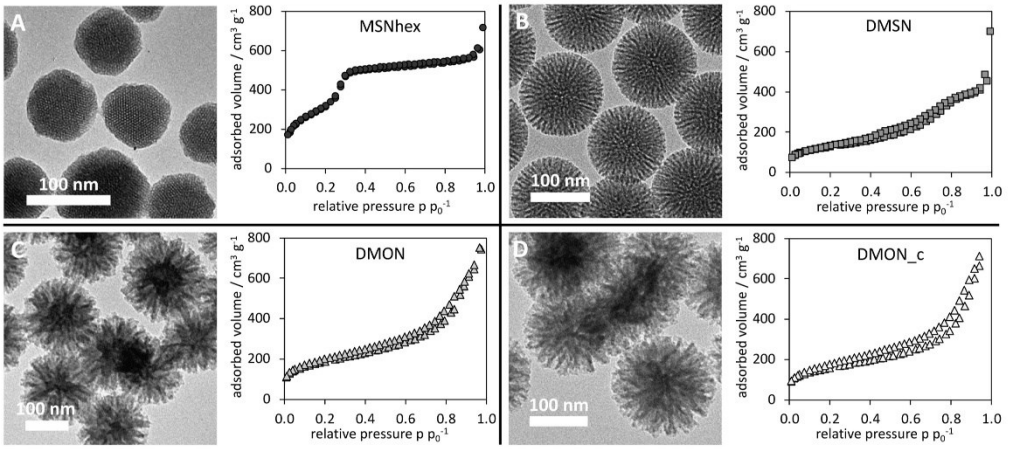

Figure 2. Transmission electron micrographs and nitrogen sorption measurements (conducted at 77 K) of the various mesoporous silica nanoparticles reveal clear structural differences of their pore system. A) MSN-hex, B) DMSN, C) DMON, and D) DMONc.

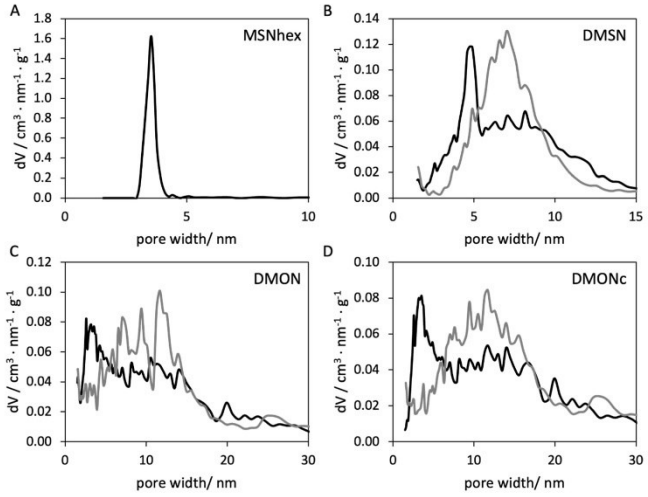

Figure 3. PSD curves of the different MSNs obtained by the NLDFT method from the equilibrium (black) and adsorption kernel (gray) of the nitrogen sorption measurements. (A) MSN-hex with a very narrow PSD of small pores and (B) DMSN, (C) DMON, and (D) DMONc with broad PSDs exhibiting maximum pore sizes of up to 12 (DMSN) and 20 nm (DMON/DMONc).

peptides.[30] Keeping this in mind, the dimerization energies at charges +4, +3, and +1 would be in the range of 4−14 room temperature (RT) in aqueous conditions (1 RT = 0.593 kcal mol^{-1}), while the dimerization energy around the pI is substantially higher and should be in the range of 17−70 RT under aqueous conditions. To obtain at least a rough estimate of the adsorbate dimensions and its spatial demand on a surface (Figure 1C−F), the obtained peptide conformations were geometrically approximated by fitting them into a cylinder volume. By this simplification approach, we could get a general idea of realistic monolayer packing densities (PD_{mono}) of minimum energy peptide structures at different charge states, neglecting interpeptide electrostatic effects. The charge distribution under different pH conditions suggests that the peptide will likely adsorb side-on (high charge, broadly distributed) or head-on (low charge, oriented toward amino terminus) onto the silica surface. Based on the derived cylinder dimensions, we calculated PD_{mono} for a head-on (hexagonal dense packing of cylinder base) and side-on (rectangular representation of cylinder side view) adsorption scenario (Table 2). In the head-on scenario, PD_{mono} is high at maximum charge due to the small cylinder diameter, reaches a minimum at z = +1, and increases again for the very compact peptide conformation near the pI. It is worth to note, though, that the very high PDs for head-on at high charge are probably unrealistic, as peptide−peptide repulsion should occur. The side-on scenario shows a similar trend with overall lower values for the PD, this time with a maximum at z = 0, a minimum at z

https://doi.org/10.1021/acs.langmuir.3c03513
Langmuir 2024, 40, 4294−4305

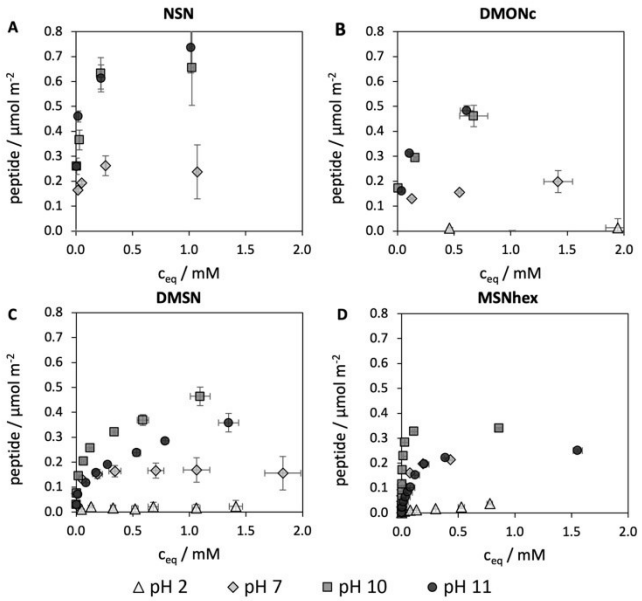

Figure 4. JM#21 adsorption isotherms onto (A) NSN, (B) DMONc, (C) DMSN, and (D) MSNhex recorded at different pH values. pH 2 (triangles), pH 7 (diamonds), pH 10 (squares), and pH 11 (circles) (n = 3, mean ± SD). Please note that no isotherm was included for the NSNs at pH 2 due to high data variance.

= +1, and similar values for high charges. The maximum PD_{mono} of JM#21 consequently is expected to be in the range of 0.4−0.75 μmol m^{-2} when the influence of repulsive electrostatic or confinement effects on the adsorption can be neglected.

Characterization of Silica Nanoparticles. To investigate the basic charge- and pH-dependent effects on the peptide packing density of JM#21 on a fully accessible silica surface, nonporous all-silica particles (NSNs) were synthesized via the Stöber method (Figure S2). The particles had a mean diameter of 169 nm, a specific surface area of 23 m^2 g^{-1}, and a zeta potential of −58 mV measured in 25 mM HEPES buffer at pH 7.2.

To evaluate the effect of different pore sizes and geometries on the adsorption of the peptide, a set of structurally different mesoporous all-silica nanoparticles were synthesized. MSNhex (Figure 2A) represent spherical nanoparticles with a hexagonally ordered system of cylindrical pores with relatively small pore diameters (3.5 nm) but a large specific surface area of 1148 m^2 g^{-1} and a pore volume of 0.82 cm^3 g^{-1}. The hexagonal order of the pore system was confirmed by small-angle X-ray diffraction (SAXS) measurements (Figure S3) and fast forward Fourier transformation of transmission electron microscopy (TEM) images (Figure S4). The pore size distribution (PSD) was very narrow for MSNhex as can be seen in Figure 3A, evidencing the uniformity of the pore system. Dendritic mesoporous silica nanoparticles (DMSNs) also had a spherical shape but exhibited an inherently different pore structure than MSNhex. It can be described as a disordered system of nonuniform, roughly conical mesopores, which are radially arranged around the particle center. This could be confirmed by TEM images (Figure 2B) and the observation of only one broad reflex at low scattering vector values in SAXS measurements (Figure S3). The DMSN had a very broad PSD ranging from 4 to 12+ nm as shown in Figure 3B. The pore opening dimensions of the DMSN were estimated from TEM images and appear to be mostly represented by the higher range of the PSD around 8−12 nm. The pore diameter is gradually decreasing from the opening toward the particle center to around 3−4 nm, which is represented by the middle to lower diameter region of the PSD. The pore volume and specific surface area of the DMSN were smaller compared to the other types of MSNs with 0.51 cm^3 g^{-1} and 474 m^2 g^{-1}, respectively.

The range of pore diameters of all-silica nanoparticles investigated was further extended by the synthesis of dendritic mesoporous organosilica nanoparticles (DMONs) and subsequent calcination, yielding their all-silica derivative DMONc, depicted in Figure 2C,D. The organic content of DMONs was determined to be about 20 wt % by thermogravimetric measurements (Figure S5), and the particles were structurally very similar to DMSNs (conical pores). In analogy to DMSNs, DMONs/DMONc exhibited a broad PSD, covering an even larger range of pore sizes (3−20+ nm) as can be seen in Figure 3C,D, with wide pore openings in the range of 10−20 nm, narrowing down to 3 nm toward the particle center. DMONs and DMONc had a specific surface area (662 and 567 m^2 g^{-1}) at a high pore volume (0.89 and 0.91 cm^3 g^{-1}), respectively. For all dendritic particles, the PSD was strongly dependent on whether the nonlocal density functional theory (NLDFT) analysis was performed based on the equilibrium or adsorption branch of the isotherm. Here, a consistent tendency was observed that the equilibrium kernel implied a higher fraction of smaller pores in the range of 3−5 nm (DMSN) and 3−10

https://doi.org/10.1021/acs.langmuir.3c03513
Langmuir 2024, 40, 4294−4305

nm (DMON/DMONc), while the adsorption kernel had its maximum at around 5−10 nm (DMSN) and 5−15 nm (DMON/DMONc). This could be indicative of partial restriction of larger pores by segments with a smaller diameter, in agreement with the overall irregular pore shape. Microporosity evaluation was done for all porous particles via the t-plot method. While no microporosity could be observed for MSNhex and DMSN, DMON and DMONc showed a small contribution of micropores, with a micropore volume of 0.067 and 0.051 $cm^3\ g^{-1}$, respectively. A tabular summary of the physicochemical characteristics of the nanoparticles primarily covered in this study is given in Table 1. All particles had a negative zeta potential at neutral pH conditions, which was below −30 mV for the all-silica particles. DMON exhibited a higher zeta potential of −19 mV against −29 mV for DMONc, indicating a reduced surface silanol concentration resulting from the incorporation of hydrophobic moieties. Changes in zeta potential upon pH variation were investigated by measuring the zeta potential exemplary for all-silica MSNs in the loading buffers without peptide (Figure S6). As expected, the zeta potential was negative in the pH range of 7−11 but was close to neutral at pH 2 due to silanol protonation around the isoelectric point of amorphous silica (pH 2−3).[19]

Peptide Packing Density on a Fully Available Surface Is Determined by Electrostatic Interactions. To elucidate the influence of peptide and silica charge on the PD on a relatively flat silica surface, adsorption isotherms of JM#21 onto nonporous silica nanoparticles (NSNs) at different pH values (2, 7, 10, and 11) were recorded, and peptide loading was normalized to the surface area to obtain packing densities. For the adsorption of a cationic peptide like JM#21 onto silica, electrostatic attractive forces between negative silanol groups and cationic side chains are reported to be a major contributor to the adsorptive interaction.[31] For pH 2, it was not possible to get consistent data due to a combination of the low affinity of the peptide to silica and the very small surface area of the NSN. However, the results from the porous all-silica nanoparticles (Figure 4B−D) consistently showed that peptide adsorption was minor at pH 2. In contrast, the isotherm recorded at pH 7 was steep in the beginning before it gradually transitioned into a plateau around a PD of 0.28 $\mu mol\ m^{-2}$ as can be seen in Figure 4A. The deprotonated silanol groups and highly charged peptide lead to strong electrostatic attraction and consequently to such a high-affinity isotherm. The maximum PD reached at the plateau is clearly lower than the calculated values from the modeled peptide dimensions, implying that the effective size of the peptide is much larger than that estimated by the model under these pH conditions. This effect can be explained by electrostatic repulsion between adsorbed peptide molecules increasing the effective size of JM#21 (repulsive charge field).[32] Supporting a strong effect of charge on the effective surface occupancy, Su et al. found that lysozyme (pI of 11) occupies 14 nm^2 at pH 8 (z = +8) versus 26.6 nm^2 at pH 5 (z = +10).[23] A similarly steep isotherm was observed at pH 10 but with a higher PD of 0.66 $\mu mol\ m^{-2}$ reached at the plateau. The decreased peptide charge still allowed for strong attractive interactions with the silica surface, while peptide−peptide repulsion was significantly decreased, reducing the effective size of the peptide. The PD reached at this pH goes beyond the estimate for a side-on adsorption, ranging just around the calculated value for the head-on adsorption state. This is in alignment with the anisotropic charge distribution over the peptide structure at higher pH values, favoring head-on adsorption. A similar change in adsorption orientation was also observed by Su et al. in neutron scattering experiments.[23] At pH 11, the isotherm was still steep at low equilibrium concentrations and transitioned toward a maximum packing density of 0.74 $\mu mol\ m^{-2}$ with no distinct plateau reached under the investigated peptide loading concentrations. The PD again was clearly higher than the calculation for the side-on adsorption but fit well to values expected for head-on adsorption. The reduced affinity of the peptide toward silica may be balanced out by adsorption of dimers and aggregates (close to pI), leading to a relatively steep isotherm and high peptide PD due to possible lateral attractive interaction of the peptide adsorbing on the surface. The observations are in good agreement with literature reports stating that the adsorption of peptides is highly sensitive to the charge states of peptide and silica, respectively. As the surface of NSN is fully accessible for the peptide, the PD is mainly governed by charge-induced peptide properties, like effective size, conformation, and adsorption orientation. In all cases, the measured PDs either were below or equal to the calculated PDs based on peptide dimensions and preferential adsorption orientation, indicating that multilayer adsorption did not occur.

Adsorbent Pore Size Limits the Peptide Adsorption onto MSNs. To evaluate the effect of different pore system characteristics on the peptide adsorption, adsorption isotherms of JM#21 onto MSNhex, DMSN, and DMONc (Figure 4B−D) were measured at the same pH values as for a NSN. The loading degrees derived by UV/vis measurements were exemplarily validated for JM#21-loaded MSNhex by thermogravimetric measurements (Figure S7).

As already stated above, at pH 2, all nanoparticle types exhibited similarly low peptide adsorption capacities. As virtually no peptide adsorbed at this pH, the contribution of van der Waals and hydrogen bonding forces to the adsorption can be assumed to be almost neglectable, irrespective of the pore size of the adsorbent.

In accordance with NSN, the adsorption isotherms at pH 7 showed a steep initial rise for MSNhex, DMSN, and DMONc, striving to a plateau for all particle types at a c_{eq} of around 0.19 mM. The PDs reached at the plateau were in a similar range for all porous particles (0.21 for MSNhex, 0.16 for DMSN, and 0.2 $\mu mol\ m^{-2}$ for DMONc) and comparable, albeit slightly lower, to the values obtained for the NSN (0.24 $\mu mol\ m^{-2}$). This leads to the conclusion that the maximum PD is independent of the pore size at pH 7 and mainly governed by the effective area that the peptide occupies on the surface. All adsorption isotherms at pH 7 showed a relatively flat transition from the initial steep rise into the plateau, which would be much more abrupt for, e.g., an ideal Langmuir isotherm with a similarly steep initial rise (high-affinity isotherm). This flat transition could be explained by effects like a change in the conformation or orientation of the adsorbed peptide, approaching maximum surface coverage under the given conditions as suggested by Latour.[24] In the case of JM#21 at pH 7, the high charge state of the small peptide may lead to an initial adsorption in a flat conformation at low loading concentrations. This flat and spread-out conformation can be supported by the availability of multiple anchoring points, i.e., positively charged amino acid side chains. The calculated peptide structures show that JM#21 is very elongated at this pH, which is rather space demanding and, with increasing peptide concentration, may transform into a more compact

https://doi.org/10.1021/acs.langmuir.3c03513
Langmuir 2024, 40, 4294−4305

conformation or tilted adsorption orientation, enabling higher surface PDs. In such a case, a strong binding of the peptide to the surface will lead to a pronounced flattening of the isotherm's transition point into the saturation plateau.

The overall similar adsorption behavior of the three porous particles drastically changed at pH 10, where clear differences were observed in dependency of the pore characteristics. JM#21 having a lower but still net positive charge resulted in a steep initial rise of the isotherms for all particles, which could be observed up to a PD of 0.3 μmol m^{-2} for MSNhex and up to 0.15 and 0.19 μmol m^{-2} for DMSN and DMONc, respectively. These relatively small surface access values for DMSN and DMONc may indicate that part of the surface is inaccessible for peptide adsorption, as some microporosity was observed for DMONc, and both particles exhibit an irregular pore structure. Due to a smaller effective size of the peptide at this pH, the isotherm of MSNhex transitioned into a plateau at a higher maximum PD of around 0.34 μmol m^{-2} as compared to pH 7, which is still clearly lower than the respective value observed for NSN. The PD reached is even below the theoretical PD calculated for side-on adsorption at this pH, indicating that the small pore size clearly limits the dense packing of the peptide (confinement effect). In contrast to that, the less steep isotherms obtained for DMSN and DMONc transitioned into a linear upward progression at around 0.2 μmol m^{-2} with a measured maximum PD of 0.47 and 0.46 μmol m^{-2}, respectively. The fact that no distinct adsorption plateau was observed indicates that with the larger pores, the peptide can approach a densely packed monolayer as there is enough space for PD-optimizing rearrangement processes. Consequently, the linear progression could be interpreted as a heavily extended transition phase into a plateau beyond the experimental conditions. The PD values were in the range of the theoretical values for side-on and below head-on adsorption, which shows that confinement limitations of the adsorption can also be observed at larger pore sizes. This is probably connected to the conical shape of the pores with decreasing pore diameters toward the particle center causing PD limiting confinement effects, as observed for MSNhex. These confinement effects should be mainly connected to the curvature of the adsorbent surface and the limited space provided by the pores. The surface curvature effect suggests a higher surface occupancy of an adsorbate molecule interacting with a negatively curved surface as described by Yin et al.[28] The limited pore space not only physically restricts the extent of head-on adsorption in a densely packed monolayer but also has a negative influence on the ability of the peptide to rearrange into a conformation or orientation that is favorable for denser packing. At pH 10, the transition of the MSNhex isotherm into the plateau is less flat as compared to pH 7. This could indicate that at pH 10, the peptide either undergoes only a minor conformational transition (less flat initial adsorption) with increasing loading concentration or that the conformational transition comes at a lower energy cost as the peptide has less excess charge enabling for multipoint interactions with the surface. The reduced electrostatic repulsion should further lower the barrier for peptide rearrangement and dense packing on the surface.

At pH 11, the reduced attractive interactions with silica and an increased tendency to dimerize or even aggregate result in pronounced pore size-related effects on the adsorption. Signs of this lower attraction could be seen in the isotherms of MSNhex and DMSN, both of which revealed a lower affinity of the peptide to silica, resulting in a relatively flat isotherm compared to pH 7 or 10. For DMONc, however, the isotherm progressed in a steeper fashion up to a PD of around 0.18 μmol m^{-2} even at this pH. For the small pore MSNhex, the isotherm flattened out toward a maximum loading degree of around 0.25 μmol m^{-2} which is comparable to the value reached at pH 7, while the isotherms of DMSN and DMONc again transitioned into a linear continuation up to a PD of 0.36 and 0.48 μmol m^{-2}, respectively. All particles reached lower maximum PDs within the investigated peptide concentration range compared to those of the NSNs (0.74 μmol m^{-2}), which were even below the theoretical maximum PD for side-on adsorption. Interestingly, MSNhex and DMSN even reach a lower maximum PD as compared to pH 10, which is clearly different from what was observed for the NSN where the PD at pH 11 was even slightly higher than at pH 10. This can be explained by a combination of pronounced confinement effects within the pores (lateral stacking of the peptide in a dense layer) and pore size-dependent inhibition (size exclusion) of the adsorption of peptide dimers and potential larger aggregates. It is suggested that the larger pore openings of DMSN provide at least some accessibility of the surface to peptide aggregates and sufficient space for conformational or orientational changes, causing the linear continuation of the isotherm. In contrast to that, the small pores of MSNhex do not provide enough space for these processes, leading to a pore size-limited plateau already at lower packing densities. Similar observations of loading capacity limiting confinement in dependency on the pore size were made by Andersson et al.[33] for the adsorption of Ibuprofen on MSN with different pore sizes, as well as by Katiyar et al.[27] adsorbing BSA onto SBA-15. For DMONc, however, the loading degree reached at pH 11 is similar to pH 10, and the isotherm shapes were almost identical for both pHs, as observed for NSN. This suggests that the very large pores of DMONc provide higher accessibility of the surface to peptide dimers and aggregates, however not to the same extent as the fully available surface of the NSN, which can be related to the large pores becoming narrower toward the particle center. This adsorption of peptide dimers/aggregates was also reflected in the steeper rise of the isotherm of DMONc.

To check for pore network effects aside of pore shape and PSD, the peptide adsorption onto MSNhex, MSNrad, and MSNrod which have a very similar pore diameter, but different pore lengths and connectivity, was investigated. MSNrad and MSNrod had similar specific surface areas (986 and 1031 m^2 g^{-1}) as well as pore diameters (3.2 and 3.7 nm) as MSNhex, respectively. The physicochemical properties of the particles are summarized in Table S1. TEM images, nitrogen sorption isotherms, and PSDs are shown in Figure S8. In contrast to MSNhex, MSNrad had pores that were radially aligned around the particle center, making the pores only available through one opening. Elongated MSNrod particles (aspect ratio (AR) = 2) exhibited pores aligned along the longitudinal axis, resulting in double the pore length of MSNhex (Figure S9). Across the range of pH values investigated, all the three particle types reached a comparable peptide loading, as shown in Figure S10 (MSNrod at pH 2 not shown). This result shows that a comparable amount of the pore surface area is accessible for the peptide, irrespective of the pore length and connectivity. Consequently, the diffusion length of the peptide must be long enough to not become a limiting factor for the

https://doi.org/10.1021/acs.langmuir.3c03513
Langmuir 2024, 40, 4294−4305

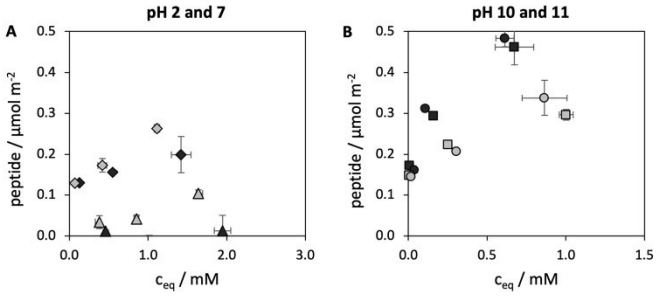

Figure 5. JM#21 adsorption isotherms onto DMON (light gray) and their all-silica structural derivative DMONc (black) recorded at (A) pH 2 (triangles) and 7 (diamonds) and (B) pH 10 (squares) and 11 (circles) (n = 3, mean ± SD).

adsorption and does not affect the results discussed for MSNhex, DMSN, and DMONc.[34]

Hydrophobic Interactions Facilitate the Adsorption of JM#21 under Electrostatically Unfavorable Conditions. To investigate the possibility of promoting peptide adsorption by enabling additional hydrophobic interactions, adsorption onto DMON, containing a benzene-bridged silica network, was investigated. The benzene bridges provide not only classical hydrophobic interactions in the form of van der Waals forces with hydrophobic amino acid side chains but also $\pi-\pi$ interactions (quadrupolar interactions) with other aromatic moieties, like the aromatic functionality of tryptophane. The hydrophobic functionalization via co-condensation was chosen over post-functionalization, as the latter technique is known for having a negative influence on the PSD of the particles, making them not comparable to the all-silica reference. As already highlighted in the nanoparticle characterization, the removal of the organic moieties via calcination preserved the structure of DMON, making the resulting DMONc a perfect all-silica reference for these experiments.

Adsorption of JM#21 onto DMON and DMONc was tested at different pH values for three different peptide loading concentrations, as shown in Figure 5. At pH 2, the adsorption onto calcined DMONc was negligible as discussed in the previous section (0.01 μmol m^{-2}), whereas the PD on DMON was increased by a striking factor of 10 (0.1 μmol m^{-2}). A similar but lower beneficial effect on the adsorption of JM#21 was observed at pH 7, where the DMON reached 0.26 μmol m^{-2} compared to 0.20 μmol m^{-2} for DMONc, i.e., values almost equal to the PD reached for the NSNs. It is known from the literature that silanol dissociation takes place over a broad range of pH, and a certain amount of the silanol groups could still be protonated at pH 7.[20] This reduces electrostatic attraction as well as repulsive charge neutralization of adsorbed peptides, and therefore, a positive contribution of hydrophobic interactions can still be plausible at this pH. In contrast, at pH 10 and 11, peptide loadings were inversed, and the DMONc outperformed the DMON, reaching about 50% higher PD. These results show that under unfavorable charge conditions, the presence of hydrophobic moieties within the silica network promotes adsorption by enabling hydrophobic interactions, while this effect diminishes under pH conditions, where the electrostatic interactions dominate adsorption. In the latter case, the lower surface concentration of silanol groups on the organo-functionalized DMON, which was indicated by the lower zeta potential of DMON (−19 mV) compared to DMONc (−29 mV), led to a decreased peptide adsorption capacity as compared to the all-silica particles. The fact that at pH 11, where electrostatic contributions to the attraction were reduced, hydrophobic interactions did not positively contribute to the adsorption (other than at pH 2 and 7) demonstrates the dominance of hydrophilic interactions still present at this pH. Interestingly, the adsorption isotherms on these large-pore particles generally do not seem to approach a plateau under the investigated adsorption conditions, and even the isotherms for pH 2 and 7 show no obvious signs of approaching a plateau, especially for DMON.

Adsorption onto MSN Retains Peptide Activity Independent of the Pore Size. Zeta potential measurements of MSNhex loaded with different amounts of peptide revealed only minor shifts toward less negative values, indicating that the peptide should reside mainly inside the pore system and provide a shielding effect against enzymatic degradation (Figure S11). To investigate pore size effects on the shielding of the peptide and to prove the conserved biological activity, a cell-based *in vitro* functional assay was performed. This assay is based on the reversible binding of the chemokine CXCL12 to the CXCR4 receptor of the primary pancreatic cancer cell line, Panc354. Upon internalization of CXCL12, remodeling of the cytoskeleton toward a mesenchymal-like form is induced. However, this structural change can be suppressed by blocking CXCR4 via irreversible binding with JM#21. Thus, inhibition of cytoskeletal changes can be used as a measure of peptide functionality and analyzed via fluorescence microscopy (Figure S12). Incubation of Panc354 cells with either free JM#21 or JM#21 loaded onto MSNhex and DMSN enabled monitoring of the biological effect of the released peptide in the presence of serum proteins, i.e., under conditions where the free peptide is rapidly degraded and nonfunctional. MSNhex and DMSN were loaded under optimal loading conditions (pH 10) and had a high loading degree of 30 and 27 wt %, respectively. The concentration of loaded nanoparticles was chosen to match the applied concentration of free JM#21 in the case of full release from the nanoparticles. Figure 6 shows the relative number of Panc354 cells with morphological changes to a more prominent mesenchymal phenotype as compared to the total number of cells after treatment for 24 h. The cells exposed to the free peptide showed CXCL12-induced structural changes to the same extent as the PBS control (CXCL12 only). JM#21 is reported to be readily degraded in human serum resulting in

https://doi.org/10.1021/acs.langmuir.3c03513
Langmuir 2024, 40, 4294−4305

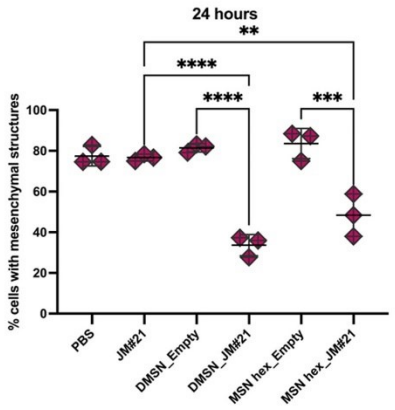

Figure 6. CXCL12-induced changes in the actin structure of Panc354 cells treated with CXCL12 (10 μM), together with PBS, JM#21 (10 μM), nonloaded MSNhex and DMSN (empty), or peptide-loaded MSNhex (30 wt % JM#21) and DMSN (27 wt % JM#21) in RPMI/10% FCS for 24 h at 37 °C. The particle concentration was normalized to 10 μM JM#21 at full release (n = 3, mean ± SD, *$p \leq$ 0.05, two-way ANOVA).

a short half-life time of 6 min.[29] Proteolytic degradation also happened in this case, as the assay was performed in serum containing cell culture medium. However, incubation with DMSN or MSNhex loaded with JM#21 clearly reduced the extent of mesenchymal actin structures by a factor of about 2, whereas the unloaded nanoparticles had no influence on the cells. It is important to note that the particles had no cytotoxic effects on the cells (Figure S13). These results not only demonstrate the release of JM#21 in a functional form and the preservation of its ability to bind to CXCR4 but also display effective peptide protection against serum protein-mediated degradation by MSNs. A similar activity level of JM#21-loaded MSNhex and DMSN shows that even the large pores of DMSNs provided efficient shielding of the peptide against degradation.

■ CONCLUSIONS

In this study, we investigated the effect of several characteristics of MSNs like pore size and structure as well as surface charge and hydrophobicity on the adsorption of the short, cationic peptide JM#21 under various pH conditions. With variation of the pH, the charge of the peptide could be modulated, resulting in changes of electrostatic interactions, peptide conformation, and aggregation, which had striking effects on the adsorption behavior of the peptide. By modeling of the peptide structure at different charge states, the monolayer PD on a surface could be estimated to be in the range of 0.4−0.75 μmol m^{-2}. Adsorption studies of JM#21 onto NSNs providing a fully accessible silica surface showed that the PD is highly sensitive to the electrostatic interactions between adsorbate molecules as well as between adsorbent and adsorptive. The highest PDs were reached near the pI of the peptide and were comparable to the maximum theoretical PD values. Adsorption was reduced under conditions in which the strong peptide−silica interaction was countered by peptide−peptide electrostatic repulsion (pH 7) or completely diminished under conditions in which the silica surface was uncharged. Importantly by comparing experimental PDs with the theoretical PD_{mono} values, multilayer adsorption could be excluded, which is an important prerequisite for the discussion of the adsorption data on MSNs.

While confirming the established trends based on electrostatic interactions, adsorption of JM#21 onto MSNs with different pore sizes and therefore a surface area with variably restricted access revealed a multitude of confinement-related effects on the adsorption. Especially under optimal loading conditions (pH 10 and 11), we discovered a strong dependency of the PD on the pore sizes of the particles. Peptide adsorption onto the MSNs was likely influenced by the confinement effects, restricting the peptide's space to achieve packing in a dense monolayer of favorable orientation and conformation. Additional factors include pore size restriction of the peptide dimer and aggregate adsorption and surface curvature effects that increase the effective surface covered by the peptide in the adsorbed state. By combination of the data on peptide charge and conformation with detailed structural information about the pore system of the different particles, a comprehensive understanding of the experimental isotherms could be gained.

The influence of surface hydrophobicity on the peptide adsorption was investigated by loading JM#21 onto DMONs that contain benzene-bridged silanes within the silica network. Particularly under unfavorable loading conditions (pH 2), where electrostatic interactions are screened, higher packing densities were reached for the hydrophobic DMON compared to their all-silica counterparts (DMONc). This effect was still observed at pH 7 but diminished at pH 10 and 11, where electrostatic attraction is the dominant driving force for the adsorption.

Moreover, in vitro studies showed that CXCL-12-induced morphological changes of Panc356 cells were diminished upon incubation with JM#21-loaded particles, contrary to the rapidly degraded free JM#21, proving the protective benefits offered by MSNs (even with large pores) for easily degradable peptide cargos.

■ EXPERIMENTAL SECTION

Chemicals and Materials. Tetramethyl orthosilicate (TMOS), (3-aminopropyl)trimethoxysilane (APTMS), tetraethyl orthosilicate (TEOS), 1,4-bis(triethoxysilyl)-benzene (BTEB), cetyltrimethylammonium chloride solution (CTAC) (25 wt % in water), triethanolamine (TEA), Phalloidin-Atto565, and paraformaldehyde (PFA) were purchased from Sigma-Aldrich Chemie GmbH, Schnelldorf, Germany. Cetyltrimethylammonium bromide (CTAB) and ammonium hydroxide (28 and 32% in water), sodium hydroxide, ethanol, methanol, acetone, ethylene glycol, sodium carbonate, sodium hydrogen carbonate, sodium dihydrogen phosphate, disodium hydrogen phosphate, cyclohexane, phosphoric acid, and hydrochloric acid were purchased from VWR International GmbH, Darmstadt, Germany. Ammonium nitrate was purchased from Carl Roth GmbH & Co. KG, Karlsruhe, Germany. Phosphate-buffered saline (PBS) was purchased from Thermo Fisher Scientific, Karlsruhe, Germany.

The CXCR-4 antagonist, JM#21, was kindly provided by Mirja Harms and Jan Münch (Institute for Molecular Virology, Ulm). The peptide was used without further purification. Six-well plates were purchased from Greiner Bio-One, Frickenhausen, Germany. FBS, RPMI (Gibco), glutamine (Gibco), and Prolong Gold reagent with DAPI were purchased from Thermo Fisher Scientific, Waltham, USA. Penicillin−streptomycin was purchased from PAN Biosystems, Aidenbach, Germany. CXCL12 was purchased from PeproTech, Cranbury, USA. Sodium salicylate (NaSal) and TritonX-100 were purchased from Fluka, Charlotte, USA.

https://doi.org/10.1021/acs.langmuir.3c03513
Langmuir 2024, 40, 4294−4305

Synthesis of DMSNs. DMSNs were synthesized according to a protocol in the literature.[35] TEA (0.45 g, 3.025 mmol) was dissolved in a CTAC solution (25 wt % in water, 60 mL, 45.375 mmol CTAC) and ultrapure water (90 mL). The solution was stirred for 30 min at 60 °C. The water phase was then overlaid with a solution of TEOS (10 mL, 44.775 mmol) in cyclohexane (40 mL). The reaction mixture was kept at 60 °C and stirred at 100 rpm for 48 h. The DMSNs were isolated by separating the water phase, diluting it with ethanol (90 mL), and centrifugation (15,650 rcf, 30 min). After washing twice with ethanol, the DMSNs were dried at 60 °C, ground to a fine powder, and calcined at 550 °C for 5.5 h (1.83 K min^{-1} heat ramp).

Synthesis of DMON and DMONc. DMONs with a benzene-bridged silane were synthesized according to a protocol based on Kalantari et al.[36] CTAB (380 mg, 1.04 mmol), NaSal (84 mg, 0.52 mmol), and TEA (68 mg, 0.45 mmol) were dissolved in ultrapure water (24 mL) and equilibrated at 80 °C for 60 min. Then, TEOS (2.68 mL, 12 mmol) was added, followed by BTEB (2.34 mL, 5.93 mmol) with a delay of 15 min. The reaction was stirred at 450 rpm at 80 °C for 18 h before the DMONs were isolated by diluting the cooled reaction mixture with ethanol (50 mL) and centrifugation (15,650 rcf, 12 min). The surfactant (CTAB) was removed by extraction with acidified ethanol (4 g of HCl per L of ethanol) for 1 h in an ultrasonic bath (repeated three times). After that, the DMONs were dried at 60 °C and ground to a fine powder.

The calcined, all-silica derivative of DMON (DMONc) was obtained by calcination of the DMON at 550 °C for 5.5 h (1.83 K min^{-1} heat ramp).

Synthesis of MSNrad. MSNs with a radially aligned pore system (MSNrad) were synthesized according to Rosenholm et al.[37] After dissolving porogen CTAB (7.88 g, 21.6 mmol) in a mixture of methanol (860 mL), water (909 mL), and sodium hydroxide solution (1 M, 4.56 mL, 4.6 mmol) in a 2 L round-bottomed flask, the mixture was equilibrated to RT. A mixture of silica precursors TMOS (2.18 mL, 14.7 mmol) and APTMS (0.36 mL, 2.1 mmol) was added at a stirring rate of 500 rpm. The stirring rate was adjusted to 300 rpm after 45 min, and the reaction proceeded for 16 h. Upon precipitation with ammonium nitrate (35 g, 27.4 mmol), the particles were separated via centrifugation and subsequently washed once with water and twice with ethanol in an ultrasonic bath for 1 h each. Finally, the particles were dried at 60 °C in vacuo and calcined at 550 °C for 5.5 h (heating rate 1.8 °C min^{-1}) yielding all-silica "MSNrad".

Synthesis of Nonporous Stöber Silica Nanoparticles. Solid, nonporous silica nanoparticles were synthesized as reported elsewhere.[38,39] The silica precursor, TEOS (3 mL, 13.5 mmol), was added to a mixture of ethanol (55.8 mL), water (44 mL), and ammonium hydroxide solution (28 wt %, 14.8 M, 6 mL, 100.7 mmol) in a 0.5 L round-bottomed flask. The mixture was stirred at a rate of 450 rpm for 19 h at RT. The particles were separated via centrifugation, washed twice with ethanol in an ultrasonic bath for 1 h, and dried at 60 °C in vacuo. Finally, the particles were calcined as described above to yield all-silica "NSN".

Synthesis of MSNs with Varying AR (MSNhex and MSNrod). MSNs with a hexagonal parallel-aligned pore system were synthesized based on the synthesis by Huang et al.[6] CTAB (1.1 g, 3 mmol) was dissolved in a mixture of water (270 mL) and ammonium hydroxide solution (32 wt %, 16.6 M, 5.7 mL, 94 mmol) in a 0.5 L round-bottomed flask. To obtain particles with a lower AR, ethylene glycol (110 mL, 1.62 mol) was added. Upon addition of TEOS (4.7 mL, 21.2 mmol), the mixture was stirred with 600 rpm for 4 h. The particles were precipitated with ammonium nitrate (5 g, 3.9 mmol), separated via centrifugation, washed twice with ethanol in an ultrasonic bath for 1 h, and dried at 60 °C in vacuo. Finally, the particles were calcined as described above for 8 h to yield all-silica "MSNhex" (AR = 1.1) and "MSNrod" (AR = 2).

Characterization of Silica Nanoparticles. The particles' diameters and pore structures were examined with a Jeol 1200 (Jeol, Germany) transmission electron microscope using a HT voltage of 120 kV and a beam current of 65 μA. Fast Fourier transformation (FFT) was used to obtain grayscale images of the electron diffraction patterns using the FFT plug-in of ImageJ version 1.52n. By filtering different frequency ranges via selection of gray values ranging from 158 to 178 or from 146 to 160 and subsequent inverse FFT calculations, electron diffracting structures were visualized. Small-angle X-ray scattering (SAXS) was performed on a Bruker Nanostar (Bruker, USA) using Cu Kα radiation (λ = 1.5406 Å) at an angle from 0.3 to 5° (2θ). Nitrogen sorption measurements were conducted at −196 °C on a Quadrasorb-1 (Quantachrome Instruments, Germany) after drying the particles in vacuo at 100 °C for 22 h. The pore diameters were calculated via the equilibrium NLDFT kernel (silica, cylindrical pores) in the relative pressure range of 0−0.9, and the pore volumes were determined at a relative pressure of 0.9. The specific surface areas were determined by using the BET method. By using the t-plot method in the relative pressure range of 0.75−0.95, the external surface areas were estimated. Zeta potentials were measured with a Zetasizer NanoZS Zen3600 (Malvern Panalytical, Germany) at a particle concentration of 0.1 mg mL^{-1} in the aqueous buffer solution as stated. Thermogravimetric analysis was performed at a heating rate of 10 °C min^{-1} in a nitrogen/oxygen (70%/30%) atmosphere on a TG209 F1 Libra (NETZSCH, Germany).

Peptide Adsorption onto Silica Nanoparticles. JM#21 adsorption was conducted in different aqueous buffer solutions: 12 mM carbonate buffer (pH 10 and 11) and 12 mM phosphate buffer (pH 2.1 and 7.4). Stock solutions of JM#21 (5 mM) in each buffer were prepared, and the pH was adjusted with sodium hydroxide solution (1 M). The different particle types were dispersed in each buffer by using a focused ultrasonic bath. After adjusting the pH value with sodium hydroxide solution, particle dispersion, peptide stock, and buffer were mixed in 2 mL centrifugal tubes (Eppendorf), resulting in a constant particle concentration of 5 mg mL^{-1} and varying peptide concentrations (0−4 mM). Upon rotating the mixture for 2 h at RT, the particles were centrifuged (14,800 rpm; 5 min) and briefly washed with acetone. The particles were dried in vacuo at 60 °C. The amount of peptide adsorbed onto the particles was determined by measuring the absorbance of the adsorption supernatants at 280 nm by using UV/vis spectroscopy.

Peptide Modeling. Molecular dynamics simulations were used to investigate the self-interactions of the JM#21 peptide. For this purpose, the atomic positions of the peptide structures with different pH values were used and equilibrated at 300 K through ReaxFF simulations in the Amsterdam Modeling Suite 2021 (http://www.scm.com) for 0.5 ns. Subsequently, two peptides were placed in the simulation box, and the system was equilibrated again for 0.5 ns at 300 K using ReaxFF simulations. Finally, the interaction energy was determined and averaged by running ReaxFF simulations in the *NVT*-ensemble for 25 ps while the system was coupled to a Berendsen heat bath with a temperature of 300 K and a coupling constant of 100 fs.

Cell Culture and Activity Assay. Primary human pancreatic cell lines (Panc354) were generated from the resected excess pancreatic carcinoma tissue that was subcutaneously implanted into nude mice in vivo.[40] Panc354 cells were maintained at 37 °C in a humidified atmosphere with 5% CO_2 in culture medium RPMI supplemented with 10% FBS, 1% penicillin−streptomycin, and 1% glutamine. For experimental setup, cells were used in early passages (Pass. 3−20) and were recovered from frozen stocks on a regular basis. Single cells were counted with Neubauer chambers and seeded accordingly.

Panc354 cells were cultured at a density of 50,000 on coverslips (24 × 60 mm, Menzel-Gläser) in a six-well plate for 24 h until attachment. Afterward, the cells were treated with CXCL12 (10 μM), together with PBS, JM#21 (10 μM), nonloaded MSNhex and DMSN, or peptide-loaded MSNhex (30 wt % JM#21) and DMSN (27 wt % JM#21). The final silica concentrations of MSNhex and DMSN were 34 μg mL^{-1} and 37 μg mL^{-1}, respectively, which corresponded to 10 μM peptide, assuming full release from the loaded particles. After treatment for 24 h, the cells were washed three times with PBS. Subsequently, they were fixed with 2% PFA for 20 min at RT and then washed again three times with PBS. Next, the cells were permeabilized with 0.7% TritonX-100 solution for 15 min at RT, followed by three PBS washing steps. Coverslips with cells were then incubated with Phalloidin-Atto565 (1:500 diluted in PBS) inside a dark humid chamber for 60 min. Finally, the cells were washed three

https://doi.org/10.1021/acs.langmuir.3c03513
Langmuir 2024, 40, 4294−4305

times in PBS and mounted on slides using Prolong Gold reagent with DAPI. Fluorescence microscopy was performed at 353 nm (cell nuclei) and 565 nm (cytoskeleton) using a Zeiss Axio Vert.A1 with an EC Plan-Neofluar 63x/1.25 oil objective and ZenBlue software. The experiments were conducted in triplicate (n = 3), and five representative pictures were taken per experiment and processed with ImageJ. The mesenchymal cytoskeletal remodeling was quantified by counting cells with stress fibers, spindle-like, and elongated actin structures in relation to the total number of cells per picture.

■ ASSOCIATED CONTENT

Data Availability Statement

The reported data are either mean values ±SD or individual values. The sample size (n) is specified in the respective figure legends and table captions. Statistical significance was tested with two-way ANOVA using GraphPad Prism.

Supporting Information

The Supporting Information is available free of charge at https://pubs.acs.org/doi/10.1021/acs.langmuir.3c03513.

Calculated peptide charge as a function of pH; NSN characterization results; SAXS measurements for the studied particles; TEM image and reconstruction of MSNhex particles; TGA results for DMONs and DMONc particles; pH-dependent zeta potential values for MSNrad particles; TGA results measured for JM#21-loaded MSNhex particles; characterization results for MSNrad and MSNrod particles; comparison of maximum JM#21 loadings into MSNrad, MSNhex, and MSNrod particles; zeta potential measurements of JM#21-loaded MSNhex particles as a function of peptide loading; and fluorescence microscopy images of CXCL12-treated Panc354 cells exposed to JM#21 and corresponding cell viability data (PDF)

■ AUTHOR INFORMATION

Corresponding Author

Mika Lindén − *Institute of Inorganic Chemistry II, Ulm University, Ulm 89081, Germany;* orcid.org/0000-0003-1736-0638; Email: mika.linden@uni-ulm.de

Authors

Bastian Beitzinger − *Institute of Inorganic Chemistry II, Ulm University, Ulm 89081, Germany*

Roman Schmid − *Institute of Inorganic Chemistry II, Ulm University, Ulm 89081, Germany;* orcid.org/0000-0002-9034-5162

Christoph Jung − *Institute of Electrochemistry, Ulm University, Ulm 89081, Germany;* orcid.org/0000-0002-1422-4991

Kanishka Tiwary − *Department of Internal Medicine I, Ulm University, Ulm 89070, Germany*

Patrick Hermann − *Department of Internal Medicine I, Ulm University, Ulm 89070, Germany*

Timo Jacob − *Institute of Electrochemistry, Ulm University, Ulm 89081, Germany;* orcid.org/0000-0001-7777-2306

Complete contact information is available at: https://pubs.acs.org/10.1021/acs.langmuir.3c03513

Author Contributions

#B.B. and R.S. contributed equally to this work.

Author Contributions

B.B. and R.S. contributed equally to this work. B.B., R.S., and M.L. conceived the study, designed the experiments, analyzed the data, and wrote the manuscript. C.J. performed peptide structure simulations and data analysis. K.T. performed the activity assay and data analysis. T.J. and P.H. edited and revised the manuscript.

Notes

The authors declare no competing financial interest.

■ ACKNOWLEDGMENTS

M.L. and T.J. are funded by the German Research Foundation through the collaborative research center, CRC-1279 (project ID: 316249678). P.H. is supported by a Max Eder Fellowship of the German Cancer Aid (70114721) and by a Hector Foundation Cancer Research grant (M2094). The authors gratefully acknowledge Cornelia Egger for performing the nitrogen sorption experiments, Kea Fedke for TGA, and Lionel Kroner for TGA and SAXS measurements, as well as Julia Krayl for peptide adsorption experiments onto DMONs and DMONc. The authors thank Mirja Harms and Jan Münch for providing peptide JM#21. Effective communication of this research was evaluated and enhanced by utilizing the artificial intelligence (AI) large language model (LLM) ChatGPT (version GPT4).

■ REFERENCES

(1) Mandal, T.; Beck, M.; Kirsten, N.; Lindén, M.; Buske, C. Targeting Murine Leukemic Stem Cells by Antibody Functionalized Mesoporous Silica Nanoparticles. *Sci. Rep.* **2018**, *8*, 989.

(2) Kramer, L.; Winter, G.; Baur, B.; Kuntz, A. J.; Kull, T.; Solbach, C.; Beer, A. J.; Lindén, M. Quantitative and Correlative Biodistribution Analysis of 89Zr-Labeled Mesoporous Silica Nanoparticles Intravenously Injected into Tumor-Bearing Mice. *Nanoscale* **2017**, *9* (27), 9743−9753.

(3) Cauda, V.; Argyo, C.; Bein, T. Impact of Different PEGylation Patterns on the Long-Term Bio-Stability of Colloidal Mesoporous Silica Nanoparticles. *J. Mater. Chem.* **2010**, *20* (39), 8693−8699.

(4) Seré, S.; De Roo, B.; Vervaele, M.; Van Gool, S.; Jacobs, S.; Seo, J. W.; Locquet, J. P. Altering the Biodegradation of Mesoporous Silica Nanoparticles by Means of Experimental Parameters and Surface Functionalization. *J. Nanomater.* **2018**, *2018*, 1−9.

(5) Björk, E. M.; Söderlind, F.; Odén, M. Tuning the Shape of Mesoporous Silica Particles by Alterations in Parameter Space: From Rods to Platelets. *Langmuir* **2013**, *29* (44), 13551−13561.

(6) Huang, X.; Teng, X.; Chen, D.; Tang, F.; He, J. The Effect of the Shape of Mesoporous Silica Nanoparticles on Cellular Uptake and Cell Function. *Biomaterials* **2010**, *31* (3), 438−448.

(7) Shen, J.; He, Q.; Gao, Y.; Shi, J.; Li, Y. Mesoporous Silica Nanoparticles Loading Doxorubicin Reverse Multidrug Resistance: Performance and Mechanism. *Nanoscale* **2011**, *3* (10), 4314−4322.

(8) Braun, K.; Pochert, A.; Gerber, M.; Raber, H. F.; Lindén, M. Influence of Mesopore Size and Peptide Aggregation on the Adsorption and Release of a Model Antimicrobial Peptide onto/from Mesoporous Silica Nanoparticles: In Vitro. *Mol. Syst. Des Eng.* **2017**, *2* (4), 393−400.

(9) Hartono, S. B.; Gu, W.; Kleitz, F.; Liu, J.; He, L.; Middelberg, A. P. J.; Yu, C.; Lu, G. Q.; Qiao, S. Z. Poly-L-Lysine Functionalized Large Pore Cubic Mesostructured Silica Nanoparticles as Biocompatible Carriers for Gene Delivery. *ACS Nano* **2012**, *6* (3), 2104−2117.

(10) Schmidtchen, A.; Frick, I. M.; Andersson, E.; Tapper, H.; Björck, L. Proteinases of Common Pathogenic Bacteria Degrade and Inactivate the Antibacterial Peptide LL-37. *Mol. Microbiol.* **2002**, *46* (1), 157−168.

(11) Veronese, F. M.; Mero, A. The Impact of PEGylation on Biological Therapies. *Biodrugs* **2008**, *22* (5), 315−329.

(12) Braun, K.; Pochert, A.; Lindén, M.; Davoudi, M.; Schmidtchen, A.; Nordström, R.; Malmsten, M. Membrane Interactions of Mesoporous Silica Nanoparticles as Carriers of Antimicrobial Peptides. *J. Colloid Interface Sci.* **2016**, *475*, 161−170.
(13) Xu, C.; Lei, C.; Yu, C. Mesoporous Silica Nanoparticles for Protein Protection and Delivery. *Front. Chem.* **2019**, *7*, 290.
(14) Deere, J.; Magner, E.; Wall, J. G.; Hodnett, B. K. Mechanistic and Structural Features of Protein Adsorption onto Mesoporous Silicates. *J. Phys. Chem. B* **2002**, *106* (29), 7340−7347.
(15) Puddu, V.; Perry, C. C. Peptide Adsorption on Silica Nanoparticles: Evidence of Hydrophobic Interactions. *ACS Nano* **2012**, *6* (7), 6356−6363.
(16) Boehnke, N.; Dolph, K. J.; Juarez, V. M.; Lanoha, J. M.; Hammond, P. T. Electrostatic Conjugation of Nanoparticle Surfaces with Functional Peptide Motifs. *Bioconjugate Chem.* **2020**, *31* (9), 2211−2219.
(17) Meissner, J.; Prause, A.; Bharti, B.; Findenegg, G. H. Characterization of Protein Adsorption onto Silica Nanoparticles: Influence of PH and Ionic Strength. *Colloid Polym. Sci.* **2015**, *293* (11), 3381−3391.
(18) Patwardhan, S. V.; Emami, F. S.; Berry, R. J.; Jones, S. E.; Naik, R. R.; Deschaume, O.; Heinz, H.; Perry, C. C. Chemistry of Aqueous Silica Nanoparticle Surfaces and the Mechanism of Selective Peptide Adsorption. *J. Am. Chem. Soc.* **2012**, *134* (14), 6244−6256.
(19) Ong, S.; Zhao, X.; Eisenthal, K. B. Polarization of Water Molecules at a Charged Interface: Second Harmonic Studies of the Silica/Water Interface. *Chem. Phys. Lett.* **1992**, *191*, 327−335.
(20) Rosenholm, J. M.; Czuryszkiewicz, T.; Kleitz, F.; Rosenholm, J. B.; Lindén, M. On the Nature of the Brønsted Acidic Groups on Native and Functionalized Mesoporous Siliceous SBA-15 as Studied by Benzylamine Adsorption from Solution. *Langmuir* **2007**, *23* (8), 4315−4323.
(21) Shaw, A. M.; Hannon, T. E.; Li, F.; Zare, R. N. Adsorption of Crystal Violet to the Silica - Water Interface Monitored by Evanescent Wave Cavity Ring-down Spectroscopy. *J. Phys. Chem. B* **2003**, *107* (29), 7070−7075.
(22) Mietner, J. B.; Brieler, F. J.; Lee, Y. J.; Fröba, M. Properties of Water Confined in Periodic Mesoporous Organosilicas: Nano-imprinting the Local Structure. *Angew. Chem., Int. Ed.* **2017**, *56* (40), 12348−12351.
(23) Su, T. J.; Lu, J. R.; Thomas, R. K.; Cui, Z. F.; Penfold, J. The Effect of Solution PH on the Structure of Lysozyme Layers Adsorbed at the Silica-Water Interface Studied by Neutron Reflection. *Langmuir* **1998**, *14* (2), 438−445.
(24) Latour, R. A. The Langmuir Isotherm: A Commonly Applied but Misleading Approach for the Analysis of Protein Adsorption Behavior. *J. Biomed. Mater. Res., Part A* **2015**, *103* (3), 949−958.
(25) Sang, L. C.; Vinu, A.; Coppens, M. O. General Description of the Adsorption of Proteins at Their Iso-Electric Point in Nanoporous Materials. *Langmuir* **2011**, *27* (22), 13828−13837.
(26) Meissner, J.; Prause, A.; Di Tommaso, C.; Bharti, B.; Findenegg, G. H. Protein Immobilization in Surface-Functionalized SBA-15: Predicting the Uptake Capacity from the Pore Structure. *J. Phys. Chem. C* **2015**, *119* (5), 2438−2446.
(27) Katiyar, A.; Ji, L.; Smirniotis, P.; Pinto, N. G. Protein Adsorption on the Mesoporous Molecular Sieve Silicate SBA-15: Effects of PH and Pore Size. *J. Chromatogr. A* **2005**, *1069*, 119−126.
(28) Yin, X.; Li, B.; Liu, S.; Gu, Z.; Zhou, B.; Yang, Z. Effect of the surface curvature on amyloid-β peptide adsorption for graphene. *RSC Adv.* **2019**, *9* (18), 10094−10099.
(29) Harms, M.; Habib, M. M. W.; Nemska, S.; Nicolò, A.; Gilg, A.; Preising, N.; Sokkar, P.; Carmignani, S.; Raasholm, M.; Weidinger, G.; Kizilsavas, G.; Wagner, M.; Ständker, L.; Abadi, A. H.; Jumaa, H.; Kirchhoff, F.; Frossard, N.; Sanchez-Garcia, E.; Münch, J. An Optimized Derivative of an Endogenous CXCR4 Antagonist Prevents Atopic Dermatitis and Airway Inflammation. *Acta Pharm. Sin. B* **2021**, *11* (9), 2694−2708.
(30) Sheu, S.-Y.; Yang, D.-Y.; Selzle, H. L.; Schlag, E. W. Energetics of Hydrogen Bonds in Peptides. *Proc. Natl. Acad. Sci. U.S.A.* **2003**, *100* (22), 12683−12687.
(31) Moerz, S. T.; Huber, P. PH-Dependent Selective Protein Adsorption into Mesoporous Silica. *J. Phys. Chem. C* **2015**, *119* (48), 27072−27079.
(32) Velasco, M. I.; Franzoni, M. B.; Franceschini, E. A.; Gonzalez Solveyra, E.; Scherlis, D.; Acosta, R. H.; Soler-Illia, G. J. A. A. Water Confined in Mesoporous TiO2 Aerosols: Insights from NMR Experiments and Molecular Dynamics Simulations. *J. Phys. Chem. C* **2017**, *121* (13), 7533−7541.
(33) Andersson, J.; Rosenholm, J.; Areva, S.; Lindén, M. Influences of Material Characteristics on Ibuprofen Drug Loading and Release Profiles from Ordered Micro- and Mesoporous Silica Matrices. *Chem. Mater.* **2004**, *16* (21), 4160−4167.
(34) Kecht, J.; Schlossbauer, A.; Bein, T. Selective Functionalization of the Outer and Inner Surfaces in Mesoporous Silica Nanoparticles. *Chem. Mater.* **2008**, *20* (23), 7207−7214.
(35) Beitzinger, B.; Gerbl, F.; Vomhof, T.; Schmid, R.; Noschka, R.; Rodriguez, A.; Wiese, S.; Weidinger, G.; Ständker, L.; Walther, P.; Michaelis, J.; Lindén, M.; Stenger, S. Delivery by Dendritic Mesoporous Silica Nanoparticles Enhances the Antimicrobial Activity of a Napsin-Derived Peptide Against Intracellular Mycobacterium Tuberculosis. *Adv. Healthcare Mater.* **2021**, *10*, 2100453.
(36) Kalantari, M.; Yu, M.; Jambhrunkar, M.; Liu, Y.; Yang, Y.; Huang, X.; Yu, C. Designed Synthesis of Organosilica Nanoparticles for Enzymatic Biodiesel Production. *Mater. Chem. Front.* **2018**, *2* (7), 1334−1342.
(37) Rosenholm, J. M.; Meinander, A.; Peuhu, E.; Niemi, R.; Eriksson, J. E.; Sahlgren, C.; Lindén, M. Targeting of Porous Hybrid Silica Nanoparticles to Cancer Cells. *ACS Nano* **2009**, *3* (1), 197−206.
(38) Stöber, W.; Fink, A.; Bohn, E. Controlled Growth of Monodisperse Silica Spheres in the Micron Size Range. *J. Colloid Interface Sci.* **1968**, *26* (1), 62−69.
(39) Baumann, B.; Wittig, R.; Lindén, M. Mesoporous Silica Nanoparticles in Injectable Hydrogels: Factors Influencing Cellular Uptake and Viability. *Nanoscale* **2017**, *9* (34), 12379−12390.
(40) Lonardo, E.; Frias-Aldeguer, J.; Hermann, P. C.; Heeschen, C. Pancreatic Stellate Cells Form a Niche for Cancer Stem Cells and Promote Their Self-Renewal and Invasiveness. *Cell Cycle* **2012**, *11* (7), 1282−1290.

https://doi.org/10.1021/acs.langmuir.3c03513
Langmuir 2024, 40, 4294−4305

VII Supporting information to the publications

1. Publication I

Supplementary Information to the article

Surface functionalization affects the retention and biodistribution of orally administered mesoporous silica nanoparticles in a colitis mouse model.

Roman Schmid, Meta Volcic, Stephan Fischer, Zhi Qu, Holger Barth, Amirali Popat, Frank Kirchhoff, Mika Lindén

Scientific Reports, 2023, 13, 20175.

https://doi.org/10.1038/s41598-023-47445-6

Published by Springer Nature, Copyright © 2023.
This is an open access article under the CC BY 4.0 license
(https://creativecommons.org/licenses/by/4.0/).

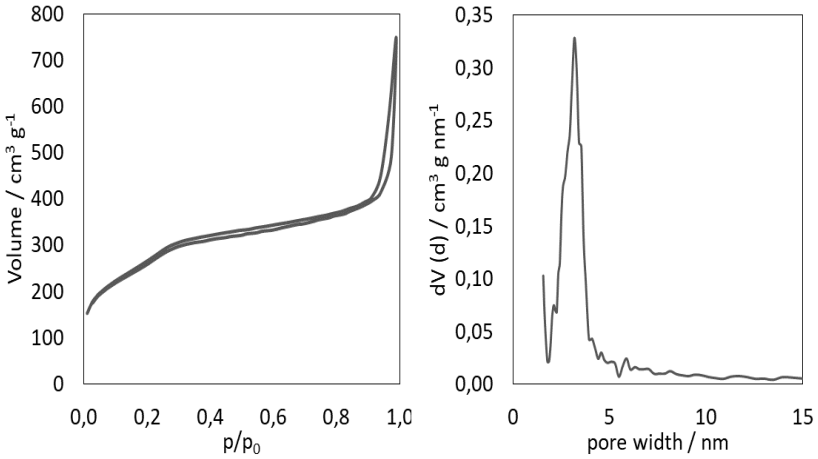

Figure S1. Nitrogen sorption isotherms of the calcined basic MSN-c (left) and corresponding pore size distributions calculated using the equilibrium NLDFT kernel developed for silica and a relative pressure range of p p_0^{-1} = 0.9 (right).

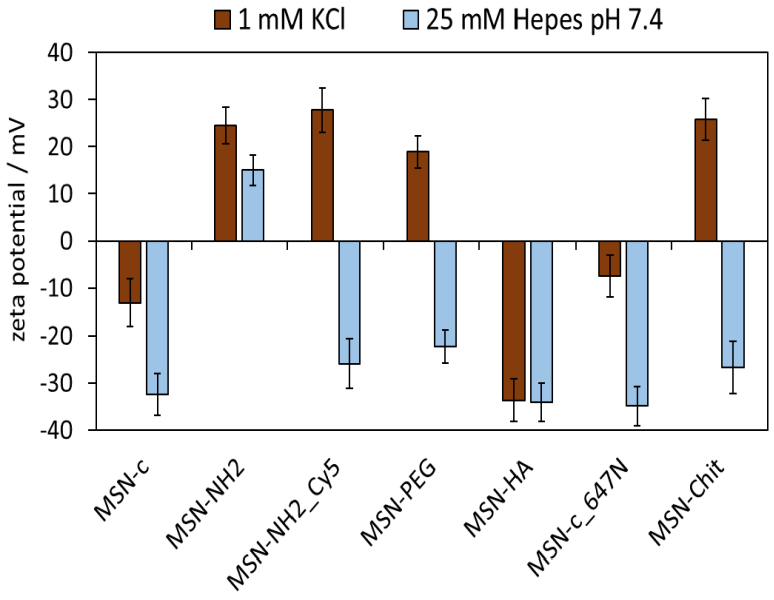

Figure S2. Zeta potential measurements of the synthesized particles at a concentration of 100 µg mL^{-1} in

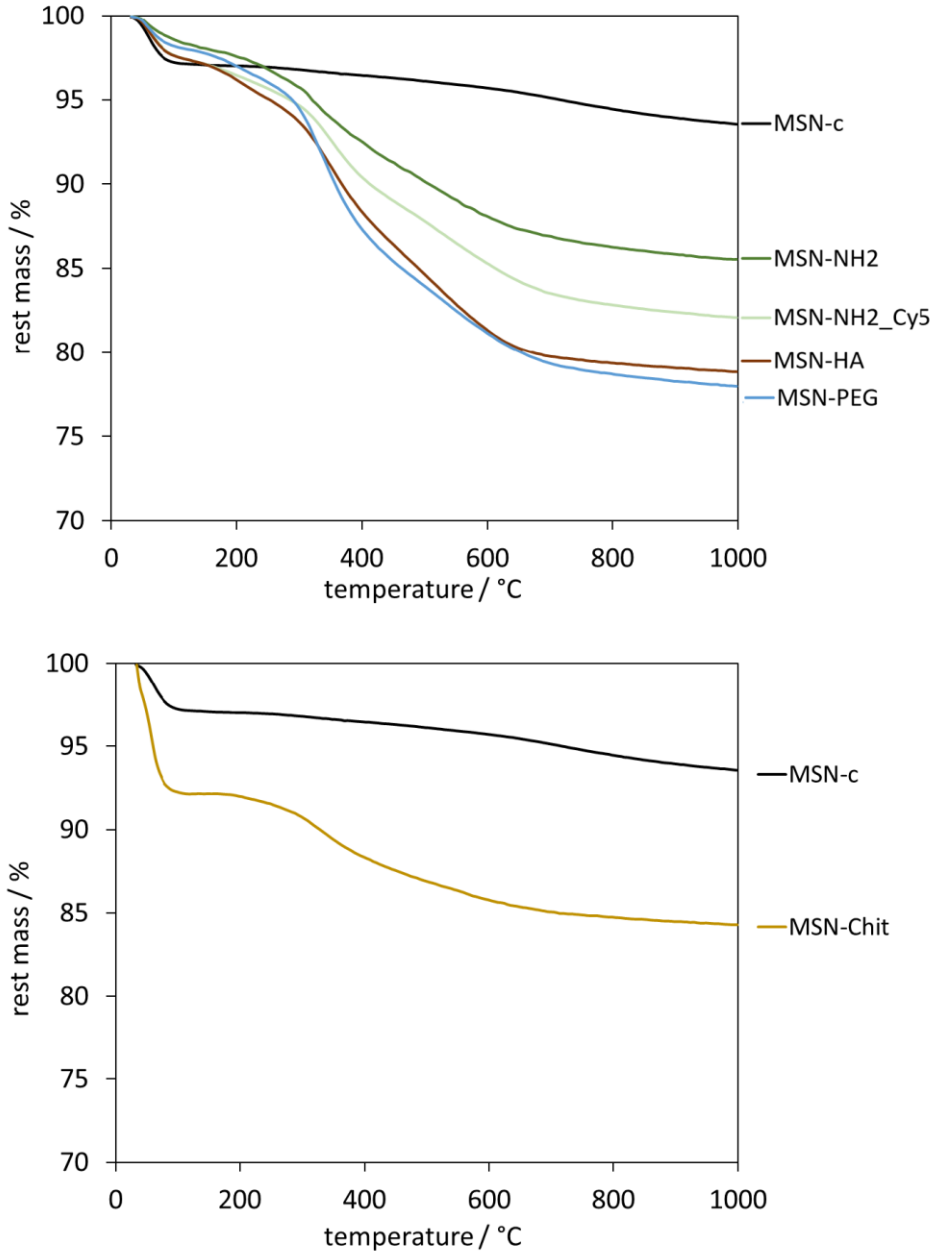

Figure S3. Thermogravimetric measurements of basic and functionalized MSNs.

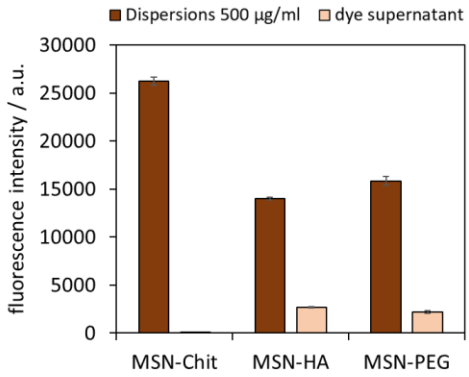

Figure S4. Fluorophore detachment from MSNs upon incubation under agitation in FaSSIF buffer for 14 h with a silica concentration of 500 µg mL^{-1} at 37°C is minor. Fluorescence intensities of supernatants were measured with an exitation and emission wavelength of 650 nm and 705 nm. Fluorescence intensities of the particle dispersions with a silica concentraton of 500 µg mL^{-1} prior incubation were measured as controls. (mean ± SD, n = 3)

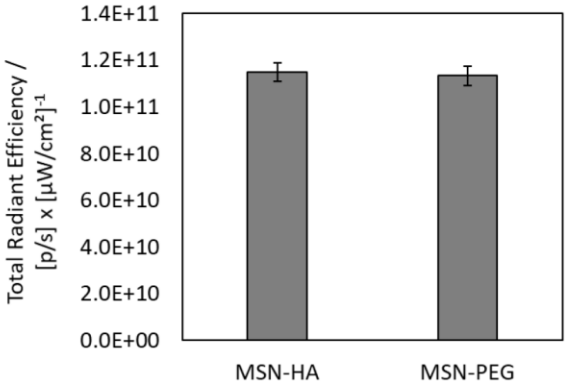

Figure S5. Total radiance efficiencies of particle dispersions at a concentration of 100 µg mL^{-1} measured via IVIS with an exitation and emission wavelength of 640 nm and 670 nm in a 96 well plates revealed no differences in fluorescence intensities. (mean ± SD, n = 3)

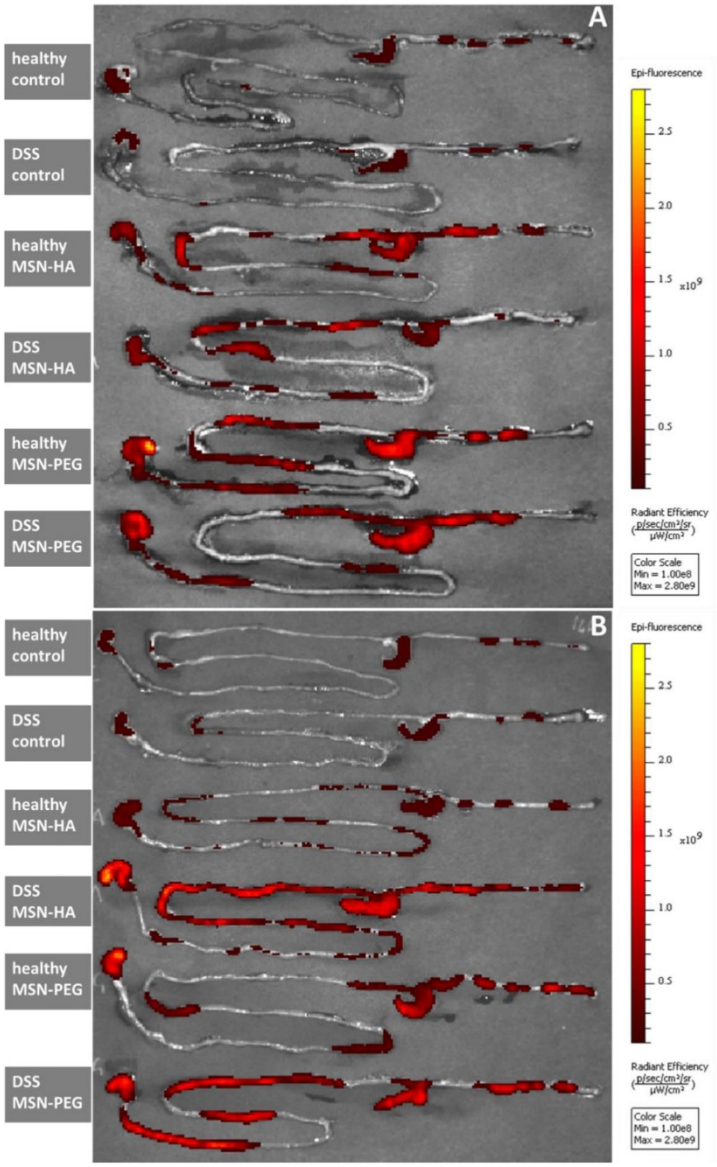

Figure S6. Exemplary fluorescence intensity measurements of excised GIT from mice measured via IVIS A) 6 h and B) 14 h after oral gavage of a single particle dose of 100 mg kg^{-1} (MSN-HA or MSN-PEG). Control animals received PBS only. Fluorescence intensities were measured with an excitation/emission wavelength of 640/670 nm. (n = 3)

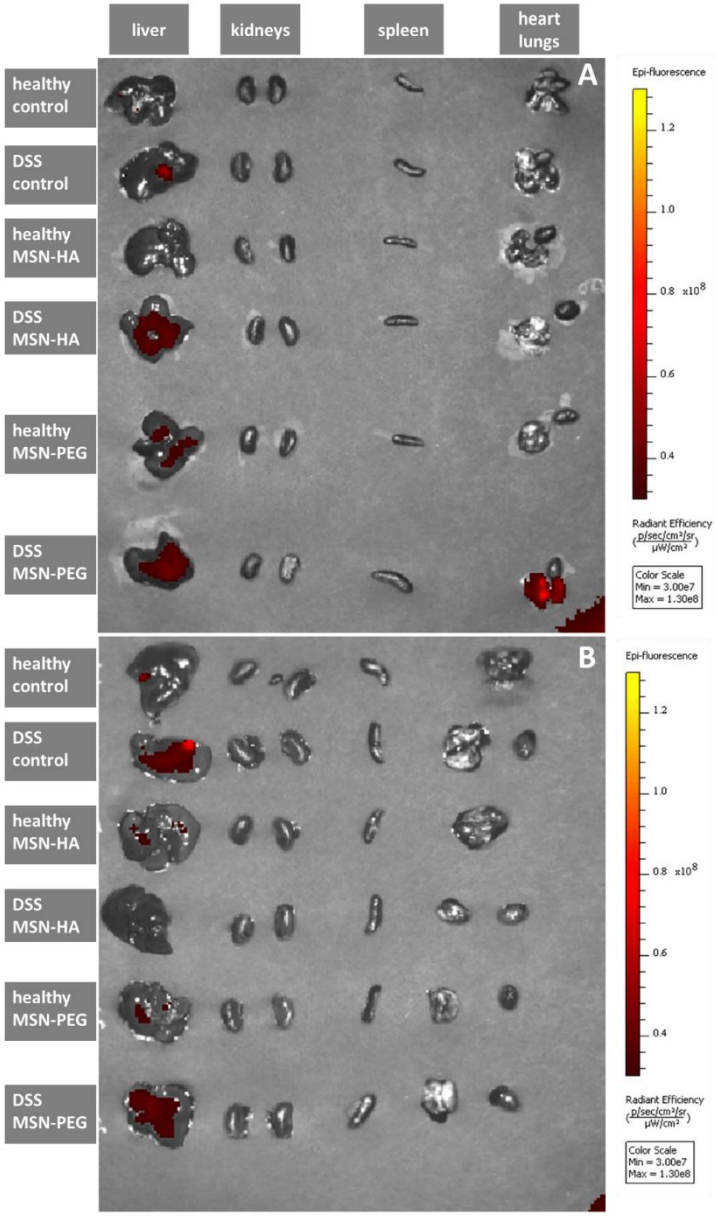

Figure S7. Exemplary fluorescence intensity measurements of excised organs from mice measured via IVIS A) 6 h and B) 14 h after oral gavage of a single particle dose of 100 mg kg^{-1} (MSN-HA or MSN-PEG). Control animals received PBS only. Fluorescence intensities were measured with an excitation/emission wavelength of 640/670 nm. (n = 3)

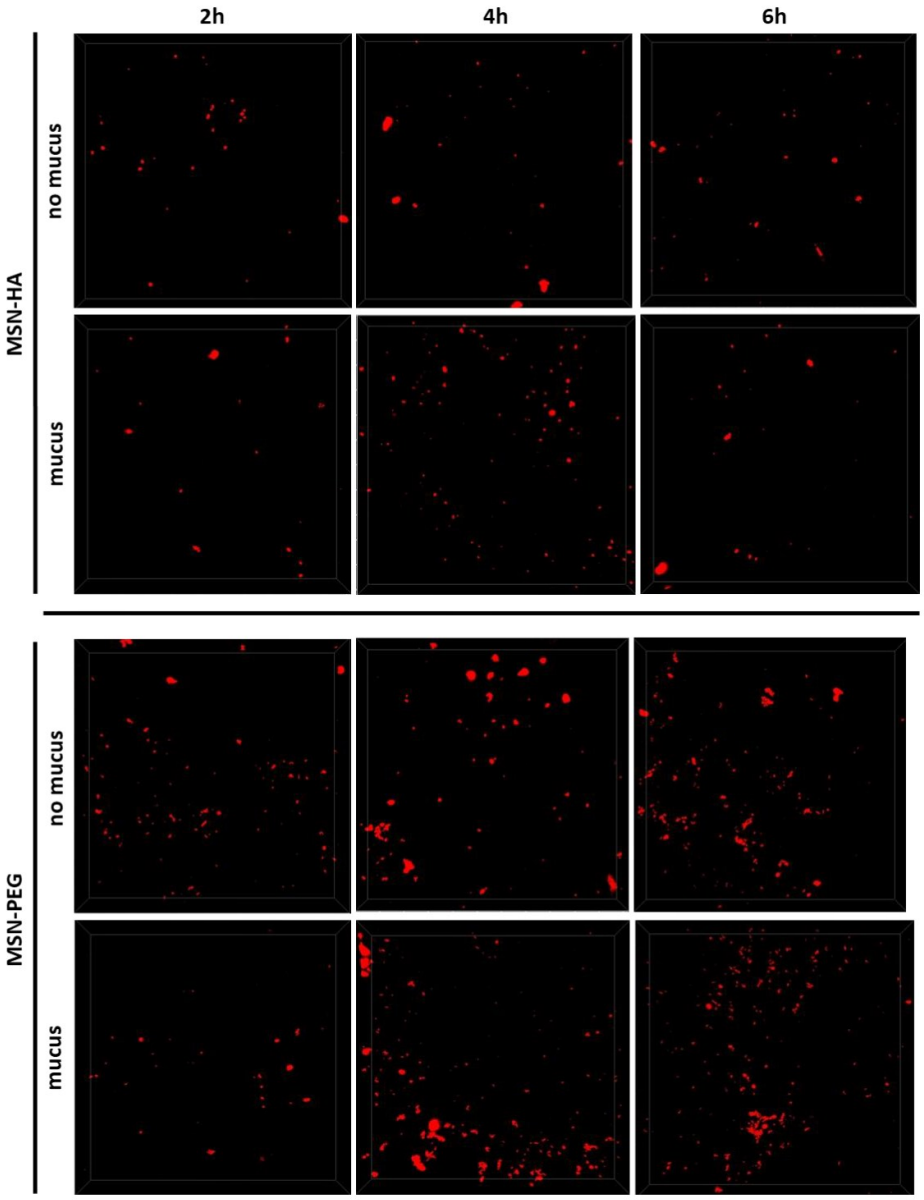

Figure S8. Representative confocal light scanning microscopy images of random areas of Caco-2/Raji ("no mucus") or Caco-2/HT28/Raji ("mucus") co-culture cell models after incubation with differently functionalized MSNs (red) at a concentration of 50 µg mL^{-1} for 2 h, 4 h and 6 h at 37°C (maximal intensity projections of on-top views of the epithelial cell model).

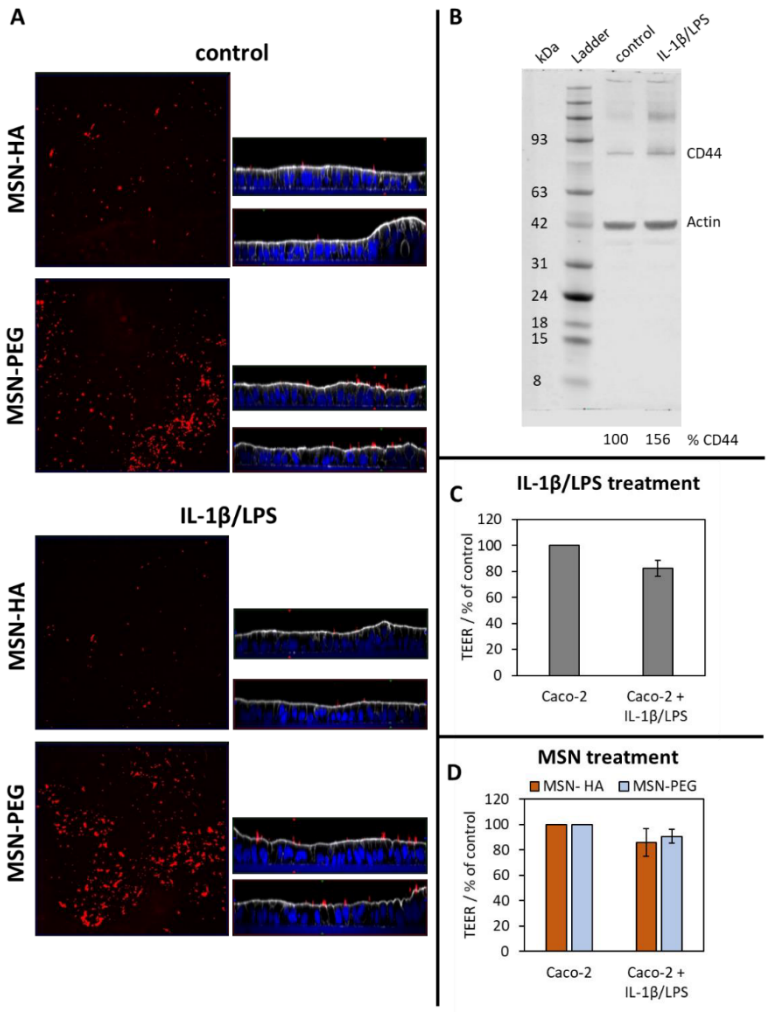

Figure S9. Caco-2/Raji co-cultures after treatment for 48 h at 37°C with ("IL-1β/LPS ") or without ("control") interleukin- 1β (IL-1β) and lipopolysaccharide (LPS) at a concentration of 50 ng mL^{-1} or 1000 ng mL^{-1}, respectively. Subsequently, cell models were incubated with differently functionalized MSNs at a concentration of 50 µg mL^{-1} for 14 h at 37°C. A) Representative confocal light scanning microscopy images of random areas. Left column: maximal intensity projection of on-top views of the epithelial cell model. Right column: channel overlay of cross-sectional x/z and y/z side views. MSNs (red), cell membrane (white), nuclei (blue). B) Verification of CD44 overexpression after treatment with IL-1β and LPS via Western Blot analysis (full-length membrane). Treated cultures exhibited a CD44 expression 156 % higher than non-treated cultures (control). For a full, non-cropped image of the plot, the reader is referred to Figure S13. C) TEER measurements of model epitheliums after treatment with IL-1β and LPS. D) TEER measurements of epithelial cell models after incubation with MSN-HA and MSN-PEG. (mean ± SD, n = 3)

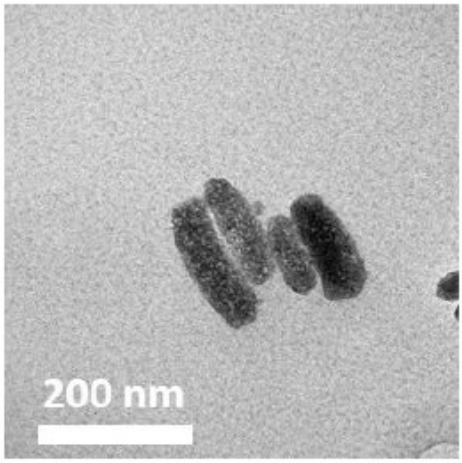

Figure S10. Transmission electron microscopy (200k magnification) of MSN-Chit after 14h incubation under agitation at 37 °C and a silica concentration of 500 µg mL^{-1} in FaSSIF buffer (pH 6.5).

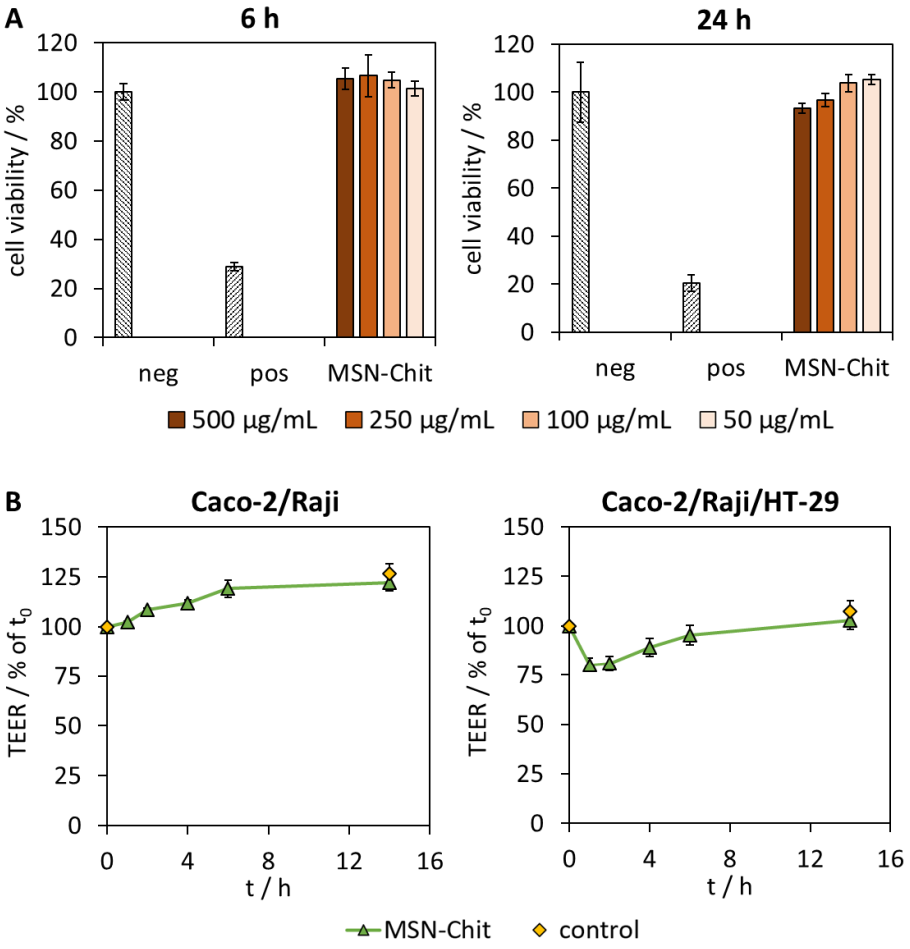

Figure S11. A) Cell viability of Caco-2 cells after incubation with MSN-Chit at varying concentrations for 6 h and 14 h as well as DMSO treated cells (pos) was measured with MTS-assay and was normalized on cells without treatment (neg). B) Measurement of the TEER of Caco-2 (left) and Caco-2/HT29 (right) epithelial cell models upon incubation with differently functionalized MSNs at a concentration of 50 µg mL^{-1}. TEER values were measured at distinct times and calculated as percentage of TEER before the addition of particles. (mean ± SD, n = 3)

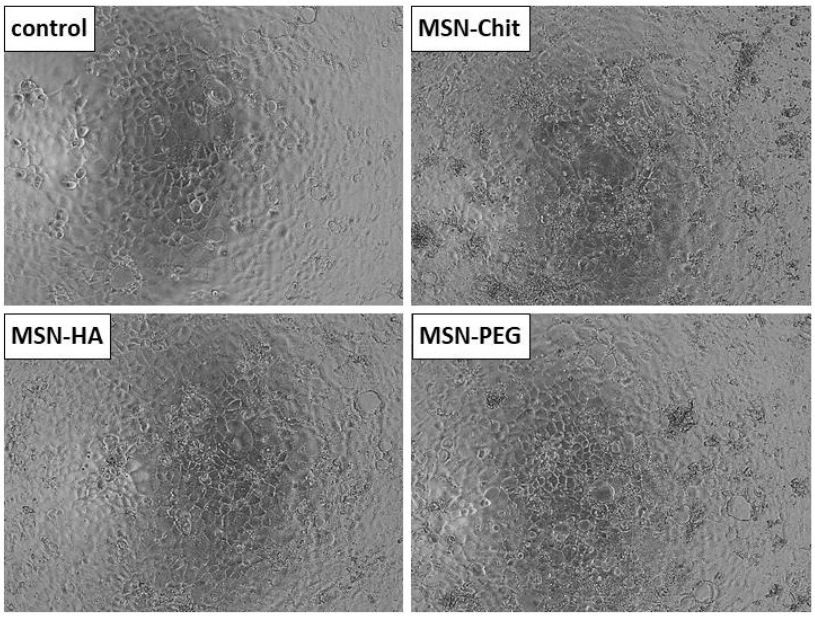

Figure S12. Representative light microscopy images of Caco-2 cells upon exposure of MSN-Chit, MSN-HA and MSN-PEG at a concentration of 500 µg mL^{-1} at 37°C for 24 h.

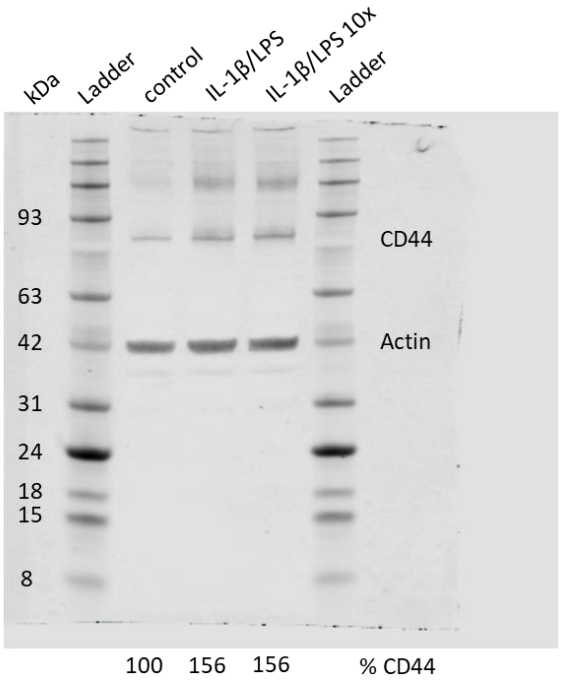

Figure S13. Full, non-cropped image of the Western Blot analysis from Figure S9. CD44 overexpression on Caco-2/Raji co-cultures was induced by treatment with ("IL-1β/LPS") or without ("control") interleukin-1β (IL-1β) and lipopolysaccharide (LPS) for 48 h at 37°C. IL-1β and LPS were applied at a concentration of 50 ng x ml^{-1} and 1000 ng x ml^{-1}, respectively, and at a concentration increased by a factor of 10, i.e. 500 ng x ml^{-1} for IL-1β and 10000 ng x ml^{-1} for LPS ("IL-1β/LPS 10x"). However, no increase in CD44 expression was observed for the increased concentrations, which is why these cell cultures were omitted in the following experiments.

2. Publication II

Supplementary Information to the article

Towards a simple in vitro surface chemistry pre-screening method for nanoparticles to be used for drug delivery to solid tumours.

Roman Schmid, Juliane Kaiser, Ramona Willbold, Nomousa Walther, Rainer Wittig, Mika Lindén

Biomaterials Science, 2023,11, 6287-6298.
https://doi.org/10.1039/D3BM00966A

Published by Royal Society of Chemistry, Copyright © 2023.
This is an open access article under the CC BY-NC 3.0 license
(https://creativecommons.org/licenses/by-nc/3.0/).

Electronic Supplementary Material (ESI) for Biomaterials Science.
This journal is © The Royal Society of Chemistry 2023

Supporting Information

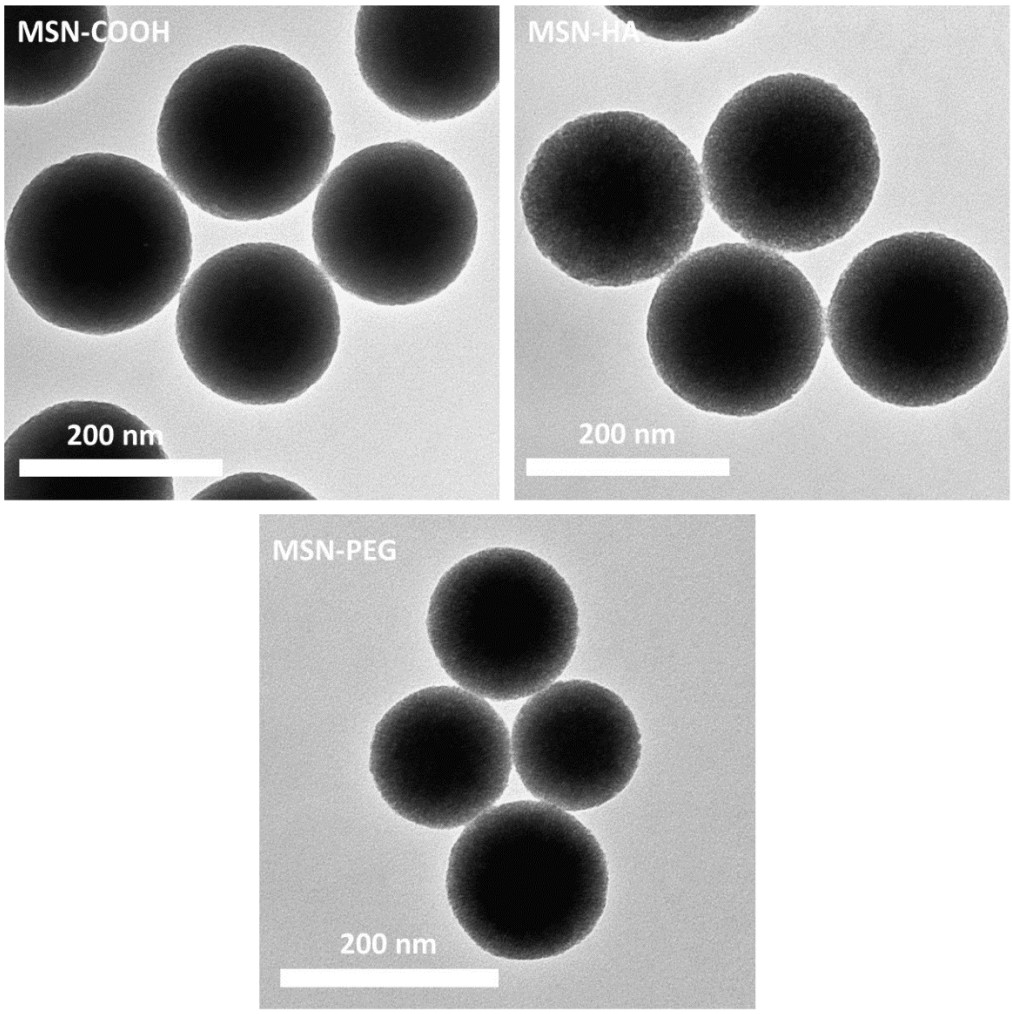

Figure S1. Exemplary transmission electron microscopy image of MSN-COOH, MSN-PEG and MSN-HA particles.

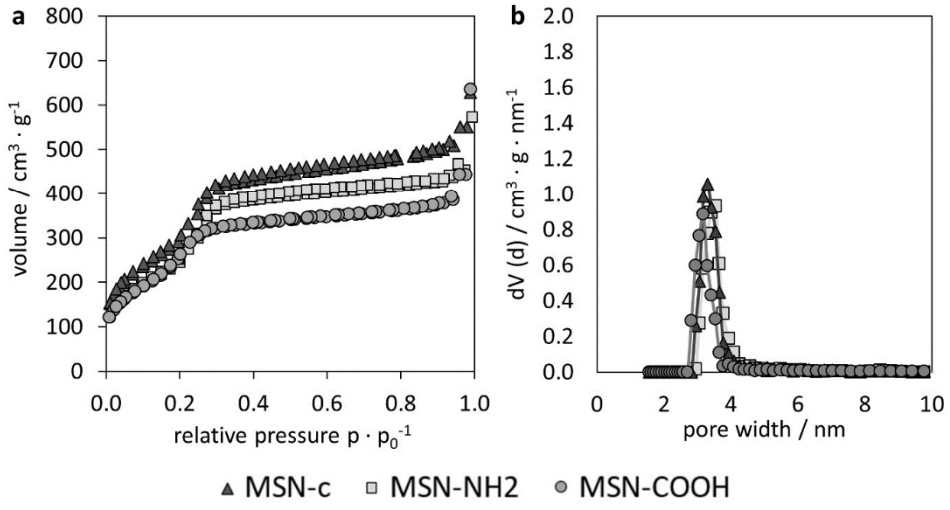

Figure S2. a) Nitrogen sorption isotherms of the basic particles MSN-NH_2, MSN-COOH and calcined MSN-c. b) Corresponding pore size distributions calculated using the equilibrium NLDFT kernel developed for silica.

Table S1. Data from the nitrogen sorption measurements of MSN-COOH, MSN-NH_2 and the basic calcined MSNc

	specific surface area / $m^2 \cdot g^{-1}$	pore volume / $cm^3 \cdot g^{-1}$	pore diameter/ nm
MSN-c	1048	0.74	3.3
MSN-NH_2	869	0.64	3.5
MSN-COOH	842	0.55	3.2

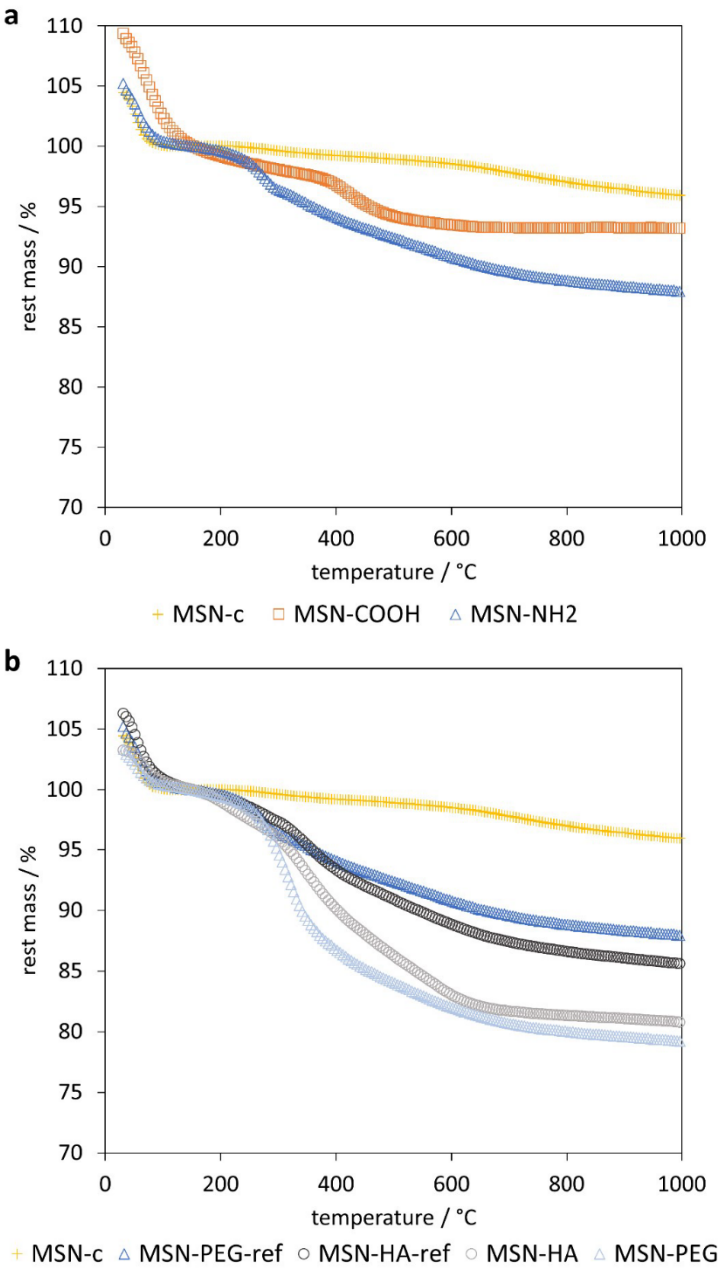

Figure S3. Exemplary thermogravimetric measurements of calcined MSN-c, MSN-COOH, MSN-NH2, MSN-HA and MSN-PEG. For the quantification of grafted polymer, the native particles were incubated in the respective solvent without HA or PEG to account for hydrolysis-related mass losses ('ref').

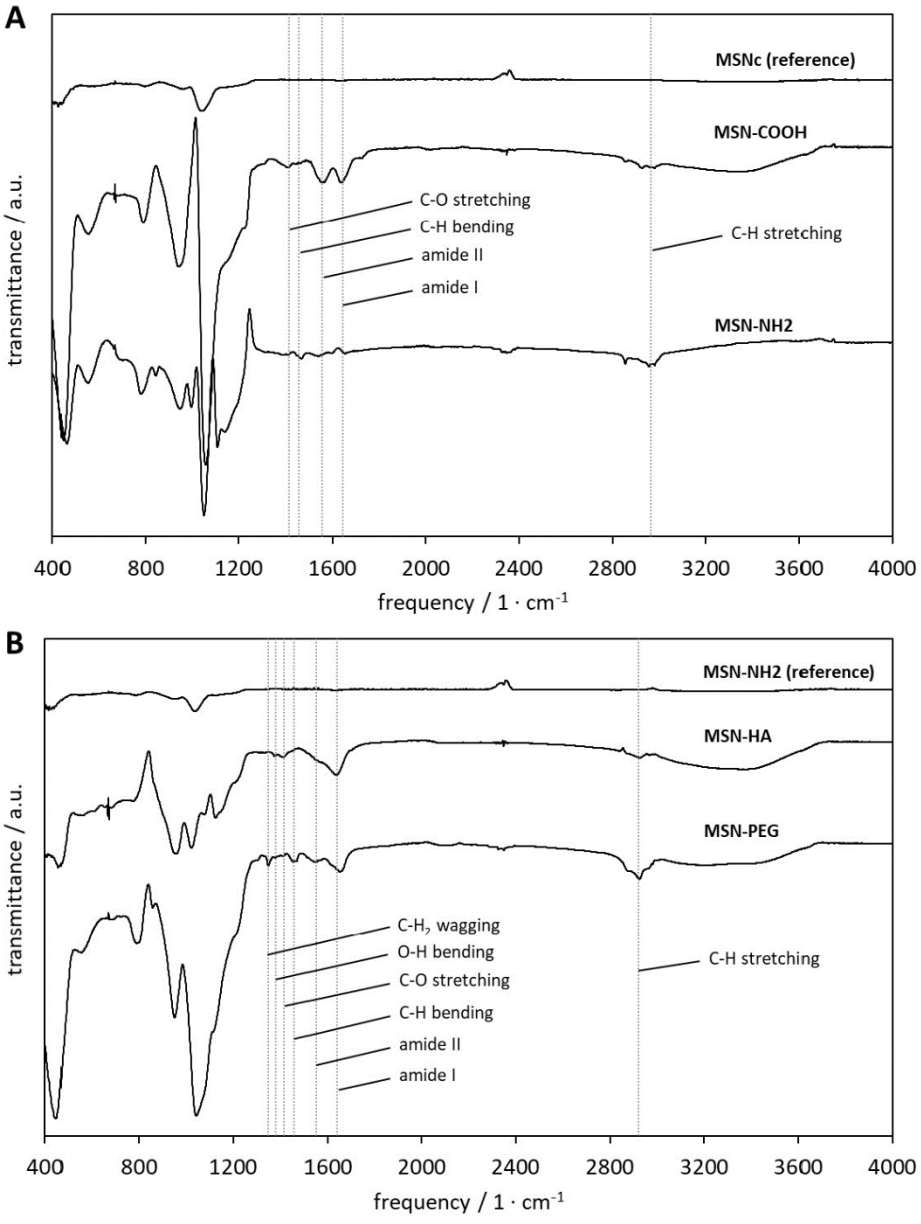

Figure S4. Exemplary ATR-IR spectroscopic analysis of different MSN types used in this study. A) IR spectra of MSN-COOH and MSN-NH2; IR spectrum of non-functionalized, calcined MSN-c particle was subtracted as background spectrum. B) IR spectra of MSN-HA and MSN-PEG; IR spectrum of the basic amino-functionalized MSN-NH2 particle was subtracted as background spectrum. Bands in the spectra of MSNs assignable to the various functional groups are highlighted in the figure (dashed lines). (doi.org/10.1002/bip.10245, doi.org/10.1016/0008-6215(94)00147-2, doi.org/10.3390/ijms13066639)

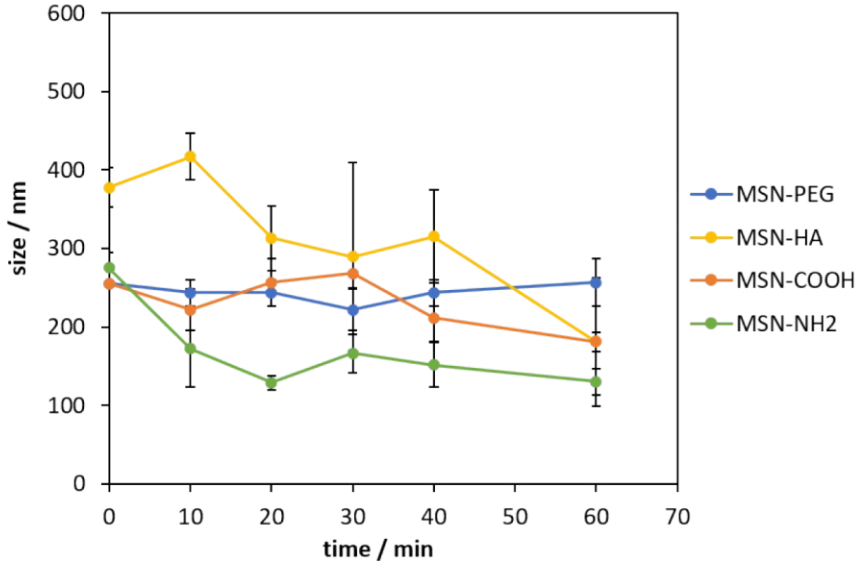

Figure S5. Mean hydrodynamic diameter measured by light-scattering as a function of incubation time in 10% FCS at a particle concentration of 10 μg/mL.

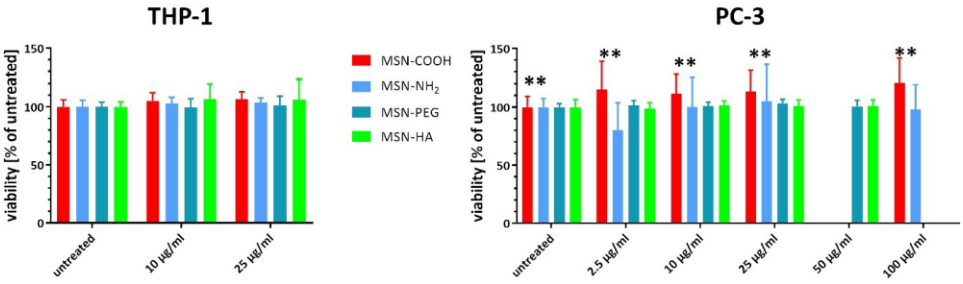

Figure S6. Cell populations were incubated with nanoparticles at indicated amounts for 24 h prior to cell viability testing using the Cell Titer Blue assay. The graph shows mean viability ± standard deviation (SD) as percentages of the untreated control, respectively. Three to four independent experiments were performed in triplicates (N = 9-12). Asterisks denote experiments which were carried out with parental, not genetically engineered PC-3 cells (please see methods section for details).

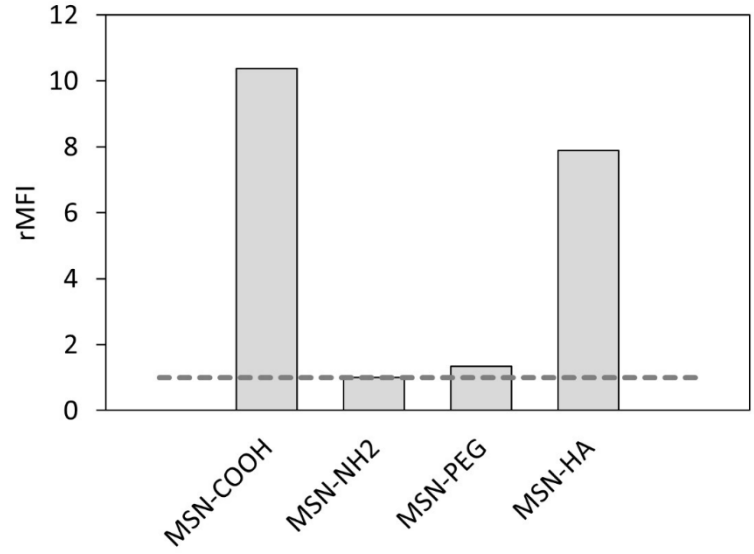

Figure S7. Mean fluorescence intensities (MFIs) of ATTO647N-labelled MSNs were measured in aqueous sucrose solution (10 %) at a particle concentration of 100 µg ml^{-1}. The respective MFIs were normalized on the MFI of MSN-NH_2 resulting in rated MFIs (rMFIs) to compensate for differences in particle fluorescence intensities. The dashed line indicates a rMFI of 1.

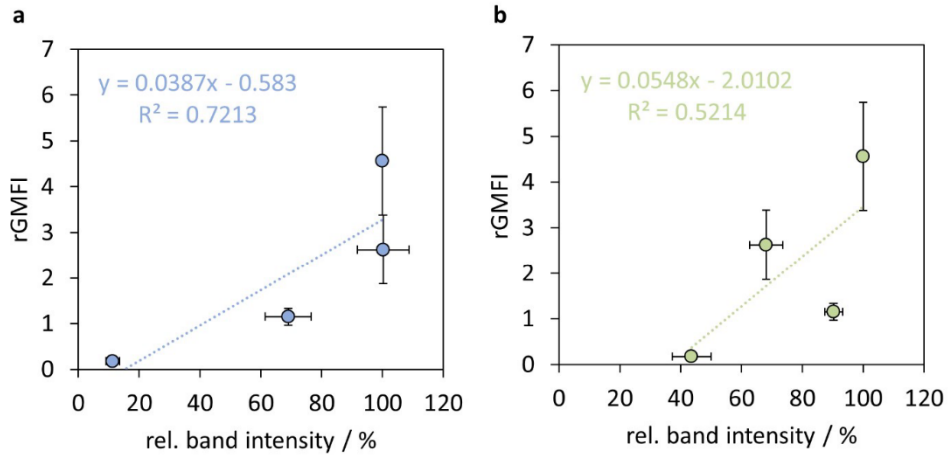

Figure S8. rGMFIs of THP-1 cells measured via flow cytometry after treatment with ATTO647-labelled MSNs at 10 µg mL^{-1} for 24 h and 37°C as a function of relative band intensity for the a) high molecular weight proteins and b) low molecular weight proteins (n = 3, error bars are SD).

3. Publication III

Supplementary Information to the article

Straightforward adsorption-based formulation of mesoporous silica nanoparticles for drug delivery applications.

Roman Schmid*, Nathalie Neffgen*, Mika Lindén
(*equal contribution)

Journal of Colloid Interface and Science, 2023, 640, 961-974.

https://doi.org/10.1016/j.jcis.2023.03.012

Published by Elsevier, Copyright © 2023.
This is an open access article under the CC BY NC 4.0 license
(https://creativecommons.org/licenses/by-nc/4.0/).

Supporting Information

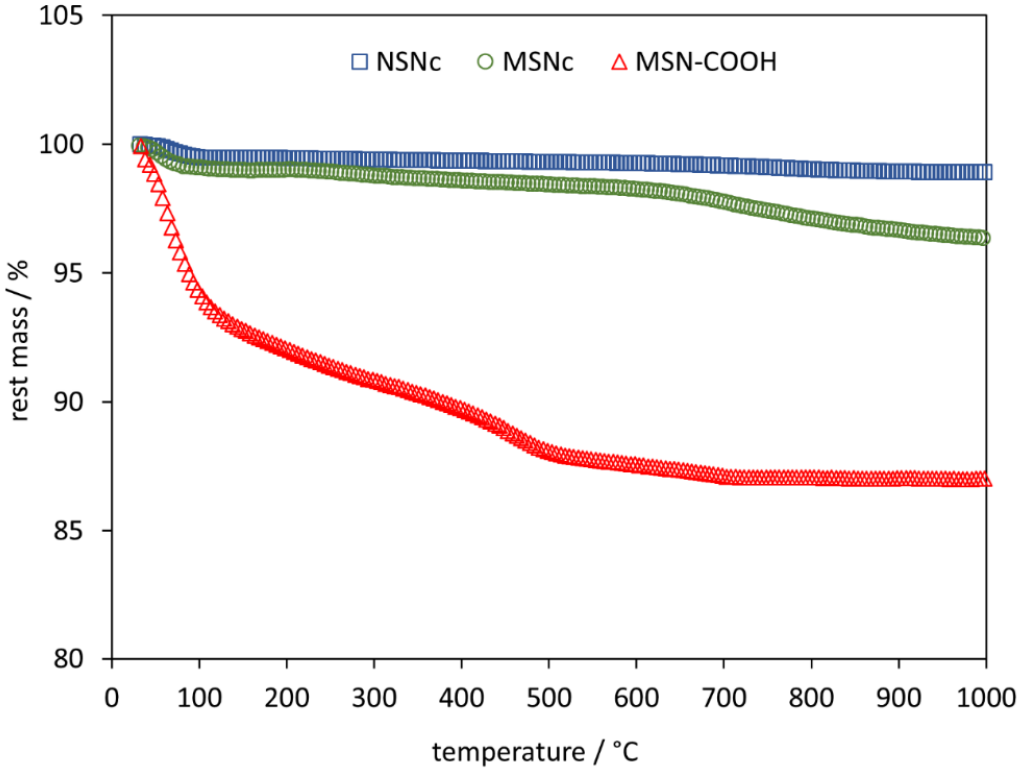

Figure S1. Exemplary thermogravimetric measurements of the native particles used in this study.

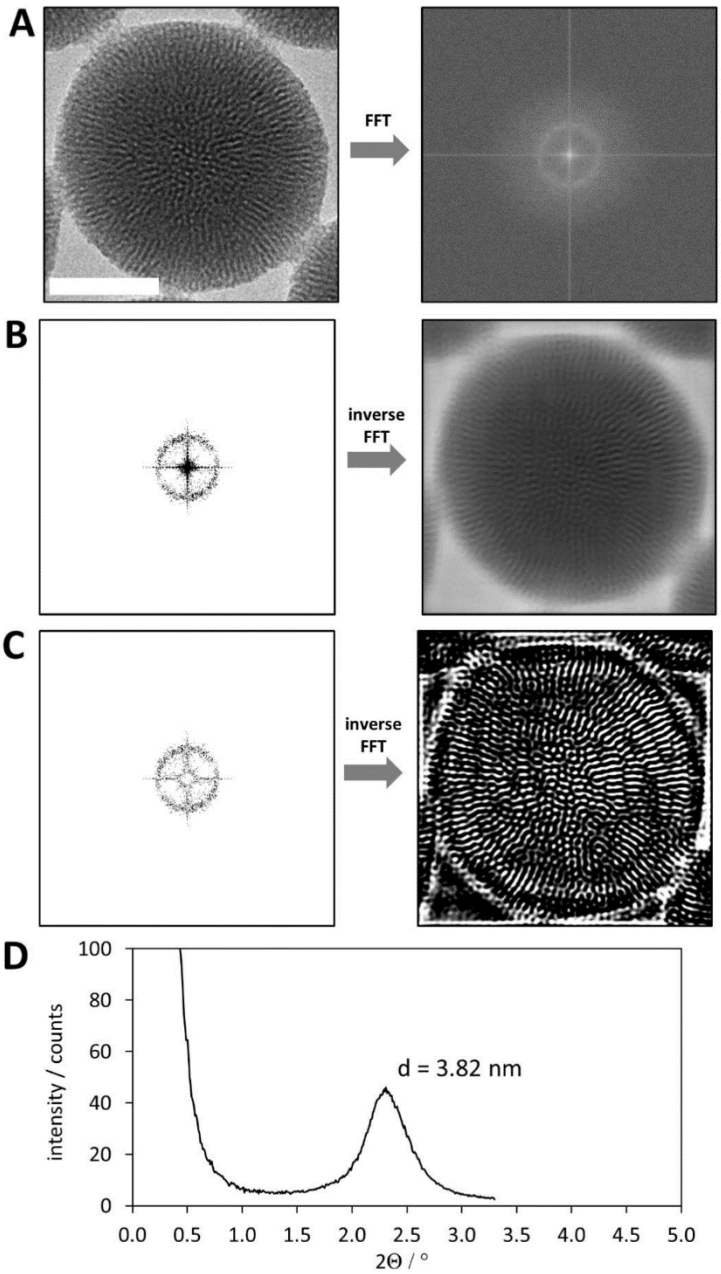

Figure S2. Examination of the porous structure of MSNc. A) representative TEM image of MSNc (scale bar: 50 nm) and fast Fourier transformation (FFT) thereof. B) and C) filtering of different frequency ranges in the diffraction pattern and subsequent inverse FFT reveal the electron diffracting structures of the particles. D) small-angle x-ray scattering (SAXS) measurement of MSNc. Calculated d-spacing at the first order maximum is indicated in the diffractogram.

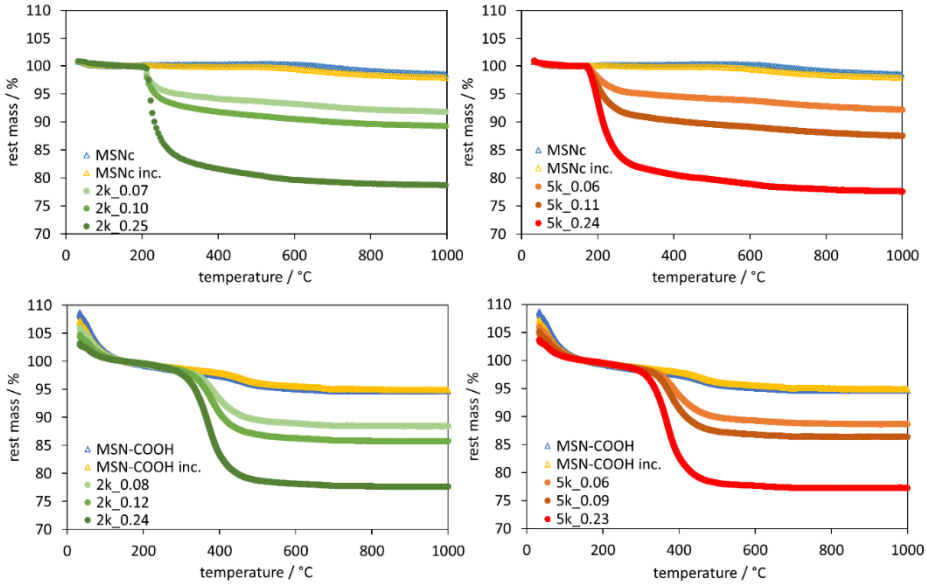

Figure S3. Exemplary thermogravimetric measurements of MSNc and MSN-COOH PEGylated with PEG_{2k} or PEG_{5k} in DCM. For the quantification of PEG, the native particles were incubated in the respective solvent without PEG to address hydrolysis-related mass losses ('inc.'). The calculated PEG masses are indicated in the figure as mg m^{-2}.

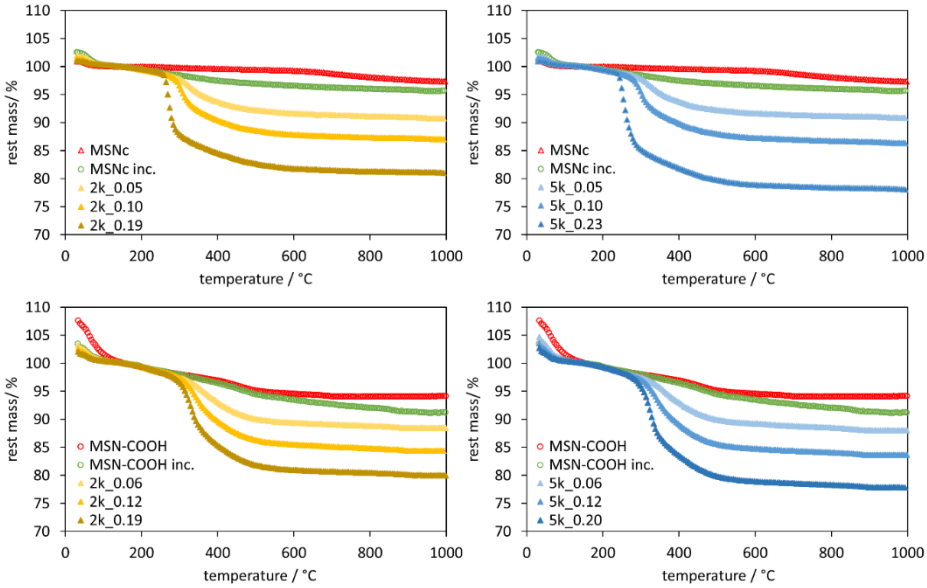

Figure S4. Exemplary thermogravimetric measurements of MSNc and MSN-COOH PEGylated with PEG_{2k} or PEG_{5k} in water. For the quantification of PEG, the native particles were incubated in the respective solvent without PEG to address hydrolysis-related mass losses ('inc.'). The calculated PEG masses are indicated in the figure as mg m^{-2}.

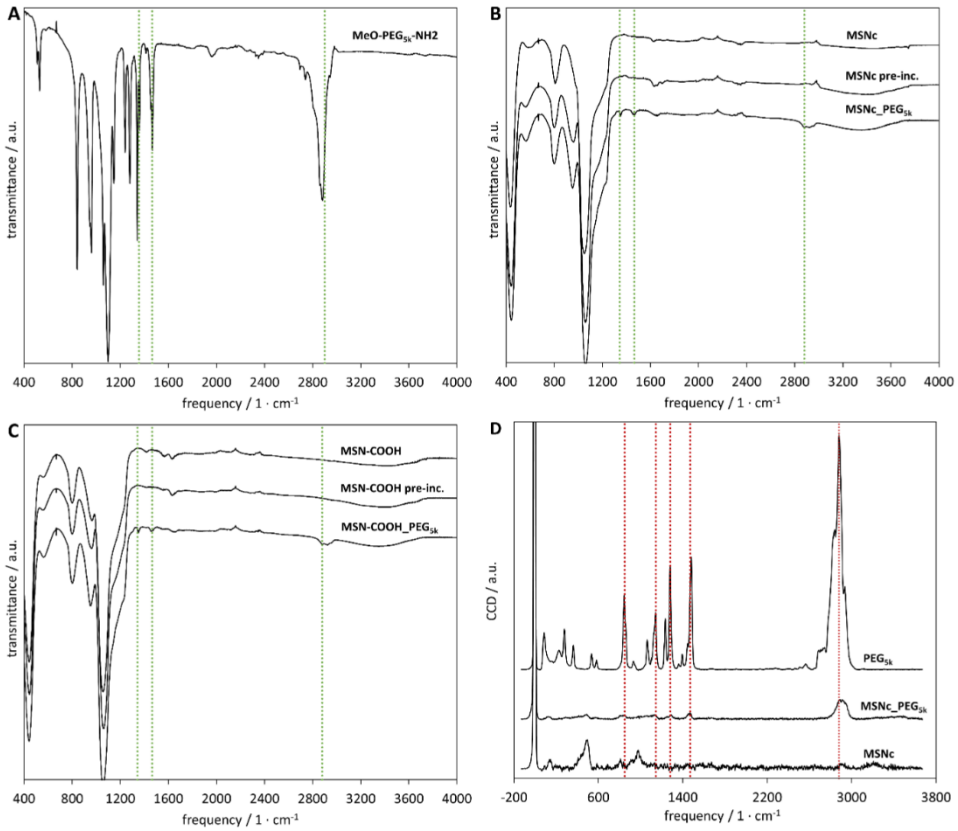

Figure S5. Exemplary spectroscopic analysis of PEG_{5k} used in this study as well as of MSNc and MSN-COOH PEGylated with the maximum amount of PEG_{5k} in water and of particles pre-incubated ("pre-inc.") for 2 h in water. A-C) ATR-IR spectra, D) Raman spectra. Bands in the spectra of MSNs assignable to PEG are highlighted in the figure (dashed lines).

Table S1. Total (BET) and outer surface areas (t-plot) of the native particles. Total PEG masses (mean ± SD, n = 3) and outer portions, chain densities and conformations of PEG_{2k} and PEG_{5k} adsorbed onto non-porous NSNc and porous MSNc and MSN-COOH were surface normalized as indicated. Calculations for NSNc PEGylated in water are based on the data range given by both PEG_{5k}/PEG_{2k} mass ratios of the third (= 2.13) and fourth (= 1.42) isotherm point. Further calculations for MSNc and MSN-COOH PEGylated in water are based on the mean mass ratio (= 1.77 ± 0.35).

	NSNc @water		**MSNc @water**		**MSN-COOH @water**	
	PEG_{2k}	**PEG_{5k}**	**PEG_{2k}**	**PEG_{5k}**	**PEG_{2k}**	**PEG_{5k}**
total PEG mass (BET) / mg · m^{-2}	0.37 ± 0.071 - 0.58 ± 0.200	0.78 ± 0.152 - 0.82 ± 0.268	0.19 ± 0.004	0.23 ± 0.004	0.19 ± 0.001	0.20 ± 0.002
outer PEG portion / %	100		23 ± 13	35 ± 11	7 ± 4	12 ± 4
chain density (t-plot) / 1 · nm^{-2}	0.11 ± 0.021 - 0.18 ± 0.062	0.09 ± 0.017 - 0.09 ± 0.029	0.18 ± 0.105	0.11 ± 0.037	0.04 ± 0.025	0.03 ± 0.009
distance S (t-plot) / nm	3.4 ± 0.37 - 2.7 ± 0.59	3.9 ± 0.43 - 3.8 ± 0.67	2.7 ± 0.63	3.3 ± 0.47	5.5 ± 1.29	6.9 ± 0.96
$S/2R_f$ (t-plot)	0.63 ± 0.069 - 0.50 ± 0.111	0.39 ± 0.043 - 0.38 ± 0.066	0.50 ± 0.117	0.33 ± 0.047	1.02 ± 0.241	0.69 ± 0.096

Table S1. (continued).

	NSNc @DCM		MSNc @DCM		MSN-COOH @DCM	
	PEG_{2k}	PEG_{5k}	PEG_{2k}	PEG_{5k}	PEG_{2k}	PEG_{5k}
total PEG mass (BET) / mg · m^{-2}	0.26 ± 0.03	0.28 ± 0.01	0.30 ± 0.001	0.28 ± 0.01	0.26 ± 0.002	0.25 ± 0.003
outer PEG portion / %	100		8 ± 0.7	8 ± 0.4	11 ± 1	11 ± 0.4
chain density (t-plot) / 1 · nm^{-2}	0.08 ± 0.009	0.03 ± 0.001	0.08 ± 0.007	0.03 ± 0.002	0.08 ± 0.007	0.03 ± 0.001

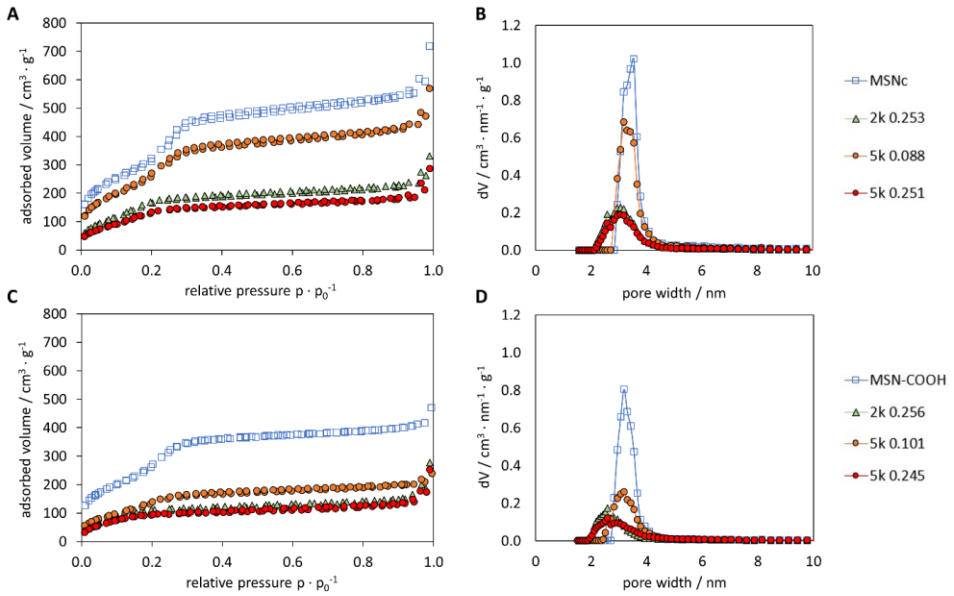

Figure S6. Nitrogen sorption isotherms of the non-PEGylated and PEGylated MSNs in DCM at indicated PEGylation levels (mg m^{-2} BET surface) of A) MSN-c, and C) MSN-COOH. Corresponding pore size distributions calculated using the equilibrium NLDFT kernel developed for silica are shown in B) and D).

Table S2. Data from the nitrogen sorption of MSNc and MSN-COOH particles PEGylated from DCM. The mass corrected pore volumes were calculated by reduction of the PEG portion of the total sample mass (mean ± SD, N = 3).

	PEG / mg · m^{-2}	pore volume / cm^3 · g^{-1}	corrected pore volume / cm^3 · g^{-1}	pore diameter/ nm
MSNc	-	0.80 ± 0.040	-	3.5
2kads@DCM	0.25	0.31 ± 0.006	0.40 ± 0.007	2.9
5kads@DCM	0.09	0.57 ± 0.008	0.63 ± 0.009	3.2
	0.25	0.33 ± 0.010	0.42 ± 0.012	3.1
MSN-COOH	-	0.58 ± 0.039	-	3.2
2kads@DCM	0.26	0.22 ± 0.008	0.27 ± 0.010	2.6
5kads@DCM	0.10	0.38 ± 0.003	0.41 ± 0.003	3.2
	0.25	0.20 ± 0.005	0.25 ± 0.007	2.6

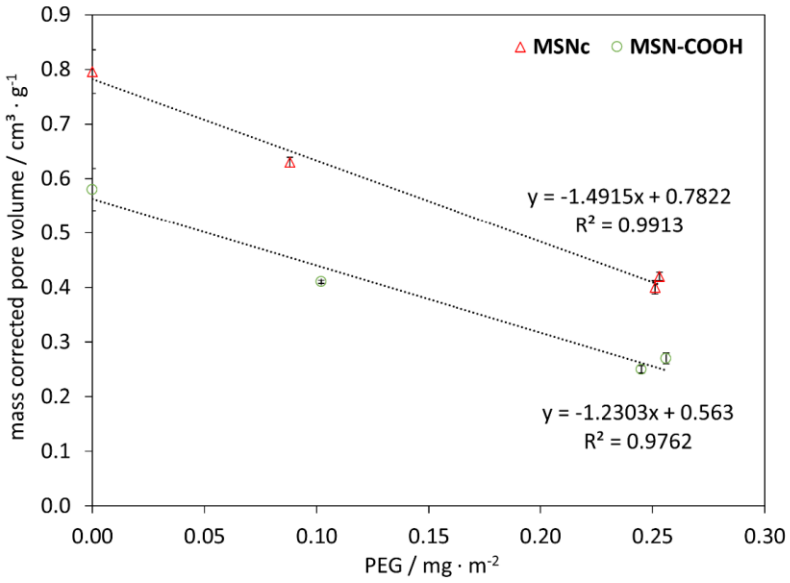

Figure S7. Mass-corrected pore volume as a function of the PEG loading degree for MSNc and MSN-COOH PEGylated in DCM. The pore volume values have been corrected for the PEG portion of the sample mass. The slope of the curve is very similar for the MSNc and the MSN-COOH particles, suggesting a similar PEG distribution inside/outside for both particles (mean ± SD, N = 3).

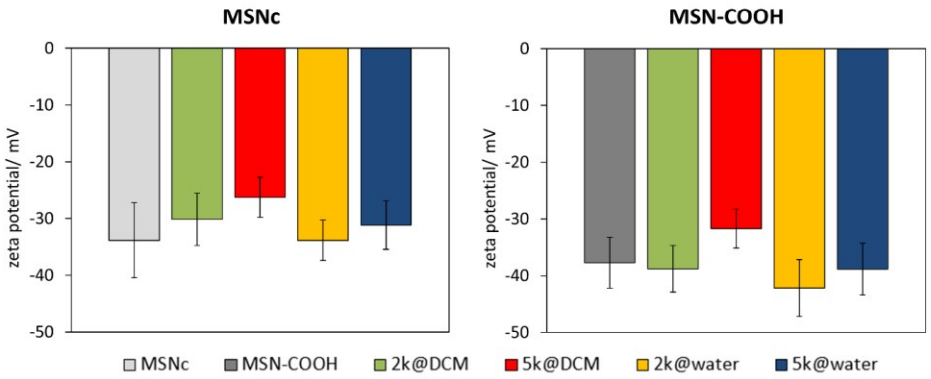

Figure S8. Zeta potentials of MSNc (left), MSN-COOH (right) and the respective particles PEGylated in water and DCM with PEG masses representing the isotherm plateau. Zeta potentials were measured in 25 mM HEPES buffer at a concentration of 0.1 mg mL^{-1} (mean ± SD, n = 3).

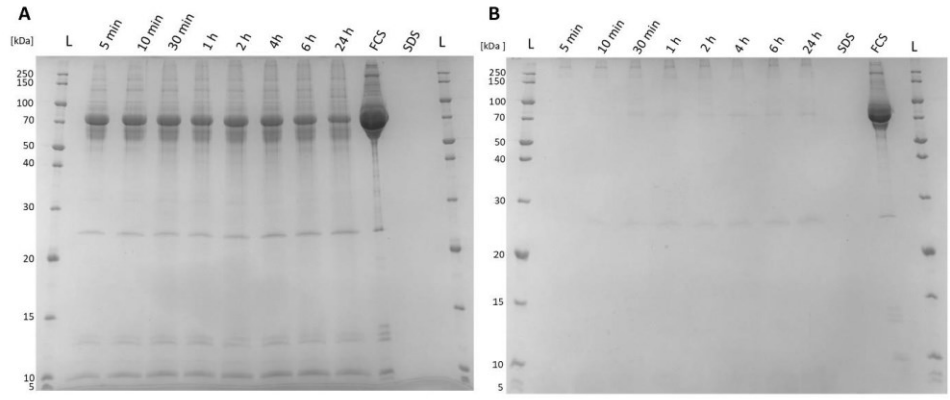

Figure S9. SDS-PAGE supernatants isolated as a function of particle incubation time. A) MSNc, and B) PEG_{5k}@MSNc with a PEG loading of 0.22 mg m^{-2}. The particles were incubated with 10 % FCS in PBS for 24 h at 37°C and a particle concentration of 5 mg mL^{-1}.

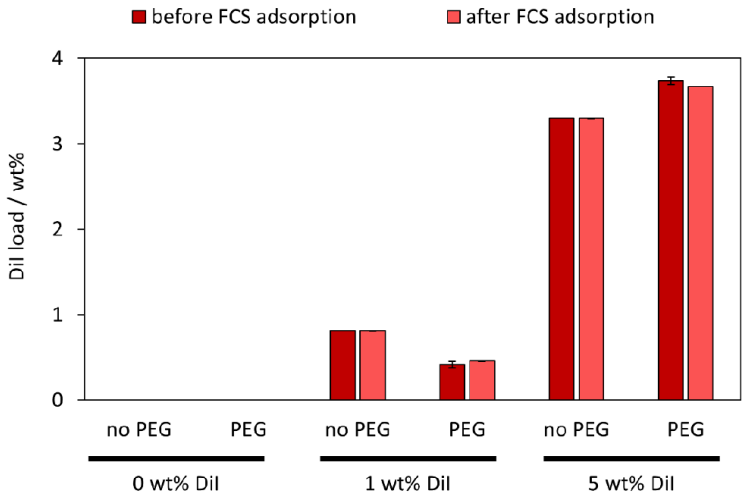

Figure S10. Dil loading degrees on non-PEGylated and PEGylated MSNc after 24 h of incubation with 10 % FCS in PBS at a temperature of 37°C (mean ± SD, n = 3).

4. Publication IV

Supplementary Information to the article

Confinement and polarity effects on the peptide packing density on mesoporous silica nanoparticles.

Bastian Beitzinger*, Roman Schmid*, Christoph Jung, Kanishka Tiwary, Patrick Hermann, Timo Jacob, Mika Lindén

(*equal contribution)

Langmuir 2024, 40, 8, 4294–4305.
https://doi.org/10.1021/acs.langmuir.3c03513

Copyright © 2024 The Authors. Published by American Chemical Society.
This is an open access article under the CC BY 4.0 license
(https://creativecommons.org/licenses/by/4.0/).

Supporting Information

Confinement and polarity effects on the peptide packing density on mesoporous silica nanoparticles

Bastian Beitzinger,[1,#] Roman Schmid,[1,#] Christoph Jung,[2] Kanishka Tiwary,[3] Patrick Hermann,[3] Timo Jacob,[2] and Mika Lindén[1,*]

[1] Institute of Inorganic Chemistry II, Ulm University, Albert-Einstein-Allee 11, 89081 Ulm, Germany

[2] Institute of Electrochemistry, Ulm University, Albert-Einstein-Allee 47, 89081 Ulm, Germany

[3] Department of Internal Medicine I, Albert-Einstein-Allee 23, Ulm University, 89070 Ulm, Germany

[#] These authors contributed equally

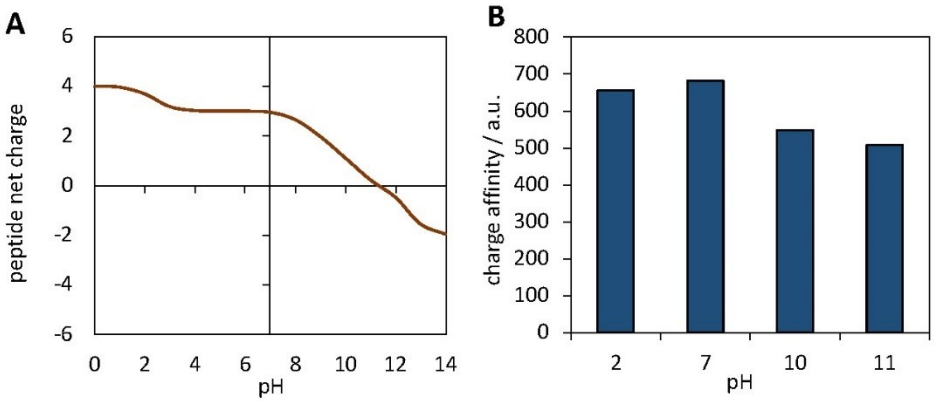

Figure S1. Calculation of peptide properties. A) The net charge of JM#21 is dependent on pH value (data based on peptide calculator tool on www.biosynth.com). B) Charge affinity of the peptide was calculated by scanning with a negatively charged hydroxide probe at varying pH-dependent peptide net charges.

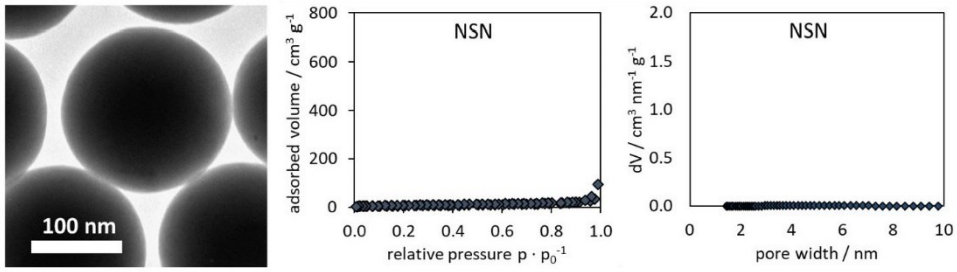

Figure S2. Transmission electron microscopy and nitrogen sorption measurements at 77K of non-porous NSN particle. Pore-size distribution curves were calculated using the equilibrium NLDFT kernel developed for silica in the relative pressure range from 0 to 0.9.

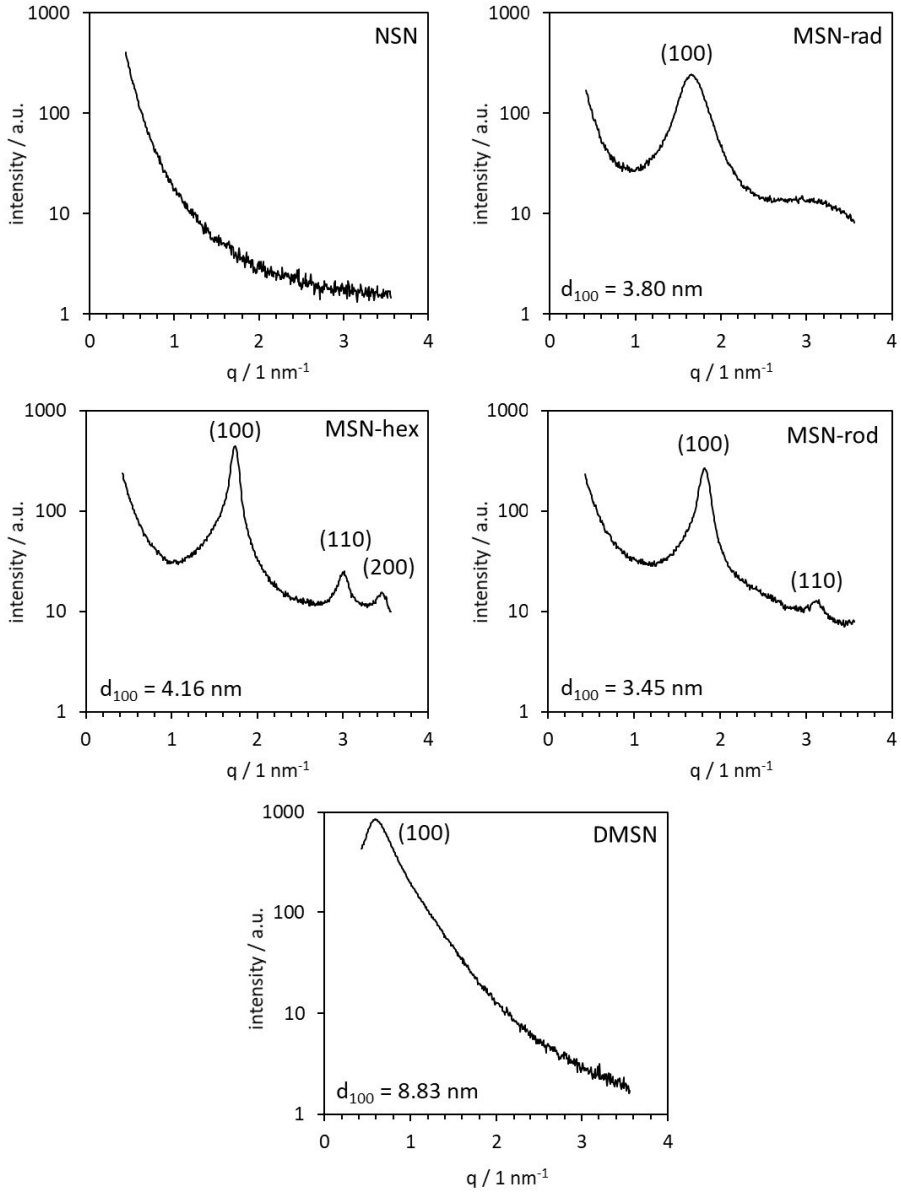

Figure S3. Small-angle x-ray scattering (SAXS) measurement of NSN, MSN-rad, MSN-hex, MSN-rod and DMSN. Calculated d-spacings (d_{100}) at the first order maximum are indicated in the diffractograms.

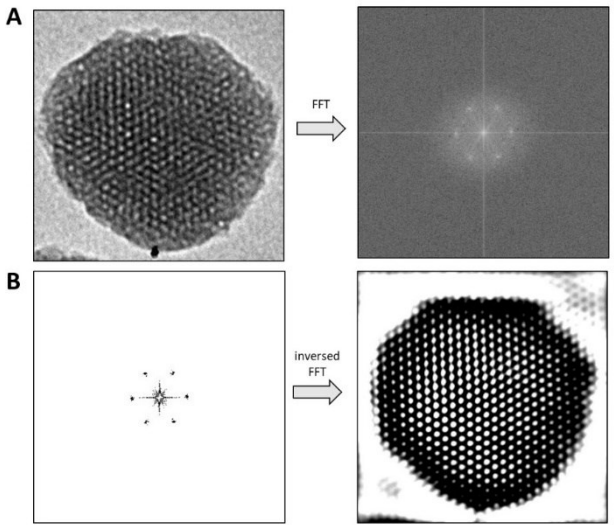

Figure S2. A) fast Fourier transformation (FFT) of a representative TEM image of MSN-hex. B) frequency range filtering of the diffraction pattern and subsequent inverse FFT revealing the electron diffracting pore structures.

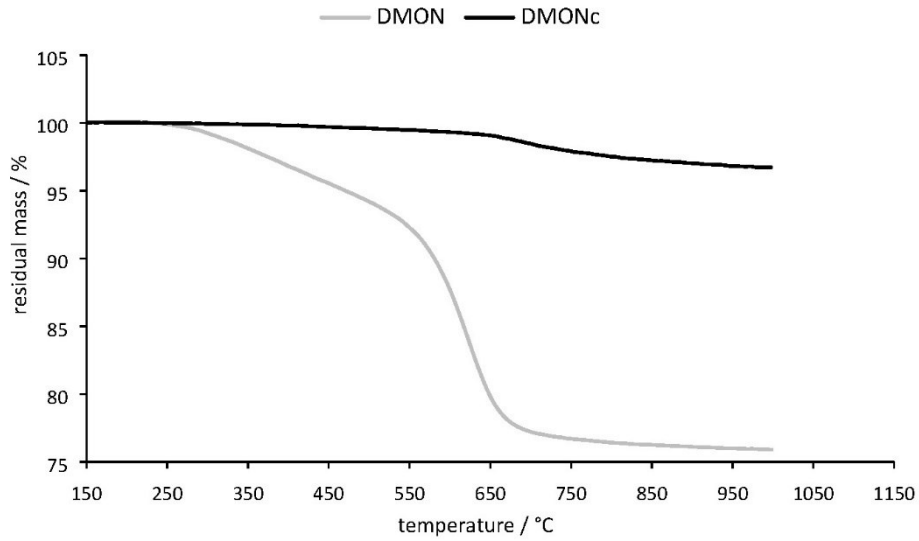

Figure S3. Thermogravimetric analysis (residual mass plots) of samples DMON and DMONc.

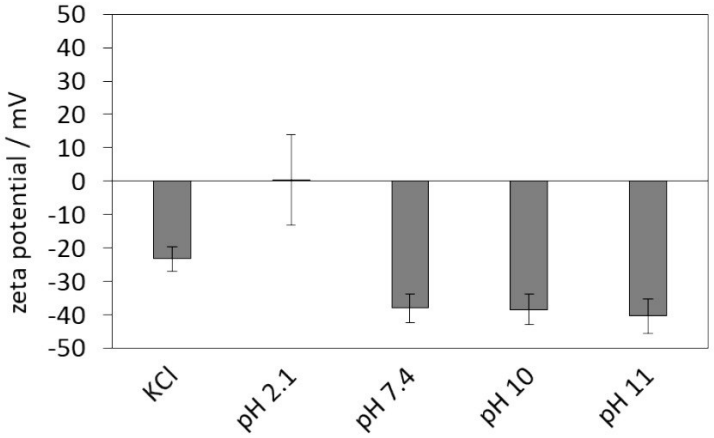

Figure S4. Exemplary zeta potentials of all-silica MSNrad in 1 mM KCl, 12 mM phosphate buffer (pH 2.1 and 7.4) or 12 mM carbonate buffer (pH 10 and 11) (n = 3, mean ± SD).

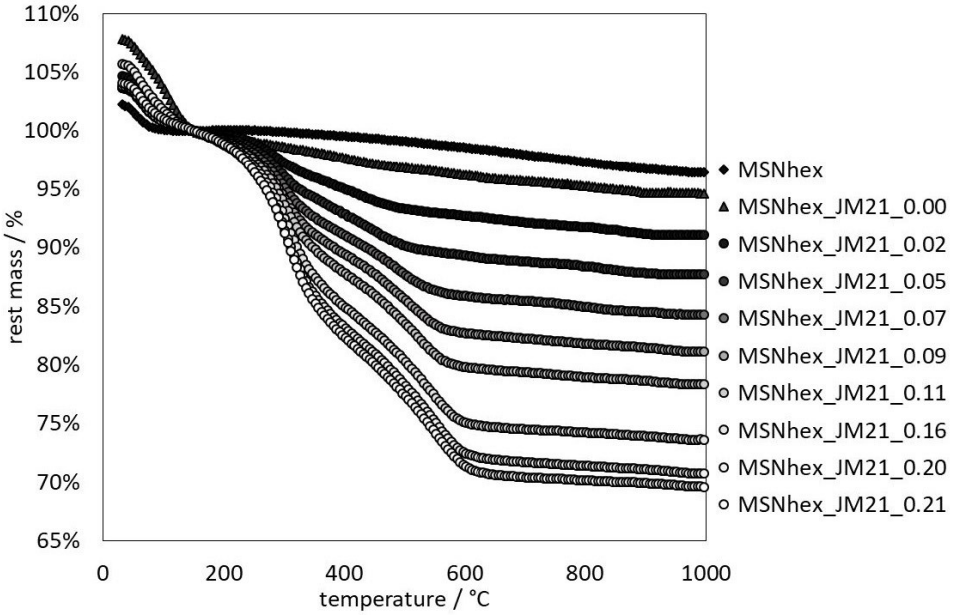

Figure S7. Exemplary thermogravimetric measurements of JM21 loaded MSNhex. The amount of JM21 determined via UV/Vis is indicated in the figure's legend as µmol m^{-2}.

Table S1. Characterization of silica nanoparticles. Specific surface areas were determined by BET analysis of nitrogen sorption measurements at 77 K. The particles' pore diameter and pore volume were calculated by NLDFT analysis for silica (equilibrium model) in the relative pressure range from 0 to 0.9. Zeta potentials were measured in aqueous 25 mM Hepes buffer (pH 7.2). The particle diameter was determined by TEM.

	MSNrod	**MSNrad**
diameter / nm	198 ± 26 (length) 105 ± 14 (width)	150 ± 13
Surface area / $m^2 \cdot g^{-1}$	1031	986
Pore diameter / nm	3.7	3.2
Pore volume (0.9 p p_0^{-1}) / $cm^3 \cdot g^{-1}$	0.79	0.65
Zeta-potential / mV	-40 ± 5	-39 ± 4

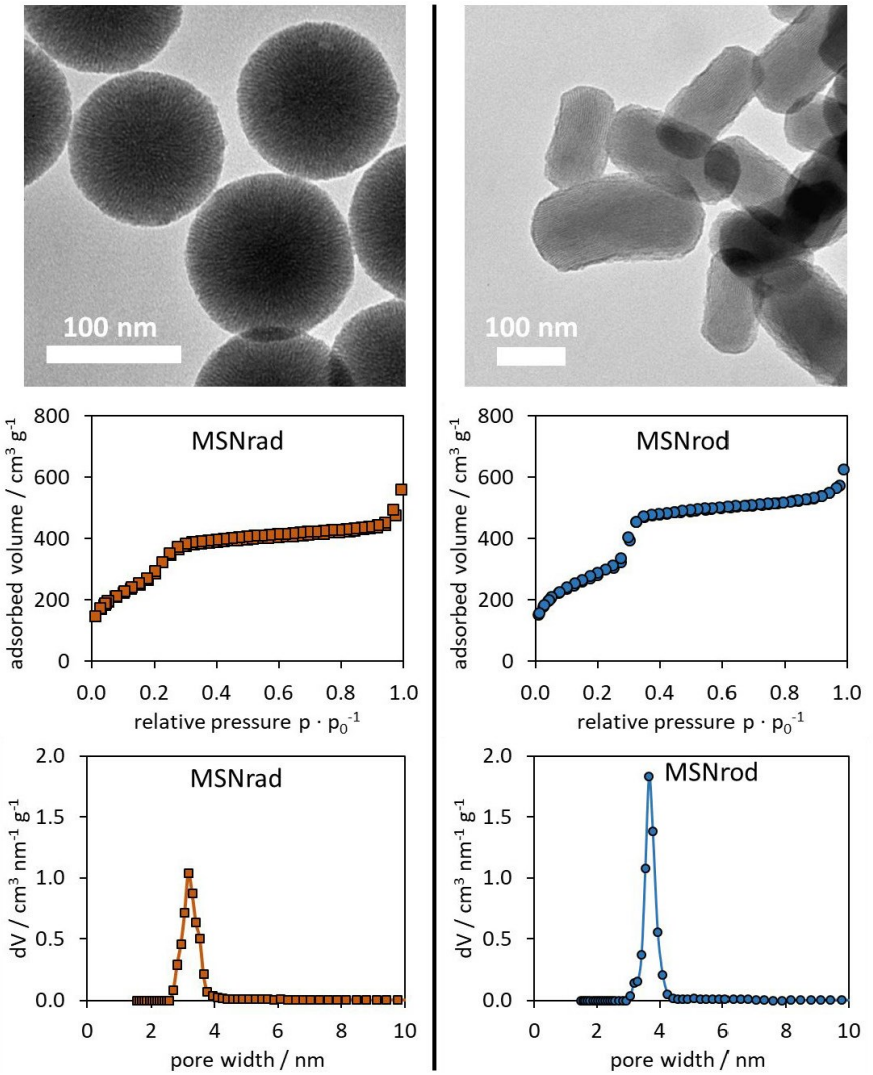

Figure S8. Transmission electron microscopy and nitrogen sorption measurements at 77 K of MSNrad (left) and MSNrod (right). Pore-size distribution curves were calculated using the equilibrium NLDFT kernel developed for silica in the relative pressure range from 0 to 0.9.

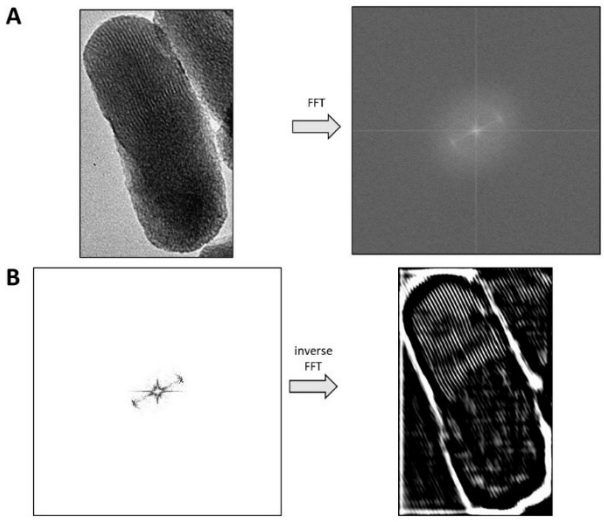

Figure S9. A) fast Fourier transformation (FFT) of a representative TEM image of MSN-rod. B) frequency range filtering of the diffraction pattern and subsequent inverse FFT revealing the electron diffracting pore structures.

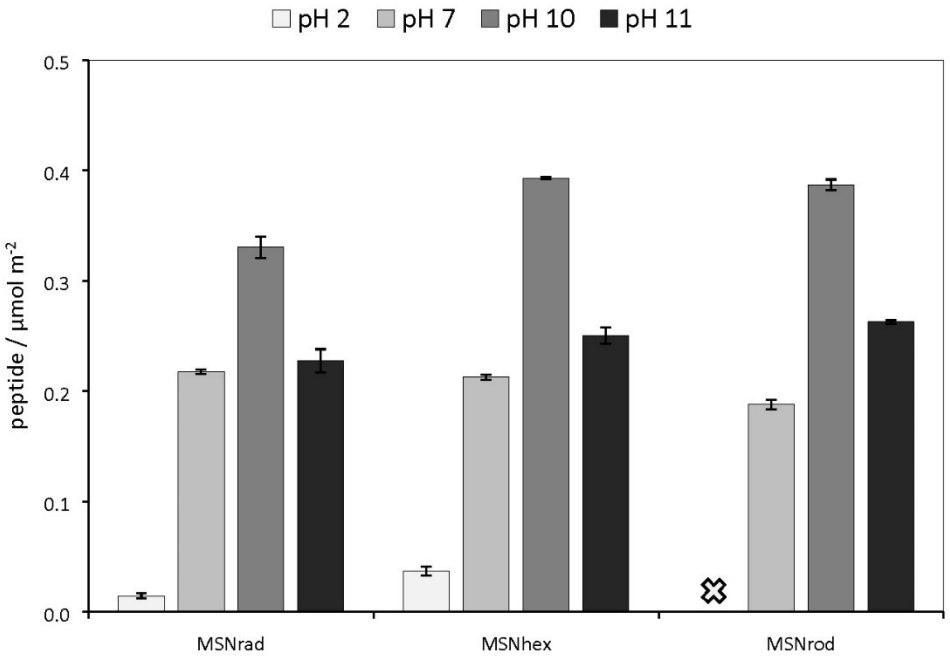

Figure S10. pH-dependent loading degrees for MSNrad, MSNhex and MSNrod. Initial peptide loading concentrations were 2.5 mM at pH 7 (MSNrod: 2 mM), 4 mM at pH 10 and pH 11, respectively (n = 3, mean ± SD).

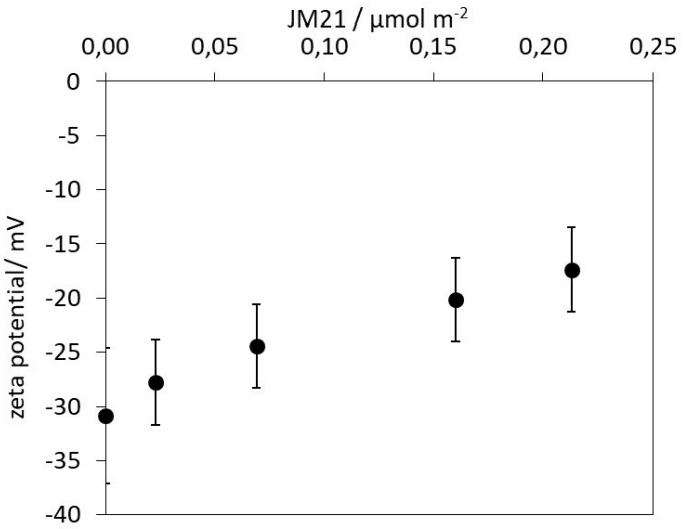

Figure S11. Zeta potential measurements in 25 mM HEPES buffer at pH 7.2 of MSNhex loaded with different amounts of JM#21 (n = 3, mean ± SD).

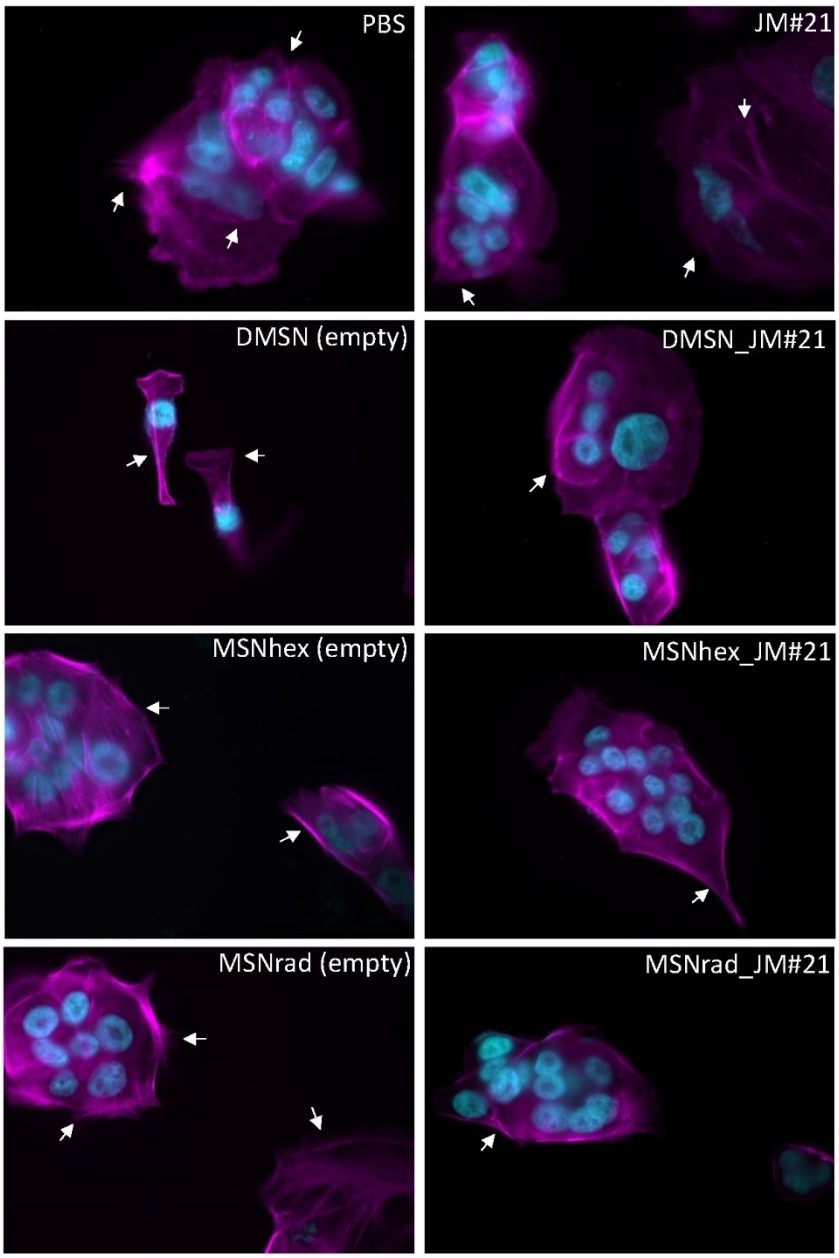

Figure S12. Exemplary fluorescence images of Panc354 treated with CXCL12 (10 µM), together with either PBS, JM#21 (10 µM), non-loaded MSNhex and DMSN (empty) or peptide-loaded MSNhex (30 wt% JM#21)

and DMSN (27 wt% JM#21) in RPMI/10 % FCS for 24 h at 37°C. The particle concentration was normalized to 10 µM of JM#21 at full release. violet: cytoskeleton, blue: cell nuclei, white arrows: indication of mesenchymal-like structural change including stress fibers, spindle like shape of the cell and actin structural changes.

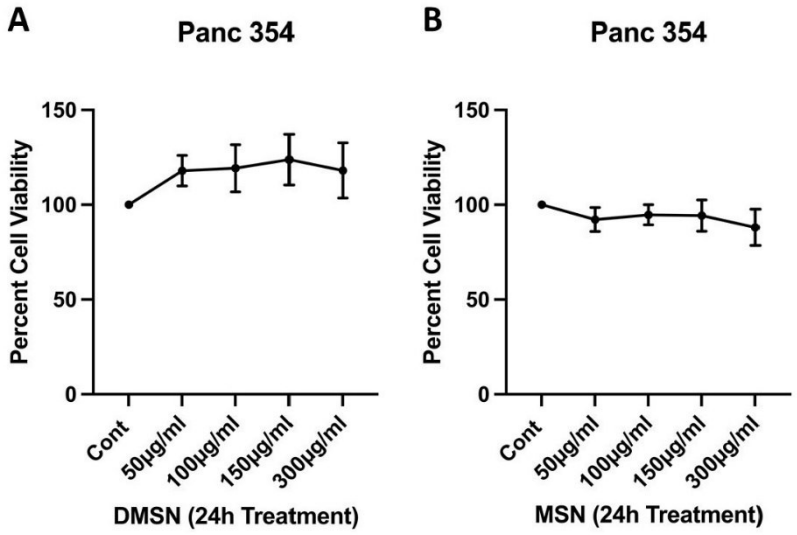

Figure S13. Cell viability measurements of Panc354 cells treated with either A) DMSN or B) MSNhex ("MSN") at different silica concentrations (normalized on residual mass at 600°C) for 24 h at 37°C. Cell culture medium served as control (cont).

VIII List of publications and Curriculum Vitae

1. List of publications during PhD research

Journal articles

- Abeer MM, Rewatkar P, Qu Z, Talekar M, Kleitz F, Schmid R, Lindén M, Kumeria T, Popat A. “Silica nanoparticles: A promising platform for enhanced oral delivery of macromolecules.” J Control Release. 2020 Oct 10; 326:544-555. https://doi.org/10.1016/j.jconrel.2020.07.021.
- Beitzinger B, Gerbl F, Vomhof T, Schmid R, Noschka R, Rodriguez A, Wiese S, Weidinger G, Ständker L, Walther P, Michaelis J, Lindén M, Stenger S. “Delivery by Dendritic Mesoporous Silica Nanoparticles Enhances the Antimicrobial Activity of a Napsin-Derived Peptide Against Intracellular Mycobacterium tuberculosis”. Adv Healthc Mater. 2021 Jul; 10(14): e2100453. https://doi.org/10.1002/adhm.202100453.
- Schmid R*, Neffgen N*, Lindén M. “Straightforward adsorption-based formulation of mesoporous silica nanoparticles for drug delivery applications”. J Colloid Interface Sci. 2023 Mar 8; 640:961-974. https://doi.org/10.1016/j.jcis.2023.03.012. (*equal contribution)
- Schmid R, Kaiser J, Willbold R, Walther N, Wittig R, Lindén M. “Towards a simple in vitro surface chemistry pre-screening method for nanoparticles to be used for drug delivery to solid tumours”. Biomater Sci. 2023 Sep 12; 11(18): 6287-6298. https://doi.org/10.1039/D3BM00966A.
- Schmid R, Volcic M, Fischer S, Qu Z, Barth H, Popat A, Kirchhoff F, Lindén M. “Surface functionalization affects the retention and biodistribution of orally administered mesoporous silica nanoparticles in a colitis mouse model”. Sci. Rep., 2023, 13, 20175. https://doi.org/10.1038/s41598-023-47445-6.
- Beitzinger B*, Schmid R*, Jung C, Tiwary K, Hermann P, Jacob T, Lindén M. “Confinement and polarity effects on the peptide packing density on mesoporous silica nanoparticles”. Langmuir; 2024, 40, 8, 4294–4305. https://doi.org/10.1021/acs.langmuir.3c03513. (*equal contribution)

Posters

- Schmid R, König D, Lindén M. „Surface functionalization of mesoporous silica nanoparticles through adsorption of the cationic polymer chitosan", 31. Deutsche Zeolith-Tagung, 2019, Dresden, Germany
- Schmid R, Fischer S, Seifert J, Barth H, Lindén M. „Synthesis and toxicological evaluation of chitosan-functionalized mesoporous silica nanoparticles for oral drug delivery", Drug Delivery CRS Australia, 2019, Brisbane, Australia
- Beitzinger B*, Schmid R*, Schweizer F, Harms M, Münch J, Lindén M. „Adsorption studies of a novel CXCR4 antagonist peptide onto mesoporous silica nanoparticles", Controlled Release Society Annual Meeting, 2019, Valencia, Spain. (*equal contribution)
- Schmid R, Lindén M. „ Surface functionalization of mesoporous silica nanoparticles and loading with therapeutic peptides", 2019, Symposium Sonderforschungsbereich SFB 1279, Lindenberg, Germany

Presentations

- Schmid R*, Pochert A, Beck M, Beitzinger B, Godaly G, Tenland E, Volcic M, Fischer S, Qu Z, Barth H, Popat A, Kirchhoff F, Lindén M*. „Pulmonary and oral administration of mesoporous silica nanoparticles", 2023, Symposium SFB 1279, Ulm, Germany (*presenting authors)
- Schmid R*, Beitzinger B*, Lindén M. Zwischenbericht zum Teilprojekt „Mesoporous silica micro- and nanoparticles for controlled release of peptide-based drugs", 2021, Symposium Sonderforschungsbereich SFB 1279, Ulm, Germany (*presenting authors)

Posters during master's curriculum

- Schmid R, Baumann B, Wilbold R, Wittig R, Lindén M. „Modulation of cellular uptake kinetics of mesoporous silica nanoparticles in hydrogels through surface functionalization", Symposium Nano-BW, 2018, Bad Herrenalb, Germany
- Schmid R, Baumann B, Wilbold R, Wittig R, Lindén M. „Modulation of cellular uptake kinetics of mesoporous silica nanoparticles in hydrogels through surface functionalization", 30. Deutsche Zeolith-Tagung, 2018, Kiel, Germany

2. Curriculum Vitae

Roman Schmid

born 1992 in Isny im Allgäu, Germany

University

10/2017 – 07/2023	Promotion Chemistry Institute for Inorganic Chemistry II Ulm University
10/2014 – 10/2017	Master of Science (MSc) in Chemistry and Management Ulm University Master's thesis: "Oberflächenfunktionalisierung von mesoporösen Silikananopartikeln und deren Verwendung in einem Peptid-basierten Hydrogel-Netzwerk"
10/2011 – 09/2014	Bachelor of Science (BSc) in Chemistry and Management Ulm University Bachelor's thesis: "Oberflächenfunktionalisierung von mesoporösen Silikananopartikeln mit PEG-Silanen"

School

09/2002 – 07/2011	Abitur Gymnasium Isny

IX Note of thanks

Mein ganz besonderer Dank gilt meinem Doktorvater Mika Lindén für seine fortwährende Unterstützung und Motivation über die Jahre hinweg. Sein fachliches Wissen und immerwährende Bereitschaft für wissenschaftliche Diskussionen waren mir stets eine große Hilfe und haben zu einem großen Teil zum Erfolg dieser Arbeit beigetragen. Auch konnte ich aufgrund seiner Förderung und Vernetzung in der Forschungsgemeinschaft an zahlreichen Konferenzen sowie einem Forschungsaufenthalt in Australien teilnehmen, was ein wichtiger Bestandteil dieser Arbeit darstellt. Für die zahlreichen fachlichen wie auch persönlichen Gespräche möchte ich mich herzlich bedanken.

Mein Dank gilt darüber hinaus Holger Barth für das Erstellen des Zweitgutachtens sowie die Kooperation im Rahmen der Publikation I.

Ich danke allen Kooperationspartnern mit deren Unterstützung die in dieser Arbeit aufgeführten Publikationen entstanden sind. Darüber hinaus gilt mein Dank den Projekt-, Bachelor-, und Masterstudenten, welche ich über die Jahre betreut habe.

Mein persönlicher Dank gilt den Mitgliedern des Instituts Anorganische Chemie II für schöne Momente wie beispielsweise die obligatorische Gruppenteilnahme am Chemikerfasching oder das Beisammensitzen während sommerlicher Grillabende. Insbesondere möchte ich hier Conny und Jürgen erwähnen für die vielen auflockernden Unterhaltungen.

Nathalie und Bastian möchte ich für eine hervorragende jahrelange Laborgemeinschaft und Zusammenarbeit danken, welche durch viele fachliche und persönliche Gespräche, sowie zahlreiche Partien Schach bereichert wurde.

Zuletzt gilt mein persönlicher Dank meiner Familie, insbesondere Anja, ohne deren jahrelange Unterstützung während meines Studiums und meiner Promotion diese Arbeit in vorliegender Form nicht möglich gewesen wäre. Vielen herzlichen Dank!

X Eidesstattliche Erklärung

Ich versichere hiermit, dass ich die Arbeit selbständig angefertigt habe und keine anderen als die angegebenen Quellen und Hilfsmittel benutzt sowie die wörtlich oder inhaltlich übernommenen Stellen als solche kenntlich gemacht habe und die Satzung der Universität Ulm zur Sicherung guter wissenschaftlicher Praxis in der jeweils gültigen Fassung beachtet habe.

Roman Schmid	Ort, Datum